Benchmarking Bimolecular Behavior and Beyond

by

Laura Dornshuld

(Under the Direction of Henry F. Schaefer III)

Abstract

For small molecular systems, advanced quantum chemical methods can be applied to deliver highly accurate energies and provide further understanding for future studies. The first project in this dissertation investigates the hydration behavior of the tetrafluoroborate anion with up to four water molecules ($BF_4^-(H_2O)_{n=1,2,3,4}$). The study identifies new hydration motifs and highlights the impact of these interactions on vibrational frequency shifts and dissociation energies, providing insights into the behavior of ionic liquids. The second project explores the hydrogen abstraction reactions of the ethynyl radical, C_2H, with various hydrogen donors, including HNCO, *cis*/*trans*-HONO, C_2H_4, and CH_3OH using state-of-the-art computational methods. The study refines reaction enthalpies and barrier heights to subchemical accuracy. The computed rate constants over a broad temperature range offer valuable benchmarks for future experimental and theoretical investigations. The third project further bolsters the benchmarks of the Concordant Mode Approach (CMA), a promising new method that increases the feasibility of larger system sizes and higher levels of theory in quantum chemical computations of molecular vibrational frequencies. Computations targeting CCSD(T)/aug-cc-pVTZ (coupled cluster singles and doubles with perturbative triples using an augmented correlation-consistent polarized-valence triple-ζ basis set) were performed on several molecules from the S22 test set.

Index Words: focal point analysis, hydrogen atom abstraction, noncovalent interactions, dimers, benchmarking

Benchmarking Bimolecular Behavior and Beyond

by

Laura Dornshuld

B.S., Mississippi State University, 2021

A Dissertation Submitted to the Graduate Faculty of The University of Georgia in Partial Fulfillment of the Requirements for the Degree

Doctor of Philosophy

Athens, Georgia

2025

Benchmarking Bimolecular Behavior and Beyond

by

Laura Dornshuld

Major Professor: Henry F. Schaefer III

Committee: Gary E. Douberly
Geoffrey D. Smith

Electronic version approved:

Ron Wolcott
Vice Provost for Graduate Education and Dean of the Graduate School
The University of Georgia
May 2025

Dedication

To my husband. I couldn't have done it without you.

Acknowledgements

I would like to acknowledge Dr. Schaefer for his support in all things, not just my research. To my committee for their time and feedback on all my milestones. I wouldn't be here without Dr. Webster or Dr. Tschumper and their encouragement during my undergraduate research. To Ian Beck, for sharing an office with me these four long years. To my family, who supported me throughout this entire journey. And finally, to my husband, words cannot describe how thankful I am for you.

Table of Contents

Acknowledgements v

List of Tables xxiii

List of Figures xxvi

1 Introduction 1

1.1 The Schrödinger Equation 1

1.2 The Born-Oppenheimer Approximation 1

1.3 The Wavefunction 2

1.4 Hartree–Fock 4

1.5 Configuration Interaction 7

1.6 Perturbation Theory 8

1.7 Coupled-Cluster Theory 10

1.8 Basis Sets 12

1.9 Focal Point Analysis 15

1.10 Potential Energy Surfaces and Reaction Pathways 15

1.11 Vibrational Frequencies 19

2 Competition Between Solvent···Solvent and Solvent···Solute Interactions in the Microhydration of the Tetrafluoroborate Anion, $BF_4^-(H_2O)_{n=1,2,3,4}$ 24

2.1 Abstract 25

2.2 Introduction 26

2.3 Computational Details 29

2.4 Results and Discussion . . . 33
2.5 Conclusions . . . 51

3 Ethynyl Radical Hydrogen Abstraction Energetics and Kinetics Utilizing High-Level Theory . . . 53
3.1 Abstract . . . 54
3.2 Introduction . . . 54
3.3 Theoretical Methods . . . 56
3.4 Results and Discussion . . . 59
3.5 Conclusions . . . 74

4 A Concordant Mode Approach to Intermolecular Vibrations . . . 75
4.1 Abstract . . . 76
4.2 Introduction . . . 76
4.3 Computational Methods . . . 78
4.4 CMA Protocol . . . 80
4.5 Benchmarking Level B for CMA-0A . . . 82
4.6 Benchmarking CMA-2A . . . 86
4.7 Conclusions . . . 88

5 Conclusion . . . 89

References . . . 91

A Supplementary Information for Project 1 . . . 118

B Supplementary Information for Project 2 . . . 184
B.1 Reactants . . . 184
B.2 Products . . . 190
B.3 Transition States . . . 196

B.4 Pre-reactive complex 202

C Supplementary Information for Project 3 205

List of Tables

2.1 Relative electronic energies (ΔE in kcal mol^{-1}) and number of imaginary modes (n_i) of the BF_4^- $(H_2O)_{n=1,2,3,4}$ structures optimized with various methods and the haTZ basis set. 36

2.2 Dissociation energies (in kcal mol^{-1}) obtained without the CP procedure for the BF_4^- $(H_2O)_{n=1,2,3,4}$ minima optimized with various methods and the haTZ basis set. 41

2.3 The harmonic OH stretching frequencies (ω in cm^{-1}) for H_2O and BF_4^- $(H_2O)_{n=1,2}$ minima computed with an haTZ basis set. 44

2.4 The harmonic OH stretching frequencies (ω in cm^{-1}) for H_2O and BF_4^- $(H_2O)_{n=3}$ minima computed with an haTZ basis set. 46

2.5 The harmonic OH stretching frequencies (ω in cm^{-1}) for BF_4^- $(H_2O)_{n=4}$ minima computed with an haTZ basis set. 48

2.6 Average absolute deviations (AvgAD) and max absolute deviations (MaxAD) of the relative energies (in kcal mol^{-1}), dissociation energies (in kcal mol^{-1}), and the harmonic OH stretching frequencies (in cm^{-1}) computed with DFT and MP2 from CCSD(T) for n=1, 2 and 2b:Mb for n=3, 4. 50

3.1 Representative incremental focal point table for the products of the C_2H + HNCO $\rightarrow$ C_2H_2 + NCO reaction relative to the reactants (in kcal mol^{-1}). 58

3.2 Enthalpies at 0K (ΔH_{0K} in kcal mol^{-1} for products relative to reactants (C_2H + HX $\rightarrow$ C_2H_2 + X) 60

3.3 Enthalpies at 0K (ΔH_{0K} in kcal mol^{-1} for transition states relative to reactants (C_2H + HX $\rightarrow$ C_2H_2 + X) 62
3.4 Reaction enthalpies ($\Delta_r H$), reaction barrier heights ($\Delta H^{\ddagger}$), and transition state imaginary frequencies ($\omega^{\ddagger}$) for C_2H + HX hydrogen abstractions at the CCSDT(Q)/CBS//CCSD(T)-F12a/cc-pVTZ-F12 level of theory. 63
3.5 Comparison of the C_2H + HNCO $\rightarrow$ C_2H_2 + NCO abstraction at different levels of theory. 65
3.6 Comparison of the C_2H + C_2H_4 $\rightarrow$ C_2H_2 + C_2H_3 abstraction at different levels of theory. 71
3.7 Rate constants for C_2H + HX $\rightarrow$ C_2H_2 + X abstractions in cm^3 molecule^{-1} s^{-1}. 72

4.1 Summary Statistics within the test set of CMA-0A Residuals for the CCSD(T)/aTZ Harmonic Vibrational Frequencies (ϵ, cm^{-1}) and ZPVEs (Δ, cm^{-1}). 82
4.2 Residuals (in cm^{-1}) of the CMA-0A data from the reference harmonic frequencies (in cm^{-1}) for $(H_2O)_2$ using natural internal coordinates with cartesian force constants. 83
4.3 Residuals (in cm^{-1}) of the CMA-0A data from the reference harmonic frequencies (in cm^{-1}) for $(HCOOH)_2$ using natural internal coordinates cartesian force constants. 85
4.4 The only cases within the frequencies of the complexes that contain benzene with CMA-0A-nc[CCSD(T)/aTZ, MP2/haTZ] residuals (ϵ, cm^{-1}) greater than 1.5 cm^{-1} in magnitude, together with CMA-0A-nc[CCSD(T)/aTZ, MP2/aTZ] residuals. 86

4.5 The only cases within the set of benchmark frequencies with CMA-0A-nc[CCSD(T)/aTZ, MP2/haTZ] residuals (ϵ, cm^{-1}) greater than 2.5 cm^{-1} in magnitude, together with the corresponding CMA-1A and CMA-2A results that target these outliers. 87

A.1 Dissociation energies (D_e in kcal mol^{-1}) of the lowest-energy monohydrate (C_{2v} DI_1) and dihydrate (C_s DI_1WI_1) structures computed with and without the CP procedure with various methods and the haTZ basis set. 118

A.2 Dissociation energies (D_e in kcal mol^{-1}) of the lowest-energy trihydrate (C_3 WI_3) and tetrahydrate (C_1 DI_1WI_3) structures computed with and without the CP procedure with various methods and the haTZ basis set. 118

A.3 Harmonic vibrational frequencies (ω in cm^{-1}) and infrared intensities (IR in km mol^{-1}) for H_2O computed with the haTZ basis set. 119

A.4 Harmonic vibrational frequencies (ω in cm^{-1}) and infrared intensities (IR in km mol^{-1}) for BF_4^- computed with the haTZ basis set. 119

A.5 Harmonic vibrational frequencies (ω in cm^{-1}) and infrared intensities (IR in km mol^{-1}) for the C_{2v} DI_1 monohydrate structure computed with the haTZ basis set. 119

A.6 CCSD(T)/haTZ harmonic vibrational frequencies (ω in cm^{-1}) and infrared intensities (IR in km mol^{-1}) for the C_{2v} DI_1 monohydrate structure computed analytically and via finite differences of analytic gradients and dipole moments. 120

A.7 Harmonic vibrational frequencies (ω in cm^{-1}) and infrared intensities (IR in km mol^{-1}) for the C_s BI_1 monohydrate structure computed with the haTZ basis set. 121

A.8 Harmonic vibrational frequencies (ω in cm^{-1}) and infrared intensities (IR in km mol^{-1}) for the C_s DI_2 dihydrate structure computed with the haTZ basis set. 122

A.9 Harmonic vibrational frequencies (ω in cm^{-1}) and infrared intensities (IR in km mol^{-1}) for the C_s DI_1WI_1 dihydrate structure computed with the haTZ basis set. 123

A.10 Harmonic vibrational frequencies (ω in cm^{-1}) and infrared intensities (IR in km mol^{-1}) for the D_{2d} DI_2 dihydrate structure computed with the haTZ basis set. 124

A.11 Harmonic vibrational frequencies (ω in cm^{-1}) and infrared intensities (IR in km mol^{-1}) for the C_s DI_1BI_1 dihydrate structure computed with the haTZ basis set. 125

A.12 Harmonic vibrational frequencies (ω in cm^{-1}) and infrared intensities (IR in km mol^{-1}) for the C_s DI_1WW_1 dihydrate structure computed with the haTZ basis set. 126

A.13 Harmonic vibrational frequencies (ω in cm^{-1}) and infrared intensities (IR in km mol^{-1}) for the C_{3v} DI_3 trihydrate structure computed with the haTZ basis set. 127

A.14 Harmonic vibrational frequencies (ω in cm^{-1}) and infrared intensities (IR in km mol^{-1}) for the C_s DI_2WI_1 trihydrate structure computed with the haTZ basis set. 128

A.15 Harmonic vibrational frequencies (ω in cm^{-1}) and infrared intensities (IR in km mol^{-1}) for the C_3 WI_3 trihydrate structure computed with the haTZ basis set. 129

A.16 Harmonic vibrational frequencies (ω in cm^{-1}) and infrared intensities (IR in km mol^{-1}) for the C_s DI_2W_1 trihydrate structure computed with the haTZ basis set. 130

A.17 Harmonic vibrational frequencies (ω in cm^{-1}) and infrared intensities (IR in km mol^{-1}) for the C_1 DI_2WW_1 trihydrate structure computed with the haTZ basis set. 131
A.18 Harmonic vibrational frequencies (ω in cm^{-1}) and infrared intensities (IR in km mol^{-1}) for the C_s DI_4 tetrahydrate structure computed with the haTZ basis set. 132
A.19 Harmonic vibrational frequencies (ω in cm^{-1}) and infrared intensities (IR in km mol^{-1}) for the C_s DI_3WI_1 tetrahydrate structure computed with the haTZ basis set. 133
A.20 Harmonic vibrational frequencies (ω in cm^{-1}) and infrared intensities (IR in km mol^{-1}) for the C_s DI_2WI_2 tetrahydrate structure computed with the haTZ basis set. 134
A.21 Harmonic vibrational frequencies (ω in cm^{-1}) and infrared intensities (IR in km mol^{-1}) for the C_s DI_2WW_2 tetrahydrate structure computed with the haTZ basis set. 135
A.22 Harmonic vibrational frequencies (ω in cm^{-1}) and infrared intensities (IR in km mol^{-1}) for the C_1 DI_1WI_3 tetrahydrate structure computed with the haTZ basis set. 136
A.23 Harmonic vibrational frequencies (ω in cm^{-1}) and infrared intensities (IR in km mol^{-1}) for the C_1 DI_2W_2 tetrahydrate structure computed with the haTZ basis set. 137
A.24 Harmonic vibrational frequencies (ω in cm^{-1}) and infrared intensities (IR in km mol^{-1}) for the D_2 DI_4 tetrahydrate structure computed with the haTZ basis set. 138
A.25 Harmonic vibrational frequencies (ω in cm^{-1}) and infrared intensities (IR in km mol^{-1}) for the S_4 DI_4 tetrahydrate structure computed with the haTZ basis set. 139

A.26 Cartesian coordinates in Angstroms (Å) for the C_{2v} DI_1 complex at the CCSD(T)/haTZ level of theory. 140
A.27 Cartesian coordinates in Angstroms (Å) for the C_{2v} DI_1 complex at the MP2/haTZ level of theory. 140
A.28 Cartesian coordinates in Angstroms (Å) for the C_{2v} DI_1 complex at the B3LYP/haTZ level of theory. 140
A.29 Cartesian coordinates in Angstroms (Å) for the C_{2v} DI_1 complex at the B3LYP–B3BJ/haTZ level of theory. 141
A.30 Cartesian coordinates in Angstroms (Å) for the C_{2v} DI_1 complex at the M06–2X/haTZ level of theory. 141
A.31 Cartesian coordinates in Angstroms (Å) for the C_s BI_1 complex at the CCSD(T)/haTZ level of theory. 141
A.32 Cartesian coordinates in Angstroms (Å) for the C_s BI_1 complex at the MP2/haTZ level of theory. 142
A.33 Cartesian coordinates in Angstroms (Å) for the C_s BI_1 complex at the B3LYP/haTZ level of theory. 142
A.34 Cartesian coordinates in Angstroms (Å) for the C_s BI_1 complex at the B3LYP–B3BJ/haTZ level of theory. 142
A.35 Cartesian coordinates in Angstroms (Å) for the C_s BI_1 complex at the M06–2X/haTZ level of theory. 143
A.36 Cartesian coordinates in Angstroms (Å) for the C_s DI_2 complex at the CCSD(T):MP2/haTZ level of theory. 143
A.37 Cartesian coordinates in Angstroms (Å) for the C_s DI_2 complex at the CCSD(T)/haTZ level of theory. 143
A.38 Cartesian coordinates in Angstroms (Å) for the C_s DI_2 complex at the MP2/haTZ level of theory. 144

A.39 Cartesian coordinates in Angstroms (Å) for the C_s DI_2 complex at the B3LYP/haTZ level of theory. 144
A.40 Cartesian coordinates in Angstroms (Å) for the C_s DI_2 complex at the B3LYP–B3BJ/haTZ level of theory. 144
A.41 Cartesian coordinates in Angstroms (Å) for the C_s DI_2 complex at the M06–2X/haTZ level of theory. 145
A.42 Cartesian coordinates in Angstroms (Å) for the C_s DI_1WI_1 complex at the CCSD(T):MP2/haTZ level of theory. 145
A.43 Cartesian coordinates in Angstroms (Å) for the C_s DI_1WI_1 complex at the CCSD(T)/haTZ level of theory. 145
A.44 Cartesian coordinates in Angstroms (Å) for the C_s DI_1WI_1 complex at the MP2/haTZ level of theory. 146
A.45 Cartesian coordinates in Angstroms (Å) for the C_s DI_1WI_1 complex at the B3LYP/haTZ level of theory. 146
A.46 Cartesian coordinates in Angstroms (Å) for the C_s DI_1WI_1 complex at the B3LYP–B3BJ/haTZ level of theory. 146
A.47 Cartesian coordinates in Angstroms (Å) for the C_s DI_1WI_1 complex at the M06–2X/haTZ level of theory. 147
A.48 Cartesian coordinates in Angstroms (Å) for the D_{2d} DI_2 complex at the CCSD(T):MP2/haTZ level of theory. 147
A.49 Cartesian coordinates in Angstroms (Å) for the D_{2d} DI_2 complex at the CCSD(T)/haTZ level of theory. 147
A.50 Cartesian coordinates in Angstroms (Å) for the D_{2d} DI_2 complex at the MP2/haTZ level of theory. 148
A.51 Cartesian coordinates in Angstroms (Å) for the D_{2d} DI_2 complex at the B3LYP/haTZ level of theory. 148

A.52 Cartesian coordinates in Angstroms (Å) for the D_{2d} DI_2 complex at the B3LYP–B3BJ/haTZ level of theory. 148
A.53 Cartesian coordinates in Angstroms (Å) for the D_{2d} DI_2 complex at the M06–2X/haTZ level of theory. 149
A.54 Cartesian coordinates in Angstroms (Å) for the C_s DI_1BI_1 complex at the CCSD(T):MP2/haTZ level of theory. 149
A.55 Cartesian coordinates in Angstroms (Å) for the C_s DI_1BI_1 complex at the CCSD(T)/haTZ level of theory. 149
A.56 Cartesian coordinates in Angstroms (Å) for the C_s DI_1BI_1 complex at the MP2/haTZ level of theory. 150
A.57 Cartesian coordinates in Angstroms (Å) for the C_s DI_1BI_1 complex at the B3LYP/haTZ level of theory. 150
A.58 Cartesian coordinates in Angstroms (Å) for the C_s DI_1BI_1 complex at the B3LYP–B3BJ/haTZ level of theory. 150
A.59 Cartesian coordinates in Angstroms (Å) for the C_s DI_1BI_1 complex at the M06–2X/haTZ level of theory. 151
A.60 Cartesian coordinates in Angstroms (Å) for the C_s DI_1W_1 complex at the B3LYP/haTZ level of theory. 151
A.61 Cartesian coordinates in Angstroms (Å) for the C_{3v} DI_3 complex at the CCSD(T):MP2/haTZ level of theory. 152
A.62 Cartesian coordinates in Angstroms (Å) for the C_{3v} DI_3 complex at the MP2/haTZ level of theory. 152
A.63 Cartesian coordinates in Angstroms (Å) for the C_{3v} DI_3 complex at the B3LYP/haTZ level of theory. 153
A.64 Cartesian coordinates in Angstroms (Å) for the C_{3v} DI_3 complex at the B3LYP–B3BJ/haTZ level of theory. 154

A.65 Cartesian coordinates in Angstroms (Å) for the C_{3v} DI_3 complex at the M06–2X/haTZ level of theory. 154
A.66 Cartesian coordinates in Angstroms (Å) for the C_s DI_2WI_1 complex at the CCSD(T):MP2/haTZ level of theory. 155
A.67 Cartesian coordinates in Angstroms (Å) for the C_s DI_2WI_1 complex at the MP2/haTZ level of theory. 155
A.68 Cartesian coordinates in Angstroms (Å) for the C_s DI_2WI_1 complex at the B3LYP/haTZ level of theory. 156
A.69 Cartesian coordinates in Angstroms (Å) for the C_s DI_2WI_1 complex at the B3LYP–B3BJ/haTZ level of theory. 156
A.70 Cartesian coordinates in Angstroms (Å) for the C_s DI_2WI_1 complex at the M06–2X/haTZ level of theory. 157
A.71 Cartesian coordinates in Angstroms (Å) for the C_3 WI_3 complex at the CCSD(T):MP2/haTZ level of theory. 157
A.72 Cartesian coordinates in Angstroms (Å) for the C_3 WI_3 complex at the MP2/haTZ level of theory. 158
A.73 Cartesian coordinates in Angstroms (Å) for the C_3 WI_3 complex at the B3LYP/haTZ level of theory. 158
A.74 Cartesian coordinates in Angstroms (Å) for the C_3 WI_3 complex at the B3LYP–B3BJ/haTZ level of theory. 159
A.75 Cartesian coordinates in Angstroms (Å) for the C_3 WI_3 complex at the M06–2X/haTZ level of theory. 159
A.76 Cartesian coordinates in Angstroms (Å) for the C_s DI_2W_1 complex at the CCSD(T):MP2/haTZ level of theory. 160
A.77 Cartesian coordinates in Angstroms (Å) for the C_s DI_2W_1 complex at the MP2/haTZ level of theory. 160

A.78 Cartesian coordinates in Angstroms (Å) for the C_s DI_2W_1 complex at the B3LYP/haTZ level of theory. 161
A.79 Cartesian coordinates in Angstroms (Å) for the C_s DI_2W_1 complex at the B3LYP–B3BJ/haTZ level of theory. 161
A.80 Cartesian coordinates in Angstroms (Å) for the C_s DI_2W_1 complex at the M06–2X/haTZ level of theory. 162
A.81 Cartesian coordinates in Angstroms (Å) for the C_1 DI_2W_1 complex at the B3LYP–B3BJ/haTZ level of theory. 162
A.82 Cartesian coordinates in Angstroms (Å) for the C_1 DI_2W_1 complex at the M06–2X/haTZ level of theory. 163
A.83 Cartesian coordinates in Angstroms (Å) for the C_s DI_4 complex at the CCSD(T):MP2/haTZ level of theory. 163
A.84 Cartesian coordinates in Angstroms (Å) for the C_s DI_4 complex at the MP2/haTZ level of theory. 164
A.85 Cartesian coordinates in Angstroms (Å) for the C_s DI_4 complex at the B3LYP/haTZ level of theory. 164
A.86 Cartesian coordinates in Angstroms (Å) for the C_s DI_4 complex at the B3LYP–B3BJ/haTZ level of theory. 165
A.87 Cartesian coordinates in Angstroms (Å) for the C_s DI_4 complex at the M06–2X/haTZ level of theory. 165
A.88 Cartesian coordinates in Angstroms (Å) for the C_s DI_3WI_1 complex at the CCSD(T):MP2/haTZ level of theory. 166
A.89 Cartesian coordinates in Angstroms (Å) for the C_s DI_3WI_1 complex at the MP2/haTZ level of theory. 166
A.90 Cartesian coordinates in Angstroms (Å) for the C_s DI_3WI_1 complex at the B3LYP/haTZ level of theory. 167

A.91 Cartesian coordinates in Angstroms (Å) for the C_s DI_3WI_1 complex at the B3LYP–B3BJ/haTZ level of theory. 167
A.92 Cartesian coordinates in Angstroms (Å) for the C_s DI_3WI_1 complex at the M06–2X/haTZ level of theory. 168
A.93 Cartesian coordinates in Angstroms (Å) for the C_s DI_2WI_2 complex at the CCSD(T):MP2/haTZ level of theory. 168
A.94 Cartesian coordinates in Angstroms (Å) for the C_s DI_2WI_2 complex at the MP2/haTZ level of theory. 169
A.95 Cartesian coordinates in Angstroms (Å) for the C_s DI_2WI_2 complex at the B3LYP/haTZ level of theory. 169
A.96 Cartesian coordinates in Angstroms (Å) for the C_s DI_2WI_2 complex at the B3LYP–B3BJ/haTZ level of theory. 170
A.97 Cartesian coordinates in Angstroms (Å) for the C_s DI_2WI_2 complex at the M06–2X/haTZ level of theory. 170
A.98 Cartesian coordinates in Angstroms (Å) for the C_s DI_2WW_2 complex at the CCSD(T):MP2/haTZ level of theory. 171
A.99 Cartesian coordinates in Angstroms (Å) for the C_s DI_2WW_2 complex at the MP2/haTZ level of theory. 171
A.100 Cartesian coordinates in Angstroms (Å) for the C_s DI_2WW_2 complex at the B3LYP/haTZ level of theory. 172
A.101 Cartesian coordinates in Angstroms (Å) for the C_s DI_2WW_2 complex at the B3LYP–B3BJ/haTZ level of theory. 172
A.102 Cartesian coordinates in Angstroms (Å) for the C_s DI_2WW_2 complex at the M06–2X/haTZ level of theory. 173
A.103 Cartesian coordinates in Angstroms (Å) for the C_1 DI_1WI_3 complex at the CCSD(T):MP2/haTZ level of theory. 173

A.104 Cartesian coordinates in Angstroms (Å) for the C_1 DI_1WI_3 complex at the MP2/haTZ level of theory. 174
A.105 Cartesian coordinates in Angstroms (Å) for the C_1 DI_1WI_3 complex at the B3LYP/haTZ level of theory. 174
A.106 Cartesian coordinates in Angstroms (Å) for the C_1 DI_1WI_3 complex at the B3LYP–B3BJ/haTZ level of theory. 175
A.107 Cartesian coordinates in Angstroms (Å) for the C_1 DI_1WI_3 complex at the M06–2X/haTZ level of theory. 175
A.108 Cartesian coordinates in Angstroms (Å) for the D_2 DI_4 complex at the CCSD(T):MP2/haTZ level of theory. 176
A.109 Cartesian coordinates in Angstroms (Å) for the D_2 DI_4 complex at the MP2/haTZ level of theory. 177
A.110 Cartesian coordinates in Angstroms (Å) for the D_2 DI_4 complex at the B3LYP/haTZ level of theory. 177
A.111 Cartesian coordinates in Angstroms (Å) for the D_2 DI_4 complex at the B3LYP–B3BJ/haTZ level of theory. 178
A.112 Cartesian coordinates in Angstroms (Å) for the D_2 DI_4 complex at the M06–2X/haTZ level of theory. 178
A.113 Cartesian coordinates in Angstroms (Å) for the C_1 DI_2W_2 complex at the CCSD(T):MP2/haTZ level of theory. 179
A.114 Cartesian coordinates in Angstroms (Å) for the C_1 DI_2W_2 complex at the MP2/haTZ level of theory. 179
A.115 Cartesian coordinates in Angstroms (Å) for the C_1 DI_2W_2 complex at the B3LYP/haTZ level of theory. 180
A.116 Cartesian coordinates in Angstroms (Å) for the C_1 DI_2W_2 complex at the B3LYP–B3BJ/haTZ level of theory. 180

A.117 Cartesian coordinates in Angstroms (Å) for the C_1 DI_2W_2 complex at the M06–2X/haTZ level of theory. 181
A.118 Cartesian coordinates in Angstroms (Å) for the S_4 DI_4 complex at the CCSD(T):MP2/haTZ level of theory. 181
A.119 Cartesian coordinates in Angstroms (Å) for the S_4 DI_4 complex at the MP2/haTZ level of theory. 182
A.120 Cartesian coordinates in Angstroms (Å) for the S_4 DI_4 complex at the B3LYP/haTZ level of theory. 182
A.121 Cartesian coordinates in Angstroms (Å) for the S_4 DI_4 complex at the B3LYP–B3BJ/haTZ level of theory. 183
A.122 Cartesian coordinates in Angstroms (Å) for the S_4 DI_4 complex at the M06–2X/haTZ level of theory. 183

C.1 Residuals (in cm^{-1}) of the CMA-0A data from the reference harmonic frequencies (in cm^{-1}) for $(H_2O)_2$ using natural internal coordinates with cartesian force constants. 205
C.2 Residuals (in cm^{-1}) of the CMA-0A data from the reference harmonic frequencies (in cm^{-1}) for $(NH_3)_2$ using natural internal coordinates with cartesian force constants. 206
C.3 Residuals (in cm^{-1}) of the CMA-0A data from the reference harmonic frequencies (in cm^{-1}) for $H_2O\cdots NH_3$ using natural internal coordinates with cartesian force constants. 207
C.4 Residuals (in cm^{-1}) of the CMA-0A data from the reference harmonic frequencies (in cm^{-1}) for $H_2O\cdots C_2H_2$ using natural internal coordinates cartesian force constants. 207
C.5 Residuals (in cm^{-1}) of the CMA-0A data from the reference harmonic frequencies (in cm^{-1}) for $(HCONH_2)_2$ using natural internal coordinates cartesian force constants. 208

C.6 Residuals (in cm^{-1}) of the CMA-0A data from the reference harmonic frequencies (in cm^{-1}) for $(HCOOH)_2$ using natural internal coordinates cartesian force constants. 209
C.7 Residuals (in cm^{-1}) of the CMA-0A data from the reference harmonic frequencies (in cm^{-1}) for $(H_2O)_3$ using natural internal coordinates cartesian force constants. 210
C.8 Residuals (in cm^{-1}) of the CMA-0A data from the reference harmonic frequencies (in cm^{-1}) for $CH_3NO\cdots NH_3$ using natural internal coordinates cartesian force constants. 211
C.9 Residuals (in cm^{-1}) of the CMA-0A data from the reference harmonic frequencies (in cm^{-1}) for $C_2H_4\cdots C_2H_2$ using natural internal coordinates cartesian force constants. 212
C.10 Residuals (in cm^{-1}) of the CMA-0A data from the reference harmonic frequencies (in cm^{-1}) for $(C_2H_4)_2$ using natural internal coordinates cartesian force constants. 213
C.11 Residuals (in cm^{-1}) of the CMA-0A data from the reference harmonic frequencies (in cm^{-1}) for $(HF)_2$ using natural internal coordinates cartesian force constants. 214
C.12 Residuals (in cm^{-1}) of the CMA-0A data from the reference harmonic frequencies (in cm^{-1}) for $(CH_4)_2$ using natural internal coordinates cartesian force constants. 214
C.13 Residuals (in cm^{-1}) of the CMA-0A data from the reference harmonic frequencies (in cm^{-1}) for $CH_3COOH\cdots H_2O$ using natural internal coordinates cartesian force constants. 215
C.14 Residuals (in cm^{-1}) of the CMA-0A data from the reference harmonic frequencies (in cm^{-1}) for Benzene$\cdots$HCN using natural internal coordinates cartesian force constants. 216

C.15 Residuals (in cm^{-1}) of the CMA-0A data from the reference harmonic frequencies (in cm^{-1}) for Benzene$\cdots NH_3$ using natural internal coordinates cartesian force constants. 217
C.16 Residuals (in cm^{-1}) of the CMA-0A data from the reference harmonic frequencies (in cm^{-1}) for Benzene$\cdots H_2O$ using natural internal coordinates cartesian force constants. 218
C.17 Residuals (in cm^{-1}) of the CMA-0A data from the reference harmonic frequencies (in cm^{-1}) for Benzene$\cdots CH_4$ using natural internal coordinates cartesian force constants. 219

List of Figures

2.1 CCSD(T)/haTZ optimized stationary points of $BF_4^-(H_2O)_1$ with select intermolecular R(H$\cdots$F) distances in Å 27

2.2 CCSD(T)/haTZ optimized stationary points of $BF_4^-(H_2O)_2$ with select intermolecular R(H$\cdots$F) and R(H$\cdots$O) distances in Å. The 2b:Mb/haTZ optimized intermolecular R(H$\cdots$F) and R(H$\cdots$O) distances are identical to (or within 0.01 Å) of the corresponding CCSD(T) values. 29

2.3 2b:Mb/haTZ optimized stationary points of $BF_4^-(H_2O)_3$ with select intermolecular R(H$\cdots$F) and R(H$\cdots$O) distances in Å. 34

2.4 2b:Mb/haTZ optimized stationary points of $BF_4^-(H_2O)_4$ with select intermolecular R(H$\cdots$F) and R(H$\cdots$O) distances in Å 35

3.1 Qualitative geometries of C_2H + HX transition states. 61

3.2 General representation of the transition state geometrical features. 63

3.3 Potential energy surface of the C_2H + HNCO $\rightarrow$ C_2H_2 + NCO reaction at 0K at the CCSDT(Q)/CBS//CCSD(T)-F12a/cc-pVTZ-F12 level of theory. 64

3.4 Potential energy surface of the C_2H + *trans*-HONO $\rightarrow$ C_2H_2 + NO_2 reaction at 0K at the CCSDT(Q)/CBS//CCSD(T)-F12a/cc-pVTZ-F12 level of theory. 66

3.5 Potential energy surface of the C_2H + *cis*-HONO $\rightarrow$ C_2H_2 + NO_2 reaction at 0K at the CCSD(T)-F12a/cc-pVTZ-F12//MP2/aug-cc-pVTZ level of theory. 66

3.6 Potential energy surface of the $C_2H + CH_3OH \rightarrow C_2H_2 + CH_3O$ reaction at 0K at the CCSDT(Q)/CBS//CCSD(T)-F12a/cc-pVTZ-F12 level of theory. The asterisk (*) denotes the energy is at the CCSD(T)-F12a/cc-pVTZ-F12 level of theory with no additional corrections. 67

3.7 Qualitative geometries of $C_2H + CH_3OH$ methyl abstraction transition state. Bond distances are given in Å and angles in degrees. 68

3.8 Potential energy surface of the $C_2H + CH_3OH \rightarrow C_2H_2 + CH_2OH$ reaction at 0K at the CCSD(T)-F12a/cc-pVTZ-F12//MP2/aug-cc-pVTZ level of theory. 69

3.9 Potential energy surface of the $C_2H + C_2H_4 \rightarrow C_2H_2 + C_2H_3$ reaction at 0K at the CCSDT(Q)/CBS//CCSD(T)-F12a/cc-pVTZ-F12 level of theory. 70

3.10 Experimental and theoretical rate constants for the $C_2H + C_2H_4 \rightarrow C_2H_2 + C_2H_3$ reaction. 73

4.1 Hydrogen bonded complexes 79

4.2 Dispersion bound complexes 80

4.3 Mixed complexes 80

B.1 C_2H 184

B.2 HNCO 185

B.3 *trans*-HONO 186

B.4 *cis*-HONO 187

B.5 CH_3OH 188

B.6 C_2H_4 189

B.7 C_2H_2 190

B.8 NCO 191

B.9 NO_2 192

B.10 CH_3O 193
B.11 CH_2OH 194
B.12 C_2H_3 195
B.13 C_2H + HNCO 196
B.14 C_2H + *cis*-HONO 197
B.15 C_2H + *trans*-HONO 198
B.16 C_2H + CH_3OH 199
B.17 C_2H + CH_3OH 200
B.18 C_2H + C_2H_4 201
B.19 C_2H + CH_3OH (R1) 202
B.20 C_2H + CH_3OH 203
B.21 C_2H + *cis*-HONO 204

Chapter 1

Introduction

1.1 The Schrödinger Equation

One of the central goals of quantum chemistry is to find approximate solutions of the non-relativistic time-independent Schrödinger equation.

$$\hat{H}|\Psi\rangle = E|\Psi\rangle \tag{1.1}$$

The Hamiltonian can be separated into electronic and nuclear parts to include the kinetic energy of both the electrons and nuclei as well as the pair-wise potential energy of the coulombic attraction between electrons and nuclei and both the electron-electron and nuclei-nuclei repulsion. In atomic units, the Hamiltonian can be written as the following:

$$\hat{H} = -\sum_{i=1}^{N} \frac{1}{2}\nabla_i^2 - \sum_{A=1}^{M} \frac{1}{2M_A}\nabla_A^2 - \sum_{i=1}^{N}\sum_{A=1}^{M} \frac{Z_A}{r_{iA}} + \sum_{i=1}^{N}\sum_{j>i}^{N} \frac{1}{r_{ij}} + \sum_{A=1}^{M}\sum_{B>A}^{M} \frac{Z_A Z_B}{R_{AB}} \tag{1.2}$$

where the indices i and j correspond to the electrons and A and B correspond to the nuclei.

1.2 The Born-Oppenheimer Approximation

To further simplify the Hamiltonian operator given in Equation 1.2, one can invoke the Born-Oppenheimer approximation. Nuclei are much heavier than electrons and therefore move on a different time scale. Because of this, it is assumed that the positions of the nuclei are fixed relative to the positions of the electrons. Within this approximation, the second term of Equation 1.2, the kinetic energy of the nuclei, vanishes and the last term of Equation

1.2, the nuclei-nuclei repulsion, becomes a constant (V_{nuc}).

$$\hat{H} = -\sum_{i=1}^{N} \frac{1}{2}\nabla_i^2 - \sum_{i=1}^{N}\sum_{A=1}^{M} \frac{Z_A}{r_{iA}} + \sum_{i=1}^{N}\sum_{j>i}^{N} \frac{1}{r_{ij}} + V_{nuc} \tag{1.3}$$

As shown in Equation 1.3, the solution to the new Hamiltonian explicitly depends on on the electronic coordinates and parametrically depends on the nuclear coordinates. Eliminating those two terms from the Hamiltonian yields the electronic Schrödinger equation.

$$\hat{H}_{\text{elec}}\Psi_{\text{elec}} = E_{\text{elec}} + \Psi_{\text{elec}} \tag{1.4}$$

Moving forward, the "elec" subscript will be dropped and only the electronic Hamiltonian and electronic wavefunctions will be considered. The nuclear repulsion energy term, V_{nuc}, is a constant that will be added to the electronic energy later. The Hamiltonian can now be expressed as a sum of one-electron, $\hat{h}$, and two-electron, $\hat{g}$, operators.

$$\hat{H} = \sum_{i} \hat{h}(i) + \sum_{i<j} \hat{g}(i,j) \tag{1.5}$$

1.3 The Wavefunction

The electronic Hamiltonian given in Equation 1.3 depends only on the spatial coordinates of the electrons, and the wavefunction can be simplified as a product of one-electron wavefunctions (ϕ). These one-electron wavefunctions are called molecular orbitals (MOs) which depend on the spatial coordinates of a single electron (x, y, z) where the μth electron is placed in the ith MO.

$$\phi_i^u = \phi_i(r^\mu) = \phi_i(x^\mu, y^\mu, z^\mu) \tag{1.6}$$

However, to completely describe an electron it is necessary to specify its spin. Additionally, the Pauli exclusion principle must be taken into account. The Pauli exclusion principle states that no more than two electrons can occupy each MO and the signs of these electrons must

be opposite.[1] To account for spin and avoid violation of the Pauli exclusion principle a new set of orbitals known as spin orbitals can be defined.

$$\Psi_i^{\mu}(r,s) = \phi_i(r^{\mu})\omega_i(s^{\mu}) \tag{1.7}$$

The spin coordinate is an abstract, discrete, two-level quantity that is typically expressed as spin up (α) or spin down (β). The spin states are integrally orthonormal and can be expressed as the following:

$$\int \alpha^*(s)\alpha(s)ds = \int \beta^*(s)\beta(s)ds = 1 \tag{1.8}$$

$$\int \alpha^*(s)\beta(s)ds = \int \beta^*(s)\alpha(s)ds = 0 \tag{1.9}$$

In order to satisfy the Pauli exclusion principle, the wavefunction must be antisymmetric and change signs after the exchange of electrons. This can be done by writing the wavefunction as an antisymmetric product of molecular spin orbitals, known as a Slater determinant.

$$\Psi = \frac{1}{\sqrt{N!}} \begin{vmatrix} \psi_1^1 & \psi_2^1 & \cdots & \psi_N^1 \\ \psi_1^2 & \psi_2^2 & \cdots & \psi_N^2 \\ \vdots & \vdots & \ddots & \vdots \\ \psi_1^N & \psi_2^N & \cdots & \psi_N^N \end{vmatrix} \tag{1.10}$$

Ψ is a linear combination of products of one-electron wavefunctions and each term is some possible permutation of electrons and spin orbitals. These permutations capture the required sign change where odd permutations give a minus sign, and even permutations give a positive sign. Additionally, orthonormality is imposed on the set of spin orbitals.

$$\langle \Psi_i | \Psi_j \rangle = \delta_{ij} \tag{1.11}$$

1.4 Hartree–Fock

Except in simplistic cases, exact solutions to the electronic Schrödinger equation given in Equation 1.4 do not exist as quantum chemists are faced with the many-electron problem. Identifying highly accurate approximate solutions to this many-electron problem has been the cornerstone of quantum chemistry. The Hartree–Fock approximation is typically the first step in dealing with the many-electron problem.

With this it is possible to get an equation for the electronic energy of a system. Equation 1.1 can be rearranged to solve for the energy by left multiplying each side by $\langle\Psi|$ and integrating over all space. Inserting Equation 1.10 takes advantage of the orthonormality of the molecular spin orbitals and further simplifies the equation.

$$E_{\mathrm{HF}} = \langle\Psi|\hat{H}|\Psi\rangle = \sum_i \langle\psi_i^i|\hat{h}(i)|\psi_i^i\rangle + \sum_{i>j} \langle\psi_i^i\psi_j^j|\hat{g}(i,j)|\psi_i^i\psi_j^j\rangle - \langle\psi_i^i\psi_j^j|\hat{g}(i,j)|\psi_j^i\psi_i^j\rangle \quad (1.12)$$

This energy expression given in Equation 1.12 is the Hartree–Fock energy and the first Slater-Condon rule can be used to evaluate the matrix elements of the one and two electron operators in the Hamiltonian resulting in the following simplified energy expression.

$$E_{\mathrm{HF}} = \sum_i h_{ii} + \frac{1}{2}\sum_{ij} \langle ij||ij\rangle \quad (1.13)$$

The second term is the anti-symmetrized two-electron integral ($\langle ij||ij\rangle = \langle ij|ji\rangle - \langle ij|ji\rangle$) which takes on a condensed notation of the occupied indices i, j, ... to denote the orbitals being integrated.

$$\langle i|\hat{h}(i)|i\rangle = h_{ii} \quad (1.14)$$

$$\langle ij|\hat{g}(i,j)|ij\rangle = \langle ij|ij\rangle \quad (1.15)$$

Every wavefunction is a product of spatial and spin functions, $\psi_i^i = \phi_i^i \omega(i)$. The spin function, $\omega(i)$, can be separated out and reduced using the integration results from Equations 1.8 and 1.9. Additionally, it is possible to put two electrons of opposite spin in the exact same spatial orbital. Therefore, the energy expression in Equation 1.12 can be re-evaluated where $N = 2n$ electrons in n doubly occupied spatial orbitals.

$$E = 2\sum_{i}^{N/2}\langle\phi_i|\hat{h}(i)|\phi_j\rangle + \sum_{i}^{N/2}\sum_{j}^{N/2} 2\langle\phi_i\phi_j|\hat{g}(i,j)|\phi_i\phi_j\rangle - \langle\phi_i\phi_j|\hat{g}(i,j)|\phi_j\phi_i\rangle \tag{1.16}$$

To further simplify the energy expression, the "coulomb", $\hat{J}_j$, and "exchange", $\hat{K}_j$, operators will be introduced and are as follows:

$$\hat{J}_j|\phi_i\rangle = \langle\phi_j|\hat{g}(i,j)|\phi_j\phi_i\rangle \tag{1.17}$$

$$\hat{K}_j|\phi_i\rangle = \langle\phi_j|\hat{g}(i,j)|\phi_i\phi_j\rangle \tag{1.18}$$

The energy expression is now

$$E = 2\sum_{i}^{N/2}\langle\phi_i|\hat{h}(i)|\phi_j\rangle + \sum_{i}^{N/2}\sum_{j}^{N/2} 2\langle\phi_i|\hat{J}_j|\phi_i\rangle - \langle\phi_i|\hat{K}_j|\phi_i\rangle \tag{1.19}$$

The two-electron integrals in Equation 1.19 can act as one-electron integrals which allows them to be easily grouped with $\hat{h}$ to create the Fock operator, $\hat{f}$, which gives rise to the Hartree–Fock equations.

$$\hat{f}\phi_i = \left[\hat{h} + \sum_j (2\hat{J}_j - \hat{K}_j)\right]\phi_i = \epsilon_i\phi_i \tag{1.20}$$

The Hartree–Fock equations are quite expensive to solve analytically or numerically. For molecules, it is nearly impossible to solve these equations. In order to apply the Hartree–Fock method to molecules, the spatial orbitals are constructed as a linear combination of atomic

orbitals (LCAO).

$$\phi_i = \sum_q \chi_q C_{qi} \tag{1.21}$$

The Hartree–Fock MO's can be approximated with the LCAO-MO's by inserting Equation 1.21 into Equation 1.20.

$$\hat{f} \sum_q \chi_q C_{qi} = \epsilon_i \sum_q \chi_q C_{qi} \tag{1.22}$$

Left multiplying by χ_p^* and integrating on both sides yields

$$\sum_q \langle \chi_p | \hat{f} | \chi_q \rangle C_{qi} = \epsilon_i \sum_q \langle \chi_p | \chi_q \rangle C_{qi} \tag{1.23}$$

where $\langle \chi_p | \hat{f} | \chi_q \rangle$ is defined as F_{pq} (Fock matrix) and $\langle \chi_p | \chi_q \rangle$ as S_{pq} (overlap matrix),

$$\sum_q F_{pq} C_{qi} = \epsilon_i \sum_q S_{pq} C_{qi} \tag{1.24}$$

which leads to the Roothaan-Hall equations.[2]

$$\mathbf{FC} = \mathbf{SC}\boldsymbol{\epsilon} \tag{1.25}$$

The $\mathbf{C}$ matrix contains the expansion coefficients for MO's constructed from AO's and $\boldsymbol{\epsilon}$ contains the eigenvalues of the Fock matrix. Now the problem of solving the Hartree–Fock equations revolves around determining the best coefficients in $\mathbf{C}$ that minimize the variational energy. The $\mathbf{S}$ matrix can be transformed to the identity matrix which leaves a true eigenvalue problem

$$\widetilde{\mathbf{F}}\widetilde{\mathbf{C}} = \widetilde{\mathbf{C}}\boldsymbol{\epsilon} \tag{1.26}$$

where

$$\widetilde{\mathbf{F}} = \widetilde{\mathbf{S}}^{-1/2} \mathbf{F} \widetilde{\mathbf{S}}^{-1/2} \tag{1.27}$$

$$\widetilde{\mathbf{C}} = \widetilde{\mathbf{S}}^{-1/2} \mathbf{C} \tag{1.28}$$

The coefficient matrix, $\mathbf{C}$, is the starting point to iteratively solve for the variational energy using the Roothaan-Hall equations. From the coefficient matrix, the transformed Fock matrix, $\widetilde{\mathbf{F}}$, can be built. Then the Fock matrix is diagonalized which provides a new coefficient matrix. A new density matrix can then be built from the coefficient matrix and the difference between the old density matrix and new density matrix can be determined. If the convergence is not satisfactory, these steps are repeated. This procedure is commonly referred to as self-consistent field.

1.5 Configuration Interaction

For numerous molecular systems, the Hartree-Fock energy accounts for approximately 99% of the total electronic energy.[3] The uncaptured 1% is typically referred to as the correlation energy and is the difference between the exact energy and the HF energy.

$$E_{\text{correlation}} = E_{\text{exact}} - E_{\text{HF}} \tag{1.29}$$

This correlation energy is extremely important as the Hartree–Fock description is often insufficient for chemically meaningful results such as dissociation energies or reaction energies. Consequently, it becomes necessary to calculate the correlation energy. The exact way to achieve this involves constructing the wavefunction as a linear combination of all possible Slater determinants.

$$|\Psi\rangle = \sum_{p_1<\cdots<p_N} c_p |\Phi_{p_1\cdots p_N} \tag{1.30}$$

An equivalent way is to choose a reference determinant, typically the Hartree–Fock wavefunction, and then consider all possible excitations from the reference determinant.

$$|\Psi\rangle = c_0|\Phi\rangle + \left(\frac{1}{1!}\right)^2 \sum_{ia} c_i^a |\Phi_i^a\rangle + \left(\frac{1}{2!}\right)^2 \sum_{\substack{ij \\ ab}} c_{ij}^{ab} |\Phi_{ij}^{ab}\rangle + \left(\frac{1}{3!}\right)^2 \sum_{\substack{ijk \\ abc}} c_{ijk}^{abc} |\Phi_{ijk}^{abc}\rangle + \cdots \tag{1.31}$$

The indices $i, j, k, \cdots$ correspond to the occupied orbitals in the reference determinant and the indices $a, b, c, \cdots$ correspond to the newly occupied orbitals from the excitations, and the pre-factors account for equivalent terms.

Full configuration interaction calculations rapidly become impractical as the number of basis functions grows, necessitating alternative approaches for handling electron correlation. One approach is to truncate the terms in Equation 1.31 and include only the most important excited states. However, limiting the order of excitations in the configuration interaction space results in a truncated CI wavefunction that is neither size-consistent nor size-extensive. Because of this, it is necessary to find other methods that can capture as much correlation energy as possible in a cost-effective manner.

1.6 Perturbation Theory

In physics, a system of interest is often closely related to a well-defined or analytically solvable system, with a minor modification or perturbation. In such cases, perturbation theory provides an approximate solution to problems that have either an excessively complex analytic solution or no analytic solution at all.

1.6.1 Rayleigh-Schrödinger Perturbation Theory

In order to arrive at the discussion of Møller-Plesset perturbation theory, it is necessary to discuss Rayleigh-Schrödinger perturbation theory which applies the ideas of perturbation theory to the time-independent Schrödinger equation. The Hamiltonian, $\hat{H}$, is expressed as a sum of an exactly solvable component, $\hat{H}_0$, and a perturbation, $\hat{V}$, to the system.

$$\hat{H}|\Psi_i\rangle = (\hat{H}_0 + \hat{V})|\Psi_i\rangle = E_i|\Psi_i\rangle \tag{1.32}$$

It is assumed that $\hat{H}_0$ is a simple, solvable system for which all eigenstates and eigenvalues are known.

$$\hat{H}_0|\Phi_i^{(0)}\rangle = E_i^{(0)}|\Phi_i^{(0)}\rangle \tag{1.33}$$

Next, a continuous parameter, λ, is introduced to Equation 1.32 to scale the perturbation that is bound by the values of 0 and 1 ($0 \leq \lambda \leq 1$).

$$(\hat{H}_0 + \lambda\hat{V})|\Psi_i\rangle = E_i|\Psi_i\rangle \tag{1.34}$$

If the perturbation is small, the eigensolutions of the exact Hamiltonian will closely approximate those of the zeroth-order Hamiltonian. Since the wavefunction $|\Psi_i\rangle$ and energy E_i depend on λ we can represent the eigensolutions of the exact Hamiltonian as a Taylor series expansion in terms of λ.

$$\begin{aligned} E_i &= E_i^{(0)} + \lambda E_i^{(1)} + \lambda^2 E_i^{(2)} + \cdots & E_i^{(k)} &= \frac{1}{k!}\frac{d^k E_i}{d\lambda^k}\Big|_{\lambda=0} \\ |\Psi_i\rangle &= \Phi_i^{(0)} + \lambda\Phi_i^{(1)} + \lambda^2\Phi_i^{(2)} + \cdots & |\Phi_i^{(k)}\rangle &= \frac{1}{k!}\frac{d^k|\Phi_i\rangle}{d\lambda^k}\Big|_{\lambda=0} \end{aligned} \tag{1.35}$$

It is assumed that the reference state is normalized $\langle\Phi_i^{(0)}|\Phi_i^{(0)}\rangle = 1$ and the exact wavefunction is intermediately normalized $\langle\Phi_i^{(0)}|\Psi_i\rangle = 1$. Substituting Equation 1.35 into Equation 1.34 yields:

$$(\hat{H}_0+\lambda\hat{V})(\Phi_i^{(0)}+\lambda\Phi_i^{(1)}+\lambda^2\Phi_i^{(2)}+\cdots) = (E_i^{(0)}+\lambda E_i^{(1)}+\lambda^2 E_i^{(2)}+\cdots)(\Phi_i^{(0)}+\lambda\Phi_i^{(1)}+\lambda^2\Phi_i^{(2)}+\cdots) \tag{1.36}$$

The resulting expression is then broken down into terms with like powers of λ to solve for the associated wavefunction and energy corrections. All corrections to the zeroth-order energy can be obtained by left projecting each equation in the system with the zeroth-order

wavefunction, $\langle\Phi_i^{(0)}|$, and the corrections up to second order are summarized as follows:

$$\begin{aligned} E_i^{(0)} &= \langle\Phi_i^{(0)}|\hat{H}_0|\Phi_i^{(0)}\rangle \\ E_i^{(1)} &= \langle\Phi_i^{(0)}|\hat{V}|\Phi_i^{(0)}\rangle \\ E_i^{(2)} &= \langle\Phi_i^{(0)}|\hat{V}|\Phi_i^{(1)}\rangle \end{aligned} \tag{1.37}$$

1.6.2 Møller-Plesset Perturbation Theory

Møller-Plesset perturbation theory applies Rayleigh-Schrödinger perturbation theory to calculate the electronic energies of molecules. The Fock operator in Equation 1.20 is selected to represent the unperturbed system. The energy expressions up to the second order are then given by the following:

$$E_0^{(0)} = \sum_i \epsilon_i \tag{1.38}$$

$$E_0^{(1)} = -\frac{1}{2}\sum_{ij}\langle ij||ij\rangle \tag{1.39}$$

$$E_0^{(2)} = \frac{1}{4}\sum_{ijab}\frac{|\langle ij||ab\rangle|^2}{\epsilon_i + \epsilon_j - \epsilon_a - \epsilon_b} \tag{1.40}$$

The indices $i, j, k, l, \cdots$ denote the occupied molecular orbitals in the Hartree–Fock reference determinant while the indices $a, b, c, d, \cdots$ denote the virtual or unoccupied orbitals. The zeroth order energy correction, or MP0, given in Equation 1.38 is the sum of the orbital energies. The Hartree–Fock energy can be obtained by adding the MP0 and MP1 (Equation 1.39) energies together. Therefore, any further energy corrections correspond to the correlation energy.

1.7 Coupled-Cluster Theory

As mentioned previously, the treatment of correlation energy in molecular systems is crucial and can be essential for generating chemically accurate results. Another post-Hartree–Fock

method used to determine approximate solutions to the Schrödinger equation is coupled-cluster theory which uses an exponential ansatz to estimate the true wavefunction, Ψ.

$$|\Psi\rangle = e^{\hat{T}}|\Phi\rangle \tag{1.41}$$

Here, Φ is the reference wavefunction and is typically taken to be the Hartree–Fock wavefunction. The $\hat{T}$ term is the cluster operator and is a sum of excitation cluster operators

$$\hat{T} = \hat{T}_1 + \hat{T}_2 + \hat{T}_3 + \cdots + \hat{T}_N \tag{1.42}$$

where N is the total number of electrons. $\hat{T}_1$ corresponds to the operator that includes all possible single excitations, $\hat{T}_2$ includes double excitations and so on. Each excitation cluster operator can be further defined below.

$$\hat{T}_n = \left(\frac{1}{n!}\right)^2 \sum_{ij..ab..}^{n} t_{ij..}^{ab..} a_a^\dagger a_b^\dagger \cdots a_j a_i \tag{1.43}$$

The t terms represent the coupled cluster amplitudes, which are connected to the probability of the corresponding excitations and serve to parameterize the coupled-cluster wavefunction. The subscripts $ij...$ refer to the indices of occupied orbitals, while the subscripts $ab...$ denote the indices of unoccupied orbitals. The operators a_i and $a_a^\dagger$ correspond to the annihilation of the i^{th} orbital in the target determinant and the creation of the a^{th} orbital in the target determinant, respectively. For instance, the $\hat{T}_2$ operator will include all possible determinants formed by removing two reference orbitals from the reference determinant and replacing them with two previously unoccupied orbitals, each weighted by their corresponding cluster amplitudes. With these terms defined, we can return to the wavefunction expressed in terms of an exponential ansatz that can be expanded via a Taylor series.

$$e^{\hat{T}} = 1 + \hat{T} + \frac{\hat{T}^2}{2!} + \frac{\hat{T}^3}{3!} + \cdots \tag{1.44}$$

If the full $\hat{T}$ operator is used, it generates all possible excitations, and the result is equivalent to full configuration interaction (FCI). In practice; however, the $\hat{T}$ operator is truncated to a specific excitation level, as each additional level of excitation significantly increases the computational cost. The coupled cluster method is particularly advantageous because, unlike truncated CI, it is both size-extensive and size-consistent. Additionally, it can be truncated without introducing significant errors into the system. If the $\hat{T}$ operator was truncated at $\hat{T}_2$, ($\hat{T} = \hat{T}_1 + \hat{T}_2$) this corresponds to coupled-cluster with singles and doubles (CCSD). Truncating the $\hat{T}$ operator at $\hat{T}_3$ ($\hat{T} = \hat{T}_1 + \hat{T}_2 + \hat{T}_3$) yields coupled-cluster with singles and doubles and triples (CCSDT). CCSDT results, which scale as $O(N^8)$, are computationally too expensive to calculate for most systems. A solution to this issue is to apply a perturbative correction for the triples term to the CCSD result. This perturbative triples approach is referred to as CCSD(T) and is regarded as the gold standard in electronic structure theory due to its high accuracy (within $\pm$ 1 kcal mol^{-1}) for many chemical systems and relatively affordable computational scaling, $O(N^7)$.

1.8 Basis Sets

We have reviewed the methods that will be employed to approximate exact solutions of the Schrödinger equation. For a given molecule, the individual atoms are represented by atomic orbitals. Taking linear combinations of the atomic orbitals forms molecular orbitals, which can then describe the molecule as a whole. The set of functions used to represent the wavefunction is referred to as the basis set. With an infinitely large and complete basis set, one can reach the complete basis set (CBS) limit. At this limit, the calculated energy and other properties of a system would converge to their exact values, assuming no other approximations are involved. However, this theoretical "perfect" result is computationally unfeasible. Instead, basis sets are designed and chosen to approximate this limit. Increasing the number of basis functions typically brings the calculation closer to the CBS limit, but also significantly raises the computational cost. As a result, considerable effort has been

devoted to developing basis sets that efficiently approach the CBS limit while using as few functions as possible.

A typical starting point for basis functions comes from the exact hydrogen atom wavefunctions. The wavefunction is separated into radial (R_{nl}) and angular parts, with the radial part determined by the quantum numbers n and l, and the angular part represented by spherical harmonics (Y_{lm}).

$$\psi_{nlm}(r, \theta, \phi) = R_{nl}(r) Y_{lm}(\theta, \phi) \tag{1.45}$$

However these hydrogenic orbitals, which are obtained from a one electron system, turn out to be an inefficient choice for systems with multiple electrons. One solution to this problem is to implement Slater Type Orbitals (STO) which resemble the exact solutions to the Schrödinger equation for hydrogen-like atoms and have the form below.

$$\phi^{\mathrm{STO}}(r) = N^{\mathrm{STO}} e^{-\alpha r} \tag{1.46}$$

STOs are characterized by a sharp cusp at the nuclear center and exhibit the correct radial decay as the electron moves farther from the nucleus, but they are more computationally challenging to work with due to their complicated integrals. Gaussian-type orbitals (GTOs) are often used in practice instead and have the form below.

$$\phi^{\mathrm{GTO}}(r) = N^{\mathrm{GTO}} e^{-\alpha r^2} \tag{1.47}$$

Unfortunately, GTOs have notable limitations, such as their overly rapid decay in electron density as the distance from the nucleus increases, and their failure to represent the undifferentiable cusp at the nuclear center. In order to remedy these limitations, the individual Gaussian functions are combined as linear combinations to form a contracted basis function (CGTO). The orbital exponents (α) and contraction coefficients (c_i) of each basis set are

optimized variationally.

$$\phi^{\mathrm{CGTO}}(r) = \sum_i c_i \phi^{\mathrm{GTO}}(r) \tag{1.48}$$

These contracted basis functions can tune the functional form of a GTO to behave more like an STO. This can be seen in the minimal STO-nG basis sets, where n represents the number of Gaussian functions included in the linear combination. A basis set that includes a single basis function for each occupied atomic orbital is referred to as a minimal or single zeta (SZ) basis set. For example, a double zeta (DZ) basis set includes two basis functions for each occupied atomic orbital. This can be further extended to the XZ basis sets, where X is the cardinality of the basis set and describes the number of basis functions for each atomic orbital. Various modifications can be applied to a basis set to better represent a specific physical characteristic of a system. Two noteworthy modifications are the inclusion of functions with different radial exponents and the addition of polarization functions. These polarization functions are higher angular momentum basis functions used to represent the polarization of an atom's electron density in a molecule.[4] In addition, diffuse functions are necessary to accurately describe electron density at distances far from the nucleus, such as in chemical systems with anions or long-range attractive forces. Atoms that are described using diffuse functions are referred to as being augmented.

The Dunning basis sets, or the correlation-consistent polarized valence basis sets, abbreviated as cc-pVXZ, are a particular basis set family that was designed to guarantee systematic convergence to the CBS limit as the cardinality of the basis set is increased.[5,6] The core atomic orbitals are described by one basis function and the valence atomic orbitals are described by polarization functions. The inclusion of diffuse functions is denoted by the abbreviation "aug" and can be added to any cc-pVXZ basis set. Additionally, these diffuse functions can be excluded from hydrogen atoms and is typically denoted by "heavy-aug". However, other abbreviations and notations exist for this exclusion of diffuse functions from hydrogen and can be seen in Chapter 2 of this work.

1.9 Focal Point Analysis

As discussed previously, the inability to use a complete basis set (CBS) and the impracticality of including all possible excited configurations (FCI) in the wavefunction limit the achievable accuracy when solving the multi-electron Schrödinger equation. One approach to obtain an accurate approximation of the FCI/CBS energy is the focal point analysis (FPA) method by Allen and coworkers.[7,8]

Several single point energies are computed with an array of different method and basis set combinations followed by extrapolations using these energies. The focal point method leverages the fact that incorporating higher-order correlation terms generally has increasingly small effects on the energy. Therefore, the effect of including higher ordered excitations can be included as an additive correction using a high-level coupled cluster method in conjunction with a small basis set. Due to their systematic design to converge to the CBS limit, the Dunning basis sets are employed for these computations.

Various additive corrections can be added to account for any assumptions made when computing the electronic energies. These corrections might include the zero-point vibrational energy (ZPVE) or determining the influence of the frozen core approximation. Others play a more diagnostic role, helping to justify the assumptions underlying the geometry optimization and FPA such as the diagonal Born–Oppenheimer correction (DBOC) or scalar relativistic effects. Combining the extrapolated FPA energy and the additive corrections results in a flexible method that can provide highly accurate energies for molecules.

1.10 Potential Energy Surfaces and Reaction Pathways

An important ramification of the Born-Oppenheimer approximation (Section 1.2) is the potential energy surface (PES). A PES is a multidimensional function that represents the energy of a molecular system based on the positions of its nuclei. The PES contains several key points of interest that are crucial for understanding chemical reactions. Minimum points

correspond to wells of potential energy where the molecular geometry is most likely in its lowest energy state. These minimum points are characterized by the first and second derivative of the curve ("bottom-of-the-well") being zero and positive, respectively, for all coordinates. A minimum energy structure will have all real (non-imaginary) vibrational modes, as confirmed by a vibrational frequency analysis. First-order saddle points are the highest energy points along the minimum energy pathway, which is the lowest energy trajectory connecting two minima on the potential energy surface. The maximum peak along this pathway is known as a first-order saddle point, also called the transition state. Similarly, the first derivative of the curve is zero; however, the second derivative is positive for all coordinates except one, for which it is negative. Additionally, a transition state structure will have one imaginary mode. These minimum points and transition states are often referred to as stationary points and much of this work focuses on the characterization of these stationary points for benchmarking purposes.

Reaction pathways are trajectories on a potential energy surface that pass through key features, including minima and first-order saddle points. Characterizing the features of the PES helps predict the type of mechanism a chemical reaction will follow, including the quantification of transition state barriers. The transition state barrier represents the minimum energy needed for the reaction to occur, excluding factors like tunneling effects. With highly accurate transition state barriers, it is possible to utilize transition state theory to compute rate constants for these reaction pathways.

1.10.1 Transition State Theory

Canonical transition state theory (TST) only requires an accurate characterization of the stationary points on a reaction pathway. A bimolecular reaction that forms a favorable pre-reactive complex prior to reacting could be described as the following:

$$\text{Reactants} \underset{k_{-1}}{\overset{k_1}{\rightleftharpoons}} \text{PRC} \xrightarrow{k_2} \text{Products} \tag{1.49}$$

The overall rate constant for the forward direction is expressed as

$$k_{\text{total}} = k_2 \frac{k_1}{k_{-1} + k_2} \tag{1.50}$$

because the transition state lies above the relative enthalpy of the dissociated reactants, we can assume $k_{-1} \gg k_2$ which simplifies the overall rate constant expression

$$k_{\text{total}} = k_2 K_{\text{eq}} \tag{1.51}$$

where K_{eq} is the equilibrium constant between the pre-reactive complex (PRC) and the reactants (R), which can be determined as the ratio of their respective canonical partition functions.

$$K_{\text{eq}} = \frac{Q^{\text{PRC}}}{Q^{\text{R}}} \tag{1.52}$$

The rate constant for the conversion of the PRC into the products (k_2) can be expressed as[9]

$$k_2 = \kappa(T) \frac{k_B T}{h} \frac{Q^{\text{TS}}(T)}{Q^{\text{PRC}}(T)} \tag{1.53}$$

where $\kappa(T)$ is the temperature dependent transmission coefficient, k_B is the Boltzmann constant, T is the temperature (in Kelvin), h is Planck's constant, and Q^{TS} and Q^{PRC} are the canonical partition functions for the transition state and pre-reactive complex, respectively. Combining Equations 1.52 and 1.53 yields the following expression for k_{total}:

$$k_{\text{total}} = \kappa(T) \frac{k_B T}{h} \frac{Q^{\text{TS}}(T)}{Q^{\text{R}}(T)} e^{-\Delta H^{\ddagger}/k_B T} \tag{1.54}$$

where $\Delta H^{\ddagger}$ is the transition state barrier. The exponential dependence of k_{total} on $\Delta H^{\ddagger}$ indicates that accurately determining $\Delta H^{\ddagger}$ is especially important at low temperatures. Therefore, $\Delta H^{\ddagger}$ must be converged within subchemical accuracy (≤ 0.5 kcal mol^{-1}) to ensure reliable theoretical rate constants at moderate to low temperatures.

A simple approximation, known as the Wigner correction, can be used to represent the transmission coefficient

$$\kappa(T) = 1 + \frac{1}{24}\left[\frac{h\omega^{\ddagger}}{k_B T}\right]^2 \tag{1.55}$$

where $\omega^{\ddagger}$ is the imaginary mode of the transition state. This approximation is sufficient for systems where $\frac{h\omega^{\ddagger}}{k_B T} < 1$.[10] However, a more detailed model is required for reactions where tunneling contributions are more significant. Alternatively, the potential energy surface can be approximated using an Eckart barrier where the transmission probability can be expressed analytically in terms of the relative enthalpy of the PRC, TS, and products, along with $\omega^{\ddagger}$.[11] The transmission coefficient is then calculated from a Boltzmann-weighted integral over the transmission probability.[12] Other models exist for treating reactions with tunneling contributions, such as small curvature tunneling (SCT), but require a description of the potential energy surface that extends beyond the characterization of the stationary points. However, Eckart tunneling has been shown to be an adequate model for many reactions, especially at moderate to high temperatures.[12–16]

To calculate the partition functions in Equation 1.54, generally the rigid rotor harmonic oscillator (RRHO) approximation is used. This approximation assumes that the molecule behaves as a rigid rotor for rotational motions and a harmonic oscillator for vibrational motions. The partition function, $Q(T)$, can be expressed as the product of the partition functions for the individual degrees of freedom in a molecule

$$Q(T) = q_{trans}(T) q_{elec}(T) q_{rot}(T) q_{vib}(T) \tag{1.56}$$

where

$$q_{contrib}(T) = \sum_j \exp\left(-\frac{\epsilon_j^{contrib}}{k_B T}\right) \tag{1.57}$$

denotes a particular contribution to the molecular partition function. For a non-linear molecule, these contributions to the partition function are as follows:

$$q_{trans}(T) = \left(\frac{2\pi M k_B T}{h^2}\right) V \tag{1.58}$$

$$q_{rot}(T) = \frac{\sqrt{\pi}}{\sigma}\left(\frac{8\pi^2 k_B T}{h^2}\right)^{\frac{3}{2}} \sqrt{I_M} \tag{1.59}$$

$$q_{vib}(T) = \prod_{i=1}^{3N-6} \frac{1}{1 - e^{h\omega_i / k_B T}} \tag{1.60}$$

$$q_{elec}(T) = \sum g_i e^{-\epsilon_i / k_B T} \approx g_0 \tag{1.61}$$

$M, \sigma, I_M, \omega_i, g_i$, and ϵ_i correspond to the mass, symmetry index, inertia product, harmonic vibrational frequencies, electronic degeneracies, and electronic energies, respectively, for each molecule.

From Equation 1.60, the lowest frequency vibrational modes have the greatest contribution to the partition function at any given temperature. These low-frequency modes are often associated with bending motions or hindered rotations, which typically exhibit significant anharmonicity. One limitation to treating these modes as harmonic oscillators can result in an overestimation of the vibrational partition function, particularly at higher temperatures. Overall, the RRHO approximation is a useful tool for estimating molecular partition functions, which in turn can be used to compute thermodynamic properties and predict reaction rates, especially for simpler molecules where the assumptions hold reasonably well.

1.11 Vibrational Frequencies

As noted above in Section 1.10, vibrational frequencies are important in identifying and confirming the nature of each stationary point on the PES, whether it is a minimum or a transition state. Additionally, the vibrational degrees of freedom are important for determining the rate constants of a chemical reaction as shown in Section 1.10.1. To calculate these

frequencies, the system's potential is required and can be expressed as the following:

$$V(\mathbf{x}) = V_0 + \sum_{i}^{3N-6} \frac{\partial V}{\partial x_i} + \frac{1}{2!} \sum_{ij}^{3N-6} \frac{\partial^2 V}{\partial x_i x_j} x_i x_j + \frac{1}{3!} \sum_{ijk}^{3N-6} \frac{\partial^3 V}{\partial x_i x_j x_k} x_i x_j x_k + \cdots \tag{1.62}$$

This is a standard Taylor expansion of the potential in the $3N$-6 dimensional space ($3N$-5 for linear molecules) of the molecule's internal coordinates. Often, the quadratic terms are most dominant in Equation 1.62 and the harmonic approximation is made which truncates the potential expansion at the second order terms. V_0 is arbitrarily set to 0 and the linear term is ignored.

$$V(\mathbf{x}) = \frac{1}{2} \sum_{ij}^{3N-6} \frac{\partial^2 V}{\partial x_i x_j} x_i x_j \tag{1.63}$$

1.11.1 GF Matrix Method

The GF matrix method aims to compute harmonic vibrational frequencies using internal coordinates. Unlike Cartesian coordinates, which describe the position of atoms in three-dimensional space, internal coordinates describe the relative positions of atoms in terms of bond lengths, bond angles, and torsional angles. This is especially useful for large molecules where internal coordinates offer a more intuitive and computationally efficient representation of the molecular structure. Another advantage to using these internal coordinates is that the force constants of the Hessian are much less coupled in this basis compared to the Cartesian coordinate basis. To compute the harmonic vibrational frequencies, the following eigenvalue problem must be solved

$$(\mathbf{GF})\mathbf{L} = \mathbf{L}(\boldsymbol{\mu}\boldsymbol{\Lambda}) \tag{1.64}$$

where the eigenvalues yield the square of the angular frequencies.

$$\omega_i = \sqrt{\mu_i \lambda_i} \tag{1.65}$$

This process simultaneously solves the eigenvalue problems for both kinetic and potential energy.

$$\mathbf{L}^{-1}\mathbf{G}(\mathbf{L}^{-1})^{\mathrm{T}} = \boldsymbol{\mu} \tag{1.66}$$

$$\mathbf{L}^{\mathrm{T}}\mathbf{F}\mathbf{L} = \boldsymbol{\Lambda} \tag{1.67}$$

The matrix $\mathbf{G}$ of this method contains the kinetic energy information of the molecule expressed in terms of the internal coordinates. The elements of the matrix $\mathbf{G}$ are as follows:

$$G_{ij} = \sum_{n} \frac{B_n^i B_n^j}{m_n} \tag{1.68}$$

where i and j represent internal coordinates, n corresponds to the $3N$ Cartesian coordinates, m_n refers to the mass of the atom belonging to coordinate n, and B_n^i is the first-order B-matrix element, defined as the derivative of the internal coordinate i with respect to the Cartesian coordinate n.

$$B_n^i = \frac{\partial S_i}{\partial x_n} \tag{1.69}$$

The matrix $\mathbf{F}$ is the Hessian, a second-order force constant matrix, which can be computed either analytically (when available for certain levels of theory) or numerically using finite differences of gradients or energies. The matrix $\mathbf{L}$ can then transform between the internal coordinates and the normal coordinates, as follows:

$$\mathbf{s} = \mathbf{L}\mathbf{Q} \tag{1.70}$$

As it stands, the **GF** matrix is not symmetric, but substituting $\mathbf{L}' = \mathbf{G}^{-1/2}\mathbf{L}$ into Equation 1.64 yields a symmetric eigenvalue problem.

$$(\mathbf{GF})\mathbf{G}^{1/2}\mathbf{L}' = \mathbf{G}^{1/2}\mathbf{L}'(\boldsymbol{\mu}\boldsymbol{\Lambda} \tag{1.71}$$

$$(\mathbf{G}^{1/2}\mathbf{F}\mathbf{G}^{1/2})\mathbf{L}' = \mathbf{L}'(\boldsymbol{\mu}\boldsymbol{\Lambda}) \tag{1.72}$$

The symmetric $\mathbf{G}^{1/2}\mathbf{F}\mathbf{G}^{1/2}$ matrix can be diagonalized and through a back-transformation with $\mathbf{G}^{1/2}$ would return **L**.

1.11.2 Concordant Mode Approach

Calculating the full force constant matrix can become computationally prohibitive as the size of the molecule system increases. As previously mentioned, when the force constants of the Hessian are represented in the internal coordinate basis, the coupling force constants become smaller. This sparsity of the force constant matrix can be further increased by selecting a more optimal set of coordinates. The Concordant Mode Approach (CMA) utilizes a normal mode basis (**L**) from a more affordable level of theory B to selectively calculate elements of the force constant matrix at a more computationally expensive target level A.[17] The key concept behind CMA is that, in contrast to the curvature of the PES, the normal modes of vibration are less sensitive to changes in the level of theory. The outline of the CMA protocol is as follows:

1. Choose a set of complete, nonredundant set of internal coordinates (**S**) for the molecular system.

2. Optimize the molecular geometry at the high level of theory A.

3. Compute the low level of theory B frequencies using the GF matrix method on top of the high level of theory A stationary point.

4. Transform the basis used to compute the force constants via

   $\mathbf{F}_{\mathrm{A}} = \mathbf{L}_{\mathrm{B}}^{-1}\ \mathbf{F}_{\mathrm{CMA}}(\mathrm{A})\ \mathbf{L}_{\mathrm{B}}$.

5. Select the matrix elements of $\mathbf{F}_{\mathrm{CMA}}(\mathrm{A})$ based on the chose CMA protocol. These force constants are calculated using finite differences of single-point energies at level A.

6. Use the GF matrix method to obtain the high-level A frequencies and normal modes.

If it is assumed that $\mathbf{L}_{\mathrm{A}} \approx \mathbf{L}_{\mathrm{B}}$ then all coupling (or off-diagonal) force constants are reduced to zero. This assumption corresponds to CMA-0A. However, if coupling occurs in the force constant matrix, CMA does not provide a procedure for predicting which modes will couple. Additional work has addressed this shortcoming and provides a systematic approach for selecting and computing off-diagonal force constants using physically motivated criterion.[18] This new methodology is known as CMA-2A. Both of these methodologies will be implemented in Chapter 4 of this work.

Chapter 2

Competition Between Solvent···Solvent and Solvent···Solute Interactions in the Microhydration of the Tetrafluoroborate Anion, $BF_4^-(H_2O)_{n=1,2,3,4}$[1]

[1]Olive, L.N., Dornshuld, E.V., Schaefer III, H.F., and Tschumper, G.S. 2023. *The Journal of Physical Chemistry A*. 127:8806–8820. Reprinted (adapted) with permission from J. Phys. Chem. A 2023, 127, 42, 8806–8820. Copyright 2023, American Chemical Society.

2.1 Abstract

This study systematically examines the interactions of the tetrafluoroborate anion (BF_4^-) with up to four water molecules ($BF_4^-(H_2O)_{n=1,2,3,4}$). Full geometry optimizations and subsequent harmonic vibrational frequency computations are performed using a variety of density functional theory (DFT) methods (B3LYP, B3LYP–D3BJ, and M06–2X), and the MP2 *ab initio* method with a triple-ζ correlation consistent basis set augmented with diffuse functions on all non-hydrogen atoms (cc-pVTZ for H and aug-cc-pVTZ for B, O, F; denoted haTZ). Optimized structures and harmonic vibrational frequencies were also obtained with the CCSD(T) *ab initio* method and the haTZ basis set for the mono- and di-hydrate (n=1, 2) structures. The 2-body:Many-body (2b:Mb) technique, in which CCSD(T) computations capture the 1- and 2-body contributions to the interactions and MP2 computations recover all higher-order contributions, was used to extend these demanding computations to the tri-, and tetrahydrate (n=3, 4) systems. Four, five, and eight new stationary points have been identified for the di-, tri-, and tetrahydrate systems, respectively. The global minimum of the monohydrate adopts a symmetric double ionic hydrogen bonded motif with C_{2v} symmetry and an electronic dissociation energy of 13.17 kcal mol^{-1} at the CCSD(T)/haTZ level of theory. This strong solvent$\cdots$solute interaction, however, competes with solute$\cdots$solute interactions in the lowest-energy $BF_4^-(H_2O)_{n=2,3,4}$ minima that are not seen in the other di-, tri-, or tetrahydrate minima. The latter interactions help increase the 2b:Mb dissociation energies to more than 26, 41, and 51 kcal mol^{-1} for n = 2, 3, and 4, respectively. Structures that form hydrogen bonds between the solvating water molecules also exhibit the largest shifts in the harmonic OH stretching frequencies for the waters of hydration. These shifts can exceed -280 cm^{-1} relative to an isolated H_2O molecule at the 2b:Mb/haTZ level of theory.

2.2 Introduction

The tetrafluoroborate anion (BF_4^-) is popular in stable, room temperature ionic liquids (RTILs).[19] A variety of practical applications using RTILs were suggested such as use in solar and fuel cells, capacitors, and batteries.[20–24] The ionic nature of RTILs makes them hygroscopic.[25] The presence of water as an impurity or as a co-solvent can effect the physical properties of RTILs such as viscosity, solubility, electrical conductivity, or even reactivity.[26–34] Due to the varying effects of water, the interactions between water and the BF_4^--containing RTILs have been the focus of different experimental and theoretical studies.[26,35–38]

BF_4^--containing RTILs have been shown to exhibit weak associations with water, but not as weak as those containing the larger SbF_6^- and PF_6^- moieties.[35] Infrared (IR) spectroscopic measurements indicate OH stretching frequencies in water interacting with the RTIL shift to lower energy (i.e. red-shift) with respect to water vapor. The OH antisymmetric stretching mode, ν_3, and symmetric stretching mode ν_1, in water vapor were reported to be 3756 cm^{-1} and 3657 cm^{-1}, respectively.[39,40] The OH shifts in water toward lower energy for these modes ($\Delta\nu_3$ and $\Delta\nu_1$, respectively) were larger with BF_4^- ($\Delta\nu_3 = -116$ cm^{-1} and $\Delta\nu_1 = -97 cm^{-1}$) compared to their SbF_6^- ($\Delta\nu_3 = -93 cm^{-1}$ and $\Delta\nu_1 = -77$ cm^{-1}) and PF_6^- ($\Delta\nu_3 = -84$ cm^{-1} and $\Delta\nu_1 = -62$ cm^{-1}) counterparts and were unusually large overall.[35] Corresponding measurements in the same study using singly deuterated water (HDO), a useful probe of ion hydration, confirmed these results. Computational *ab initio* molecular dynamics (AIMD) simulations[41] of aqueous BF_4^- and PF_6^- probed these unusually large shifts in the absence of a cation. Smiechowski reported OH stretching frequency shifts ($\Delta\nu_{OH}$) to higher energy (i.e. blue-shift) of +264 cm^{-1} for the BF_4^- solute and +306 cm^{-1} for the PF_6^- solute when compared to the computed bulk water OH stretching mode of 3320 cm^{-1}.

In ion hydration, when a water molecule binds to small atomic anions, the water generally adopts an asymmetric, single ionic hydrogen bond (SIHB) motif where one hydrogen is attached to the ion and the other hydrogen is free.[42–50] For larger systems and molecular

anions with extended charge distributions, the symmetric configuration is favored, in which the water molecule binds along the axis of symmetry and adopts a double ionic hydrogen bond (DIHB) motif.[47,50–55] The transition from SIHB to DIHB occurs when the hydrogen bond acceptors are separated by about 2.2 Å.[51] The C_{2v} DI_1 structure (Figure 4.1a) is a monohydrate BF_4^- anion where the one (1) water molecule is consistent with the DIHB motif, hence labeled DI_1.

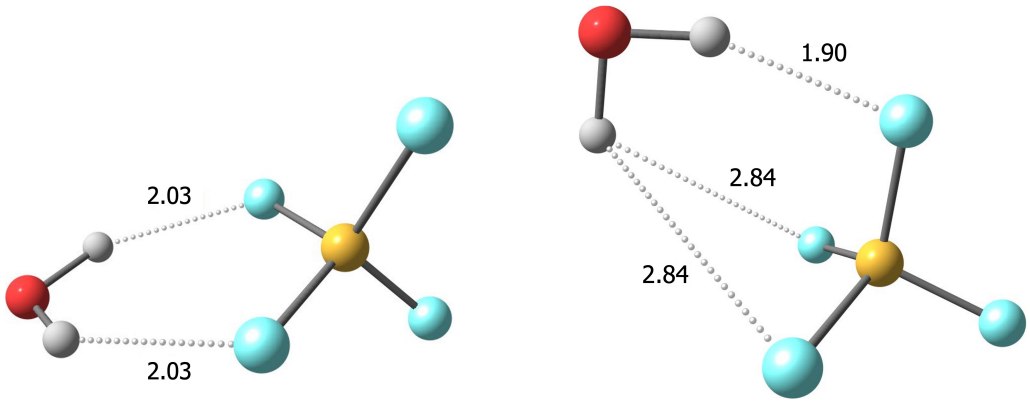

(a) C_{2v} DI_1 (b) C_s BI_1

Figure 2.1: CCSD(T)/haTZ optimized stationary points of $BF_4^-(H_2O)_1$ with select intermolecular R(H$\cdots$F) distances in Å

A previous study characterized microsolvated $PF_6^-(H_2O)_{n=1,2}$ conformers with quantum mechanical wave function theory (WFT) and density functional theory (DFT) and examined the OH vibrational shifts of individual H_2O molecules allowing for the exploration of not only solute$\cdots$solvent influences, but also solvent$\cdots$solvent influences on the hydration of this fluorinated anion.[56] For the four PF_6^- dihydrate minima that only exhibit solvent$\cdots$solute DIHB contacts, CCSD(T)/haTZ computations indicate the lowest-energy harmonic OH stretches fall in a very narrow window from 3799 to 3801 cm^{-1} with IR intensities ranging from 54 to 125 km mol^{-1} (Table S7 from Ref. 56). The OH stretching frequencies become even smaller when solute$\cdots$solute interactions are present, such as the water$\cdots$water hydrogen bond formed in the lowest-energy structure identified for $PF_6^-(H_2O)_2$ (C_s WW−Edge−Face in Figure 2 of Ref. 56) for which the smallest CCSD(T)/haTZ OH stretching frequency

decreases to 3721 cm^{-1} with a commensurate increase in the corresponding IR intensity to 211 km mol^{-1}. This harmonic OH vibration is only 95 cm^{-1} larger than that predicted from DFT AIMD simulations of BF_4^- hydration.[41] Computed dissociation energies of microhydrated PF_6^- were the largest when solvent$\cdots$solvent interactions were present highlighting the importance of these cooperative effects on the hydration of the anion.

The $BF_4^-(H_2O)_{n=1,2}$ system has been previously characterized with B3LYP and MP2 methods along with basis sets as large as triple-ζ.[57] Two following two minimum energy structures were reported: a monohydrate complex (denoted as C_{2v} DI_1 in Figure 4.1a) and a dihydrate complex (denoted as D_{2d} DI_2 in Figure 4.2c). The dihydrate complex was devoid of any solvent$\cdots$solvent interactions and both waters only interact directly with the solute. The reported MP2 harmonic OH stretching frequency shifts of water (denoted here as $\Delta\omega$ to distinguish from shifts associated with fundamental frequencies, $\Delta\nu$) relative to an isolated water molecule were $\Delta\omega_1 = -41$ cm^{-1} and $\Delta\omega_3 = -110$ cm^{-1} in the monohydrate complex and $\Delta\omega_1 = -33$ cm^{-1} and $\Delta\omega_3 = -95$ cm^{-1} in the dihydrate complex. This study addresses the microsolvated nature of BF_4^- but considers complexes with up to four water molecules (i.e. $BF_4^-(H_2O)_{n=1,2,3,4}$) while employing robust WFT methods and a variety of DFT methods with a flexible, correlation-consistent basis set. Computed OH vibrational shifts will be referenced to an isolated water molecule, resulting in a reported red-shift unlike commonly reported blue-shifts in work that commonly references bulk phase water. Solute$\cdots$solvent and solvent$\cdots$solvent effects on the hydration of BF_4^- will be discussed as well as the dissociation energies of these complexes.

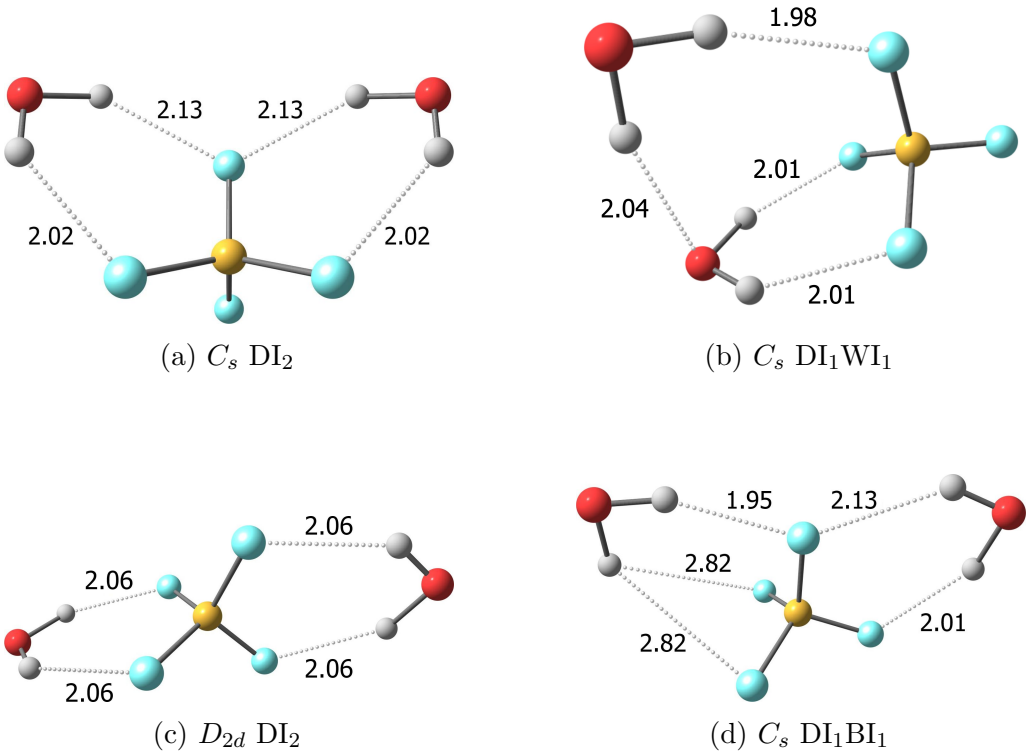

(a) C_s DI_2 (b) C_s DI_1WI_1

(c) D_{2d} DI_2 (d) C_s DI_1BI_1

Figure 2.2: CCSD(T)/haTZ optimized stationary points of $BF_4^-(H_2O)_2$ with select intermolecular R(H$\cdots$F) and R(H$\cdots$O) distances in Å. The 2b:Mb/haTZ optimized intermolecular R(H$\cdots$F) and R(H$\cdots$O) distances are identical to (or within 0.01 Å) of the corresponding CCSD(T) values.

2.3 Computational Details

Many of the optimized structures reported here were generated by replicating the hydration patterns previously identified for BF_4^- and related anions such as BeF_4^{2-}, SO_4^{2-}, and PF_6^-.[56–59] Additional structures were obtained by systematically introducing additional water molecules along the edges and faces of the BF_4^- tetrahedron to consider unique permutations of solvent$\cdots$solute and solvent$\cdots$solvent interactions. All of these starting structures optimized to one of the various stationary points presented in the Results and Discussion. Although other minima certainly exist, these should provide a good representation of the lowest-energy hydrogen bonding motifs for the mono-, di-, tri- and tetrahydrates of BF_4^-.

For each configuration of the $BF_4^-(H_2O)_{n=1,2,3,4}$ clusters and the isolated fragments (BF_4^- and H_2O), fully optimized geometries and corresponding harmonic vibrational frequencies were computed with three different density functional theory (DFT) methods (B3LYP,[60] B3LYP-D3,[60,61] and M06-2X[62]) as well as the MP2[63] *ab initio* method utilizing the analytic gradients and Hessians available in Gaussian 16.[64] For the mono- and di-hydrate (n=1, 2) structures, CCSD(T) optimized structures were also obtained using the analytic gradients in CFOUR.[65] The corresponding CCSD(T) harmonic vibrational were computed from finite differences of gradients. The finite difference procedure was validated with the MP2 method for which the frequencies computed in this manner never differed by more than 0.1 cm^{-1} from those obtained analytically.

The N-body:Many-body (Nb:Mb) method for non-covalent clusters[66–69] has been employed to help extend the demanding CCSD(T) computations to the larger complexes in this study ($n = 2,\ 3,\ 4$). In the hierarchy of Nb:Mb procedures, the multi-centered[70–74] extension of the ONIOM technique[75–77] is used to recast the traditional many-body expansion[78] of the cluster interaction energy as an ONIOM-based fragmentation scheme. In this procedure the leading dominant N terms in the many-body expansion are computed with an accurate high-level method, whereas the remaining terms are recovered with a less demanding but less robust low-level method. For this study, we have selected the 2b:Mb version of the Nb:Mb procedure which can obtain results nearly identical to those from canonical CCSD(T) computations for these di-, tri- and tetrahydrate systems. In this implementation, CCSD(T) is used as the high-level (hi) method to describe all 1-body contributions (E_1) and 2-body interactions (ΔE_2) in the cluster while MP2 is used as the low-level (lo) method to recover the remaining ($\geq$ 3-body) interactions via a computation on the entire cluster (E_{cluster}). This method gives the following linear expression for the 2b:Mb energy:

$$E_{\text{cluster}}^{\text{2b:Mb}} = E_{\text{cluster}}^{lo} + E_1^{hi} + \Delta E_2^{hi} - E_1^{lo} - \Delta E_2^{lo} \tag{2.1}$$

Analogous expressions can readily be obtained for properties associated with linear operators such as geometrical derivatives. Consequently, the 2b:Mb geometry optimizations and harmonic vibrational frequency computations[67–69,74] were carried out in this study with Gaussian 16 utilizing its own MP2 analytic gradients and Hessians along with CCSD(T) analytic gradients and numerical Hessians from CFOUR.

A formally equivalent approach has been developed by Raghavachari and co-workers. They have used the molecules-in-molecules (MIM) method[79] to efficiently compute MP2 energies[80,81] and DFT spectra for large systems, such as IR,[82] Raman,[83] Vibrational Circular Dichroism (VCD),[84] Raman Optical Activity (ROA)[85] and NMR[86] for large systems. Like other techniques based on the many-body expansion of the interaction energy for non-covalent molecular clusters,[78] these approaches take advantage of the rapid convergence typically observed for this property in such systems.[87–90] Although conceptually simple, the idea of dividing a large system into a number of smaller interacting fragments method is quite powerful.[91–93] As the number of these techniques continues to grow, particularly for non-covalent clusters, two classification schemes have been helpful for identifying their similarities and differences. Richard and Herbert introduced the generalized many-body expansion (GMBE) framework,[94–96] whereas Mayhall and Raghavachari have broadly classified methods into either top-down or bottom-up approaches.[97] A complete literature review is beyond the scope of this work, but some related efforts include: the effective fragment potential (EFP) method,[98–100] the fragment molecular orbital (FMO) method,[101–103] the molecular tailoring approach (MTA),[104,105] the embedded-fragment scheme[106–108] the electrostatically embedded many-body (EE-MB) method,[109–111] the generalized energy-based fragmentation (GEBF) method,[112–114] the hybrid many-body interaction (HMBI) method,[115–117] the extended ONIOM (XO) method,[118,119] the explicit polarization (X-Pol) methods,[120,121] and the stratified approximation many-body approach (SAMBA).[122]

All computations for this investigation employed Dunning's correlation consistent triple-ζ basis sets augmented with diffuse functions on all non-hydrogen (or "heavy") atoms (cc-pVTZ

for H and aug-cc-pVTZ for B, O, F; denoted haTZ).[5,123] As early as 1993, Del Bene began demonstrating that diffuse functions were not needed on H atoms to reliably characterize the energetics of hydrogen bonding with correlation consistent basis sets, including complexes containing a negatively charged fragment.[124,125] In fact, MP2 dissociation energies for the water dimer and trimer tend to be much closer to the complete basis set limit when diffuse functions are omitted from the H atoms.[126–128] Those early studies by Del Bene introduced a modified aug′ prefix to denote the mixed basis sets where cc-pVXZ is used for H and aug-cc-pVXZ was used for the other atomic centers (i.e., aug′cc-pVXZ or simply a′XZ where X is the cardinal number of the basis set). Although still utilized,[58,129] the prime designation in the basis set name has sometimes been adopted in other contexts. Consequently, an alternative heavy-aug-cc-pVXZ or haug-cc-pVXZ (or simply ha$X$Z) notation was introduced around 2007 to indicate that only the basis sets for the "heavy" (i.e., non-hydrogen) atoms were augmented with diffuse functions,[74,128,130–132] and that nomenclature has been adopted in a number of important studies on non-covalent interactions from other groups.[133–138] Another naming scheme was introduced in 2011 that uses prefixes based on the months of the calendar year leading up to August (e.g., may-, jun-, jul-, aug-)[139,140] in which jul-cc-pVXZ is equivalent to the earlier aug′-cc-pVXZ and haug-cc-pVXZ designations. Spherical harmonic $5d$ and $7f$ basis functions were used rather than their $6d$ and $10f$ Cartesian counterparts for all computations, and all DFT computations utilized a dense pruned numerical integration grid composed of 99 radial shells and 590 angular points per shell (corresponding to the UltraFine keyword).

In order to evaluate the electronic dissociation energies (D_e) of the complexes computed via the supermolecular approach given in Equation 2.2.

$$D_e = E(\mathrm{BF_4}^-) + nE(\mathrm{H_2O}) - E([\mathrm{BF_4}^-(\mathrm{H_2O})_n]) \tag{2.2}$$

This scheme for computing the dissociation energies introduces an inconsistency commonly referred to as basis set superposition error (BSSE).[141,142] To assess the impact of this inconsistency, a counterpoise (CP) procedure[143,144] was applied to the lowest-energy minima identified for $n = 1$, defined below in Equation 2.3.[145]

$$D_e^{\mathrm{CP}} = E(\mathrm{dimer}) - \sum_{i=1}^{2}\Big[E(\mathrm{fragment}_i)^{\text{dimer basis}}_{\text{dimer geometry}} + E(\mathrm{fragment}_i)^{\text{fragment basis}}_{\text{fragment geometry}} - E(\mathrm{fragment}_i)^{\text{fragment basis}}_{\text{dimer geometry}}\Big] \tag{2.3}$$

The extension of this procedure is not uniquely defined for systems with ≥ 3 fragments. However, a detailed protocol described elsewhere[128] for flexible fragments was followed for the $BF_4{}^-(H_2O)_{n=2,3,4}$ systems.

2.4 Results and Discussion

When a water molecule interacts with $BF_4{}^-$, there are four structural motifs observed for the mono-, di-, tri-, and tetrahydrate stationary points shown in Figures 2.1, 2.2, 2.3, and 2.4. The "DI_w" label denotes that w water molecules have formed double ionic hydrogen bonds with a pair of fluorine atoms (Figure 4.1a). This is the same motif that was recently reported for the microsolvation of the isovalent $BeF_4{}^{2-}$ ion.[58] The "BI_x" label denotes that x water molecules have formed one hydrogen bond with one fluorine atom and a separate bifurcated hydrogen bond with two other fluorine atoms (Figure 4.1b). When two or more water molecules are present, hydrogen bonding between the waters can also occur. The "WI_y" label denotes that y water molecules have formed a hydrogen bond with one fluorine atom and a hydrogen bond with another water molecule (Figure 4.2b). The "W_z" label denotes that z water molecules have formed one or two hydrogen bonds with at least one other water molecule but not the ion (Figure 2.3d). For each motif, $w + x + y + z = n$ where n is the number of water

molecules present. The Cartesian coordinates and harmonic vibrational frequencies for the mono-, di-, tri-, and tetrahydrated structures are reported in the Supporting Information.

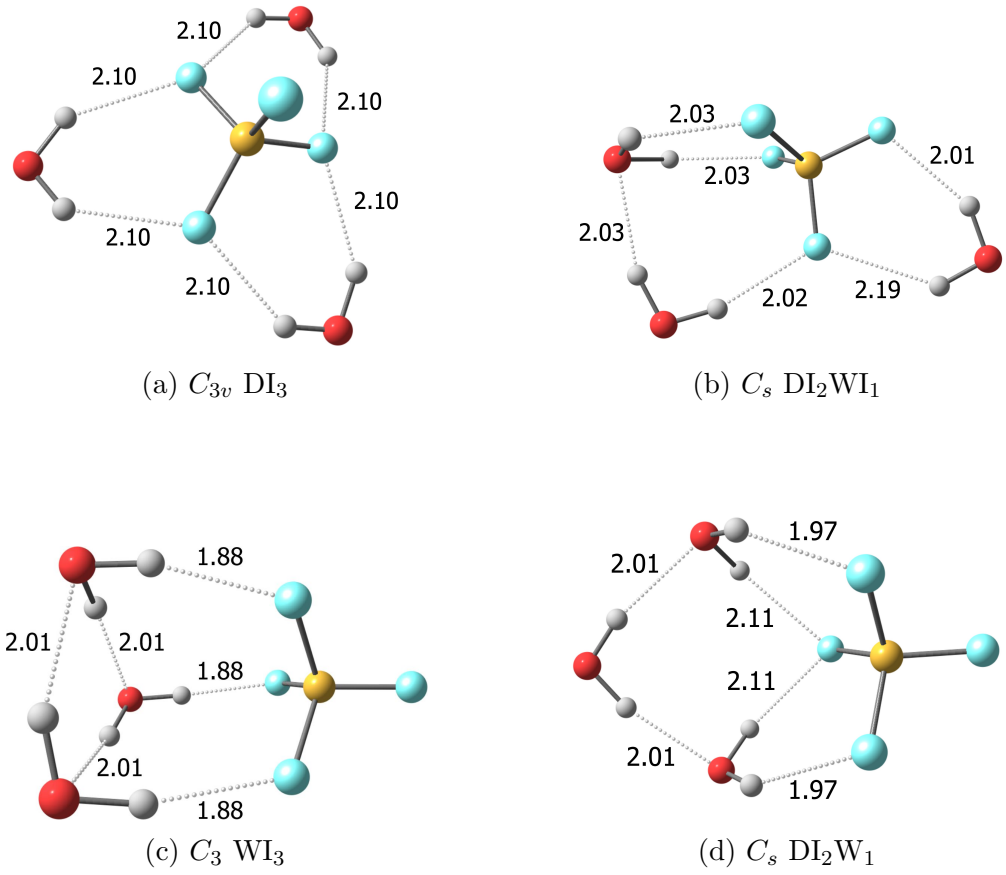

(a) C_{3v} DI_3 (b) C_s DI_2WI_1

(c) C_3 WI_3 (d) C_s DI_2W_1

Figure 2.3: 2b:Mb/haTZ optimized stationary points of $BF_4^-(H_2O)_3$ with select intermolecular R(H$\cdots$F) and R(H$\cdots$O) distances in Å.

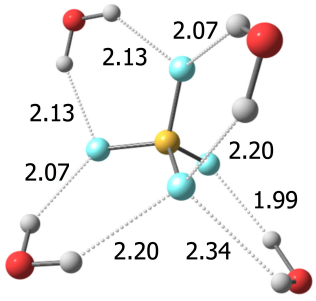

(a) C_s DI_4

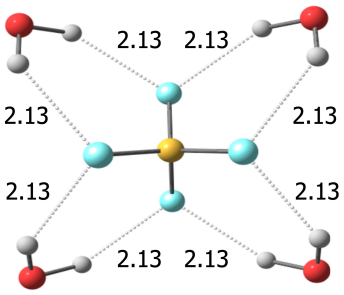

(b) D_2 DI_4

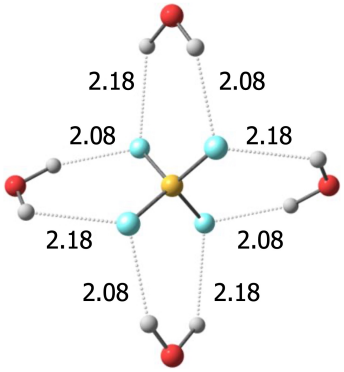

(c) S_4 DI_4

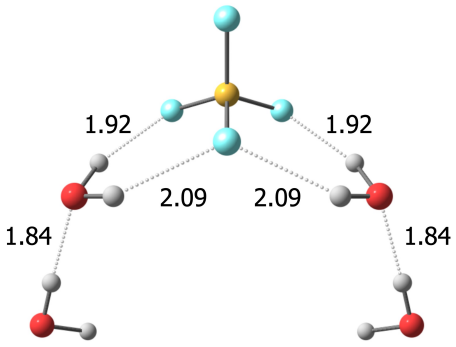

(d) C_s DI_2W_2

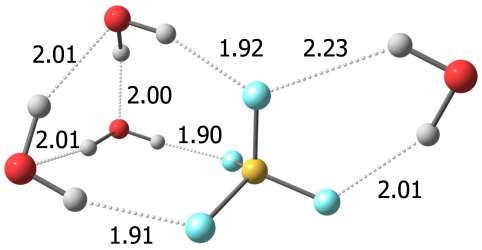

(e) C_1 DI_1WI_3

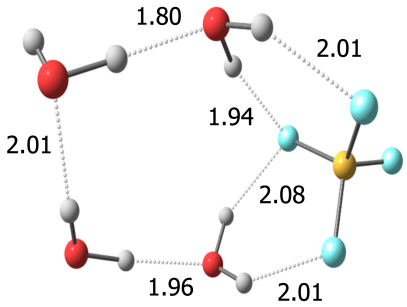

(f) C_1 DI_2W_2

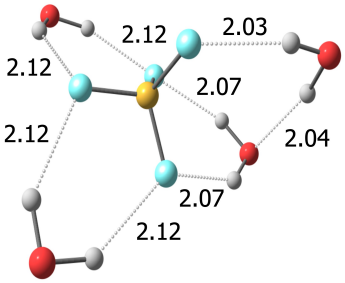

(g) C_s DI_3WI_1

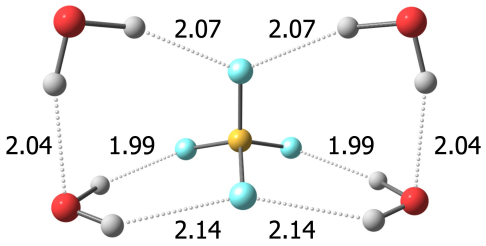

(h) C_s DI_2WI_2

Figure 2.4: 2b:Mb/haTZ optimized stationary points of $BF_4^-(H_2O)_4$ with select intermolecular R(H$\cdots$F) and R(H$\cdots$O) distances in Å

Table 2.1: Relative electronic energies (ΔE in kcal mol^{-1}) and number of imaginary modes (n_i) of the BF_4^- $(H_2O)_{n=1,2,3,4}$ structures optimized with various methods and the haTZ basis set.

Structure	n_i	B3LYP	B3LYP–D3BJ	M06–2X	MP2	CCSD(T)	2b:Mb
$n = 1$							
C_{2v} DI_1	0	0.00	0.00	0.00	0.00	0.00	-
C_s BI_1	1	1.15	1.27	1.19	1.24	1.28	-
$n = 2$							
D_{2d} DI_2	0	0.00	0.00	0.00	0.00	0.00	0.00
C_s DI_2	0	0.40	0.36	0.47	0.39	0.39	0.39
C_s DI_1BI_1	1	1.43	1.51	1.45	1.49	1.52	1.52
C_s DI_1WI_1	0	−1.03	−1.64	−1.35	−1.32	−1.30	−1.35
$n = 3$							
C_{3v} DI_3	0	0.00	0.00	0.00	0.00	-	0.00
C_s DI_2WI_1	0	−2.01	−2.50	−2.43	−2.24	-	−2.25
C_s DI_2W_1	0	−2.90	−3.55	−3.03	−2.95	-	−2.88
C_3 WI_3	0	−5.92	−7.35	−6.61	−6.32	-	−6.31
$n = 4$							
S_4 DI_4	0[a]	0.00	0.00	0.00	0.00	-	0.00
D_2 DI_4	1	0.12	0.00	−0.01	0.02	-	0.00
C_s DI_4	1[b]	0.12	0.10	0.19	0.13	-	0.14
C_s DI_2W_2	0	−2.47	−1.79	−0.33	−1.13	-	−0.56
C_s DI_3WI_1	0	−2.13	−2.67	−2.61	−2.42	-	−2.44
C_1 DI_2W_2	0	−3.96	−4.26	−4.49	−3.34	-	−2.92
C_s DI_2WI_2	0	−3.50	−4.62	−4.43	−4.09	-	−4.12
C_1 DI_1WI_3	0	−6.78	−8.21	−7.60	−7.20	-	−7.18

[a] $n_i = 1$ for M06–2X
[b] $n_i = 0$ for B3LYP–D3BJ

2.4.1 Monohydrate Structures and Relative Energies

In addition to the C_{2v} DI_1 minimum reported by Wang, Li, and Han[57] (Figure 4.1a), a second stationary point has been identified in the current work for the monohydrated BF_4^- system (Figure 4.1b). The C_s BI_1 configuration is a transition state lying 1.28 kcal mol^{-1} above the C_{2v} DI_1 structure according to the CCSD(T)/haTZ electronic energy (ΔE values in

Table 2.1). Compared to the monohydrated structures of PF_6^-, the C_s Face transition state lies 0.30 kcal mol^{-1} above the C_{2v} Edge structure at the CCSD(T)/haTZ level of theory.[56]

The distance between the F atoms that interact with the H_2O molecule in the C_{2v} DI_1 structure (Figure 4.1a) is 2.0 Å, which is only 0.1 Å smaller than the corresponding distance for the analogous structure of $PF_6^-(H_2O)_1$ (denoted C_{2v} Edge in Figure 1 of Ref. 56). Both of these values are similar to but slightly smaller than the usual distance-based threshold of 2.2 Å for the transition between single and double ionic hydrogen bonding motifs.[51] The F$\cdots$HO angle about the hydrogen bond in the C_{2v} DI_1 structure is 143°, similar to analogous angles for other DIHB monohydrates (146 ± 2 degrees).[51]

2.4.2 Dihydrate Structures and Relative Energies

In addition to the D_{2d} DI_2 minimum characterized in a prior study,[57] three new stationary points were identified with correlated WFT methods (MP2, CCSD(T), and 2b:Mb) for the $BF_4^-(H_2O)_2$ system and to our knowledge, have not been reported before in the literature. These four configurations are shown in Figure 2.2. For two of the four structures, both waters bridge an edge of the BF_4^- tetrahedron which includes the C_s DI_2 and the D_{2d} DI_2 structures (Figure 4.2a and 4.2c, respectively). The C_s DI_1BI_1 dihydrate structure (Figure 2.2d) was generated from the D_{2d} DI_2 configuration by moving one of the water molecules from the edge to an adjacent face. The C_s DI_1WI_1 configuration (Figure 4.2b) exhibits a completely different hydrogen bonding topology with one hydrogen bond forming between the two water molecules along with three hydrogen bonds between the water molecules and the tetrafluoroborate anion.

The D_{2d} DI_2 structure was used as the reference for the dihydrate relative energies in Table 2.1, because it has been previously characterized in a prior study as a minimum for $BF_4^-(H_2O)_2$.[57] The other dihydrate structure with a similar DIHB motif (C_s DI_2), lies 0.39 kcal mol^{-1} above the D_{2d} DI_2 structure according to the MP2, 2b:Mb, and canonical CCSD(T) relative electronic energies in Table 2.1. The C_s DI_1BI_1 is a transition state lying 1.49 to 1.52

kcal mol^{-1} higher in energy according to the MP2, 2b:Mb, and canonical CCSD(T) results in Table 2.1. Similar to the hydration of other molecular anions, the introduction of a second water molecule leads to water$\cdots$water interactions that are significant.[146–150] The newly identified C_s DI_1WI_1 structure that exhibits water$\cdots$water hydrogen bonding consistently has the lowest MP2, 2b:Mb, and canonical CCSD(T) electronic energies and lies 1.30 to 1.35 kcal mol^{-1} below the D_{2d} DI_2 structure only involving water$\cdots$ion interactions according to the MP2 and CCSD(T) results in Table 2.1, respectively. These results could be indicative that the solvent$\cdots$solvent interactions between the water molecules could be just as important as the solvent$\cdots$solute interactions between water and BF_4^- in the characterization of the hydration of this ion. The analogous PF_6^- structure exhibiting water$\cdots$water hydrogen bonding (C_s WW$-$Edge$-$Face in Figure 2 of Ref. 56) lies approximately 2 kcal mol^{-1} below the other structures only involving water$\cdots$ion interactions.[56]

MP2 and CCSD(T) harmonic vibrational frequencies indicate that both of the DI_2 stationary points are minima. The C_s DI_1BI_1 configuration is a transition state and the C_s DI_1WI_1 structure appears to be a strong candidate for the global minimum of the $BF_4^-(H_2O)_2$ system.

2.4.3 Trihydrate Structures and Relative Energies

Four new stationary points were identified for the $BF_4^-(H_2O)_3$ system with the MP2 and 2b:Mb methods and these configurations are shown in Figure 2.3. To the best of our knowledge, these structures have not been reported before in the literature, and the MP2 and 2b:Mb harmonic vibrational frequencies indicate each one is a minimum. In the C_{3v} DI_3 structure (Figure 4.3a), all three waters bridge an edge of the BF_4^- tetrahedron. For two of the five structures, all three waters interact with one another. This includes the C_3 WI_3 and the C_s DI_2W_1 structures (Figure 4.3d and 2.3d, respectively). In the C_s DI_2WI_1 structure (Figure 4.3b), two water molecules interact with one another while the third water molecule only forms hydrogen bonds with the ion.

All of the structures that exhibit water$\cdots$water hydrogen bonding have electronic energies at least 2 kcal mol^{-1} lower than the C_{3v} DI_3 structure that only has water$\cdots$ion interactions. The C_3 WI_3 and C_s DI_2W_1 structures where multiple hydrogen bonds are formed between the three waters lie lower than the C_s DI_2WI_1 structure that only has one hydrogen bond formed between two of the three waters. The 2b:Mb energetics in Table 2.1 indicate that the C_s DI_2WI_1 structure lies 2.25 kcal mol^{-1} lower than the C_{3v} DI_3 structure compared to the C_s DI_2W_1 and C_3 WI_3 structures that lie 2.88 and 6.31 kcal mol^{-1} lower, respectively. These results further demonstrate the importance of solvent$\cdots$solvent interactions when characterizing the hydration of the BF_4^- ion. The C_3 WI_3 structure consistently has the lowest electronic energy and appears to be a strong candidate as the global minimum of the $BF_4^-(H_2O)_3$ system.

2.4.4 Tetrahydrate Structures and Relative Energies

Eight new stationary points were identified for the $BF_4^-(H_2O)_4$ system and all eight configurations are shown in Figure 2.4. To our knowledge, these structures have not been reported before in the literature. In three of the eight configurations, all four waters bridge an edge of the BF_4^- tetrahedron. This includes the S_4 DI_4 minimum (Figure 2.4c), and the two other DI_4 structures (C_s and D_2), which are symmetry unique permutations along the different edges of BF_4^-, and can be see in Figure 2.4a and 2.4b, respectively. All three of the DI_4 structures have very similar electronic energies (within 0.2 kcal mol^{-1} of each other) at all levels of theory used in this study, but the MP2 and 2b:Mb harmonic vibrational frequencies indicate the C_s and D_2 stationary points are transition states.

The structures that exhibit water$\cdots$water hydrogen bonding (Figure 2.4d - 2.4h) all lie lower than the DI_4 structures that only exhibit water$\cdots$ion interactions, and they are all minima based on the harmonic vibrational frequencies computed at each level of theory. The C_s DI_2W_2 structure (Figure 2.4d) and the C_1 DI_2W_2 (Figure 2.4f) both have two water molecules that form hydrogen bonds with the other two water molecules that bridge an edge

of the BF_4^- tetrahedron. However, when the symmetry is relaxed from C_s to C_1 in the C_1 DI_2W_2 structure (Figure 2.4f), a new water$\cdots$water hydrogen bond is formed which leads to a hydrogen-bond bridge being formed between the other two water molecules that have adopted the DIHB motif. The 2b:Mb energetics in Table 2.1 indicate that the C_1 DI_2W_2 structure lies 2.92 kcal mol^{-1} lower in energy than the S_4 DI_4 structure, compared to the C_s DI_2W_2 structure that lies 0.56 kcal mol^{-1} lower. Interestingly, the C_s DI_3WI_1 structure (Figure 2.4b), which has one water molecule that forms hydrogen bonds to both the ion and to one other water molecule, lies lower in energy than the C_s DI_2W_2 structure that exhibits more water$\cdots$water interactions. The C_s DI_3WI_1 lies 2.44 kcal mol^{-1} lower than the S_4 DI_4 structure according to the 2b:Mb energetics in Table 2.1. Two of the four water molecules form hydrogen bonds to both the ion and to one other water molecule in the C_s DI_2WI_2 structure (Figure 2.4c), which lies 4.12 kcal mol^{-1} below the S_4 DI_4 structure, according the 2b:Mb results in Table 2.1. The C_1 DI_1WI_3 structure (Figure 2.4e) has three out of the four water molecules forming hydrogen bonds to both the ion and to each other. It consistently has the lowest electronic energy and is significantly lower than the S_4 DI_4 structure by 7.18 kcal mol^{-1} according the 2b:Mb relative energetics. Thus the C_1 DI_1WI_3 structure appears to be a strong candidate as the global minimum of the $BF_4^-(H_2O)_4$ system. As with both the di- and tri- hydrate relative energies, we see that the solvent$\cdots$solvent interactions between the water molecules should also be taken into consideration in addition to the solvent$\cdots$solute interactions between water and BF_4^- in the characterization of the hydration of this ion.

2.4.5 Dissociation Energies

The electronic dissociation energies (D_e) of the optimized minima for the mono-, di-, tri-, and tetrahydrate systems (i.e. the relative energy of the isolated, optimized fragments: one BF_4^- ion and $n H_2O$ molecules) are given in Table 2.2. According to the MP2 and CCSD(T) results obtained with the haTZ basis set, the monohydrate C_{2v} DI_1 structure has a dissociation energy near 13 kcal mol^{-1} and, as expected, is significantly larger (by more than a factor

of two) than the dissociation energy of the water dimer computed at a comparable level of theory (*ca.* 5 kcal mol^{-1}).[126,151,152] Furthermore, BF_4^- interacts more strongly with water (C_{2v} DI_1; D_e = 13.17 kcal mol^{-1} at the CCSD(T)/haTZ level of theory) than the larger PF_6^- anion (C_{2v} Edge; D_e = 10.55 kcal mol^{-1} at the CCSD(T)/haQZ level of theory from Ref. 56). Interestingly, the additional charge associated with the analogous monohydrate structure of BeF_4^{2-} increases the dissociation energy by a factor of nearly 2.4 according to MP2 computations with the haTZ basis set (12.92 vs 31.00 kcal mol^{-1}).[58]

Table 2.2: Dissociation energies (in kcal mol^{-1}) obtained without the CP procedure for the BF_4^- $(H_2O)_{n=1,2,3,4}$ minima optimized with various methods and the haTZ basis set.

Structure	B3LYP	B3LYP–D3BJ	M06–2X	MP2	CCSD(T)	2b:Mb
$n = 1$						
C_{2v} DI_1	11.77	12.98	13.84	12.92	13.17	-
$n = 2$						
D_{2d} DI_2	22.28	24.68	26.34	24.61	25.12	25.11
C_s DI_2	21.89	24.33	25.87	24.22	24.73	24.73
C_s DI_1WI_1	23.31	26.32	27.69	25.93	26.43	26.46
$n = 3$						
C_{3v} DI_3	30.61	34.29	36.39	34.16	-	34.93
C_s DI_2WI_1	32.61	36.79	38.82	36.40	-	37.18
C_s DI_2W_1	33.50	37.83	39.42	37.11	-	37.81
C_3 WI_3	36.52	41.64	42.99	40.48	-	41.24
$n = 4$						
S_4 DI_4	38.41	43.23	45.76	43.07	-	44.09
C_s DI_2W_2	40.88	45.03	46.09	44.20	-	44.65
C_s DI_3WI_1	40.54	45.91	48.36	45.49	-	46.53
C_1 DI_2W_2	42.37	47.49	50.25	46.41	-	47.01
C_s DI_2WI_2	41.91	47.85	50.19	47.16	-	48.21
C_1 DI_1WI_3	45.18	51.44	53.36	50.27	-	51.27

Perhaps unsurprisingly, the tabulated dissociation energies for the dihydrate structures (Table 2.2) indicate that the introduction of a second solute$\cdots$solvent interaction is nearly perfectly additive. For example, when two water molecules attach to different edges of the

BF_4^- tetrahedron to form the C_s DI_2 and D_{2d} DI_2 minima, the D_e increases by a factor of ≈1.9, or to approximately 25 kcal mol^{-1}, relative to the corresponding value of the monohydrate minimum, C_{2v} DI_1, according to the MP2, 2b:Mb, and canonical CCSD(T) results in Table 2.2. Compared to the analogous all edge structures of $PF_6^-(H_2O)_2$, the D_e increase factor is also ≈1.9 relative to the corresponding value of the monohydrate minimum. At the CCSD(T)/haQZ level of theory, the dissociation energies for the all edge dihydrate minima of PF_6^- are approximately 20 kcal mol^{-1}. One dihydrate complex was reported for BeF_4^{2-} and has a dissociation energy of 59.37 kcal mol^{-1} according to MP2/haTZ.[58] The D_e increase factor is also ≈1.9 relative to the monohydrate structure.

Moving to the trihydrate structures without solvent$\cdots$solvent interactions, larger deviations from pairwise additivity are observed when a third water molecule forms a DIHB with the ion. D_e for the C_{3v} DI_3 structure increases by a factor of ≈2.7 relative to the monohydrate minimum to a value of 34.93 kcal mol^{-1} according to the 2b:Mb/haTZ data in Table 2.2. For the tetrahydrate DI_4 structures the attenuation is even more pronounced, and D_e only increases by a factor of ≈3.3 relative to the monohydrate minimum, or to 44.09 kcal mol^{-1} as seen in the S_4 DI_4 configuration devoid of solvent$\cdots$solvent contacts. Compared to the one tetrahydrate complex of BeF_4^{2-}, the dissociation energy is 105.71 kcal mol^{-1} at the MP2/haTZ level of theory, which gives a similar D_e increase factor of ≈3.4 relative to the monohydrate structure.[58]

The presence of interactions between solute and solvent molecules can significantly impact the dissociation energies of the complex. An almost perfectly pairwise additive increase close to exactly 2 is observed for the dissociation energy of the C_s DI_1WI_1 structure relative to the monohydrate minimum, C_{2v} DI_1. In comparison to the C_s WW−Edge−Face structure of $PF_6^-(H_2O)_2$, cooperative effects were displayed with the water$\cdots$water hydrogen bonding that enhanced the D_e to greater than 22 kcal mol^{-1}, or by a factor of ≈2.1.[56]

In the trihydrate complexes, the C_3 WI_3 configuration that contains both solute$\cdots$solute and solvent$\cdots$solvent interactions has the lowest D_e for all levels of theory. When the three

waters are able to interact with two neighboring water molecules, as well as having a direct interaction with the solute anion, the 2b:Mb dissociation energy is 41.24 kcal mol^{-1}. Large dissociation energies are also observed for the other trihydrate structures that contain both solute$\cdots$solvent and solvent$\cdots$solvent interactions. The D_e increases by a factor of $\approx$3.1, which is larger than the increase of $\approx$2.7 as seen in the DIHB motif.

A similar trend is seen with the tetrahydrate structures. The configurations with numerous solute$\cdots$solvent and solvent$\cdots$solvent interactions lead to larger D_e. In fact, the C_1 DI_1WI_3 complex, consisting of four water molecules interacting with the anion and three water molecules directly interacting with two neighboring molecules, gives the largest 2b:Mb D_e of 51.27 kcal mol^{-1}, 7.18 kcal mol^{-1} stronger than when solvent$\cdots$solvent interactions are not present. Compared to the DIHB motif with an increase factor of $\approx$3.3, the D_e increases by a factor of $\approx$3.9.

When the appropriate CP procedure is applied to the lowest-energy structures identified for the mono-, di-, tri-, and tetrahydrate systems (C_{2v} DI_1, C_s DI_1WI_1, C_3 WI_3, and C_1 DI_1WI_3, respectively) the MP2/haTZ dissociation energies decrease by less than 5-6% for all four configurations. All dissociation energies computed with the CP procedure can be found in the Supporting Information.

2.4.6 Vibrational Frequencies

The first two rows of Tables 2.3 and 2.4 contain the harmonic symmetric (a_1) and antisymmetric (b_2) OH stretching frequencies (ω) computed for an isolated water molecule. As a water molecule binds to an edge of the BF_4^- tetrahedron, the OH$\cdots$F hydrogen bonds perturb the OH stretching vibrations of the water molecule which induces a shift in the corresponding frequency ($\Delta\omega$). For example, in the C_{2v} DI_1 monohydrate structure, the energy of the symmetric a_1 stretching mode decreases by 41 cm^{-1} and the antisymmetric b_2 mode decreases by 110 cm^{-1} according to the CCSD(T)/haTZ results reported in Table 2.3.

Table 2.3: The harmonic OH stretching frequencies (ω in cm^{-1}) for H_2O and BF_4^- $(H_2O)_{n=1,2}$ minima computed with an haTZ basis set.

Structure	Irreps	B3LYP	B3LYP–D3BJ	M06–2X	MP2	CCSD(T)	2b:Mb
H_2O (ω)	a_1	3802	3802	3872	3824	3814	-
	b_2	3905	3905	3977	3952	3924	-
C_{2v} DI_1 (ω)	a_1	3744	3743	3820	3770	3772	-
	b_2	3776	3773	3852	3825	3815	-
C_s DI_2 (ω)	a''	3740	3746	3828	3774	3778	3778
	a'	3742	3748	3830	3776	3779	3780
	a''	3809	3801	3873	3848	3835	3835
	a'	3813	3806	3879	3853	3839	3839
C_s DI_1WI_1 (ω)	a'	3673	3667	3764	3706	3716	3714
	a'	3721	3719	3793	3746	3750	3750
	a'	3749	3745	3830	3795	3790	3790
	a''	3757	3752	3830	3803	3795	3796
D_{2d} DI_2 (ω)	b_2	3754	3753	3828	3779	3780	3781
	a_1	3756	3755	3829	3780	3782	3782
	e	3794	3792	3868	3842	3830	3831
	e	3794	3792	3868	3842	3830	3831

In the DI_2 dihydrate minima (C_s and D_{2d}), where two water molecules bind to different edges of the anion tetrahedron, the magnitudes of the vibrational frequency shifts are smaller than those reported for the monohydrate. According to the CCSD(T)/haTZ harmonic vibrational frequencies in Table 2.3, the OH stretching frequencies shift to lower energy by -34 ± 2 cm^{-1} and -90 ± 5 cm^{-1} for the symmetric and antisymmetric modes, respectively, in the two DI_2 dihydrate minima (C_s and D_{2d}). The shifts are slightly larger than the corresponding changes seen in $PF_6^-(H_2O)_2$, where the symmetric OH stretch shifted to lower energy by -19 ± 7 cm^{-1}, and the antisymmetric OH stretch shifted to lower energy by -75 ± 14 cm^{-1}.[56]

The C_s DI_1WI_1 structure has a different hydrogen bond topology than that of the DI_2 structures and, therefore, exhibits much larger OH stretching frequency shifts than that of the DI_2 minima. According to the CCSD(T)/haTZ harmonic vibrational frequencies in Table 2.3, all but one of the OH stretching modes shift by at least 95 cm^{-1}. The $\Delta\omega$ value of

-64 cm^{-1} is associated with the mode that is dominated by the synchronous OH stretching motion in the water molecule that accepts the hydrogen bond from the other water molecule. In contrast, the $\Delta\omega$ value of -98 cm^{-1} can be seen for the water molecule that donates the hydrogen bond. For the asynchronous stretching modes associated with the donor and acceptor of the hydrogen bond, the $\Delta\omega$ values are -134 and -129 cm^{-1}, respectively. A similar trend is seen for the analogous C_s WW$-$Edge$-$Face dihydrate structure of PF_6^-,[56] although 3 of the 4 shifts are smaller in magnitude by approximately 30 cm^{-1} according to the CCSD(T)/haTZ harmonic frequencies reported in Table S7 from Ref 38.

The magnitudes of the vibrational frequency shifts in systems where three water molecules bind to different edges of the anion tetrahedron as seen in the DI_3 trihydrate minimum (C_{3v}) are smaller than those reported for the mono- and dihydrate. According to the 2b:Mb/haTZ harmonic vibrational frequencies in Table 2.4, the symmetric OH stretch shifts to lower energy by -21 ± 2 cm^{-1}, and the antisymmetric OH stretch shifts to lower energy by -75 ± 3 cm^{-1}. As seen with the C_s DI_1WI_1 dihydrate that exhibits water$\cdots$water hydrogen bonding, all of the remaining trihydrate structures that also exhibit water$\cdots$water hydrogen bonding which induces much larger OH stretching frequency shifts than that of the DI_3 minimum. According the 2b:Mb/haTZ level of theory, the C_3 WI_3 structure where all three waters interact with each other exhibits the largest OH stretching frequency shifts. The largest shifts of the OH stretches are approximately -180 cm^{-1} for vibrations regardless of whether they have symmetric and antisymmetric character.

Table 2.4: The harmonic OH stretching frequencies (ω in cm^{-1}) for H_2O and BF_4^- $(H_2O)_{n=3}$ minima computed with an haTZ basis set.

Structure	Irreps	B3LYP	B3LYP–D3BJ	M06–2X	MP2	CCSD(T)	2b:Mb
H_2O (ω)	a_1	3802	3802	3872	3824	3814	-
	b_2	3905	3905	3977	3952	3924	-
C_{3v} DI_3 (ω)	e	3767	3767	3839	3792	-	3791
	e	3767	3767	3839	3792	-	3791
	a_1	3770	3770	3843	3795	-	3794
	a_2	3813	3810	3884	3859	-	3846
	e	3819	3817	3891	3866	-	3852
	e	3819	3817	3891	3866	-	3852
C_s DI_2WI_1 (ω)	a′	3671	3666	3768	3708	-	3717
	a′	3733	3732	3806	3758	-	3761
	a′	3740	3750	3834	3778	-	3783
	a′	3772	3768	3845	3815	-	3807
	a″	3773	3769	3850	3819	-	3811
	a′	3828	3819	3886	3865	-	3850
C_3 WI_3 (ω)	a	3589	3575	3691	3618	-	3635
	e	3640	3631	3736	3671	-	3683
	e	3640	3631	3736	3671	-	3683
	e	3688	3681	3785	3737	-	3738
	e	3688	3681	3785	3737	-	3738
	a	3707	3702	3801	3753	-	3754
C_s DI_2W_1 (ω)	a′	3636	3634	3740	3672	-	3685
	a″	3646	3677	3779	3731	-	3739
	a′	3697	3723	3816	3755	-	3766
	a″	3743	3724	3819	3768	-	3774
	a″	3779	3794	3855	3835	-	3821
	a′	3839	3800	3865	3841	-	3828

As four water molecules bind to different edges of the anion tetrahedron in the DI_4 tetrahydrate minimum (S_4), the magnitudes of the $\Delta\omega$ values are the smallest for the entire $DI_{n=1-4}$ series of minima that only exhibit DIHB interactions. According to the 2b:Mb/haTZ harmonic vibrational frequencies in Table 2.5, the symmetric OH stretches shift to lower energy by -16 ± 2 cm^{-1}, and the antisymmetric OH stretches shift to lower energy by -61 ± 4 cm^{-1}. As shown before, the structures with water$\cdots$water hydrogen bonding induce much larger OH stretching frequency shifts. At the 2b:Mb/haTZ level of theory, the C_1 DI_2W_2 structure that forms a bridge between all four molecules exhibits the largest OH stretching frequency shifts with symmetric character of -281 cm^{-1}. However, the C_1 DI_1WI_3 structure that has three out of the four water molecules interacting with each other exhibits the largest OH stretching frequency shifts with antisymmetric character of -167 cm^{-1}.

Due to solvent$\cdots$solute interactions, vibrational frequency shifts are also induced in the BF stretching modes of the tetrafluoroborate anion. However, these shifts tend to be slightly smaller. In the C_{2v} DI_1 monohydrate structure, the CCSD(T)/haTZ harmonic vibrational frequencies demonstrate that one of the BF stretching frequencies shift by -50 cm^{-1} to lower energy while another shifts by $+30$ cm^{-1} to higher energy. The other two stretching modes shift by no more than -6 cm^{-1}. These shifts are much larger than those observed for the PF stretching modes.[56] When a second water molecule is added, the frequency shifts in the C_s DI_2 and the C_s DI_1BI_1 structures are similar to the monohydrate shifts. However, the CCSD(T)/haTZ frequency shifts do not exceed ± 11 cm^{-1} for the D_{2d} DI_2 structure. When a third or fourth water molecule is added, the frequency shifts are similar to that of the mono- and dihydrate structures. The computed harmonic vibrational frequencies and corresponding IR intensities can be found in the Supporting Information.

Table 2.5: The harmonic OH stretching frequencies (ω in cm^{-1}) for BF_4^- $(H_2O)_{n=4}$ minima computed with an haTZ basis set.

Structure	Irreps	B3LYP	B3LYP-D3BJ	M06–2X	MP2	2b:Mb
C_s DI_3WI_1 (ω)	a′	3680	3675	3774	3716	3725
	a′	3748	3747	3817	3771	3772
	a″	3773	3773	3845	3797	3796
	a′	3775	3775	3848	3799	3798
	a′	3781	3777	3857	3824	3816
	a″	3796	3794	3866	3841	3831
	a″	3825	3823	3898	3871	3857
	a′	3828	3827	3902	3875	3861
C_s DI_2WI_2 (ω)	a″	3671	3669	3772	3711	3721
	a′	3673	3671	3774	3713	3723
	a″	3719	3730	3812	3757	3764
	a′	3721	3732	3814	3759	3765
	a″	3786	3781	3857	3826	3817
	a′	3794	3790	3863	3835	3826
	a″	3804	3795	3867	3840	3828
	a′	3807	3799	3869	3844	3831
C_s DI_2W_2 (ω)	a″	3505	3492	3614	3555	3588
	a′	3509	3496	3618	3559	3592
	a″	3694	3703	3801	3735	3750
	a′	3698	3707	3804	3739	3753
	a″	3797	3786	3852	3828	3818
	a′	3802	3791	3860	3834	3824
	a″	3868	3868	3938	3908	3882
	a′	3868	3868	3939	3909	3883
C_1 DI_1WI_3 (ω)	a	3585	3569	3685	3616	3634
	a	3638	3628	3736	3674	3686
	a	3641	3631	3738	3676	3688
	a	3710	3704	3798	3754	3754
	a	3713	3708	3802	3757	3757
	a	3730	3728	3819	3774	3774
	a	3736	3750	3837	3779	3785
	a	3840	3830	3896	3875	3858
S_4 DI_4 (ω)	e	3728	3769	3847	3789	3796
	e	3728	3770	3849	3790	3797
	b	3729	3770	3849	3790	3797
	a	3732	3772	3853	3793	3800
	a	3851	3829	3898	3877	3859
	e	3851	3832	3904	3881	3863
	e	3851	3832	3904	3881	3863
	b	3853	3836	3909	3885	3867
C_1 DI_2W_2 (ω)	a	3437	3422	3506	3491	3533
	a	3629	3620	3716	3660	3676
	a	3692	3692	3753	3738	3752
	a	3702	3719	3757	3752	3759
	a	3736	3746	3784	3773	3780
	a	3773	3748	3813	3804	3798
	a	3809	3797	3837	3845	3833
	a	3865	3865	3927	3902	3877

2.4.7 Performance of B3LYP, B3LYP–D3BJ, M06–2X, and MP2

The average absolute deviations (AvgAD) and max absolute deviations (MaxAD) of the relative and dissociation energies (in kcal mol^{-1}), as well as the harmonic vibrational frequencies of the OH stretching modes (in cm^{-1}) computed with B3LYP, B3LYP–D3BJ, M06–2X, and MP2 from CCSD(T) for n=1, 2 and 2b:Mb for n=3, 4 are given in Table 2.6. The column N denotes the number of values used for determining the AvgAD and MaxAD. For the relative energies, N is the number of structures identified excluding the reference structure. As for the dissociation energies, N is the number of minimum energy structures. And for the harmonic vibrational frequencies of the OH stretching modes, N is the number of OH stretching modes associated with all of the minimum energy structures.

When comparing the performance of the DFT methods and MP2, there is one clear top performer for dissociation energies. B3LYP–D3BJ consistently gives the smallest AvgAD and MaxAD values for $n > 1$, even outperforming MP2. B3LYP performed the worst and always gives the largest AvgAD and MaxAD results of all the methods, with the latter ranging from 1.40 kcal mol^{-1} for n=1 to 6.30 kcal mol^{-1} for n=4. Those trends do not, however, extend to the relative energies where MP2 clearly has the advantage and M06–2X tends to yield the smallest AvgADs for the DFT methods but not necessarily the smallest MaxADs. Similarly, the three DFT methods did not perform as well as MP2 when characterizing the harmonic vibrational frequencies of the OH stretching modes. On average, all of the DFT methods predict larger shifts by about 40 cm^{-1}. Although the MaxADs for B3LYP and B3LYP–D3BJ grew with the size of the cluster (up to 96 and 111 cm^{-1}, respectively), the MaxAD for M06–2X remained remarkably consistent from n=1 to n=4.

An additional dihydrate structure (C_s DI_1W_1; whose Cartesian coordinates are the Supporting Information) was only located at the B3LYP/haTZ level of theory. This structure is characterized by a single water molecule only interacting with the other water molecule and does not form any hydrogen bonds with the ion. All other levels of theory optimized to the C_s DI_1WI_1 structure. Additionally, for the trihydrate structures, only the B3LYP

and M06–2X methods located the C_1 DI_2W_1 structure (whose Cartesian coordinates are in the Supporting Information). Similar to the C_s DI_1W_1 dihydrate structure, one of the water molecules is only interacting with the other water molecule and no hydrogen bonds are formed with the ion. The B3LYP–D3BJ and MP2 methods did not locate the C_1 DI_2W_1 structure and instead converged to the C_s DI_2W_1 structure.

Table 2.6: Average absolute deviations (AvgAD) and max absolute deviations (MaxAD) of the relative energies (in kcal mol^{-1}), dissociation energies (in kcal mol^{-1}), and the harmonic OH stretching frequencies (in cm^{-1}) computed with DFT and MP2 from CCSD(T) for n=1, 2 and 2b:Mb for n=3, 4. The column N denotes the number of values used for determing the AvgAD and MaxAD.

	Relative Energies			Dissociation Energies			OH Stretching Frequencies		
	N	AvgAD	MaxAD	N	AvgAD	MaxAD	N	AvgAD	MaxAD
$n = 1$									
B3LYP	1	-	0.12	1	-	1.40	2	33	38
B3LYP–D3BJ	1	-	0.01	1	-	0.19	2	36	42
M06–2X	1	-	0.09	1	-	0.67	2	42	47
MP2	1	-	0.04	1	-	0.25	2	6	10
$n = 2$									
B3LYP	3	0.12	0.27	3	2.93	3.12	12	34	43
B3LYP–D3BJ	3	0.13	0.33	3	0.32	0.44	12	36	49
M06–2X	3	0.06	0.08	3	1.21	1.26	12	43	51
MP2	3	0.02	0.03	3	0.51	0.52	12	7	14
$n = 3$									
B3LYP	3	0.22	0.39	4	4.48	4.71	24	40	93
B3LYP–D3BJ	3	0.65	1.04	4	0.36	0.64	24	41	62
M06–2X	3	0.21	0.30	4	1.62	1.76	24	45	56
MP2	3	0.03	0.07	4	0.75	0.78	24	8	17
$n = 4$									
B3LYP	7	0.63	1.92	6	5.41	6.30	48	40	96
B3LYP–D3BJ	7	0.63	1.34	7	0.53	0.85	56	39	111
M06–2X	7	0.40	1.57	5	2.12	3.24	40	39	56
MP2	7	0.15	0.57	6	0.86	1.05	48	12	42

2.5 Conclusions

Low energy configurations of the BF_4^- $(H_2O)_{n=1,2,3,4}$ systems have been identified with the MP2, canonical CCSD(T) and 2b:Mb *ab initio* WFT methods in conjunction with the haTZ basis set. Two low-lying stationary points have been found for the $BF_4^-(H_2O)_1$ system, which include the C_{2v} DI_1 minimum and the C_s BI_1 transition state. For the $BF_4^-(H_2O)_2$ system, three minima and one transition state have been identified, with the lowest energy minimum being 1.30 kcal mol^{-1} lower than the D_{2d} DI_2 structure at the CCSD(T)/haTZ level of theory. Four new minima have been identifed for the $BF_4^-(H_2O)_3$ system, with the lowest energy minimum being 6.31 kcal mol^{-1} lower than the C_{3v} DI_3 structure at the 2b:Mb/haTZ level of theory. For the $BF_4^-(H_2O)_4$ system, six new minima and two new transition states have been identified, with the lowest energy minimum being 7.18 kcal mol^{-1} lower than the S_4 DI_4 structure at the 2b:Mb/haTZ level of theory.

The CCSD(T)/haTZ electronic dissociation energy is larger than 13 kcal mol^{-1} for the C_{2v} DI_1 monohydrate minimum. When increasing the number of water molecules to form the dihydrate structures, this interaction is almost perfectly additive in the D_{2d} DI_2 and C_s DI_2 minima. For the trihydrate C_{3v} DI_3 minimum and the tetrahydrate S_4 DI_4 mimimum, the D_e increases by a factor of $\approx$2.7 and $\approx$3.3 relative to the monohydrate, respectively. However, when the water molecules interact with one another and form hydrogen bonds, cooperative effects manifest and are observed and the D_e increases to larger than 26, 41, and 51 kcal mol^{-1} in the di-, tri-, and tetrahydrate structures, respectively. For comparison, the D_e is about 5 kcal mol^{-1} for the water dimer,[126,152] and approaches 16 kcal mol^{-1} for the water trimer.[127]

Relative to the a_1 and b_2 modes for an isolated H_2O molecule, the solvent$\cdots$solute interactions induce significant shifts in the harmonic OH stretching frequencies of the hydrating water molecule(s). In the monohydrate minimum (C_{2v} DI_1), the CCSD(T)/haTZ symmetric and antisymmetric OH stretching frequency shifts by -41 and -110 cm^{-1}, respectively.

Similar modest $\Delta\omega$ values are also observed in the D_{2d} DI_2, C_{3v} DI_3, and S_4 DI_4 minima of $BF_4^-(H_2O)_{n=2,3,4}$. The most significant vibrational shifts are seen when the solvent molecules interact with one another and the ion. In the C_s DI_1WI_1 structure, the CCSD(T)/haTZ synchronous and asynchronous OH stretching modes shift by as much as -98 and -134 cm^{-1}, respectively. Even larger shifts are seen in the trihydrate and tetrahydrate systems. In the C_3 WI_3 structure, the CCSD(T)/haTZ synchronous and asynchronous OH stretching modes shift by as much as -179 and -186 cm^{-1}, respectively.

The lowest-energy harmonic OH stretching frequency for the C_3 WI_3 minimum of $BF_4^-(H_2O)_3$ is computed to be 3635 and 3589 cm^{-1} at the 2b:Mb/haTZ and B3LYP/haTZ levels of theory, respectively. The B3LYP/haTZ harmonic value is only 5 cm^{-1} larger than the results from DFT AIMD simulations that predicted a shift of $+264$ cm^{-1} relative to bulk water.[41] The C_1 DI_1WI_3 tetrahydrate structure also has frequencies that approach the DFT AIMD result with the lowest-energy harmonic OH stretching frequency computed as 3634 and 3638 cm^{-1} at the 2b:Mb/haTZ and B3LYP/haTZ levels of theory. This work indicates the importance of solvent$\cdots$solvent interactions when describing the hydration of BF_4^- and demonstrates that solvent$\cdots$solute interactions alone do not encapsulate the total hydration of BF_4^-. In order to identify the lowest-energy structures and to completely capture the observed spectroscopic shifts, these solvent$\cdots$solvent interactions must be considered, as reported here.

Chapter 3

Ethynyl Radical Hydrogen Abstraction Energetics and Kinetics Utilizing High-Level Theory[2]

[2]Olive, L.N., Heide, A. D., Turney, J. M., and Schaefer III, H.F. 2024. *ACS Earth and Space Chemistry.* 8:1349–1358. Reprinted here with permission of the American Chemical Society. Copyright 2024, This publication is licensed under CC-BY 4.0. https://doi.org/10.1021/acsearthspacechem.4c00040.

3.1 Abstract

The ethynyl radical, C_2H, is found in a variety of different environments ranging from interstellar space and planetary atmospheres to playing an important role in the combustion of various alkynes under fuel-rich conditions. Hydrogen-atom abstraction reactions are common for the ethynyl radical in these contrasting environments. In this study, the C_2H + HX $\rightarrow$ C_2H_2 + X, HX = HNCO, *trans*-HONO, *cis*-HONO, C_2H_4, and CH_3OH, reactions have been investigated at rigorously high levels of theory including CCSD(T)-F12a/cc-pVTZ-F12. For the stationary points thus located, much higher levels of theory have been used with basis sets as large as aug-cc-pV5Z and methods up to CCSDT(Q), core correlation was also included. These molecules were chosen because they can be found in either interstellar or combustion environments. Various additive energy corrections have been included to converge the relative enthalpies of the stationary points to subchemical accuracy ($\leq$0.5 kcal mol^{-1}). Barriers predicted here (2.19 kcal mol^{-1} for the HCNO reaction and 0.47 kcal mol^{-1} for C_2H_4) are significantly lower than previous predictions. Reliable kinetics were acquired over a wide range of temperatures (50 - 5000K), which may be useful for future experimental studies of these reactions.

3.2 Introduction

The ethynyl radical, C_2H ($^2\Sigma^+$), is known to be a key intermediate in a number of diverse environments. It has been observed in both combustion reactions[153,154] and planetary atmospheres.[155,156] Additionally, it is one of the most abundant polyatomic radicals in interstellar space.[157–160] In combustion environments, the ethynyl radical is a common intermediate in fuel-rich hydrocarbon combustion processes of various alkynes that can take place at temperatures in excess of 1800K.[161] Furthermore, it plays an important role as a key precursor in the synthesis of polyynes, polycyclic aromatic hydrocarbons (PAHs), and soot particles.[153,162–165] It is also a reactive species in Titan's atmosphere where the temperature

is altitude-dependent (70K at the tropopause and 94K at the surface). To better understand the importance of these reactions involving the ethynyl radical in these drastically different environments, there is a need to accurately model the reactions of C_2H with a variety of reactants over an extremely broad range of temperatures.

Hydrogen-atom abstraction is among the most prevalent reactions for the ethynyl radical and is commonly the main reaction pathway or a feasible alternative.[16,166,167] The sizeable dissociation energy of acetylene's *sp*-hybridised C-H bond thermodynamically drives these hydrogen abstraction reactions. Large rate constants have been calculated by kinetic studies for the reaction of C_2H with different saturated hydrocarbons over a broad range of temperatures, implying moderately low barriers for abstraction.[154,161,168–170] Theoretical results corroborate this claim with moderate to low reported barrier heights for several hydrogen atom donors[166,171]. At this time, most experimental and theoretical studies involving ethynyl radical hydrogen abstractions have focused on hydrocarbon hydrogen atom donors. Over the years, numerous studies have been done on these types of reactions with a wide variety of small molecules or radicals.[16,154,163,166,172–181] However, little work has been done on larger molecules.

Reactions involving nitrogen containing radicals and their kinetics in the gas phase are also of considerable interest due to the role these species play in the formation and removal of NO_x pollutants in combustion processes.[182] NCO plays a key intermediate in combustion, however, very little is known of the kinetics of the reactions of NCO with hydrocarbons.[170,183] No previous experimental studies on C_2H + HNCO have been reported, but a theoretical study in 2003 by Chen and Ho[182] addressed the reaction mechanisms for NCO and C_2H_2 at the CCSD(T)/6-31++G**//B3LYP/6-31++G** level of theory and they were able to find a direct pathway for the NCO + C_2H_2 → C_2H + HNCO reaction.

Additionally, nitrous acid, HONO, has been detected in the interstellar medium,[184] and the reaction involving CN has been explored theoretically[185] with MP2 and CCSD(T); however, no study has been reported involving C_2H. Furthermore, the kinetics of the pyrolysis

and oxidation of methanol, CH_3OH, which could be considered as an alternative, more environmentally friendly fuel or fuel additive to gasoline, have been of great interest in the last several years.[186] Hydrogen abstraction reactions could happen at two different sites for CH_3OH. The hydrogen could be abstracted off the hydroxyl, -OH, group (R1), or the methyl, -CH_3, group (R2).

$$C_2H + CH_3OH \rightarrow C_2H_2 + CH_3O \quad \text{(R1)}$$

$$C_2H + CH_3OH \rightarrow C_2H_2 + CH_2OH \quad \text{(R2)}$$

In 2011, a theoretical paper by Tri and Huê studied the C_2H + CH_3OH reaction mechanism with B3LYP and the 6-311++G(*d*,*p*) and 6-311++G(3*df*,2*p*) basis sets.[187] They investigated twelve different reaction pathways and found that the formations of C_2H_2 + CH_3O and C_2H_2 + CH_2OH were the most favorable.

A recent study by Bowman et al. investigated numerous C_2H hydrogen abstraction reactions with highly accurate *ab initio* methods.[16] In the present study, a similar computational approach will be utilized to investigate the C_2H + HX $\rightarrow$ C_2H_2 + X reactions, where HX = HNCO, *trans*-HONO, *cis*-HONO, C_2H_4, and CH_3OH. Our study will provide high-level *ab initio* characterization of hydrogen abstraction reactions of the ethynyl radical with various medium sized molecules including HNCO, *trans*-HONO, *cis*-HONO, C_2H_4, and CH_3OH. A composite approach will be implemented to converge the energies within subchemical accuracy ($\leq$0.5 kcal mol^{-1}). These highly accurate energetics will be used to compute reliable rate constants with canonical transition state theory that can be used in future kinetic studies.

3.3 Theoretical Methods

Full geometry optimizations and corresponding harmonic vibrational frequency computations were performed on each of the stationary points for the C_2H + HX, HX = HNCO, *trans*-HONO, C_2H_4, and CH_3OH (R1), reactive surfaces using the explicitly correlated CCSD(T)-F12a method[188] in conjuction with the cc-pVTZ-F12 basis set[189,190] as implemented in Molpro

2010.[191] A restricted open-shell Hartree–Fock (ROHF) reference was used for all open-shell computations to avoid issues with spin contamination that are sometimes prevalent with the ethynyl radical. For the C_2H + HX, HX = *cis*-HONO and CH_3OH (R2), reactive surfaces, full geometry optimizations and corresponding harmonic vibrational frequency computations were performed on each of the stationary points at the MP2[63]/aug-cc-pVTZ[6] level of theory as implemented in Psi4.[192] Single point energy computations were performed on the MP2/aug-cc-pVTZ geometries with CCSD(T)-F12a/cc-pVTZ-F12 in Molpro 2010.

The electronic energies of the CCSD(T)-F12a/cc-pVTZ-F12 stationary points were computed according to the focal point analysis (FPA) of Allen and coworkers.[7,8] For the present study, methods that describe electron correlation up to CCSDT(Q)[193] and basis sets as large as aug-cc-pV5Z[194] were used. Single point energy computations were performed on the CCSD(T)-F12a/cc-pVTZ-F12 optimized geometries with CCSD(T)[195,196]/aug-cc-pVXZ (where X = D, T, Q, 5)[6] in Molpro 2010, and CCSDT[197]/aug-cc-pVDZ and CCSDT(Q)/aug-cc-pVDZ as implemented in MRCC 2018.[198] As shown in Table 3.1, there is excellent convergence to the complete basis set (CBS) limit. The CCSD(T)/CBS energies were obtained through extrapolation of the Hartree–Fock (HF) and correlation energies. The three-parameter exponential function by Feller is used to extrapolate to the HF/CBS limit.[199]

$$E_{\mathrm{ref}}(X) = E_{\mathrm{HF}}^{\infty} + a\mathrm{e}^{-bX} \tag{1}$$

The two-parameter cubic function of Helgaker *et al.*[200] is used to extrapolate the correlation energies (E_{corr}) to the CBS limit.

$$E_{\mathrm{corr}}(X) = E_{\mathrm{corr}}^{\infty} + aX^{-3} \tag{2}$$

The focal point energies were obtained with the following formula:

$$\Delta E_{\mathrm{CCSDT(Q)/CBS}} = \Delta E_{\mathrm{CCSD(T)/CBS}} + \delta E_{\mathrm{T(Q)}} \tag{3}$$

Table 3.1: Representative incremental focal point table for the products of the C_2H + HNCO $\rightarrow$ C_2H_2 + NCO reaction relative to the reactants (in kcal mol^{-1}). Additional focal point tables can be found in the supplementary material.

Basis Set	HF	+δMP2	+δCCSD	+δ(T)	+δT	+δ(Q)	Net
aug-cc-pVDZ	−23.32	+4.64	−4.01	+0.30	−0.10	−0.05	[−22.54]
aug-cc-pVTZ	−23.54	+4.52	−4.20	+0.27	[−0.10]	[−0.05]	[−23.09]
aug-cc-pVQZ	−23.34	+4.76	−4.11	+0.26	[−0.10]	[−0.05]	[−22.58]
aug-cc-pV5Z	−23.33	+4.80	−4.08	+0.25	[−0.10]	[−0.05]	[−22.51]
CBS Limit	[−23.34]	[+4.83]	[−4.05]	[+0.25]	[−0.10]	[−0.05]	[−22.46]

Note: δ denotes the change in the relative energy with respect to the previous level of theory. The numbers in [ ] are obtained by the extrapolation schemes found in the Methods section.

Additional corrections were made to account for approximations made during the focal point computations. To account for the core-correlation neglected under the frozen-core approximation, the CCSD(T)/aug-cc-pCVQZ energy with all electrons correlated was computed and the difference between the energies with and without the core-electrons was determined (δ_{CORE}). A scalar relativistic correction (δ_{REL}) was obtained at the X2C-CCSD(T)/aug-cc-pCVTZ-X2C level of theory.[201] The clamped-nuclei approximation was treated with the diagonal Born–Oppenheimer correction (δ_{DBOC})[202,203] performed at the ROHF/aug-cc-pVTZ level of theory. Spin-orbit coupling constants (δ_{SO}) were included for the NCO and CH_3O products in order to account for the splitting of the electronic ground state.[204,205] Lastly, zero-point vibrational energies (δ_{ZPVE}) were obtained from the CCSD(T)-F12a/cc-pVTZ-F12 harmonic vibrational frequencies. All of these corrections were added together to obtain the relative enthalpies at 0K using the following equation:

$$\Delta H_{0\mathrm{K}} = \Delta E_{\mathrm{CCSDT(Q)/CBS}} + \delta_{\mathrm{CORE}} + \delta_{\mathrm{REL}} + \delta_{\mathrm{DBOC}} + \delta_{\mathrm{ZPVE}}(+\delta_{\mathrm{SO}}) \tag{4}$$

Using canonical transition state theory,[206,207] the rate constants were computed over a wide range of temperatures:

$$k^{\mathrm{TST}}(T) = \kappa(T)\frac{k_{\mathrm{B}}T}{h}\frac{Q^{\mathrm{TS}}(T)}{Q^{\mathrm{R}}(T)}exp\left(\frac{-\Delta H^{\ddagger}}{k_{\mathrm{B}}T}\right) \quad (5)$$

where $\mathrm{Q}^{\mathrm{TS}}(T)$ and $\mathrm{Q}^{\mathrm{R}}(T)$ are the partition functions of the transition state and reactants, respectively, and $\Delta H^{\ddagger}$ is the reaction barrier height from Equation 4. The transmission coefficient, $\kappa(T)$, was determined with an asymmetric Eckart potential barrier using the relative enthalpies of the pre-reactive complex, transition state, and products for each reaction, and the imaginary harmonic vibrational frequency corresponding to the reaction mode of the transition state.[208]

Bowman and coworkers demonstrated that an Eckart tunneling model provides accurate kinetics in agreement with experimental results for hydrogen abstraction reactions involving the ethynyl radical;[16] therefore, Eckart tunneling was used here. Additionally, other studies have achieved past success in accurately describing the tunneling of hydrogen transfer reactions at moderate to high temperatures using Eckart tunneling.[209–211] In this work, pressure dependence will not be taken into account.

3.4 Results and Discussion

3.4.1 Energies and Geometries

Table 3.2 shows the reaction enthalpies at 0K for the C_2H hydrogen-abstractions involving HNCO, *trans*-HONO, C_2H_4, and CH_3OH (R1). The last column of Table 3.2 demonstrates excellent agreement between our computed reaction enthalpies and the reaction enthalpies reported in the Active Thermochemical Tables (ATcT) (Version 1.122r) of Ruscic and coworkers.[212,213] The mean absolute error (MAE) between the two is 0.19 kcal mol^{-1}. The root mean square error (RMSE) is 0.25 kcal mol^{-1}. The largest deviation is found for the $CH_3OH + C_2H \rightarrow CH_3O + C_2H_2$ reaction with a difference of 0.48 kcal mol^{-1}.

Figure 3.1 depicts the geometries of the hydrogen abstraction transition states found for each reaction studied in this research. Table 3.3 shows the reaction enthalpies of the CCSD(T)-

Table 3.2: Enthalpies at 0K (ΔH_{0K} in kcal mol^{-1} for products relative to reactants (C_2H + HX $\rightarrow$ C_2H_2 + X)

Donor	CBS[a]	$\delta_{T(Q)}$	δ_{CORE}	δ_{REL}	δ_{DBOC}	δ_{ZPVE}	δ_{SO}	Total	ATcT[b]	$\Delta\|E\|$[c]
HNCO	−22.31	−0.15	0.08	−0.16	0.00	0.63	−0.14	−22.05	−22.02	0.03
trans-HONO	−53.93	0.15	−0.47	0.02	0.00	0.53	–	−53.69	−53.82	0.13
C_2H_4	−21.25	0.13	−0.17	−0.02	−0.04	−1.24	–	−22.58	−22.68	0.10
CH_3OH[d]	−26.22	0.21	−0.20	−0.14	0.47[e]	−1.49	−0.41	−28.25	−27.77	0.48

Note: δ denotes various corrections. See Theoretical Methods section for details
[a]CBS denotes the CCSD(T)/CBS relative energy
[b]Enthalpies obtained from the ATcT[212,213]
[c]Absolute value of the difference between Total and ATcT
[d]$CH_3OH + C_2H \rightarrow CH_3O + C_2H_2$
[e]DBOC correction not included in final Total

F12a/cc-pVTZ-F12 transition states relative to their respective reactants. According to the results in Table 3.2, the energetics of the products are expected to be accurate within 0.48 kcal mol^{-1}; however, the relative energetics of the transition states are highly dependent on the employed level of theory. Because of this, we expect the barrier heights to be reliable well within chemical accuracy (1 kcal mol^{-1}). Of the corrections listed in Table 3.3, δ_{ZPVE} is the largest suggesting that obtaining accurate barrier heights not only requires accurate electronic energies, but also reliable vibrational frequencies. Additionally, δ_{REL} is small, but not negligible for these reactions which involve 1st and 2nd row atoms. The diagonal Born–Oppenheimer corrections for the reaction enthalpies and transition state barriers were consistently small ($\leq$0.2 kcal mol^{-1}) for almost all of the reactions. However, for the CH_3OH + $C_2H \rightarrow CH_3O + C_2H_2$ reaction where δ_{DBOC} is computed as 0.47 kcal mol^{-1}. Bartlett and coworkers proposed that δ_{DBOC} can be utilized as a diagnostic for the presence of a nearby conical intersection.[214] Typically for most well-behaved systems without a nearby conical intersection, the δ_{DBOC} is small, but this is not true in the proximity of a conical intersection. The E_{DBOC} becomes non-integrable over domains that include a conical intersection because the second-derivative of the $\hat{T}_n$ operator blows up, as shown by Meek and Levine.[215] It is recommended that DBOC not be included when employing mixed quantum-classical methods and approximate quantum dynamical methods. Therefore, the δ_{DBOC} was not included in

determining the final reaction enthalpy and transition state barrier of the $CH_3OH + C_2H \rightarrow CH_3O + C_2H_2$ reaction.

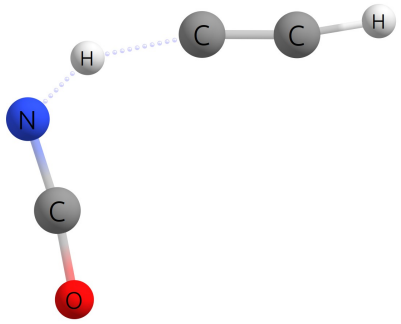

(a) HNCO (C_s)

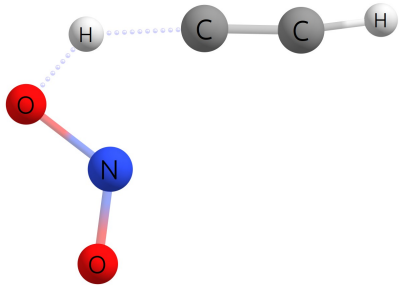

(b) *trans*-HONO (C_s)

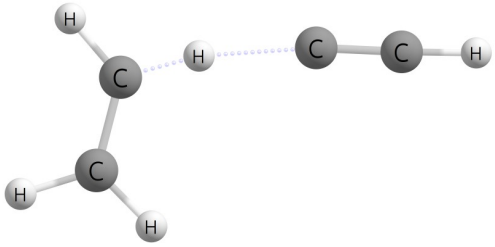

(c) C_2H_4 (C_s)

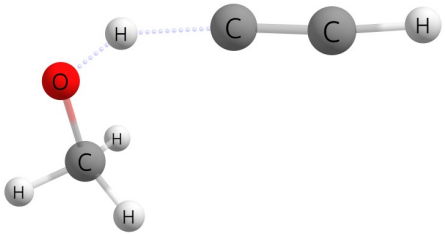

(d) CH_3OH O-abstraction (C_1)

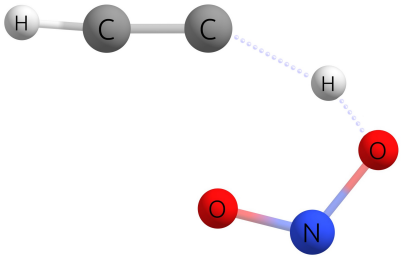

(e) *cis*-HONO (C_1)

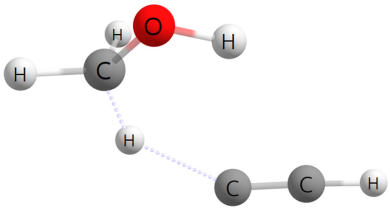

(f) CH_3OH C-abstraction (C_1)

Figure 3.1: Qualitative geometries of C_2H + HX transition states.

As shown in Table 3.3, the $C_2H + CH_3OH$ reaction has a very slightly submerged transition state barrier of -0.27 kcal mol^{-1}, suggesting that this reaction will be rapid even at low temperatures. The C_2H + HNCO and C_2H + *trans*-HONO reactions have low barriers less

Table 3.3: Enthalpies at 0K (ΔH_{0K} in kcal mol^{-1} for transition states relative to reactants ($C_2H + HX \rightarrow C_2H_2 + X$)

Donor	CBS[a]	$\delta_{T(Q)}$	δ_{CORE}	δ_{REL}	δ_{DBOC}	δ_{ZPVE}	Total
HNCO	4.06	−0.19	0.14	−0.14	0.23	−1.90	2.19
trans-HONO	6.38	−0.96	0.03	0.23	−0.01	−0.76	4.91
C_2H_4	1.74	−0.11	−0.01	−0.01	0.02	−1.17	0.47
CH_3OH[b]	1.49	−0.28	0.01	−0.21	0.11[c]	−1.28	−0.27

Note: δ denotes various corrections. See Theoretical Methods section for details
[a]CBS denotes the CCSD(T)/CBS relative energy
[b]$CH_3OH + C_2H \rightarrow CH_3O + C_2H_2$
[c]DBOC correction not included in final Total

than 5 kcal mol^{-1}, meaning these reactions will likely proceed more slowly than the barrierless reaction.

Table 3.4 compares the reaction enthalpies ($\Delta_r H$), the barrier heights ($\Delta H^{\ddagger}$), important transition state features (shown in Figure 3.2), and the imaginary mode frequency ($\omega^{\ddagger}$) of the transition state of the C_2H + HX, HX = HNCO, *trans*-HONO, C_2H_4, and CH_3OH (R1) reactions. To better determine if these hydrogen abstraction reactions follow the Evans−Polanyi principle, the reactions have been listed in order of decreasing exothermicity ($\Delta_r H$). The Evans-Polanyi principle observes that the activation energy between two similar reactions is inversely proportional to the reaction exothermicity.[216,217] The reactions studied here, in general, appear to follow the Evans-Polanyi principle; however, the C_2H + *trans*-HONO reaction seems to be an exception. One might expect the abstraction of the hydrogen from *trans*-HONO to have a submerged barrier of around −2 kcal mol^{-1}. Instead, the barrier height for *trans*-HONO is 4.91 kcal mol^{-1}. The interaction between the nitrogen of *trans*-HONO and the terminal carbon of C_2H could potentially be causing the unexpected $\Delta H^{\ddagger}$ increase.

To better understand the relationship between the reaction rates and how closely the transition states match the isolated reactants, Hammond's postulate is assessed. The Hammond idea states that the geometry of the transition state resembles either the reactants or products depending on the exothermicity of the reaction, and this was also taken into

Table 3.4: Reaction enthalpies ($\Delta_r H$), reaction barrier heights ($\Delta H^{\ddagger}$), and transition state imaginary frequencies ($\omega^{\ddagger}$) for C_2H + HX hydrogen abstractions at the CCSDT(Q)/CBS//CCSD(T)-F12a/cc-pVTZ-F12 level of theory.

Donor	$\Delta_r H$	$\Delta H^{\ddagger}$	R_{CH}	ΔR^a_{XH}	θ_1	θ_2	$\omega^{\ddagger}$
trans-HONO	−53.7	4.9	1.480	17.7%	176.2	133.2	1703i
CH_3OH^b	−27.8	−0.3	1.540	6.8%	174.4	134.4	794i
C_2H_4	−22.6	0.5	1.653	4.7%	173.4	168.7	267i
HNCO	−22.1	2.2	1.500	9.1%	168.2	145.9	947i

[a] ΔR_{XH} = ($R_{XH,TS}$ − $R_{XH,eq}$) / $R_{XH,eq}$
[b] $CH_3OH + C_2H \rightarrow CH_3O + C_2H_2$

consideration in this study. In order to determine how closely the transition state resembles the isolated reactants, the distance between the terminal carbon of the ethynyl radical and the hydrogen that is being abstracted in the transition state (R_{CH}), was considered. The percent change between the XH bond length in the donor bond and the transition state (ΔR_{XH}) was also taken into account. The transition state will more closely resemble the reactants than the products if the ΔR_{XH} value is less than 50%. The reactions in this study *do* follow Hammond's postulate. For example, the ΔR_{XH} value of the C_2H + HNCO reaction is 9.1%, and the energy difference of the reactants and transition state is 2.2 kcal mol^{-1} while the energy difference of the transition state and products is 24.3 kcal mol^{-1}. Energetically, the transition state lies closer to the reactants than the products, which corresponds to the calculated ΔR_{XH} value that is less than 50%.

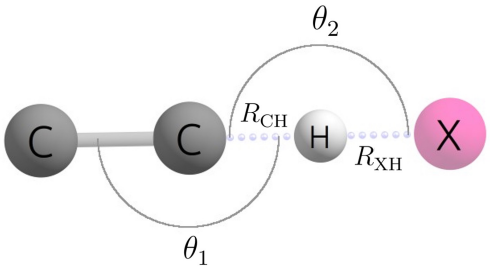

Figure 3.2: General representation of the transition state geometrical features.

C_2H + HNCO

A previous study by Chen and Ho investigated the C_2H + HNCO → C_2H_2 + NCO reaction at the CCSD(T)/6-311++G**//B3LYP/6-311++G** level of theory.[182] They found that the reaction proceeded through a transition state barrier of 6.23 kcal mol^{-1} and ended with the products at −21.79 kcal mol^{-1} relative to the reactants.

As seen in Figure 3.3, the reaction pathway found in this study is qualitatively similar to that of Chen and Ho. As laid out in Table 3.5, our transition state barrier of 2.19 kcal mol^{-1} is 4.04 kcal mol^{-1} lower than that of Chen and Ho. However, the ending products of −22.05 kcal mol^{-1} relative to reactants show less than a 0.3 kcal mol^{-1} difference. The bond lengths of the transition state geometry are also similar to that of Chen and Ho with the largest difference being 0.14 Å for the H-C bond between HNCO and C_2H. However, there is an 11.5° difference for the CNH angle in HNCO. Chen and Ho did not report rate constants for this reaction.

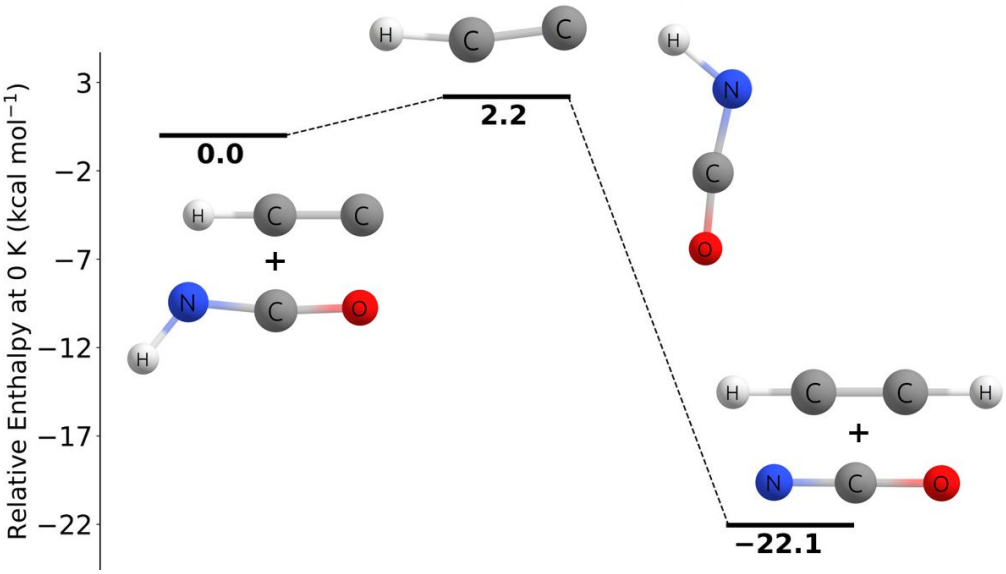

Figure 3.3: Potential energy surface of the C_2H + HNCO → C_2H_2 + NCO reaction at 0K at the CCSDT(Q)/CBS//CCSD(T)-F12a/cc-pVTZ-F12 level of theory.

Table 3.5: Comparison of the C_2H + HNCO → C_2H_2 + NCO abstraction at different levels of theory. Enthalpies are given in kcal mol^{-1}, bond distances in Å and angles in degrees.

	$\Delta H^{\ddagger}$	ΔH_r	R_{CH}	R_{NH}	θ_{CHN}
Chen and Ho[a]	6.23	−21.79	1.644	1.071	129.29
This work[b]	2.19	−22.05	1.500	1.096	117.77

[a]CCSD(T)/6-31++G**//B3LYP/6-31++G**
[b]CCSDT(Q)/CBS//CCSD(T)-F12a/cc-pVTZ-F12

C_2H + HONO

Both the *trans* and *cis* isomers of HONO were considered for this study; however, only the reaction pathway involving the *trans* isomer was characterized at the highest level of theory implemented in this study. The study that investigated the CN + HONO reaction found that the *trans* isomer is 0.45 kcal mol^{-1} lower in energy than the *cis* isomer with an isomerization barrier of 9.46 kcal mol^{-1} at the CCSD(T)/aug-cc-pVTZ//UMP2/6-311++G(d,p) level of theory.[185]

There have been no previously reported theoretical studies or experimental measurements involving the C_2H + HONO → C_2H_2 + NO_2 reaction. As shown in Figure 3.4, the reaction pathway involving the *trans* isomer found in this work at the CCSDT(Q)/CBS//CCSD(T)-F12a/cc-pVTZ-F12 level of theory proceeds through a transition state barrier of 4.91 kcal mol^{-1}. Due to the stabilities of the ethylene and nitrogen dioxide, the energy of the products is −53.69 kcal mol^{-1} relative to the reactants. In Figure 3.5, the reaction pathway involving the *cis* isomer found in this work at the CCSD(T)-F12a/cc-pVTZ-F12//MP2/aug-cc-pVTZ level of theory proceeds through a pre-reactive complex at −0.91 kcal mol^{-1} followed by a submerged transition state barrier of −3.62 kcal mol^{-1} and ends with the products at −56.17 kcal mol^{-1} relative to the reactants.

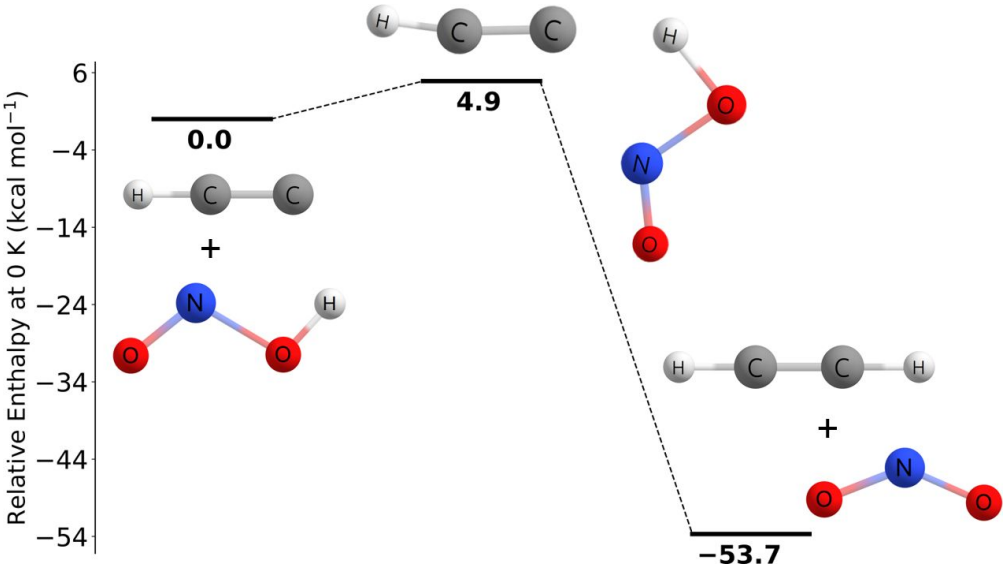

Figure 3.4: Potential energy surface of the C_2H + *trans*-HONO → C_2H_2 + NO_2 reaction at 0K at the CCSDT(Q)/CBS//CCSD(T)-F12a/cc-pVTZ-F12 level of theory.

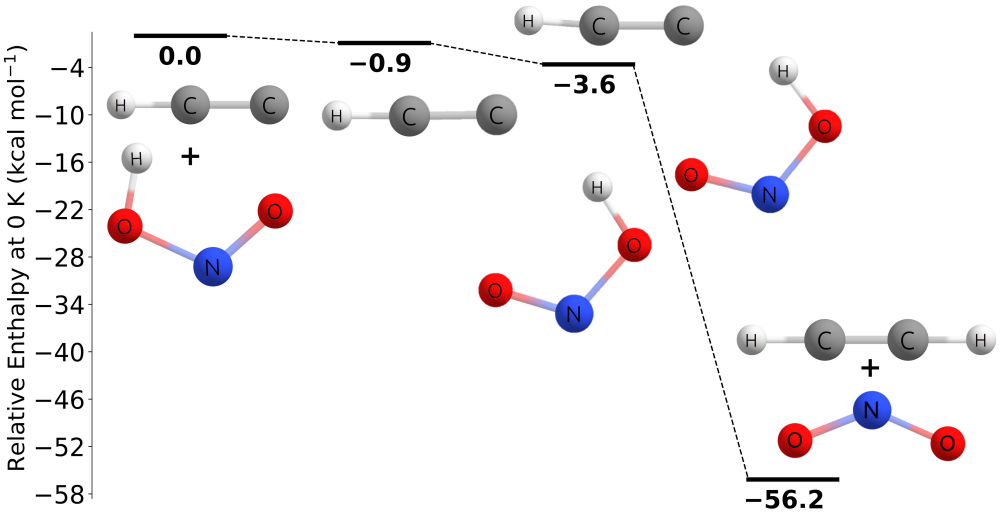

Figure 3.5: Potential energy surface of the C_2H + *cis*-HONO → C_2H_2 + NO_2 reaction at 0K at the CCSD(T)-F12a/cc-pVTZ-F12//MP2/aug-cc-pVTZ level of theory.

C_2H + CH_3OH

There have been no previously reported experimental measurements involving the C_2H + CH_3OH → C_2H_2 + CH_3O/CH_2OH reactions. One previous study by Tri and Huê investigated the C_2H + CH_3OH reaction mechanism theoretically and determined the potential energy surfaces of twelve different reaction pathways.[187] They determined that the pathways that

formed C_2H_2 + CH_3O and C_2H_2 + CH_2OH were the most favorable with submerged barrier heights of -4.01 and -0.14 kcal mol^{-1}, and ended with the products at -32.32 and -38.45 kcal mol^{-1}, respectively, at the B3LYP/6-311++G(3*df*,2*p*)//B3LYP/6-311++G(*d*,*p*) level of theory. For the C_2H + $CH_3OH \rightarrow C_2H_2$ + CH_3O reaction, they were able to locate a pre-reactive complex at -4.06 kcal mol^{-1}, but they did not report a pre-reactive complex for the C_2H + $CH_3OH \rightarrow C_2H_2$ + CH_2OH reaction.

As shown in Figure 3.6, the C_2H + $CH_3OH \rightarrow C_2H_2$ + CH_3O reaction proceeds through a pre-reactive complex at -6.45 kcal mol^{-1} and then through a very slightly submerged transition barrier of -0.27 kcal mol^{-1}, and ends in the products at -28.25 kcal mol^{-1} relative to the reactants, which is qualitatively in agreement to that of Tri and Huê. The pre-reactive complex energy was determined at the CCSD(T)-F12a/cc-pVTZ-F12 level of theory with no additional corrections.

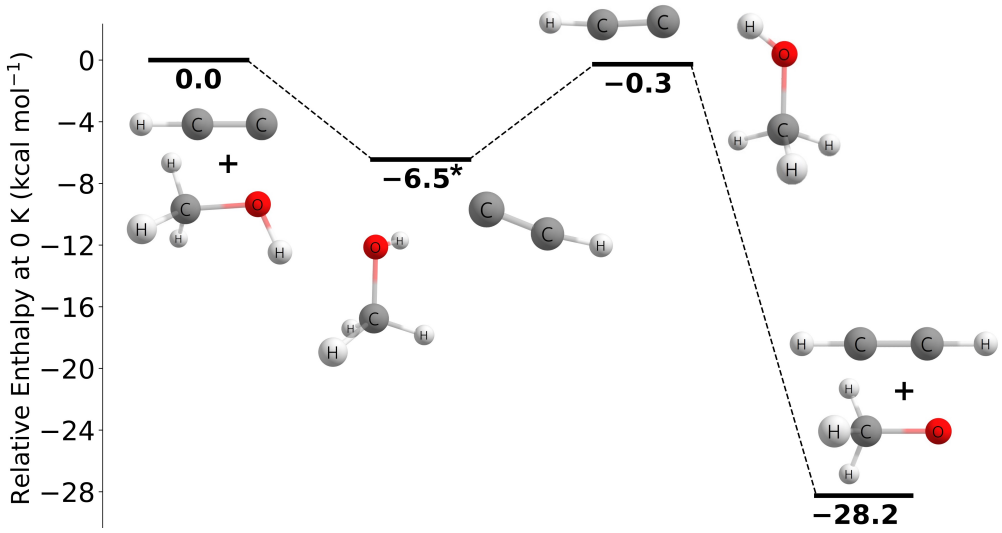

Figure 3.6: Potential energy surface of the C_2H + $CH_3OH \rightarrow C_2H_2$ + CH_3O reaction at 0K at the CCSDT(Q)/CBS//CCSD(T)-F12a/cc-pVTZ-F12 level of theory. The asterisk (*) denotes the energy is at the CCSD(T)-F12a/cc-pVTZ-F12 level of theory with no additional corrections.

Additionally, the C_2H + CH_3OH → C_2H_2 + CH_2OH reaction was also investigated for this study; however, no direct transition state was found for CH_2OH production at our highest-level of theory. The reported transition state geometry of Tri and Huê appears to be in C_s symmetry (Figure 3.7a) with a H_a-O-C-H_b dihedral angle of 180.0°. Calculations at the MP2/aug-cc-pVTZ level of theory determined a transition state with a H_a-O-C-H_b dihedral angle of 45.9° (Figure 3.7b). This floppy dihedral angle made this transition state difficult to optimize and locate.

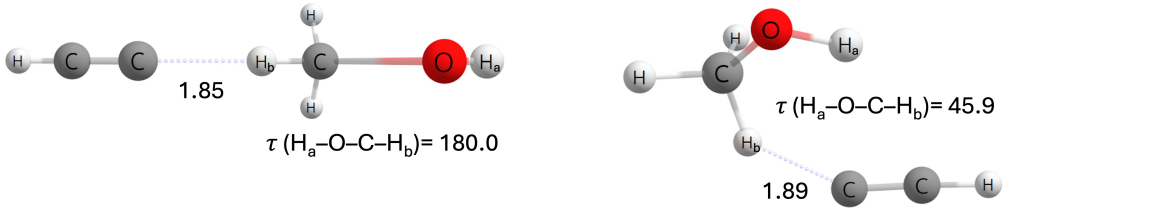

(a) B3LYP/6-311++G(d,p) CH_3OH (C_s) (b) MP2/aug-cc-pVTZ CH_3OH (C_1)

Figure 3.7: Qualitative geometries of C_2H + CH_3OH methyl abstraction transition state. Bond distances are given in Å and angles in degrees.

As shown in Figure 3.8, the C_2H + CH_3OH → C_2H_2 + CH_2OH reaction pathway characterized at the CCSD(T)-F12a/cc-pVTZ-F12//MP2/aug-cc-pVTZ level of theory proceeds through a pre-reactive complex at -1.64 kcal mol^{-1} followed by a submerged transition state barrier of -2.58 kcal mol^{-1} and ends with the products at -37.63 kcal mol^{-1} relative to the reactants. MP2/aug-cc-pVTZ gives an imaginary mode of $32i$ for the pre-reactive complex, but we believe this mode is an artefact of the level of theory and will likely disappear at a more rigorous level of theory. In terms of chemical reactivity, it appears this reaction pathway where the hydrogen is abstracted from the methyl group will likely prevail because it has a lower barrier height compared to the hydrogen being abstracted from the hydroxyl group. However, Tri and Huê report that the reaction pathway where the hydrogen is abstracted from the hydroxyl group has a lower transition state barrier; therefore, it would be beneficial to further study this reaction pathway in a future study.

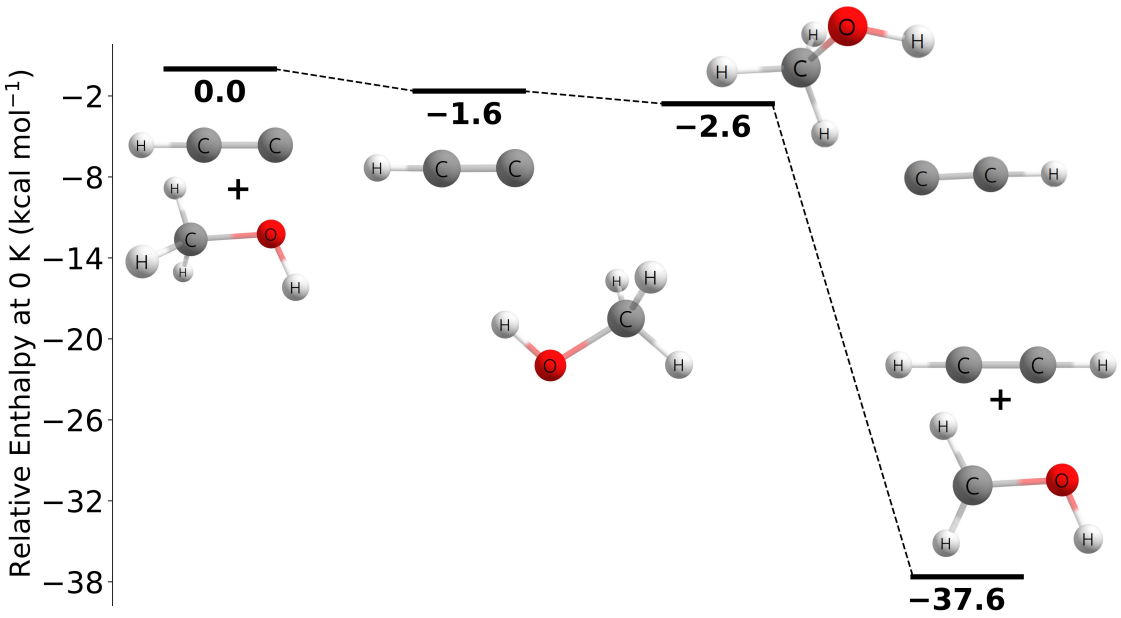

Figure 3.8: Potential energy surface of the C_2H + CH_3OH → C_2H_2 + CH_2OH reaction at 0K at the CCSD(T)-F12a/cc-pVTZ-F12//MP2/aug-cc-pVTZ level of theory.

C_2H + C_2H_4

A previous study by Temelso and coworkers studied the C_2H + C_2H_4 → C_2H_2 + C_2H_3 reaction with the B3LYP, BHLYP, MP2, and CCSD(T) methods in conjunction with the cc-pVXZ (where X = D, T, Q) basis sets.[218] However, CCSD(T)/cc-pVDZ was the highest level of theory reported for the barrier height. They found that the reaction proceeds through a transition barrier of 1.7 kcal mol^{-1}, and ends in the products at −19.5 kcal mol^{-1} at the CCSD(T)/cc-pVDZ level of theory using an ROHF reference. They also calculated the $\Delta H(0K)$ at the CCSD(T)/cc-pVTZ level of theory and determined it to be −22.6 kcal mol^{-1}, which is in excellent agreement with our results.

As shown in Figure 3.9, the reaction pathway characterized in this study is qualitatively similar to that of Temelso and coworkers. Our transition state barrier of 0.47 kcal mol^{-1} is 1.23 kcal mol^{-1} lower than that of Temelso and coworkers, but their ending product energy of −22.6 kcal mol^{-1} relative to reactants at the CCSD(T)/cc-pVTZ level of theory is in excellent agreement with our results. The transition state geometries are quite similar as

shown in Table 3.6, with the largest difference being the CHC angle. Temelso and coworkers report a linear angle while we predict a 168.7 degree angle. Rate constants were not reported for this reaction by Temelso and coworkers.

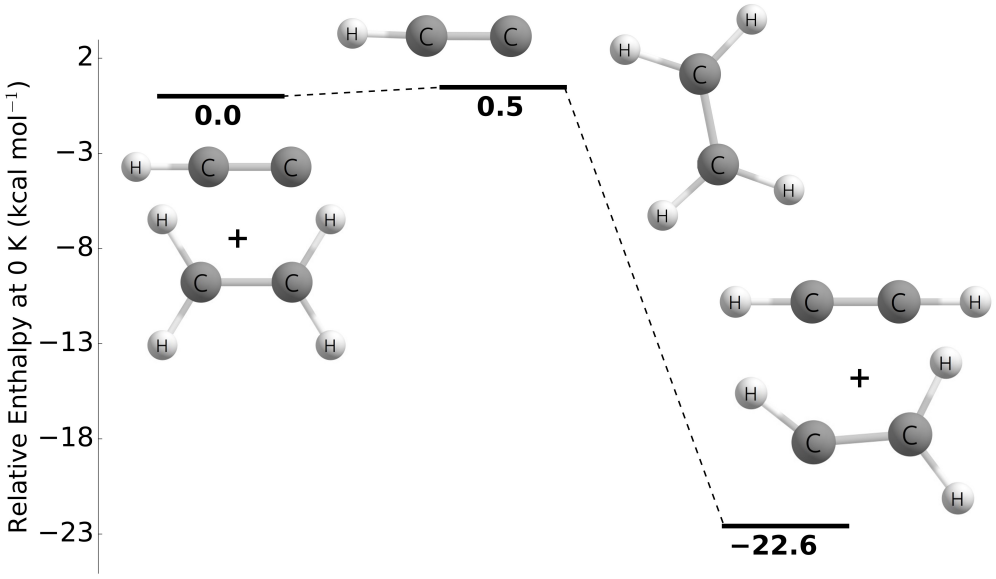

Figure 3.9: Potential energy surface of the $C_2H + C_2H_4 \rightarrow C_2H_2 + C_2H_3$ reaction at 0K at the CCSDT(Q)/CBS//CCSD(T)-F12a/cc-pVTZ-F12 level of theory.

Additionally, Dash and Rajakumar studied the $C_2H + C_2H_4 \rightarrow C_2H_2 + C_2H_3$ reaction and computed the CCSD(T)/cc-pVTZ and G3(MP2) electronic energies at each stationary point. However, they employed the M06−2X/6-31+G(d,p) level of theory to optimize the geometries and determine the harmonic vibrational frequencies.[171] The transition state barrier is quite different at each level of theory as seen in Table 3.6. The M06-2X/6-31+G(d,p) pathway is in good agreement with our results, but the CCSD(T)/cc-pVTZ//M06−2X/6-31+G(d,p) transition state barrier of 2.25 kcal mol^{-1} is 1.78 kcal mol^{-1} higher than our transition state barrier. The G3(MP2)//M06−2X/6-31+G(d,p) pathway predicts a submerged transition state barrier of −1.43 kcal mol^{-1}. The transition state geometries are quite similar and the largest difference is the CHC angle again. Rate constants were reported by Dash and Rajakumar and will be discussed in the Kinetics section.

Table 3.6: Comparison of the $C_2H + C_2H_4 \rightarrow C_2H_2 + C_2H_3$ abstraction at different levels of theory. Enthalpies are given in kcal mol^{-1}, bond distances in Å and angles in degrees. $R_{CH(2)}$ is the C–H bond distance to the H that is being abstracted from C_2H_4.

	$\Delta H^{\ddagger}$	ΔH_r	R_{CH}	$R_{CH(2)}$	θ_{CHC}
This work[a]	0.5	−22.6	1.653	1.133	168.7
Temelso[b]	1.7	−22.6[c]	1.610	1.155	180.0
Dash and Rajakumar[d]	0.3	−21.9	1.653	1.136	172.0
Dash and Rajakumar[e]	2.3				
Dash and Rajakumar[f]	−1.4	−23.0			

[a]CCSDT(Q)/CBS//CCSD(T)-F12a/cc-pVTZ-F12
[b]CCSD(T)/cc-pVDZ with an ROHF reference
[c]CCSD(T)/cc-pVTZ with an ROHF reference
[d]M06−2X/6-31+G(*d*,*p*)
[e]CCSD(T)/cc-pVTZ//M06−2X/6-31+G(*d*,*p*)
[f]G3(MP2)//M06−2X/6-31+G(*d*,*p*)

3.4.2 Kinetics

The rate constants computed in this study using the rigid-rotor harmonic oscillator approximation can be found in Table 3.7. The theoretical methods section contains the methods used for obtaining these rate constants. The abstractions from *cis*-HONO and CH_3OH (both R1 and R2) have submerged barriers, and as such the rate constants for these reaction will likely be large at all temperatures. Because of this, we have only examined the rate constants for the abstractions from HNCO, *trans*-HONO, and C_2H_4.

Quantitatively accurate kinetic models require highly accurate barrier heights of reaction. This makes the rate constants highly dependent on the calculated barrier heights. Additionally, the reaction barriers are low, therefore, variational effects are likely to be important which could be beneficial to explore in a future study.

Table 3.7: Rate constants for C_2H + HX $\rightarrow$ C_2H_2 + X abstractions in cm^3 $molecule^{-1}$ s^{-1}.

T(K)	HNCO	*trans*-HONO	C_2H_4
50	3.93×10^{-16}	6.20×10^{-18}	2.45×10^{-14}
100	1.06×10^{-15}	8.39×10^{-18}	1.07×10^{-13}
150	3.22×10^{-15}	1.66×10^{-17}	2.67×10^{-13}
175	5.33×10^{-15}	2.46×10^{-17}	3.77×10^{-13}
200	8.41×10^{-15}	3.66×10^{-17}	5.07×10^{-13}
225	1.27×10^{-14}	5.44×10^{-17}	6.57×10^{-13}
250	1.84×10^{-14}	8.02×10^{-17}	8.29×10^{-13}
275	2.57×10^{-14}	1.17×10^{-16}	1.02×10^{-12}
295	3.29×10^{-14}	1.56×10^{-16}	1.19×10^{-12}
298	3.40×10^{-14}	1.62×10^{-16}	1.22×10^{-12}
300	3.48×10^{-14}	1.67×10^{-16}	1.24×10^{-12}
325	4.61×10^{-14}	2.34×10^{-16}	1.48×10^{-12}
350	5.95×10^{-14}	3.22×10^{-16}	1.74×10^{-12}
375	7.55×10^{-14}	4.35×10^{-16}	2.03×10^{-12}
400	9.40×10^{-14}	5.76×10^{-16}	2.35×10^{-12}
500	1.99×10^{-13}	1.52×10^{-15}	3.90×10^{-12}
1000	1.88×10^{-12}	2.58×10^{-14}	2.10×10^{-11}
1500	6.78×10^{-12}	1.17×10^{-13}	6.03×10^{-11}
2000	1.66×10^{-11}	3.23×10^{-13}	1.29×10^{-10}
3000	5.68×10^{-11}	1.25×10^{-12}	3.82×10^{-10}
4000	1.32×10^{-10}	3.10×10^{-12}	8.19×10^{-10}
5000	2.51×10^{-10}	6.10×10^{-12}	1.47×10^{-9}

$\mathbf{C_2H + C_2H_4}$

The computed rate constants from this study for the C_2H + C_2H_4 hydrogen abstraction reaction are plotted in Figure 3.10 (solid red line). Additionally, the canonical variational transition state theory (CVT) theoretical rate constants of Dash and Rajakumar, as well as various experimental rate constants have been included. The rate constants of Dash and Rajakumar were obtained from the sum of the individual rate coefficients associated with abstraction (C_2H + C_2H_4 $\rightarrow$ C_2H_2 + C_2H_3) and addition (C_2H + C_2H_4 $\rightarrow$ C_2H_4CCH) channels. The sum of the individual rate coefficients at the G3(MP2)//M06-2X/6-31+G(*d*,*p*) and CCSD(T)/cc-pVTZ//M06-2X/6-31+G(*d*,*p*) levels of theory are given by the dashed

purple line and dashed pink line, respectively. The rate constants for only the abstraction channel by Dash and Rajakumar at the CCSD(T)/cc-pVTZ//M06-2X/6-31+G(d,p) level of theory are given by the red dotted line. Our computed rate constants for the abstraction channel are in good agreement with theirs at the CCSD(T)/cc-pVTZ//M06-2X/6-31+G(d,p) level of theory. Dash and Rajakumar observed a strong negative temperature dependence for their computed rate constants, and the hydrogen abstraction contribution to the total rate constant is negligible below 250K. Above 1000K, the abstraction and addition reactions are in competition with each other. However, this competition is outside of the scope of the present study but it could be beneficial to explore the effects in the future. A negative temperature dependence was also reported in earlier experimental studies, but not to the same degree as that of Dash and Rajakumar. The experiments were performed using supersonic expansion methods. Opansky and Leone used transient infrared laser absorption spectroscopy,[161] Chastaing et. al used CRESU (laval nozzle expansion),[219] and Vakhtin et al. used pulsed nozzle expansion methods.[220]

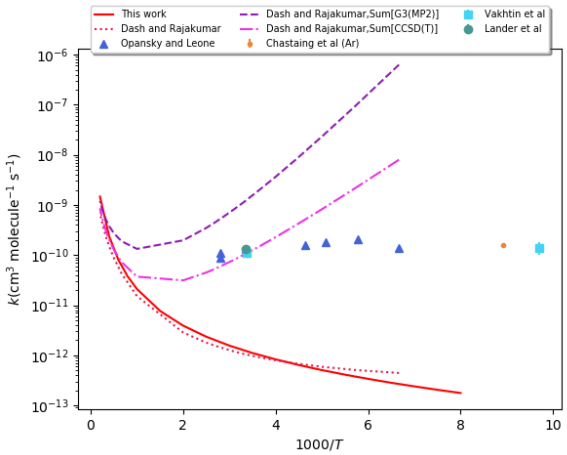

Figure 3.10: Experimental and theoretical rate constants for the $C_2H + C_2H_4 \rightarrow C_2H_2 + C_2H_3$ reaction. Theoretical rate constants are illustrated as solid curves and experimental rate constants are given as points.[161,169,171,219,220]

3.5 Conclusions

The energetics of ethynyl radical hydrogen abstraction reactions involving HNCO, *trans*-HONO, *cis*-HONO, C_2H_4, and CH_3OH have been determined using highly accurate *ab initio* methods. Sub-chemical accuracy was achieved through various additive energy corrections, and shows excellent agreement with the available Active Thermochemical Table values. Additionally, accurate transition state barriers have been determined for the reactions involving HNCO, *trans*-HONO, C_2H_4, and CH_3OH (R1) in this study. The reaction pathways involving *cis*-HONO and CH_3OH (R2) have been determined at the CCSD(T)-F12a/cc-pVTZ-F12//MP2/aug-cc-pVTZ level of theroy. The reactions with CH_3OH (R1 and R2) and *cis*-HONO have submerged barriers below the relative enthalpies of the reactants. Abstractions of *trans*-HONO, HNCO, and C_2H_4 have barriers between 0.5 and 5.0 kcal mol^{-1}. The reactions appear to follow the Evans-Polanyi principle and a strong correlation between the barrier height and reaction enthalpy was seen. One exception to the Evans-Polanyi principle was found with the C_2H + *trans*-HONO reaction, which is believed to be due to the interaction between the nitrogen in *trans*-HONO and the terminal carbon of the ethynyl radical. This interaction raises the barrier height of the transition state to almost 5 kcal mol^{-1}.

Reliable kinetics were obtained for a subset of the above reactions implementing an Eckart tunnelling model. The computed rate constants for the $C_2H + C_2H_4 \rightarrow C_2H_2 + C_2H_3$ reaction are in good agreement with those computed by Dash and Rajakumar. However, there appears to be a potential competition between the abstraction and addition channels of this reaction which could explain the disagreement between the computed rate constants and experiment. The kinetics of the reactions with *trans*-HONO and HNCO have not yet been explored, so the results presented in this study may aid in future experimental studies.

Chapter 4

A Concordant Mode Approach to Intermolecular Vibrations[3]

[3]Dornshuld, L.N.O., Lahm, M.E., Kitzmiller, N.L., Allen, W.D., and Schaefer III, H.F. 2025. To be submitted to a peer-reviewed journal.

4.1 Abstract

A recent and novel method, referred to as the Concordant Mode Approach (CMA), offers tremendous potential for increasing the system size and the level of theory attainable in quantum chemical computations of molecular vibrational frequencies. Computations targeting CCSD(T)/aug-cc-pVTZ (coupled cluster singles and doubles with perturbative triples using an augmented correlation-consistent polarized-valence triple-ζ basis set) were performed on several molecules from the S22 test set to further bolster the benchmarks of the CMA method. It was found that MP2/heavy-aug-cc-pVTZ (second order Møller-Plesset perturbation theory with a similar basis set that excludes the diffuse functions on all hydrogen atoms) proves to be a remarkable choice for generating the underlying (Level B) normal modes of the CMA scheme. Employing this Level B within the CMA-0A method reproduces 434 benchmark frequencies with a mean absolute error of 0.52 cm^{-1} and a corresponding standard deviation of 1.93 cm^{-1}. Only 18 frequencies gave residuals larger than 2.5 cm^{-1}. Utilizing the CMA-2A method with this same Level B and a cutoff of $\xi = 0.02$, 16 out of the 18 outliers greater than 2.5 cm^{-1} were successfully eliminated.

4.2 Introduction

The precise physical description of noncovalent interactions in chemical systems using robust electronic structure methods has constituted a significant challenge to theory. This challenge permeates out to properties such as vibrational frequencies, which are fundamentally important for spectroscopic assignment and thermodynamic analysis. While quantitative accuracy can be obtained by methods with a high-level treatment of electron correlation such as, coupled-cluster theory with singles, doubles, and perturbative triples, CCSD(T),[195,196] the computational demands of CCSD(T) calculations, which scale $O(N^7)$, significantly limit the number of atoms and size of basis set used. Considerable progress has been made in the literature of noncovalent systems and the interaction energies of systems with up to 24 atoms

can be estimated at the CCSD(T) level with an infinite basis set through extrapolation to the complete basis set (CBS) limit.[221–224] Rigorous electronic structure computations on small model systems provide the first step toward definitively describing these effects.

Numerous benchmark interaction energy databases for noncovalent dimer complexes (hydrogen-bonded, dispersion bound, and mixed complexes) have been compiled utilizing highly accurate quantum mechanical calculations.[133,225–230] These databases are useful for determining appropriate methods for larger systems, because they document the performance of lower scaling *ab initio* methods and density functional theory approximations. Despite the plethora of data for these benchmark energetics for dimer systems, vibrational frequencies computed with highly accurate *ab initio* methods are far less common. Therefore, it is possible that the minimum energy conformations of these systems have not been determined due to the prohibitive cost of calculating the vibrational frequencies at a high-level of theory. Obtaining highly accurate interfragment vibrational frequencies is a challenging task that nevertheless holds the promise of elucidating and improving the computation of vibrational frequencies of larger molecules.

A recent, novel method dubbed the Concordant Mode Approach (CMA),[17] holds incredible potential for the accurate computation of interfragmental frequencies as it reduces the scaling with respect to system size of necessary single point energy computations at a target level of theory from quadratic to linear. The CMA-0A protocol, which centers on computing only diagonal force constants at the higher-level of theory A in a normal mode basis generated by a lower-level of theory B, was tested on over 120 molecules (1580 targeted CCSD(T)/cc-pVTZ benchmark vibrational frequencies) from the G2 test set.[231] Remarkably, CMA-0A was successful in reducing all except three and seven frequency residuals to less than 2.5 cm^{-1} when Level B was chosen as B3LYP/6-31G(2*df,p*) and CCSD(T)/cc-pVDZ, respectively. Further research was done to create a new method (CMA-2A) that would rapidly and systematically eliminate all outliers and converge to the exact Level A frequencies.[18] The CMA-2A protocol selects which off-diagonal force constants to explicitly evaluate at Level A

based on dimensionless ξ parameters that can be evaluated at an additional Level C which comes with little to no further computational cost. When ξ is equal to 0.02, only a 33% increase in number of computed displacements from CMA-0A, the CMA-2A protocol was able to reduce the residuals of the entire database to less than 1.8 cm^{-1}. The CMA-N hierarchy results holds incredible potential and as a severe test, the following study will apply the CMA-0A, CMA-1A, and CMA-2A protocols to non-bonded chemical interactions.

4.3 Computational Methods

Several molecules from the S22 set[225] were used for benchmarking purposes and are shown in Figures 4.1 – 4.3. Full geometry optimizations and corresponding harmonic vibrational frequency computations were performed using the *ab initio* method CCSD(T) and Dunning's correlation consistent triple-ζ basis set augmented with diffuse functions, aug-cc-pVTZ, denoted as aTZ.[123,194] New force fields at the reference geometries were computed with the Hartree–Fock (HF), second-order Møller-Plesset (MP2),[63] and CCSD(T) *ab initio* methods in conjunction with the following correlation consistent basis sets of double-, and triple-ζ quality: cc-pVXZ[5], heavy-aug-cc- pVXZ[5,123,194], and aug-cc- pVXZ[123,194] (where X = D, T). The heavy-aug-cc-pVXZ basis set incorporates diffuse functions on all non-hydrogen (or "heavy") atoms (cc-pVXZ for H and aug-cc- pVXZ for all other atoms). The basis sets cc-pVXZ, heavy-aug-cc-pVXZ, aug-cc-pVXZ are denoted as XZ, ha$X$Z, and aXZ, respectively, where X is the cardinality of the basis set.

The Level B quadratic force constants and gradients were computed in the cartesian basis via finite differences at fourth-order accuracy with a displacement size of 0.01 Bohr. A second-order scheme[232] was utilized to transform the Cartesian force constants and gradient into an internal coordinate basis. The internal coordinate force constants are then transformed into the proper natural internal coordinate (NIC) basis.[233,234] The corresponding vibrational normal modes were computed with the GF-matrix method.[235] The reference force constants of Level A were transformed from the Cartesian basis to the previously calculated normal

mode basis of Level B to obtain the matrix $\mathbf{F}_{\mathrm{CMA}}$. In order to completely eliminate numerical errors in the current benchmark research, the CMA frequencies were obtained by zeroing out off-diagonal elements of $\mathbf{F}_{\mathrm{CMA}}$ according to the employed CMA protocol. The HF, MP2, and CCSD(T) energies were computed with the Molpro program[191] and and the SCF and CC energy residuals were reduced to 10^{-12} Hartrees upon convergence. The frozen core approximation was invoked for all coupled cluster and MP2 computations.

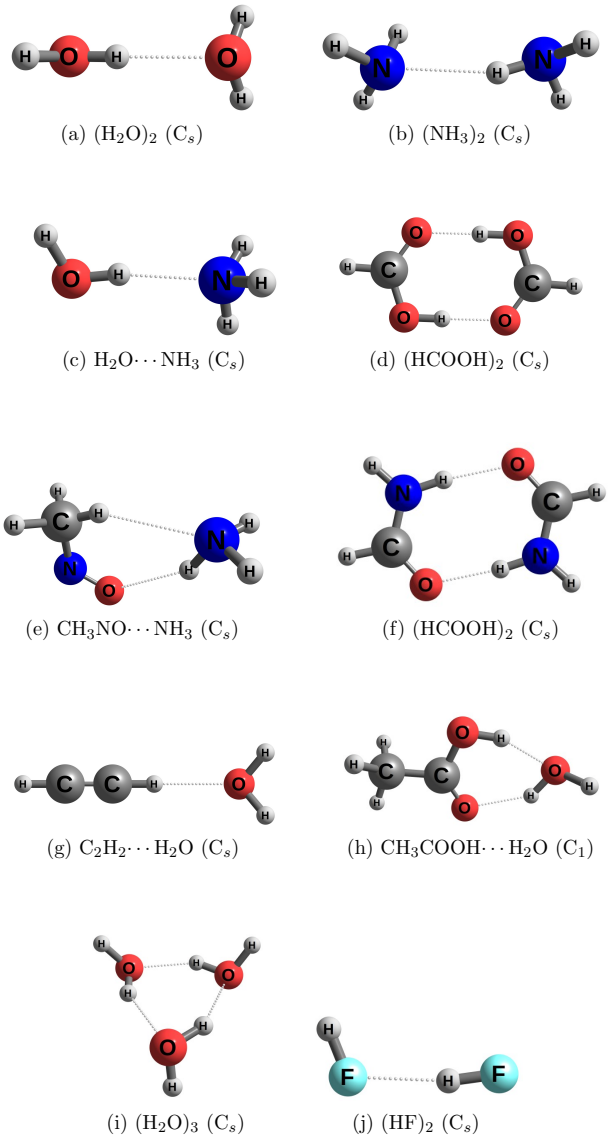

(a) $(H_2O)_2$ (C_s) (b) $(NH_3)_2$ (C_s)

(c) $H_2O\cdots NH_3$ (C_s) (d) $(HCOOH)_2$ (C_s)

(e) $CH_3NO\cdots NH_3$ (C_s) (f) $(HCOOH)_2$ (C_s)

(g) $C_2H_2\cdots H_2O$ (C_s) (h) $CH_3COOH\cdots H_2O$ (C_1)

(i) $(H_2O)_3$ (C_s) (j) $(HF)_2$ (C_s)

Figure 4.1: Hydrogen bonded complexes

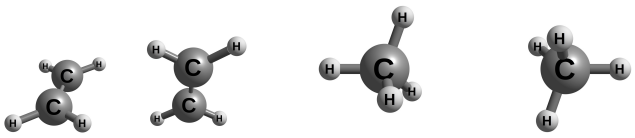

(a) $(C_2H_4)_2$ (C_s)

(b) $(CH_4)_2$ (C_s)

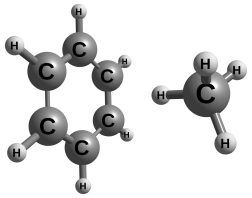

(c) $C_6H_6\cdots CH_4$ (C_s)

Figure 4.2: Dispersion bound complexes

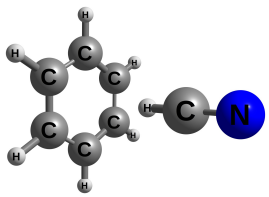

(a) $C_6H_6\cdots HCN$ (C_s)

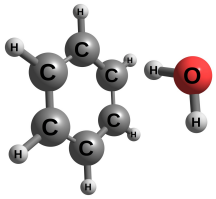

(b) $C_6H_6\cdots H_2O$ (C_s)

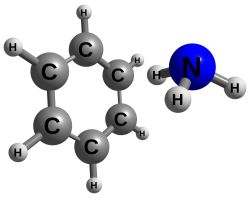

(c) $C_6H_6\cdots NH_3$ (C_s)

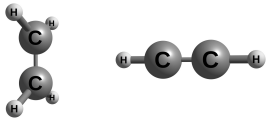

(d) $C_2H_4\cdots C_2H_2$ (C_s)

Figure 4.3: Mixed complexes

4.4 CMA Protocol

As outlined previously, the detailed protocols for CMA-0A[17], CMA-1A[17], and CMA-2A[18] were followed for this study. For the application of CMA to dimer systems, special internal coordinates must be utilized for the description of intermolecular motions, defined as follows. For a dimer molecular system of N total atoms, where the monomers are denoted by A and B, define three non-collinear points within each monomer as functions of the nuclear positions only within A or B: $\mathbf{d}_K^A(\mathbf{r}_1^{\mathrm{A}}, \mathbf{r}_2^{\mathrm{A}}, \ldots, \mathbf{r}_m^{\mathrm{A}})$ and $\mathbf{d}_K^B(\mathbf{r}_1^{\mathrm{B}}, \mathbf{r}_2^{\mathrm{B}}, \ldots, \mathbf{r}_n^{\mathrm{B}})$ $(K = 1, 2, 3)$, where

the Cartesian coordinates are denoted as $\mathbf{r}_i^{\mathrm{A}}$ $(i = 1, 2, \ldots, m)$ and $\mathbf{r}_j^{\mathrm{B}}$ $(j = 1, 2, \ldots, n)$ and $m + n = N$. A set of Euler angle coordinates are employed in conjunction with the monomer internal points. The first coordinate utilized is the monomer-monomer distance, mathematically defined as,

$$R = |\mathbf{d}_1^{\mathrm{A}} - \mathbf{d}_1^{\mathrm{B}}|. \tag{4.1}$$

The next two are the monomer polar angles. The terms (P, Q) are utilized as dimer complements, when $P = \mathrm{A}$, $Q = \mathrm{B}$ and vice versa,

$$\cos(\theta_P) = \frac{(\mathbf{d}_2^P - \mathbf{d}_1^P) \cdot (\mathbf{d}_1^Q - \mathbf{d}_1^P)}{|\mathbf{d}_2^P - \mathbf{d}_1^P||\mathbf{d}_1^Q - \mathbf{d}_1^P|}. \tag{4.2}$$

The monomer-monomer torsion angle, which corresponds to the azimuthal Euler angles ϕ_{A} and ϕ_{B} of the two monomers, may be defined as,

$$\cos(\tau) = \frac{\mathbf{e}_{12}^{\mathrm{A}} \cdot (\mathbf{e}_{12}^{\mathrm{B}} \times \mathbf{e}_R^{\mathrm{A}})}{\sin(\theta_{\mathrm{A}})\sin(\theta_{\mathrm{B}})}. \tag{4.3}$$

Where,

$$\mathbf{e}_{12}^P = \frac{(\mathbf{d}_2^P - \mathbf{d}_1^P)}{|\mathbf{d}_2^P - \mathbf{d}_1^P|} \tag{4.4}$$

$$\mathbf{e}_R^P = \frac{(\mathbf{d}_1^Q - \mathbf{d}_1^P)}{|\mathbf{d}_1^Q - \mathbf{d}_1^P|}. \tag{4.5}$$

Finally, the two monomer internal rotation angles are defined as,

$$\sin(\chi_P) = \frac{\mathbf{e}_{32}^P \cdot (\mathbf{e}_R^P \times \mathbf{e}_{12}^P)}{\sin(\theta_P)\sin(\alpha_P)} \tag{4.6}$$

where $(P = \mathrm{A}, \mathrm{B})$, and

$$\mathbf{e}_{32}^P = \frac{(\mathbf{d}_2^P - \mathbf{d}_3^P)}{|\mathbf{d}_2^P - \mathbf{d}_3^P|}. \tag{4.7}$$

4.5 Benchmarking Level B for CMA-0A

The CMA-0A procedure was performed for eleven Level B theories, as shown in Table 4.1. The mean absolute error (MAE) of the CMA-0A residuals ranges from 0.10 to 1.38 cm^{-1} for all Level B theories tested. The mean CMA residuals fall within a small range of 0.03 to 0.45 cm^{-1}, and the standard deviation (σ_ϵ) ranges from 0.17 to 3.69 cm^{-1}. The maximum absolute error (ϵ_{MAX}) over the entire test set is between 0.89 and 39.21 cm^{-1}. The MAEs for the zero-point vibrational energy (ZPVE) residuals fall into a range of 0.26 to 4.23 cm^{-1} and the standard deviation (σ_Δ) of the ZPVE Δ lies between 0.09 and 4.48 cm^{-1}. These statistical signatures for the ZPVEs are larger than those observed previously,[17,18] but are still negligible in thermochemical applications. Kitzmiller and coworkers showed that the basis set quality was more important than higher-order treatment of electron correlation in the selection of Level B.[18] The same can be shown here where the CMA-0A MP2 statistics are almost as good as the coupled cluster results, again making MP2 a promising candidate as a Level B theory which scales as N^5 with basis set size as compared to the N^7 scaling of conventional CCSD(T).

Table 4.1: Summary Statistics within the test set of CMA-0A Residuals for the CCSD(T)/aTZ Harmonic Vibrational Frequencies (ϵ, cm^{-1}) and ZPVEs (Δ, cm^{-1}).

Level B	N[a]	MAE ϵ	mean ϵ	ϵ_{max}[b]	σ_ϵ	ϵ_{MAX}[c]	MAE Δ	mean Δ	σ_Δ
MP2/DZ	243	1.37	0.42	8.05	3.31	26.82	4.23	4.23	4.48
MP2/haDZ	243	0.52	0.09	3.10	1.91	20.85	0.88	0.88	0.30
MP2/aDZ	243	0.80	0.16	6.04	3.69	39.21	1.45	1.45	1.24
MP2/TZ	243	0.38	0.13	2.30	0.93	7.12	0.95	0.95	0.90
MP2/haTZ	434	0.52	0.13	4.50	1.93	19.56	1.63	1.63	2.41
MP2/aTZ	408	0.34	0.08	2.54	1.09	12.24	1.00	1.00	1.46
CCSD(T)/DZ	243	1.31	0.45	2.38	3.41	29.25	3.70	3.70	4.63
CCSD(T)/haDZ	243	0.44	0.09	9.18	1.54	16.72	0.88	0.88	0.49
CCSD(T)/aDZ	219	0.57	0.15	2.70	1.49	16.46	1.47	1.47	1.54
CCSD(T)/TZ	219	0.36	0.13	2.70	0.94	7.14	1.27	1.27	1.29
CCSD(T)/haTZ	219	0.10	0.03	0.48	0.17	0.89	0.26	0.26	0.09

[a]Number of benchmark vibrational frequencies included.
[b]Average maximum absolute ϵ per molecule.
[c]Maximum absolute ϵ over the entire data set.

The importance of the basis set quality in the accurate description of normal modes can further be shown in Table 4.2, which contains the CMA-0A residuals for the water dimer at various levels of theories and systemically increasing basis set sizes. Perhaps unsurprisingly, MP2 and CCSD(T) with the unaugmented, DZ basis set yield the largest residuals of 24.3 and 25.7 cm^{-1}, respectively, for a couple of intermolecular modes. Moving to the haDZ basis set brings the residuals of these modes down to 2.0 and 1.3 cm^{-1}, respectively. Further improvement can be seen moving to the aDZ basis set where the residuals decrease to 0.4 and -1.2 cm^{-1}, respectively. Results with a TZ basis set are significantly better than that of the DZ basis set; nevertheless, three residuals above the 2.5 cm^{-1} threshold occur for both MP2 and CCSD(T). Moving to the haTZ basis set with MP2 remarkably reduces all residuals below 0.5 cm^{-1}, rivaling MP2/aTZ in accuracy with a substantially smaller set of basis functions.

Table 4.2: Residuals (in cm^{-1}) of the CMA-0A data from the reference harmonic frequencies (in cm^{-1}) for $(H_2O)_2$ using natural internal coordinates with cartesian force constants.

Reference	CMA-0A										
CCSD(T)	MP2						CCSD(T)				
aTZ	DZ	haDZ	aDZ	TZ	haTZ	aTZ	DZ	haDZ	aDZ	TZ	haTZ
130.0	2.0	1.0	0.1	6.8	0.5	0.1	5.0	1.3	0.1	3.9	0.7
143.4	17.0	1.9	1.0	7.1	0.1	0.5	14.0	2.8	3.2	7.1	0.0
153.5	24.3	2.0	0.4	−0.4	0.0	0.3	25.7	1.3	−1.2	2.1	0.1
185.1	−5.8	−0.1	0.0	−2.6	0.0	−0.2	−5.3	0.5	−0.4	−2.5	−0.1
359.8	−0.2	−0.7	−0.3	0.0	0.0	0.0	−0.3	−0.8	−0.3	0.0	0.0
621.8	−9.4	−0.4	0.2	−2.0	0.3	0.3	−9.0	−0.2	0.2	−2.0	0.2
1646.3	0.1	0.0	0.0	0.1	0.0	0.0	0.1	0.0	0.0	0.1	0.1
1667.5	−0.1	0.0	0.0	0.0	0.0	0.0	−0.1	0.0	0.1	0.0	0.0
3731.1	1.2	0.0	0.1	0.1	0.0	0.0	1.8	0.0	0.1	0.1	0.0
3805.5	−0.1	0.0	0.0	0.0	0.0	0.0	0.0	0.0	0.0	0.0	0.0
3891.4	−1.1	−0.1	−0.1	−0.1	0.0	0.0	−1.7	−0.1	−0.1	−0.1	0.0
3911.1	0.0	0.0	0.0	0.0	0.0	0.0	0.1	0.1	0.0	0.0	0.0

One abnormal case for basis set quality can be seen for the formic acid dimer [$(HCOOH)_2$] residuals shown in Table 4.3. Quite fortuitously, all interfragmental modes of this system are

well described with every Level B tested here. However, an unusual discrepancy arises for the mixing of the C−H and O−H symmetric stretches. By symmetry, the C−H stretches on either HCOOH unit will mix, as well as the O−H stretches. Harmonic vibrational frequencies computed at the CCSD(T)/aTZ level of theory yield no mixing between these sets of stretches; however, at the MP2/aDZ level these sets of stretches mix in an almost 50/50 proportion. This leads to MP2/aDZ yielding quite significant residuals of 39.2 and -38.6 cm^{-1}. Similar large residuals of 7.4 and -7.2 cm^{-1} can be seen for MP2/DZ as well as 20.8 and -20.4 cm^{-1} for MP2/haDZ. It is unclear why these DZ basis sets struggle so exceptionally to describe these motions, but it is clear that even for polymeric systems a basis set of adequate cardinality must be employed to properly describe the interactions of intrafragmental modes that mix between fragments. It is evident that an ideal Level B basis set for polymeric systems will be of TZ cardinality with some degree of augmentation.

A key conclusion, pending further research, from Kitzmiller and coworkers is that when targeting CCSD(T)/cc-pVXZ frequencies with the CMA-0A approach, MP2/cc-pVXZ (or its df-variant) is the preferred Level B method.[18] Based on the statistics in Table 4.1, and the prior analysis of Tables 4.2 and 4.3, the most promising Level B method to target these CCSD(T)/aTZ frequencies is MP2/haTZ. Arguably it appears that MP2/TZ or MP2/aTZ would be the preferred Level B choice; however, the sample sizes for both of these methods are smaller than that of MP2/haTZ. Additionally, it is only the benzene containing complexes (Figures 4.2c, 4.3a − 4.3d) that MP2/haTZ struggles to characterize completely. These benzene containing complexes were not included in the sample size for MP2/TZ. As shown in Table 4.4, only 9, 9, 5, and 7 frequencies give rise to residuals greater than 1.5 cm^{-1} in magnitude of the 39, 42, 39, and 45 total frequencies for Benzene$\cdots$HCN, Benzene$\cdots$NH$_3$, Benzene$\cdots$H$_2$O, and Benzene$\cdots$CH$_4$, respectively. This reduces to 4, 5, 3, 6, respectively, when increasing the basis set to aTZ (includes diffuse functions on all the atoms). With Level B = MP2/haTZ, the largest residual across all of these benzene containing complexes corresponds to the benzene ring puckering mode that is significantly shifted from that of

Table 4.3: Residuals (in cm^{-1}) of the CMA-0A data from the reference harmonic frequencies (in cm^{-1}) for $(HCOOH)_2$ using natural internal coordinates cartesian force constants.

Reference	CMA-0A										
CCSD(T)	MP2						CCSD(T)				
aTZ	DZ	haDZ	aDZ	TZ	haTZ	aTZ	DZ	haDZ	aDZ	TZ	haTZ
69.5	0.1	0.1	0.1	0.1	0.0	0.1	0.2	0.1	0.2	0.2	0.0
168.2	0.2	0.0	0.1	0.5	0.1	0.1	0.1	0.2	0.3	0.2	0.0
175.9	0.2	0.1	0.1	0.0	0.1	0.0	0.1	0.0	0.1	0.0	0.0
211.1	−0.1	0.1	0.0	−0.3	0.0	0.0	0.1	0.0	−0.1	−0.1	0.0
252.6	0.3	0.0	0.0	0.1	0.0	0.0	0.3	0.0	0.0	0.1	0.0
277.1	0.1	0.1	0.1	0.1	0.1	0.1	0.2	0.2	0.2	0.1	0.1
682.2	0.1	0.1	0.1	0.0	0.0	0.0	0.1	0.0	0.0	0.0	0.0
710.8	0.1	0.0	0.0	0.0	0.0	0.0	0.1	0.0	0.0	0.0	0.0
963.2	1.0	0.5	0.4	0.3	0.2	0.2	0.6	0.3	0.2	0.1	0.1
987.1	1.1	0.4	0.3	0.2	0.1	0.2	0.8	0.2	0.1	0.1	0.1
1080.2	−0.8	−0.4	−0.3	−0.2	−0.1	−0.1	−0.6	−0.1	−0.1	0.0	0.0
1101.7	−0.9	−0.3	−0.2	−0.1	0.0	−0.1	−0.6	−0.1	0.0	0.0	0.0
1250.2	0.9	0.4	0.4	0.8	0.5	0.3	0.7	0.2	0.2	0.1	0.0
1254.8	0.9	0.4	0.3	0.7	0.6	0.4	0.3	0.1	0.1	0.1	0.0
1401.5	3.0	1.0	0.7	1.1	1.6	0.9	0.5	0.0	0.0	0.1	0.1
1404.2	0.4	0.4	0.3	0.4	0.6	0.5	0.1	−0.1	−0.1	0.0	0.0
1458.2	−2.4	−0.7	−0.3	−1.4	−1.7	−0.9	0.0	0.0	0.1	0.0	−0.1
1486.8	1.6	0.3	0.4	−0.5	−0.6	−0.4	1.4	0.2	0.3	0.0	0.0
1708.0	−2.4	−0.8	−0.9	−0.5	−0.3	−0.3	−1.7	−0.3	−0.3	−0.1	0.0
1772.6	−0.9	−0.4	−0.5	−0.3	−0.2	−0.2	−0.6	−0.1	−0.1	−0.1	0.0
3094.7	1.5	3.0	2.4	0.1	0.1	0.1	0.7	1.5	1.1	0.0	0.0
3098.5	7.4	20.8	39.2	0.1	0.1	0.1	0.8	16.7	5.9	0.0	0.0
3190.6	−7.2	−20.4	−38.6	−0.1	−0.1	−0.1	−0.9	−16.4	−5.8	0.0	0.0
3294.4	−1.5	−2.8	−2.3	−0.1	−0.1	−0.1	−0.7	−1.4	−1.1	0.0	0.0

monomeric benzene. Increasing the basis set to aTZ brings all of these residuals to under 0.3 cm^{-1}. Another large residual that can be eliminated by increasing the basis set to aTZ is the benzene C−H antisymmetric wagging mode. However, not all of the residuals are taken care of when moving to aTZ, and in some cases, the residuals grow larger. Two residuals that seem constant for MP2/haTZ and MP2/aTZ are the benzene ring deformation modes around 1159 and 1328 cm^{-1}. These are modes that deviate for monomeric benzene at a highly similar magnitude when Level B = MP2/TZ, as seen in Table 2 from Kitzmiller and coworkers.[18]

Table 4.4: The only cases within the frequencies of the complexes that contain benzene with CMA-0A-nc[CCSD(T)/aTZ, MP2/haTZ] residuals (ϵ, cm^{-1}) greater than 1.5 cm^{-1} in magnitude, together with CMA-0A-nc[CCSD(T)/aTZ, MP2/aTZ] residuals.

Benzene$\cdots$HCN			Benzene$\cdots NH_3$			Benzene$\cdots H_2O$			Benzene$\cdots CH_4$		
Reference	CMA-0A		Reference	CMA-0A		Reference	CMA-0A		Reference	CMA-0A	
CCSD(T)	MP2		CCSD(T)	MP2		CCSD(T)	MP2		CCSD(T)	MP2	
aTZ	haTZ	aTZ	aTZ	haTZ	aTZ	aTZ	haTZ	aTZ	aTZ	haTZ	aTZ
13.1	1.5	0.9	13.7	8.2	1.6	16.3	3.7	2.3	18.0	2.2	4.9
13.5	2.4	1.4	27.6	−1.6	7.2	554.8[a]	10.2	0.2	22.5	0.1	4.1
557.4[a]	19.6	0.3	71.2	−0.2	−2.1	899.5[b]	−6.2	−0.1	25.0	1.0	2.4
728.5	−1.5	−2.3	548.0[a]	17.3	0.2	1154.5[c]	4.2	4.5	82.4	−1.9	−1.8
728.7	1.7	2.4	685.0	−2.4	0.0	1326.3[c]	−3.7	−3.9	541.7[a]	19.1	0.2
915.2[b]	−10.4	−0.2	896.6[b]	−7.4	−0.1	$\cdots$	$\cdots$	$\cdots$	900.4[b]	−10.3	−0.1
1011.5	−1.6	0.0	963.1	−0.6	0.0	$\cdots$	$\cdots$	$\cdots$	1153.5[c]	4.1	4.4
1156.4[c]	4.0	4.3	1154.0[c]	4.2	4.4	$\cdots$	$\cdots$	$\cdots$	1328.8[c]	−3.6	−3.8
1328.2[c]	−3.5	−3.7	1327.3[c]	−3.6	−3.9	$\cdots$	$\cdots$	$\cdots$	$\cdots$	$\cdots$	$\cdots$

[a]Benzene ring puckering mode.
[b]Benzene C−H antisymmetric wagging mode.
[c]Benzene ring deformation mode. Residuals similar to CMA-0A(MP2/TZ) for monomeric benzene.[18]

4.6 Benchmarking CMA-2A

For the purpose of benchmarking the convergent CMA-2 theory, in this section we will consider any frequency residuals greater than 1.5 cm^{-1} in magnitude. Such outliers for CMA-0A[CCSD(T)/aTZ, MP2/haTZ] are presented in Table 4.5, where 18 cases are found from 4 distinct molecules from the test set, all of which contain benzene. The size of these residuals ranges from 3.5 to 19.6 cm^{-1}. When the vibrational modes are treated by CMA-1A(1) (fifth column), all absolute residuals are less than 1.7 cm^{-1}, excluding the 4.0 cm^{-1} residual for Benzene$\cdots NH_3$, which can be reduced to 1.8 cm^{-1} with only three extra couplings. Again, the inclusion of a single off-diagonal force constant per molecule is sufficient to make almost all the outliers disappear! CMA-0A is quite close to being an spotless method for this test set of small and large dimer systems.

To apply the CMA-2A protocol, a Level C is necessary. With Level B = MP2/haTZ, then Level C is chosen as HF/haTZ to not incur any additional computational cost. The CMA-2A protocol that incorporates all $\mathbf{F}_{\mathrm{CMA}}$ force constants corresponding to $\xi > 0.02$ is assessed in

Table 4.5. Overall, 16 out of the 18 outliers are successfully eliminated by CMA-2A ($|\epsilon| < 1.2$ cm^{-1}). The other two outliers both correspond to the ring puckering motion in benzene for the Benzene$\cdots$CH$_4$ and Benzene$\cdots$NH$_3$ complexes. As mentioned previously, the 4.0 cm^{-1} residual for Benzene$\cdots$NH$_3$ can be reduced to 1.8 cm^{-1} with three extra couplings. However, the CMA-2A result for Benzene$\cdots$CH$_4$ requires 235 off-diagonal elements and an over 500% additional computational cost. It also did not capture the same couplings as CMA-1A and further research seems necessary for this peculiar system. Overall, CMA-2A does perform well for this test set given that CMA-0A already reduces the cost of Level A frequency computations by 700-1000%,[17] any η value less than 100% still constitutes a rather marginal price to pay for the added certainty afforded by CMA-2A.[18]

Table 4.5: The only cases within the set of benchmark frequencies with CMA-0A-nc[CCSD(T)/aTZ, MP2/haTZ] residuals (ϵ, cm^{-1}) greater than 2.5 cm^{-1} in magnitude, together with the corresponding CMA-1A and CMA-2A results that target these outliers.

Molecule and mode	Description	Benchmark	ϵ[CMA-0A]	ϵ[CMA-1A(1)]	ϵ[CMA-2A]$(n)^a$	η^b (%)
benzene$\cdots$HCN, $\omega_8(a_1)$	ring puckering	557.4	19.6	1.2	1.2(17)	44
benzene$\cdots$CH$_4$, $\omega_9(e)$	ring puckering	541.7	19.1	1.7	2.2(235)	522
benzene$\cdots$NH$_3$, $\omega_9(a')$	ring puckering	548.0	17.3	4.0[c]	4.0(42)	100
benzene$\cdots$HCN, $\omega_{16}(a_1)$	C$-$H antisym. wag	915.2	-10.4	1.0	1.0(17)	44
benzene$\cdots$CH$_4$, $\omega_{15}(e)$	C$-$H antisym. wag	900.4	-10.3	0.4	0.1(235)	522
benzene$\cdots$H$_2$O, $\omega_9(a')$	ring puckering	554.8	10.2	0.3	0.3(41)	98
benzene$\cdots$NH$_3$, $\omega_1(a')$	interfragmental	13.7	8.2	1.1	0.3(42)	100
benzene$\cdots$NH$_3$, $\omega_{15}(a'')$	C$-$H antisym. wag	896.6	-7.4	0.9	0.9(42)	100
benzene$\cdots$H$_2$O, $\omega_{15}(a')$	C$-$H antisym. wag	899.5	-6.2	0.0	0.0(41)	98
benzene$\cdots$NH$_3$, $\omega_{23}(a')$	ring deformation	1154.0	4.2	0.0	0.0(42)	100
benzene$\cdots$H$_2$O, $\omega_{22}(a')$	ring deformation	1154.5	4.2	0.0	0.0(41)	98
benzene$\cdots$HCN, $\omega_{23}(a_1)$	ring deformation	1156.4	4.0	0.0	0.0(17)	44
benzene$\cdots$CH$_4$,$\omega_{22}(a_2)$	ring deformation	1153.5	4.1	0.0	0.0(235)	522
benzene$\cdots$H$_2$O, $\omega_1(a')$	interfragmental	16.3	3.7	1.4	0.5(41)	98
benzene$\cdots$H$_2$O, $\omega_{25}(a')$	ring deformation	1326.3	-3.7	0.0	0.0(41)	98
benzene$\cdots$CH$_4$, $\omega_{25}(e)$	ring deformation	1328.8	-3.6	0.0	0.0(235)	522
benzene$\cdots$NH$_3$, $\omega_{26}(a')$	ring deformation	1327.3	-3.6	0.0	0.0(42)	100
benzene$\cdots$HCN, $\omega_{26}(a_1)$	ring deformation	1328.2	-3.5	0.0	0.0(17)	44

[a] n = the number of off-diagonal elements included for the $\xi = 0.020$ cutoff.
[b] η = number of $\mathbf{F}_{\mathrm{CMA}}$(A) off-diagonal elements included as a percentage of the vibrational degrees of freedom for the given molecule.
[c] With three extra couplings, this residual can be reduced to 1.8 cm^{-1}.

4.7 Conclusions

Kitzmiller and coworkers concluded that if targeting CCSD(T)/cc-pVXZ frequencies with CMA-0A, then MP2/cc-pVXZ (or its df-variant) is the preferred Level B method for the G2 test set.[18] Here we determine that if targeting CCSD(T)/aXZ frequencies with CMA-0A, then MP2/ha$X$Z works well as the Level B method for these small and large dimer systems from the S22 test set. This Level B reproduces 434 benchmark frequencies with a mean absolute error of 0.52 cm^{-1} and a corresponding standard deviation of 1.93 cm^{-1}. Only 18 frequencies gave residuals larger than 2.5 cm^{-1}, all of which are associated with complexes that contain benzene. MP2/haTZ struggles to characterize the benzene ring puckering mode and the benzene C−H antisymmetric wagging mode, both of which are captured with MP2/aTZ. Therefore, an aTZ basis set might be preferred for these benzene containing complexes. As shown previously,[17,18] the choice of basis set is quite important, as highlighted by the water dimer and formic acid dimer residuals in Tables 4.2 and 4.3. Additionally, the convergent CMA-2A method is further benchmarked and overall performs well by successfully eliminating 16 out of the 18 outliers greater than 2.5 cm^{-1} found with CMA-0A. However, Benzene$\cdots CH_4$ presented a challenging case for CMA-2A showing that further research is necessary for the CMA-2A method. Overall, CMA-0A is close to being a flawless method for these dimer systems and handles the diversification into intermolecular vibrations with ease.

Chapter 5

Conclusion

This work utilizes high-level *ab initio* methods to further benchmark biomolecular behavior and beyond. We have performed the first theoretical treatment of the tetrafluoroborate anion with up to four water molecules ($BF_4^-(H_2O)_{n=1,2,3,4}$) using various computational methods. The solvent$\cdots$solvent interactions become stronger with increasing number of water molecules, and significant cooperative effects in the di-, tri-, and tetrahydrate systems were observed. The data also shows that solvent$\cdots$solute interactions alone do not fully account for the total hydration of BF_4^-, emphasizing the importance of solvent$\cdots$solvent interactions to accurately capture vibrational shifts, particularly in OH stretching frequencies. These findings further improve the understanding of BF_4^- hydration and its spectroscopic behavior. Additionally, the energetics and transition state barriers of ethynyl radical hydrogen abstraction reactions with HNCO, *cis*/*trans*-HONO, C_2H_4, and CH_3OH using highly accurate *ab initio* methods were determined, achieving subchemical accuracy with computed values in good agreement with benchmark Active Thermochemical Table values. Reactions with *cis*-HONO and CH_3OH show submerged barriers below the reactants' enthalpies, while reactions with *trans*-HONO, HNCO, and C_2H_4 have barriers ranging from 0.5 to 5.0 kcal mol^{-1}. The Evans–Polanyi principle was generally followed, with one exception for the C_2H + *trans*-HONO reaction, which has a higher barrier due to nitrogen-carbon interactions. Reliable kinetics were obtained for some reactions, with rate constants for $C_2H + C_2H_4 \rightarrow C_2H_2 + C_2H_3$ in good agreement with prior calculations, though competition between abstraction and addition channels may explain discrepancies with experimental values. The study's findings could inform future experimental research on these reactions. Lastly, the Concordant Mode Approach (CMA) was further benchmarked on several molecules from the S22 data set. A previous study by Kitzmiller and coworkers determined when targeting CCSD(T)/XZ

frequencies with CMA-0A, then MP2/XZ (or its density fitted variant) is the preferred Level B method for the G2 test set. We have determined that when targeting CCSD(T)/aXZ frequencies with CMA-0A, then MP2/ha$X$Z works well as the Level B method for these dimer systems, yielding highly accurate frequency residuals with a mean absolute error of 0.52 cm^{-1} and a standard deviation of 1.93 cm^{-1} across 434 benchmark frequencies. Only 18 frequencies had residuals greater than 2.5 cm^{-1}, all involving benzene-containing complexes. The CMA-2A method successfully eliminated 16 out of the 18 residuals greater than 2.5 cm^{-1}, but did struggle with the Benzene$\cdots CH_4$ complex. Ultimately, CMA performed well for these dimer systems and effectively characterized these intermolecular vibrations with minimal error.

References

[1] Szabo, A.; Ostlund, N. S. *Modern Quantum Chemistry*; Macmillan Publising Co., 1982.

[2] Roothaan, C. C. J. New Developments in Molecular Orbital Theory. *Rev. Mod. Phys.* **1951**, *23*, 69–89.

[3] Helgaker, T.; Jorgensen, P.; Olsen, J. *Molecular Electronic-Structure Theory*; John Wiley & Sons, 2014.

[4] Hariharan, P. C.; Pople, J. A. The Influence of Polarization Functions on Molecular Orbital Hydrogenation Energies. *Theor. Chim. Acta* **1973**, *28*, 213–222.

[5] Dunning, T. H., Jr. Gaussian Basis Sets for Use in Correlated Molecular Calculations. I. The Atoms Boron through Neon and Hydrogen. *J. Chem. Phys.* **1989**, *90*, 1007–1023.

[6] Dunning, T. H., Jr.; Peterson, K. A.; Wilson, A. K. Gaussian Basis Sets for Use in Correlated Molecular Calculations. X. The Atoms Aluminum through Argon Revisited. *J. Chem. Phys.* **2001**, *114*, 9244–9253.

[7] East, A. L. L.; Allen, W. D. The Heat of Formation of NCO. *J. Chem. Phys.* **1993**, *99*, 4638–4650.

[8] Császár, A. G.; Allen, W. D.; Schaefer, H. F. In Pursuit of the *Ab Initio* Limit for Conformational Energy Prototypes. *J. Chem. Phys.* **1998**, *108*, 9751–9764.

[9] Eyring, H. The Activated Complex in Chemical Reactions. *J. Chem. Phys.* **1935**, *3*, 107–115.

[10] Wigner, E. *Z. physik. Chem.* **1932**, *19*, 203–216.

[11] Eckart, C. The Penetration of a Potential Barrier by Electrons. *Phys. Rev.* **1930**, *35*, 1303–1309.

[12] Johnston, H. S.; Heicklen, J. Tunnelling Corrections for Unsymmetrical Eckart Potential Energy Barriers. *J. Phys. Chem.* **1962**, *66*, 532–533.

[13] Zhang, F.; Dibble, T. S. Impact of Tunneling on Hydrogen-Migration of the *n*-propylperoxy Radical. *Phys. Chem. Chem. Phys.* **2011**, *13*, 17969–17977.

[14] Sirjean, B.; Dames, E.; Wang, H.; Tsang, W. Tunneling in Hydrogen-Transfer Isomerization of *n*-Alkyl Radicals. *J. Phys. Chem. A* **2012**, *116*, 319–332.

[15] Burke, A. D.; Bowman, M. C.; Turney, J. M.; Schaefer, H. F. Energetics and Kinetics of Various Cyano Radical Hydrogen Abstractions. *Phys. Chem. Chem. Phys.* **2021**, *23*, 3389–3400.

[16] Bowman, M. C.; Burke, A. D.; Turney, J. M.; Schaefer, H. F. Conclusive Determination of Ethynyl Radical Hydrogen Abstraction Energetics and Kinetics. *Molecular Physics* **2020**, *118*.

[17] Lahm, M. E.; Kitzmiller, N. L.; Mull, H. F.; Allen, W. D.; Schaefer, H. F. I. Concordant Mode Approach for Molecular Vibrations. *J. Am. Chem. Soc.* **2022**, *144*, 23271–23274.

[18] Kitzmiller, N. L.; Lahm, M. E.; Dornshuld, L. N. O.; Jin, J.; Allen, W. D.; Schaefer III, H. F. Convergent Concordant Mode Approach for Molecular Vibrations: CMA-2. *J. Chem. Theory Comput.* **2024**, *20*, 10886–10898.

[19] Wang, Y.-L.; Li, B.; Sarman, S.; Mocci, F.; Lu, Z.-Y.; Yuan, J.; Laaksonen, A.; Fayer, M. D. Microstructural and Dynamical Heterogeneities in Ionic Liquids. *Chem. Rev.* **2020**, *120*, 5798–5877.

[20] Papageorgiou, N.; Athanassov, Y.; Armand, M.; Bonhote, P.; Pettersson, H.; Azam, A.; Grätzel, M. The Performance and Stability of Ambient Temperature Molten Salts for Solar Cell Applications. *J. Electrochem. Soc.* **1996**, *143*, 3099–3108.

[21] Matsumoto, H.; Matsuda, T.; Tsuda, T.; Hagiwara, R.; Ito, Y.; Miyazaki, Y. The Application of Room Temperature Molten Salt with Low Viscosity to the Electrolyte for Dye-Sensitized Solar Cell. *Chem. Lett.* **2001**, *30*, 26–27.

[22] Doyle, M.; Choi, S. K.; Proulx, G. High-Temperature Proton Conducting Membranes Based on Perfluorinated Ionomer Membrane-Ionic Liquid Composites. *J. Electrochem. Soc.* **2000**, *147*, 34.

[23] Nanjundiah, C.; McDevitt, S. F.; Koch, V. R. Differential Capacitance Measurements in Solvent-Free Ionic Liquids at Hg and C Interfaces. *J. Electrochem. Soc.* **1997**, *144*, 3392–3397.

[24] Carlin, R. T.; Long, H. C. D.; Fuller, J.; Trulove, P. C. Dual Intercalating Molten Electrolyte Batteries. *J. Electrochem. Soc.* **1994**, *141*, L73–L76.

[25] Maiti, A.; Kumar, A.; Rogers, R. D. Water-Clustering in Hygroscopic Ionic Liquids—An Implicit Solvent Analysis. *Phys. Chem. Chem. Phys.* **2012**, *14*, 5139–5146.

[26] Huddleston, J. G.; Visser, A. E.; Reichert, W. M.; Willauer, H. D.; Broker, G. A.; Rogers, R. D. Characterization and Comparison of Hydrophilic and Hydrophobic Room Temperature Ionic Liquids Incorporating the Imidazolium Cation. *Green Chem.* **2001**, *3*, 156–164.

[27] Wang, J.; Tian, Y.; Zhao, Y.; Zhuo, K. A Volumetric and Viscosity Study for the Mixtures of 1-n-butyl-3-methylimidazolium Tetrafluoroborate Ionic Liquid with Acetonitrile, Dichloromethane, 2-butanone and N, N – dimethylformamide. *Green Chem.* **2003**, *5*, 618–622.

[28] Widegren, J. A.; Saurer, E. M.; Marsh, K. N.; Magee, J. W. Electrolytic Conductivity of Four Imidazolium-Based Room-Temperature Ionic Liquids and the Effect of a Water Impurity. *J. Chem. Thermodyn.* **2005**, *37*, 569–575.

[29] Brown, R. A.; Pollet, P.; McKoon, E.; Eckert, C. A.; Liotta, C. L.; Jessop, P. G. Asymmetric Hydrogenation and Catalyst Recycling Using Ionic Liquid and Supercritical Carbon Dioxide. *J. Am. Chem. Soc.* **2001**, *123*, 1254–1255.

[30] Najdanovic-Visak, V.; Esperanca, J. M. S. S.; Rebelo, L. P. N.; Nunes da Ponte, M.; Guedes, H. J. R.; Seddon, K. R.; de Sousa, H. C.; Szydlowski, J. Pressure, Isotope, and Water Co-solvent Effects in Liquid-Liquid Equilibria of (Ionic Liquid + Alcohol) Systems. *J. Phys. Chem. B* **2003**, *107*, 12797–12807.

[31] Widegren, J. A.; Laesecke, A.; Magee, J. W. The Effect of Dissolved Water on the Viscosities of Hydrophobic Room-Temperature Ionic Liquids. *Chem. Commun.* **2005**, 1610–1612.

[32] Gómez, E.; González, B.; Domínguez, A.; Tojo, E.; Tojo, J. Dynamic Viscosities of a Series of 1-alkyl-3-methylimidazolium Chloride Ionic Liquids and Their Binary Mixtures with Water at Several Temperatures. *J. Chem. Eng. Data* **2006**, *51*, 696–701.

[33] Yang, J.-Z.; Tong, J.; Li, J.-B.; Li, J.-G.; Tong, J. Surface Tension of Pure and Water-Containing Ionic Liquid C_5MIBF_4 (1-methyl-3-pentylimidazolium tetrafluoroborate). *J. Collid Interface Sci.* **2007**, *313*, 374–377.

[34] Kanakubo, M.; Umecky, T.; Aizawa, T.; Kurata, Y. Water-induced Acceleration of Transport Properties in Hydrophobic 1-Butyl-3-methylimidazolium Hexafluorophosphate Ionic Liquid. *Chem. Lett.* **2005**, *34*, 324–325.

[35] Cammarata, L.; Kazarian, S. G.; Salter, P. A.; Welton, T. Molecular States of Water in Room Temperature Ionic Liquids. *Phys. Chem. Chem. Phys.* **2001**, *3*, 5192–5200.

[36] Danten, Y.; Cabaço, M. I.; Besnard, M. Interaction of Water Highly Diluted in 1-Alkyl-3-methyl Imidazolium Ionic Liquids with the PF_6^- and BF_4^- Anions. *J. Phys. Chem. A* **2009**, *113*, 2873–2889.

[37] Schenk, J.; Panne, U.; Albrecht, M. Interaction of Levitated Ionic Liquid Droplets with Water. *J. Phys. Chem. B* **2012**, *116*, 14171–14177.

[38] Grabowski, S. J. Hydrogen Bonds with BF_4^- Anion as a Proton Acceptor. *Crystals* **2020**, *10*, 460–473.

[39] Conrad, M. P.; Strauss, H. L. Nearly Free Rotation of Water and Ammonia in Alkanes and Other Weakly Interacting Solvents. *J. Phys. Chem.* **1987**, *91*, 1668–1673.

[40] Backx, P.; Goldman, S. H_2O/D_2O Solubility Isotope Effects. An Estimate of the Extent of Nonclassical Rotational Behavior of Water, when Dissolved in Benzene or Carbon Tetrachloride. *J. Phys. Chem.* **1981**, *85*, 2975–2979.

[41] Śmiechowski, M. Unusual Influence of Fluorinated Anions on the Stretching Vibrations of Liquid Water. *J. Phys. Chem. B* **2018**, *122*, 3141–3152.

[42] Irle, S.; Bowman, J. M. Direct *Ab Initio* Variational Calculation of Vibrational Energies of the $H_2O\cdots Cl^-$ Complex and Resolution of Experimental Differences. *J. Chem. Phys.* **2000**, *113*, 8401–8403.

[43] Xantheas, S. S. Quantitative Description of Hydrogen Bonding in Chloride-Water Clusters. *J. Phys. Chem.* **1996**, *100*, 9703–9713.

[44] Thompson, W. H.; Hynes, J. T. Frequency Shifts in the Hydrogen-Bonded OH Stretch in Halide-Water Clusters. The Importance of Charge Transfer. *J. Am. Chem. Soc.* **2000**, *122*, 6278–6286.

[45] Johnson, M. S.; Kuwata, K. T.; Wong, C.-K.; Okumura, M. Vibrational Spectrum of $I^-(H_2O)$. *Chem. Phys. Lett.* **1996**, *260*, 551–557.

[46] Ayotte, P.; Kelley, J. A.; Nielsen, S. B.; Johnson, M. A. Vibrational Spectroscopy of the $F^-{\cdot}H_2O$ Complex via Argon Predissociation: Photoinduced, Intracluster Proton Transfer? *Chem. Phys. Lett.* **2000**, *316*, 455–459.

[47] Woronowicz, E. A.; Robertson, W. H.; Weddle, G. H.; Johnson, M. A.; Myshakin, E. M.; Jordan, K. D. Infrared Spectroscopic Characterization of the Symmetrical Hydration Motif in the $SO_2{}^-{\cdot}H_2O$ Complex. *J. Phys. Chem. A* **2002**, *106*, 7086–7089.

[48] Zhao, X. G.; Gonzalez-Lafont, A.; Truhlar, D. G.; Steckler, R. Molecular Modeling of Solvation. $Cl^-(D_2O)$. *J. Chem. Phys.* **1991**, *94*, 5544–5558.

[49] Yates, B. F.; Schaefer, H. F.; Lee, T. J.; Rice, J. E. Infrared Spectrum of $F^-{\cdot}H_2O$. *J. Am. Chem. Soc.* **1988**, *110*, 6327–6332.

[50] Bentley, J.; Collins, J. Y.; Chipman, D. M. Dissociation of Ozonide in Water. *J. Phys. Chem. A* **2000**, *104*, 4629–4635.

[51] Robertson, W. H.; Price, E. A.; Weber, J. M.; Shin, J.-W.; Weddle, G. H.; Johnson, M. A. Infrared Signatures of a Water Molecule Attached to Triatomic Domains of Molecular Anions: Evolution of the H-bonding Configuration with Domain Length. *J. Phys. Chem. A* **2003**, *107*, 6527–6532.

[52] Surber, E.; Ananthavel, S. P.; Sanov, A. Nonexistent Electron Affinity of OCS and the Stabilization of Carbonyl Sulfide Anions by Gas Phase Hydration. *J. Chem. Phys.* **2002**, *116*, 1920–1929.

[53] Myshakin, E. M.; Jordan, K. D.; Sibert, E. L.; Johnson, M. A. Large Anharmonic Effects in the Infrared Spectra of the Symmetrical $CH_3NO_2{}^-{\cdot}(H_2O)$ and $CH_3CO_2{}^-{\cdot}(H_2O)$ Complexes. *J. Chem. Phys.* **2003**, *119*, 10138–10145.

[54] Schneider, H.; Vogelhuber, K. M.; Weber, J. M. Infrared Spectroscopy of Anionic Hydrated Fluorobenzenes. *J. Chem. Phys.* **2007**, *127*, 114311.

[55] Kelly, J. T.; Ellington, T. L.; Sexton, T. M.; Fortenberry, R. C.; Tschumper, G. S.; Asmis, K. R. Communication: Gas Phase Vibrational Spectroscopy of the Azide-Water Complex. *J. Chem. Phys.* **2018**, *149*, 191101.

[56] Abdo, Y. A.; Tschumper, G. S. Competition between Solvent–Solvent and Solvent–Solute Interactions in the Microhydration of the Hexafluorophosphate Anion, $PF_6^-(H_2O)_{n=1,2}$. *J. Phys. Chem. A* **2020**, *124*, 8744–8752.

[57] Wang, Y.; Li, H.; Han, S. A Theoretical Investigation of the Interactions between Water Molecules and Ionic Liquids. *J. Phys. Chem. B* **2006**, *110*, 24646–24651.

[58] Del Bene, J. E.; Alkorta, I.; Elguero, J. Microsolvation of the Be-F bond in complexes of BeF_2, BeF_3^-, and BeF_4^{2-} with $n H_2O$, for n = 1-6. *Mol. Phys.* **2021**, *119*, e1933637.

[59] Wong, R. L.; Williams, E. R. Dissociation of $SO_4^{2-}(H_2O)_n$ Clusters, n = 3-17. *J. Phys. Chem. A* **2003**, *107*, 10976–10983.

[60] Lee, C.; Yang, W.; Parr, R. G. Development of the Colle-Salvetti Correlation-Energy Formula into a Functional of the Electron Density. *Phys. Rev. B* **1988**, *37*, 785–789.

[61] Grimme, S.; Antony, J.; Ehrlich, S.; Krieg, H. A Consistent and Accurate *Ab Initio* Parametrization of Density Functional Dispersion Correction (DFT-D) for the 94 Elements H-Pu. *J. Chem. Phys.* **2010**, *132*, 154104.

[62] Zhao, Y.; Truhlar, D. G. The M06 Suite of Density Functionals for Main Group Thermochemistry, Thermochemical Kinetics, Noncovalent Interactions, Excited States, and Transition Elements: Two New Functionals and Systematic Testing of four M06-class Functionals and 12 other Functionals. *Theo. Chem. Acc.* **2008**, *120*, 215–241.

[63] Møller, C.; Plesset, M. S. Note on an Approximation Treatment for Many-Electron Systems. *Phys. Rev.* **1934**, *46*, 618–622.

[64] Frisch, M. J. et al. Gaussian16 Revision C.01. 2016; Gaussian Inc. Wallingford CT.

[65] Matthews, D. A.; Cheng, L.; Harding, M. E.; Lipparini, F.; Stopkowicz, S.; Jagau, T.-C.; Szalay, P. G.; Gauss, J.; Stanton, J. F. Coupled-Cluster Techniques for Computational Chemistry: The CFOUR Program Package. *J. Chem. Phys.* **2020**, *152*, 214108.

[66] Bates, D. M.; Smith, J. R.; Janowski, T.; Tschumper, G. S. Development of a 3-body:Many-body Integrated Fragmentation Method for Weakly Bound Clusters and Application to Water Clusters $(H_2O)_{n=3-10,16,17}$. *J. Chem. Phys.* **2011**, *135*, 044123.

[67] Bates, D. M.; Smith, J. R.; Tschumper, G. S. Efficient and Accurate Methods for the Geometry Optimization of Water Clusters: Application of Analytic Gradients for the 2-body:Many-Body QM:QM Fragmentation Method to $(H_2O)_n$, $n = 3 - 10$. *J. Chem. Theory Comput.* **2011**, *7*, 2753–2760.

[68] Howard, J. C.; Tschumper, G. S. *N*-body:Many-body QM:QM Vibrational Frequencies: Application to Small Hydrogen-Bonded Clusters. *J. Chem. Phys.* **2013**, *139*, 184113.

[69] Howard, J. C.; Tschumper, G. S. Benchmark Structures and Harmonic Vibrational Frequencies Near the CCSD(T) Complete Basis Set Limit for Small Water Clusters: $(H_2O)_{n=2,3,4,5,6}$. *J. Chem. Theory Comput.* **2015**, *11*, 2126–2136.

[70] Hopkins, B. W.; Tschumper, G. S. A Multicentered Approach to Integrated QM/QM Calculations. Applications to Multiply Hydrogen Bonded Systems. *J. Comput. Chem.* **2003**, *24*, 1563–1568.

[71] Hopkins, B. W.; Tschumper, G. S. Multicentred QM/QM Methods for Overlapping Model Systems. *Mol. Phys.* **2005**, *103*, 309–315.

[72] Hopkins, B. W.; Tschumper, G. S. Integrated Quantum Mechanical Approaches for Extended π Systems: Multicentered QM/QM Studies of the Cyanogen and Diacetylene Trimers. *Chem. Phys. Lett.* **2005**, *407*, 362–367.

[73] Tschumper, G. S. Multicentered Integrated QM:QM methods for Weakly Bound Clusters: An Efficient and Accurate 2-body:Many-body Treatment of Hydrogen Bonding and van der Waals Interactions. *Chem. Phys. Lett.* **2006**, *427*, 185–191.

[74] ElSohly, A. M.; Shaw, C. L.; Guice, M. E.; Smith, B. D.; Tschumper, G. S. Analytic Ggradients for the Multicentred Integrated QM:QM Method for Weakly Bound Clusters: Efficient and Accurate 2-body:Many-body Geometry Optimizations. *Mol. Phys.* **2007**, *105*, 2777–2782.

[75] Maseras, F.; Morokuma, K. IMOMM: A New Integrated *Ab Initio* Plus Molecular Mechanics Geometry Optimization Scheme of Equilibrium Structures and Transition-States. *J. Comput. Chem.* **1995**, *16*, 1170–1179.

[76] Chung, L. W.; Hirao, H.; Li, X.; Morokuma, K. The ONIOM Method: Its Foundation and Applications to Metalloenzymes and Photobiology. *WIREs Comput Mol Sci.* **2012**, *2*, 327–350.

[77] Chung, L. W.; Sameera, W. M. C.; Ramozzi, R.; Page, A. J.; Hatanaka, M.; Petrova, G. P.; Harris, T. V.; Li, X.; Ke, Z.; Liu, F.; Li, H.-B.; Ding, L.; Morokuma, K. The ONIOM Method and Its Applications. *Chem. Rev.* **2015**, *115*, 5678–5796.

[78] Hankins, D.; Moskowitz, J. W.; Stillinger, F. H. Water Molecule Interactions. *J. Chem. Phys.* **1970**, *53*, 4544–4554.

[79] Mayhall, N. J.; Raghavachari, K. Molecules-in-Molecules: An Extrapolated Fragment-Based Approach for Accurate Calculations on Large Molecules and Materials. *J. Chem. Theory Comput.* **2011**, *7*, 1336–1343.

[80] Saha, A.; Raghavachari, K. Dimers of Dimers (DOD): A New Fragment-Based Method Applied to Large Water Clusters. *J. Chem. Theory Comput.* **2014**, *10*, 58–67.

[81] Saha, A.; Raghavachari, K. Analysis of Different Fragmentation Strategies on a Variety of Large Peptides: Implementation of a Low Level of Theory in Fragment-Based Methods Can Be a Crucial Factor. *J. Chem. Theory Comput.* **2015**, *11*, 2012–2023.

[82] Jovan Jose, K. V.; Raghavachari, K. Evaluation of Energy Gradients and Infrared Vibrational Spectra through Molecules-in-Molecules Fragment-Based Approach. *J. Chem. Theory Comput.* **2015**, *11*, 950–961.

[83] Jovan Jose, K. V.; Raghavachari, K. Molecules-in-Molecules Fragment-Based Method for the Evaluation of Raman Spectra of Large Molecules. *Mol. Phys.* **2015**, *113*, 3057–3066.

[84] Jovan Jose, K. V.; Beckett, D.; Raghavachari, K. Vibrational Circular Dichroism Spectra for Large Molecules through Molecules-in-Molecules Fragment-Based Approach. *J. Chem. Theory Comput.* **2015**, *11*, 4238–4247.

[85] Jovan Jose, K. V.; Raghavachari, K. Raman Optical Activity Spectra for Large Molecules through Molecules-in-Molecules Fragment-Based Approach. *J. Chem. Theory Comput.* **2016**, *12*, 585–594.

[86] Jovan Jose, K. V.; Raghavachari, K. Fragment-Based Approach for the Evaluation of NMR Chemical Shifts for Large Biomolecules Incorporating the Effects of the Solvent Environment. *J. Chem. Theory Comput.* **2017**, *13*, 1147–1158.

[87] Xantheas, S. S. Ab Initio Studies of Cyclic Water Clusters $(H_2O)_n$, $n = 1 - 6$. II. Analysis of Many-Body Interactions. *J. Chem. Phys.* **1994**, *100*, 7523–7534.

[88] Elrod, M. J.; Saykally, R. J. Many-Body Effects in Intermolecular Forces. *Chem. Rev.* **1994**, *94*, 1975–1997.

[89] Quack, M.; Suhm, M. A. In *Conceptual Perspectives in Quantum Chemistry*; J. -L. Calais,, Kryachko, E. S., Eds.; Kluwer Pub. Co.: Dordrecht, 1997; Vol. III; pp 415–464.

[90] Karpfen, A. Cooperative Effects in Hydrogen Bonding. *Adv. Chem. Phys.* **2002**, *123*, 469–510.

[91] Gordon, M. S.; Fedorov, D. G.; Pruitt, S. R.; Slipchenko, L. V. Fragmentation Methods: A Route to Accurate Calculations on Large Systems. *Chem. Rev.* **2012**, *112*, 632–672.

[92] Collins, M. A.; Bettens, R. P. A. Energy-Based Molecular Fragmentation Methods. *Chem. Rev.* **2015**, *115*, 5607–5642.

[93] Raghavachari, K.; Saha, A. Accurate Composite and Fragment-Based Quantum Chemical Models for Large Molecules. *Chem. Rev.* **2015**, *115*, 5643–5677.

[94] Richard, R. M.; Herbert, J. M. A Generalized Many-Body Expansion and a Unified View of Fragment-Based Methods in Electronic Structure Theory. *J. Chem. Phys.* **2012**, *137*, 064113.

[95] Richard, R. M.; Herbert, J. M. Many-Body Expansion with Overlapping Fragments: Analysis of Two Approaches. *J. Chem. Theory Comput.* **2013**, *9*, 1408–1416.

[96] Richard, R. M.; Lao, K. U.; Herbert, J. M. Aiming for Benchmark Accuracy with the Many-Body Expansion. *Acc. Chem. Res.* **2014**, *47*, 2828–2836.

[97] Mayhall, N. J.; Raghavachari, K. Many-Overlapping-Body (MOB) Expansion: A Generalized Many Body Expansion for Nondisjoint Monomers in Molecular Fragmentation Calculations of Covalent Molecules. *J. Chem. Theory Comput.* **2012**, *8*, 2669–2675.

[98] Day, P. N.; Jensen, J. H.; Gordon, M. S.; Webb, S. P.; Stevens, W. J.; Krauss, M.; Garmer, D.; Cohen, D. An Effective Fragment Method for Modeling Solvent Effects in Quantum Mechanical Calculations. *J. Chem. Phys.* **1996**, *105*, 1968–1986.

[99] Gordon, M. S.; Slipchenko, L.; Li, H.; Jensen, J. H. *Ann. Rep. in Comput. Chem.*; 2007; Vol. 3; pp 177–193.

[100] Pruitt, S. R.; Bertoni, C.; Brorsen, K. R.; Gordon, M. S. Efficient and Accurate Fragmentation Methods. *Acc. Chem. Res.* **2014**, *47*, 2786–2794.

[101] Kitaura, K.; Sawai, T.; Asada, T.; Nakano, T.; Uebayasi, M. Pair Interaction Molecular Orbital Method: An Approximate Computational Method for Molecular Interactions. *Chem. Phys. Lett.* **1999**, *312*, 319–324.

[102] Kitaura, K.; Ikeo, E.; Asada, T.; Nakano, T.; Uebayasi, M. Fragment Molecular Orbital Method: An Approximate Computational Method for Large Molecules. *Chem. Phys. Lett.* **1999**, *313*, 701–706.

[103] Fedorov, D. G.; Asada, N.; Nakanishi, I.; Kitaura, K. The Use of Many-Body Expansions and Geometry Optimizations in Fragment-Based Methods. *Acc. Chem. Res.* **2014**, *47*, 2846–2856.

[104] Gadre, S. R.; Shirsat, R. N.; Limaye, A. C. Molecular Tailoring Approach for Simulation of Electrostatic Properties. *J. Phys. Chem.* **1994**, *98*, 9165–9169.

[105] Sahu, N.; Gadre, S. R. Molecular Tailoring Approach: A Route for *ab Initio* Treatment of Large Clusters. *Acc. Chem. Res.* **2014**, *47*, 2739–2747.

[106] Hirata, S.; Valiev, M.; Dupuis, M.; Xantheas, S. S.; Sugiki, S.; Sekino, H. Fast Electron Correlation Methods for Molecular Clusters in the Ground and Excited States. *Mol. Phys.* **2005**, *103*, 2255–2265.

[107] Kamiya, M.; Hirata, S.; Valiev, M. Fast Electron Correlation Methods for Molecular Clusters Without Basis Set Superposition Errors. *J. Chem. Phys.* **2008**, *128*, 074103.

[108] Hirata, S.; Gilliard, K.; He, X.; Li, J.; Sode, O. Ab Initio Molecular Crystal Structures, Spectra, and Phase Diagrams. *Acc. Chem. Res.* **2014**, *47*, 2721–2730.

[109] Dahlke, E. E.; Truhlar, D. G. Electrostatically Embedded Many-Body Expansion for Large Systems, with Applications to Water Clusters. *J. Chem. Theory Comput.* **2007**, *3*, 46–53.

[110] Dahlke, E. E.; Truhlar, D. G. Electrostatically Embedded Many-Body Correlation Energy, with Applications to the Calculation of Accurate Second-Order Møller-Plesset Perturbation Theory Energies for Large Water Clusters. *J. Chem. Theory Comput.* **2007**, *3*, 1342–1348.

[111] Wang, B.; Yang, K. R.; Xu, X.; Isegawa, M.; Leverentz, H. R.; Truhlar, D. G. Quantum Mechanical Fragment Methods Based on Partitioning Atoms or Partitioning Coordinates. *Acc. Chem. Res.* **2014**, *47*, 2731–2738.

[112] Li, W.; Li, S.; Jiang, Y. Generalized Energy-Based Fragmentation Approach for Computing the Ground-State Energies and Properties of Large Molecules. *J. Phys. Chem. A* **2007**, *111*, 2193–2199.

[113] Hua, W.; Fang, T.; Li, W.; Yu, J.-G.; Li, S. Geometry Optimizations and Vibrational Spectra of Large Molecules from a Generalized Energy-Based Fragmentation Approach. *J. Phys. Chem. A* **2008**, *112*, 10864–10872.

[114] Li, S.; Li, W.; Ma, J. Generalized Energy-Based Fragmentation Approach and Its Applications to Macromolecules and Molecular Aggregates. *Acc. Chem. Res.* **2014**, *47*, 2712–2720.

[115] Beran, G. J. O. Approximating Quantum Many-Body Intermolecular Interactions in Molecular Clusters Using Classical Polarizable Force Fields. *J. Chem. Phys.* **2009**, *130*, 164115.

[116] Beran, G. J. O.; Nanda, K. Predicting Organic Crystal Lattice Energies with Chemical Accuracy. *J. Phys. Chem. Lett.* **2010**, *1*, 3480–3487.

[117] Nanda, K. D.; Beran, G. J. O. Prediction of Organic Molecular Crystal Geometries from MP2-level Fragment Quantum Mechanical/Molecular Mechanical Calculations. *J. Chem. Phys.* **2012**, *137*, 174106.

[118] Guo, W.; Wu, A.; Xu, X. XO: An Extended ONIOM Method for Accurate and Efficient Geometry Optimization of Large Molecules. *Chem. Phys. Lett.* **2010**, *498*, 203–208.

[119] Guo, W.; Wu, A.; Zhang, I. Y.; Xu, X. XO: An Extended ONIOM Method for Accurate and Efficient Modeling of Large Systems. *J. Comput. Chem.* **2012**, *33*, 2142–2160.

[120] Xie, W.; Gao, J. Design of a Next Generation Force Field: The X-POL Potential. *J. Chem. Theory Comput.* **2007**, *3*, 1890–1900.

[121] Wang, Y.; Sosa, C. P.; Cembran, A.; Truhlar, D. G.; Gao, J. Multilevel X-Pol: A Fragment-Based Method with Mixed Quantum Mechanical Representations of Different Fragments. *J. Phys. Chem. B* **2012**, *116*, 6781–6788.

[122] Góra, U.; Podeszwa, R.; Cencek, W.; Szalewicz, K. Interaction Energies of Large Clusters from Many-Body Expansion. *J. Chem. Phys.* **2011**, *135*, 224102.

[123] Kendall, R. A.; Dunning, T. H., Jr.; Harrison, R. J. Electron Affinities of the First-Row Atoms Revisited. Systematic Basis Sets and Wave Functions. *J. Chem. Phys.* **1992**, *96*, 6796–6806.

[124] Del Bene, J. E. Proton Affinities of Ammonia, Water, and Hydrogen Fluoride and their Anions: A Quest for the Basis-Set Limit using the Dunning Augmented Correlation-Consistent Basis Sets. *J. Phys. Chem.* **1993**, *97*, 107–110.

[125] Del Bene, J. E.; Shavitt, I. Basis-Set Effects on Computed Acid-Base Interaction Energies using the Dunning Correlation-Consistent Polarized Split-Valence Basis Sets. *J. Mol. Structure THEOCHEM* **1994**, *307*, 27–34.

[126] Tschumper, G. S.; Leininger, M. L.; Hoffman, B. C.; Valeev, E. F.; Schaefer, H. F.; Quack, M. Anchoring the Water Dimer Potential Energy Surface with Explicitly Correlated Computations and Focal Point Analyses. *J. Chem. Phys.* **2002**, *116*, 690–701.

[127] Anderson, J. A.; Crager, K.; Fedoroff, L.; Tschumper, G. S. Anchoring the Potential Energy Surface of the Cyclic Water Trimer. *J. Chem. Phys.* **2004**, *121*, 11023–11029.

[128] Tschumper, G. S. *Rev. Comput. Chem.*; John Wiley & Sons, Ltd, 2008; Chapter 2, pp 39–90.

[129] Sullivan, M. B.; Iron, M. A.; Redfern, P. C.; Martin, J. M. L.; Curtiss, L. A.; Radom, L. Heats of Formation of Alkali Metal and Alkaline Earth Metal Oxides and Hydroxides: Surprisingly Demanding Targets for High-Level ab Initio Procedures. *J. Phys. Chem. A* **2003**, *107*, 5617–5630.

[130] Bates, D. M.; Anderson, J. A.; Oloyede, P.; Tschumper, G. S. Probing the Effects of Heterogeneity on Delocalized $\pi \cdots \pi$ Interaction Energies. *Phys. Chem. Chem. Phys.* **2008**, *10*, 2775–2779.

[131] ElSohly, A. M.; Tschumper, G. S. Comparison of Polarization Consistent and Correlation Consistent Basis Sets for Noncovalent Interactions. *Int. J. Quantum Chem.* **2009**, *109*, 91–96.

[132] Bates, D. M.; Tschumper, G. S. CCSD(T) Complete Basis Set Limit Relative Energies for Low-Lying Water Hexamer Structures. *J. Phys. Chem. A* **2009**, *113*, 3555–3559.

[133] Marshall, M. S.; Burns, L. A.; Sherrill, C. D. Basis Set Convergence of the Coupled-Cluster Correction, $\delta_{\mathrm{MP2}}^{\mathrm{CCSD(T)}}\delta_{\mathrm{MP2}}^{\mathrm{CCSD(T)}}$: Best Practices for Benchmarking Non-covalent Interactions and the Attendant Revision of the S22, NBC10, HBC6, and HSG Databases. *J. Chem. Phys.* **2011**, *135*, 194102.

[134] Řezáč, J.; Riley, K. E.; Hobza, P. Extensions of the S66 Data Set: More Accurate Interaction Energies and Angular-Displaced Nonequilibrium Geometries. *J. Chem. Theory Comput.* **2011**, *7*, 3466–3470.

[135] Řezáč, J.; Riley, K. E.; Hobza, P. Benchmark Calculations of Noncovalent Interactions of Halogenated Molecules. *J. Chem. Theory Comput.* **2012**, *8*, 4285–4292.

[136] Brauer, B.; Kesharwani, M. K.; Kozuch, S.; Martin, J. M. L. The S66x8 Benchmark for Noncovalent Interactions Revisited: Explicitly Correlated *Ab Initio* Methods and Density Functional Theory. *Phys. Chem. Chem. Phys.* **2016**, *18*, 20905–20925.

[137] Manna, D.; Kesharwani, M. K.; Sylvetsky, N.; Martin, J. M. L. Conventional and Explicitly Correlated ab Initio Benchmark Study on Water Clusters: Revision of the BEGDB and WATER27 Data Sets. *J. Chem. Theory Comput.* **2017**, *13*, 3136–3152.

[138] Kesharwani, M. K.; Manna, D.; Sylvetsky, N.; Martin, J. M. L. The X40×10 Halogen Bonding Benchmark Revisited: Surprising Importance of (n–1)d Subvalence Correlation. *J. Phys. Chem. A* **2018**, *122*, 2184–2197.

[139] Papajak, E.; Truhlar, D. G. Convergent Partially Augmented Basis Sets for Post-Hartree-Fock Calculations of Molecular Properties and Reaction Barrier Heights. *J. Chem. Theory Comput.* **2011**, *7*, 10–18.

[140] Papajak, E.; Zheng, J.; Xu, X.; Leverentz, H. R.; Truhlar, D. G. Perspectives on Basis Sets Beautiful: Seasonal Plantings of Diffuse Basis Functions. *J. Chem. Theory Comput.* **2011**, *7*, 3027–3034.

[141] Liu, B.; McLean, A. D. Accurate Calculation of the Attractive Interaction of Two Ground State Helium Atoms. *J. Chem. Phys.* **1973**, *59*, 4557–4558.

[142] Kestner, N. R. He–He Interaction in the SCF–MO Approximation. *J. Chem. Phys.* **2003**, *48*, 252–257.

[143] Jansen, H.; Ros, P. Non-Empirical Molecular Orbital Calculations on the Protonation of Carbon Monoxide. *Chem. Phys. Lett.* **1969**, *3*, 140–143.

[144] Boys, S.; Bernardi, F. The Calculation of Small Molecular Interactions by the Differences of Separate Total Energies. Some Procedures with Reduced Errors. *Mol. Phys.* **1970**, *19*, 553–566.

[145] Dornshuld, E. V.; Holy, C. M.; Tschumper, G. S. Homogeneous and Heterogeneous Noncovalent Dimers of Formaldehyde and Thioformaldehyde: Structures, Energetics, and Vibrational Frequencies. *J. Phys. Chem. A* **2014**, *118*, 3376–3385, PMID: 24766482.

[146] Weber, J. M.; Kelley, J. A.; Robertson, W. H.; Johnson, M. A. Hydration of a Structured Excess Charge Distribution: Infrared Spectroscopy of the $O_2^-\cdot(H_2O)_n$, ($1\leq n \leq 5$) Clusters. *J. Chem. Phys.* **2001**, *114*, 2698–2706.

[147] Myshakin, E. M.; Jordan, K. D.; Robertson, W. H.; Weddle, G. H.; Johnson, M. A. Dominant Structural Motifs of $NO^-\cdot(H_2O)_n$ Complexes: Infrared Spectroscopic and Ab Initio Studies. *J. Chem. Phys.* **2003**, *118*, 4945–4953.

[148] Robertson, W. H.; Diken, E. G.; Price, E. A.; Shin, J.-W.; Johnson, M. A. Spectroscopic Determination of the OH^- Solvation Shell in the $OH^-\cdot(H_2O)_n$ Clusters. *Science* **2003**, *299*, 1367–1372.

[149] Wang, X.-B.; Kowalski, K.; Wang, L.-S.; Xantheas, S. S. Stepwise Hydration of the Cyanide Anion: A Temperature-Controlled Photoelectron Spectroscopy and Ab Initio Computational Study of $CN^-(H_2O)_n$, $n = 2 - 5$. *J. Chem. Phys.* **2010**, *132*, 124306.

[150] Gorlova, O.; DePalma, J. W.; Wolke, C. T.; Brathwaite, A.; Odbadrakh, T. T.; Jordan, K. D.; McCoy, A. B.; Johnson, M. A. Characterization of the Primary Hydration Shell of the Hydroxide Ion with H_2 Tagging Vibrational Spectroscopy of the $OH^-\cdot(H_2O)_{n=2,3}$ and $OD^-\cdot$ $(D_2O)_{n=2,3}$ Clusters. *J. Chem. Phys.* **2016**, *145*, 134304.

[151] Feyereisen, M. W.; Feller, D.; Dixon, D. A. Hydrogen Bond Energy of the Water Dimer. *J. Phys. Chem.* **1996**, *100*, 2993–2997.

[152] Howard, J. C.; Gray, J. L.; Hardwick, A. J.; Nguyen, L. T.; Tschumper, G. S. Getting down to the Fundamentals of Hydrogen Bonding: Anharmonic Vibrational Frequencies of $(HF)_2$ and $(H_2O)_2$ from Ab Initio Electronic Structure Computations. *J. Chem. Theory Comput.* **2014**, *10*, 5426–5435.

[153] Lindstedt, R. P.; Skevis, G. Chemistry of Acetylene Flames. *Combust. Sci. Technol.* **1997**, *125*, 73–137.

[154] Ceursters, B.; Nguyen, H. M. T.; Nguyen, M. T.; Peeters, J.; Vereecken, L. The Reaction of C_2H Radicals with C_2H_6: Absolute Rate Coefficient Measurements for T = 295–800 K, and Quantum Chemical Study of the Molecular Mechanism. *Phys. Chem. Chem. Phys.* **2001**, *3*, 3070–3074.

[155] Yung, Y. L.; Allen, M.; Pinto, J. P. Photochemistry of the Atmosphere of Titan: Comparison Between Model and Observations. *Astrophys. J., Suppl. Ser.* **1984**, *55*, 465–506.

[156] Gladstone, G. R.; Allen, M.; Yung, Y. L. Hydrocarbon Photochemistry in the Upper Atmosphere of Jupiter. *Icarus* **1996**, *119*, 1–52.

[157] Wootten, A.; Bozyan, E. P.; Garrett, D. B.; Loren, R. B.; Snell, R. L. Detection of C_2H in Cold Dark Clouds. *Astrophys. J.* **1980**, *239*, 844–854.

[158] Glassgold, A. E.; Lucas, R.; Omont, A. Molecular Ions in the Circumstellar Envelope of IRC+10216. *Astron. Astrophys.* **1986**, *157*, 35–48.

[159] Cherchneff, I.; Glassgold, A. E. The Formation of Carbon Chain Molecules in IRC+10216. *Astrophys. J. Lett.* **1993**, *419*, L41–L44.

[160] Beuther, H.; Semenov, D.; Henning, T.; Linz, H. Ethynyl (C_2H) in Massive Star Formation: Tracing the Initial Conditions? *Astrophys. J. Lett.* **2008**, *675*, L33–L36.

[161] Opansky, B. J.; Leone, S. R. Rate Coefficients of C_2H with C_2H_4, C_2H_6, and H_2 from 150 to 359 K. *J. Phys. Chem.* **1996**, *100*, 19904–19910.

[162] Kiefer, J. H.; Von Drasek, W. A. The Mechanism of the Homogeneous Pyrolysis of Acetylene. *Int. J. Chem. Kinet.* **1990**, *22*, 747–786.

[163] Boullart, W.; Devriendt, K.; Borms, R.; Peeters, J. Identification of the Sequence $CH(^2\Pi) + C_2H_2 \rightarrow C_3H_2 + H$ (and $C_3H + H_2$) Followed by $C_3H_2 + O \rightarrow C_2H + HCO$ (or H + CO) as C_2H Source in C_2H_2/O/H Atomic Flames. *J. Phys. Chem.* **1996**, *100*, 998–1007.

[164] Hansen, N.; Klippenstein, S. J.; Westmoreland, P. R.; Kasper, T.; Kohse-Höinghaus, K.; Wang, J.; Cool, T. A Combined *Ab Initio* and Photoionization Mass Spectrometric Study of Polyynes in Fuel-Rich Flames. *Phys. Chem. Chem. Phys.* **2008**, *10*, 366–374.

[165] Sun, Y.-L.; Huang, W.-J.; Lee, S.-H. Formation of Polyynes C_4H_2, C_6H_2, C_8H_2, and $C_{10}H_2$ from Reactions of C_2H, C_4H, C_6H, and C_8H Radicals with C_2H_2. *J. Phys. Chem. Lett.* **2015**, *6*, 4117–4122.

[166] Nguyen, H. M. T.; Chandra, A. K.; Carl, S. A.; Nguyen, M. T. Quantum Chemical Study of Hydrogen Abstraction Reactions of the Ethynyl Radical with Hydrogen Compounds (C_2H + HX). *J. Mol. Struct.: THEOCHEM* **2005**, *732*, 219–224.

[167] Tarr, A. M.; Strausz, O. P.; Gunning, H. E. Reactions of the Ethynyl Radical. Part 1.—Hydrogen abstraction from Alkanes. *Trans. Faraday Soc.* **1965**, *61*, 1946–1959.

[168] Laufer, A. H. Reactions of Ethynyl Radicals. Rate Constants with CH_4, C_2H_6, and C_2D_6. *J. Phys. Chem.* **1981**, *85*, 3828–3831.

[169] Lander, D. R.; Unfried, K. G.; Glass, G. P.; Curl, R. F. Rate Constant Measurements of C_2H with CH_4, C_2H_6, C_2H_4, D_2, and CO. *J. Phys. Chem.* **1990**, *94*, 7759–7763.

[170] Park, J.; Hershberger, J. F. Kinetics of NCO + Hydrocarbon Reactions. *Chem. Phys. Lett.* **1994**, *218*, 537–543.

[171] Dash, M. R.; Rajakumar, B. Abstraction and Addition Kinetics of C_2H Radicals with CH_4, C_2H_6, C_3H_8, C_2H_4, and C_3H_6: CVT/SCT/ISPE and Hybrid Meta-DFT Methods. *Phys. Chem. Chem. Phys.* **2015**, *17*, 3142–3156.

[172] Peeters, J.; Ceursters, B.; Nguyen, H. M. T.; Nguyen, M. T. The Reaction of C_2H with H_2: Absolute Rate Coefficient Measurements and *Ab Initio* Study. *J. Chem. Phys.* **2002**, *116*, 3700–3709.

[173] Peeters, J.; Van Look, H.; Ceursters, B. Absolute Rate Coefficients of the Reactions of C_2H with NO and H_2 between 295 and 440 K. *J. Phys. Chem* **1996**, *100*, 15124–15129.

[174] Van Look, H.; Peeters, J. Rate Coefficients of the Reactions of C_2H with O_2, C_2H_2, and H_2O between 295 and 450 K. *J. Phys. Chem* **1995**, *99*, 16284–16289.

[175] Ceursters, B.; Nguyen, H. M. T.; Peeters, J.; Nguyen, M. T. Experimental and Theoretical Study of the Reaction of the Ethynyl Radical with Acetylene (HCC+HCCH). *Chem. Phys.* **2000**, *262*, 243–252.

[176] Sengupta, D.; Peeters, J.; Nguyen, M. T. Theoretical Studies on C_2H+NO Reactions: Mechanism for HCN+CO and HCO+CN Formation. *Chem. Phys. Lett.* **1998**, *283*, 91–96.

[177] Carl, S. A.; Nguyen, H. M. T.; Nguyen, M. T.; Peeters, J. An Experimental and Theoretical Study of the Reaction of Ethynyl Radicals with Nitrogen Dioxide ($HC{\equiv}C+NO_2$). *J. Chem. Phys.* **2003**, *118*, 10996–11008.

[178] Ceursters, B.; Nguyen, H. M. T.; Peeters, J.; Nguyen, M. T. Experimental and Theoretical Study of the Gas Phase Reaction of Ethynyl Radical with Methane ($HC{\equiv}C{+}CH_4$). *Chem. Phys. Lett.* **2000**, *329*, 412–420.

[179] Carl, S. A.; Elsamra, R. M. I.; Kulkarni, R. M.; Nguyen, H. M. T.; Peeters, J. No Barrier for the Gas-Phase C_2H + NH_3 Reaction. *J. Phys. Chem. A* **2004**, *108*, 3695–3698.

[180] Nguyen, H. M. T.; Carl, S. A.; Peeters, J.; Nguyen, M. T. Theoretical Study of the Reaction of the Ethynyl Radical with Ammonia (C_2H + NH_3): Hydrogen Abstraction *versus* Condensation. *Phys. Chem. Chem. Phys.* **2004**, *6*, 4111–4117.

[181] Sumathi, R.; Peeters, J.; Nguyen, M. T. Theoretical Studies on the $C_2H{+}O_2$ Reaction: Mechanism for HCO+CO, HCCO+O and $CH{+}CO_2$ Formation. *Chem. Phys. Lett.* **1998**, *287*, 109–118.

[182] Chen, H.-T.; Ho, J.-J. Theoretical Study of Reaction Mechanisms for NCX (X = O, S) + C_2H_2. *J. Phys. Chem. A* **2003**, *107*, 7004–7012.

[183] Rim, K. T.; Hershberger, J. F. Temperature Dependence of the Product Branching Ratio of the CN + O_2 Reaction. *J. Phys. Chem. A* **1999**, *103*, 3721–3725.

[184] Coutens, A.; Ligterink, N. F. W.; Loison, J.-C.; Wakelam, V.; Calcutt, H.; Drozdovskaya, M. N.; Jørgensen, J. K.; Müller, H. S. P.; van Dishoeck, E. F.; Wampfler, S. F. The ALMA-PILS Survey: First Setection of Nitrous Acid (HONO) in the Interstellar Medium. *Astron. Astrophys.* **2019**, *623*.

[185] Wang, D.-Q.; Li, J.-L.; Huang, X.-R.; Geng, C.-Y.; Sun, C.-C. Diatomic Radical–Molecule Reactions CN+HONO: Mechanistic Study. *J. Mol. Struct.: THEOCHEM* **2008**, *857*, 20–26.

[186] Jodkowski, J. T.; Rayez, M.-T.; Rayez, J.-C.; Bérces, T.; Dóbé, S. Theoretical Study of the Kinetics of the Hydrogen Abstraction from Methanol. 2. Reaction of Methanol with Chlorine and Bromine Atoms. *J. Phys. Chem. A* **1998**, *102*, 9230–9243.

[187] Tri, T. Q.; Huê, N. T. M. Mechanism of Reaction between Ethynyl Radical with Methanol. *Tap Chi Hoa Hoc* **2011**, *49*, 286–290.

[188] Knizia, G.; Adler, T. B.; Werner, H.-J. Simplified CCSD(T)-F12 Methods: Theory and Benchmarks. *J. Chem. Phys.* **2009**, *130*, 054104.

[189] Peterson, K. A.; Adler, T. B.; Werner, H.-J. Systematically Convergent Basis sets for Explicitly Correlated Wavefunctions: The Atoms H, He, B–Ne, and Al–Ar. *J. Chem. Phys.* **2008**, *128*, 084102.

[190] Hill, J. G.; Peterson, K. A. Correlation Consistent Basis Sets for Explicitly Correlated Wavefunctions: Valence and Core–Valence Basis Sets for Li, Be, Na, and Mg. *Phys. Chem. Chem. Phys.* **2010**, *12*, 10460–10468.

[191] Werner, H.-J.; Knowles, P. J.; Knizia, G.; Manby, F. R.; Schütz, M. Molpro: a General-Purpose Quantum Chemistry Program Package. *WIREs Comput. Mol. Sci.* **2012**, *2*, 242–253.

[192] Smith, D. G. A. et al. PSI4 1.4: Open-Source Software for High-Throughput Quantum Chemistry. *J. Chem. Phys.* **2020**, *152*, 184108.

[193] Bomble, Y. J.; Stanton, J. F.; Kállay, M.; Gauss, J. Coupled-Cluster Methods Including Noniterative Corrections for Quadruple Excitations. *J. Chem. Phys.* **2005**, *123*, 054101.

[194] Woon, D. E.; Dunning, T. H., Jr. Gaussian Basis Sets for Use in Correlated Molecular Calculations. III. The Atoms Aluminum through Argon. *J. Chem. Phys.* **1993**, *98*, 1358–1371.

[195] Bartlett, R. J. Many-Body Perturbation Theory and Coupled Cluster Theory for Electron Correlation in Molecules. *Annu. Rev. Phys. Chem.* **1981**, *32*, 359–401.

[196] Purvis, G. D.; Bartlett, R. J. A Full Coupled-Cluster Singles and Doubles Model: The Inclusion of Disconnected Triples. *J. Chem. Phys.* **1982**, *76*, 1910–1918.

[197] Noga, J.; Bartlett, R. J. The Full CCSDT Model for Molecular Electronic Structure. *J. Chem. Phys.* **1987**, *86*, 7041–7050.

[198] Kállay, M. et al. The MRCC Program System: Accurate Quantum Chemistry from Water to Proteins. *J. Chem. Phys.* **2020**, *152*, 074107.

[199] Feller, D. The Use of Systematic Sequences of Wave Functions for Estimating the Complete Basis Set, Full Configuration Interaction Limit in Water. *J. Chem. Phys.* **1993**, *98*, 7059–7071.

[200] Helgaker, T.; Klopper, W.; Koch, H.; Noga, J. Basis-Set Convergence of Correlated Calculations on Water. *J. Chem. Phys.* **1997**, *106*, 9639–9646.

[201] Cheng, L.; Gauss, J. Analytic Energy Gradients for the Spin-Free Exact Two-Component Theory using an Exact Block Diagonalization for the One-Electron Dirac Hamiltonian. *J. Chem. Phys.* **2011**, *135*, 084114.

[202] Sellers, H.; Pulay, P. The Adiabatic Correction to Molecular Potential Surfaces in the SCF Approximation. *Chem. Phys. Lett.* **1984**, *103*, 463–465.

[203] Handy, N. C.; Yamaguchi, Y.; Schaefer, H. F. The Diagonal Correction to the Born–Oppenheimer Approximation: Its effect on the Singlet–Triplet Splitting of CH_2 and other Molecular Effects. *J. Chem. Phys.* **1986**, *84*, 4481–4484.

[204] Bolman, P. S. H.; Brown, J. M.; Carrington, A.; Kopp, I.; Ramsay, D. A. A Re-Investigation of the $\tilde{A}\ ^2\Sigma^+$ - $\tilde{X}\ ^2\Pi_i$ Band System of NCO. *Proc. R. Soc. Lond. A* **1975**, *343*, 17–44.

[205] Cooper, D. L. Spin–Orbit Coupling Constants for the ^2E States of CH_3O and CH_3F^+. *J. Chem. Phys.* **1982**, *76*, 2765–2766.

[206] Eyring, H. The Activated Complex in Chemical Reactions. *J. Chem. Phys.* **1935**, *3*, 107–115.

[207] Truhlar, D. G.; Garrett, B. C.; Klippenstein, S. J. Current Status of Transition-State Theory. *J. Phys. Chem.* **1996**, *100*, 12771–12800.

[208] Johnston, H. S.; Heicklen, J. Tunnelling Corrections for Unsymmettical Eckart Potential Energy Barriers. *J. Phys. Chem.* **1962**, *66*, 532–533.

[209] Zhang, F.; Dibble, T. S. Impact of Tunneling on Hydrogen-Migration of the *n*-propylperoxy Radical. *Phys. Chem. Chem. Phys.* **2011**, *13*, 17969–17977.

[210] Sirjean, B.; Dames, E.; Wang, H.; Tsang, W. Tunneling in Hydrogen-Transfer Isomerization of *n*-Alkyl Radicals. *J. Phys. Chem. A* **2012**, *116*, 319–332.

[211] Sha, Y.; Dibble, T. S. Tunneling Effect in 1,5 H-Migration of a Prototypical OOQOOH. *Chem. Phys. Lett.* **2016**, *646*, 153–157.

[212] Ruscic, B.; Pinzon, R. E.; Morton, M. L.; von Laszevski, G.; Bittner, S. J.; Nijsure, S. G.; Amin, K. A.; Minkoff, M.; Wagner, A. F. Introduction to Active Thermochemical Tables: Several "Key" Enthalpies of Formation Revisited. *J. Phys. Chem. A* **2004**, *108*, 9979–9997.

[213] Ruscic, B.; Pinzon, R. E.; von Laszewski, G.; Kodeboyina, D.; Burcat, A.; Leahy, D.; Montoy, D.; Wagner, A. F. Active Thermochemical Tables: Thermochemistry for the 21st Century. *J. Phys.: Conf. Ser.* **2005**, *16*, 561–570.

[214] Bartlett, M. A.; Liang, T.; Pu, L.; Schaefer, H. F.; Allen, W. D. The Multichannel *n*-propyl + O2 Reaction Surface: Definitive Theory on a Model Hydrocarbon Oxidation Mechanism. *J. Chem. Phys.* **2018**, *148*.

[215] Meek, G. A.; Levine, B. G. Wave Function Continuity and the Diagonal Born-Oppenheimer Correction at Conical Intersections. *J. Chem. Phys.* **2016**, *144*.

[216] Brønsted, J. N. Acid and Basic Catalysis. *Chem. Rev.* **1928**, *5*, 231–338.

[217] Evans, M. G.; Polanyi, M. Inertia and Driving Force of Chemical Reactions. *Trans. Faraday Soc.* **1938**, *34*, 11–24.

[218] Temelso, B.; Sherrill, C. D.; Merkle, R. C.; Freitas, R. A. High-Level ab Initio Studies of Hydrogen Abstraction from Prototype Hydrocarbon Systems. *J. Phys. Chem. A* **2006**, *110*, 11160–11173.

[219] Chastaing, D.; James, P. L.; Sims, I. R.; Smith, I. W. M. Neutral-Neutral Reactions at the Temperatures of Interstellar Clouds Rate coefficients for Reactions of C_2H Radicals with O_2, C_2H_2, C_2H_4 and C_3H_6 down to 15 K. *Faraday Discuss.* **1998**, *109*, 165–181.

[220] Vakhtin, A. B.; Heard, D. E.; Smith, I. W.; Leone, S. R. Kinetics of C_2H Radical Reactions with Ethene, Propene and 1-butene Measured in a Pulsed Laval Nozzle Apparatus at T = 103 and 296 K. *Chem. Phys. Lett.* **2001**, *348*, 21–26.

[221] Tsuzuki, S.; Honda, K.; Uchimaru, T.; Mikami, M. *Ab initio* Calculations of Structures and Interaction Energies of Toluene Dimers Including CCSD(T) Level Electron Correlation Correction. *J. Chem. Phys.* **2005**, *122*, 144323.

[222] Sinnokrot, M. O.; Sherrill, C. D. Substituent Effects in π-π Interactions: Sandwich and T-Shaped Configurations. *J. Am. Chem. Soc.* **2004**, *126*, 7690–7697.

[223] Tsuzuki, S.; Honda, K.; Uchimaru, T.; Mikami, M.; Tanabe, K. The Magnitude of the CH/π Interaction between Benzene and Some Model Hydrocarbons. *J. Am. Chem. Soc.* **2000**, *122*, 3746–3753.

[224] Hobza, P.; Šponer, J. Structure, Energetics, and Dynamics of the Nucleic Acid Base Pairs: Nonempirical *Ab Initio* Calculations. *Chem. Rev.* **1999**, *99*, 3247–3276.

[225] Jurečka, P.; Šponer, J.; Černý, J.; Hobza, P. Benchmark Database of Accurate (MP2 and CCSD(T) Complete Basis Set Limit) Interaction Energies of Small Model Complexes, DNA Base Pairs, and Amino Acid Pairs. *Phys. Chem. Chem. Phys.* **2006**, *8*, 1985–1993.

[226] Podeszwa, R.; Patkowski, K.; Szalewicz, K. Improved Interaction Energy Benchmarks for Dimers of Biological Relevance. *Phys. Chem. Chem. Phys.* **2010**, *12*, 5974–5979.

[227] Takatani, T.; Hohenstein, E. G.; Malagoli, M.; Marshall, M. S.; Sherrill, C. D. Basis Set Consistent Revision of the S22 Test Set of Noncovalent Interaction Energies. *J. Chem. Phys.* **2010**, *132*, 144104.

[228] Řezáč, J.; Riley, K. E.; Hobza, P. S66: A Well-balanced Database of Benchmark Interaction Energies Relevant to Biomolecular Structures. *J. Chem. Theory Comput.* **2011**, *7*, 2427–2438.

[229] Thanthiriwatte, K. S.; Hohenstein, E. G.; Burns, L. A.; Sherrill, C. D. Assessment of the Performance of DFT and DFT-D Methods for Describing Distance Dependence of Hydrogen-Bonded Interactions. *J. Chem. Theory Comput.* **2011**, *7*, 88–96.

[230] Hobza, P. Calculations on Noncovalent Interactions and Databases of Benchmark Interaction Energies. *Acc. Chem. Res.* **2012**, *45*, 663–672.

[231] Curtiss, L. A.; Raghavachari, K.; Redfern, P. C.; Pople, J. A. Assessment of Gaussian-2 and Density Functional Theories for the Computation of Enthalpies of Formation. *J. Chem. Phys.* **1997**, *106*, 1063–1079.

[232] Allen, W. D.; Császár, A. G. On the Ab Initio Determination of Higher-Order Force Constants at Nonstationary Reference Geometries. *J. Chem. Phys.* **1993**, *98*, 2983–3015.

[233] Pulay, P.; Fogarasi, G.; Pang, F.; Boggs, J. E. Systematic Ab Initio Gradient Calculation of Molecular Geometries, Force Constants, and Dipole Moment Derivatives. *J. Am. Chem. Soc.* **1979**, *101*, 2550–2560.

[234] Fogarasi, G.; Zhou, X.; Taylor, P. W.; Pulay, P. The Calculation of Ab Initio Molecular Geometries: Efficient Optimization by Natural Internal Coordinates and Empirical Correction by Offset Forces. *J. Am. Chem. Soc.* **1992**, *114*, 8191–8201.

[235] Wilson, E. B.; Decius, J. C.; Cross, P. C. *Molecular Vibrations: The Theory of Infrared and Raman Vibrational Spectra*; Courier Corporation, 1980.

Appendix A

Supplementary Information for Project 1

Table A.1: Dissociation energies (D_e in kcal mol^{-1}) of the lowest-energy monohydrate (C_{2v} DI_1) and dihydrate (C_s DI_1WI_1) structures computed with and without the CP procedure with various methods and the haTZ basis set.

	C_{2v} DI_1		C_s DI_1WI_1	
Method	D_e	D_e^{CP}	D_e	D_e^{CP}
CCSD(T)/haTZ	13.17	12.52	26.43	24.95
MP2/haTZ	12.92	12.28	25.93	24.50
B3LYP/haTZ	11.77	11.58	23.31	22.93
B3LYP–B3BJ/haTZ	12.98	12.79	26.32	25.93
M06–2X/haTZ	13.84	13.67	27.69	27.32

Table A.2: Dissociation energies (D_e in kcal mol^{-1}) of the lowest-energy trihydrate (C_3 WI_3) and tetrahydrate (C_1 DI_1WI_3) structures computed with and without the CP procedure with various methods and the haTZ basis set.

	C_3 WI_3		C_1 DI_1WI_3	
Method	D_e	D_e^{CP}	D_e	D_e^{CP}
MP2/haTZ	40.48	38.08	50.27	47.34
B3LYP/haTZ	36.52	35.96	45.18	44.45
B3LYP–B3BJ/haTZ	41.64	41.06	51.44	50.69
M06–2X/haTZ	42.99	42.42	53.36	52.63

Table A.3: Harmonic vibrational frequencies (ω in cm^{-1}) and infrared intensities (IR in km mol^{-1}) for H_2O computed with the haTZ basis set.

	CCSD(T)		MP2		B3LYP		B3LYP–B3BJ		M06–2X	
Irrep	ω	IR	ω	IR	ω	IR	ω	IR	ω	IR
a_1	1648	72.4	1630	73.8	1628	77.3	1628	77.3	1621	83.9
a_1	3814	4.6	3824	7.6	3802	6.0	3802	6.0	3872	11.7
b_2	3924	54.9	3952	75.8	3905	63.3	3905	63.3	3977	83.3

Table A.4: Harmonic vibrational frequencies (ω in cm^{-1}) and infrared intensities (IR in km mol^{-1}) for BF_4^- computed with the haTZ basis set.

	CCSD(T)		MP2		B3LYP		B3LYP–B3BJ		M06–2X	
Irrep	ω	IR	ω	IR	ω	IR	ω	IR	ω	IR
e	346	0.0	344	0.0	341	0.0	341	0.0	348	0.0
t_2	517	0.7	513	2.8	508	2.0	508	2.1	520	4.2
a_1	763	0.0	757	0.0	752	0.0	752	0.0	780	0.0
t_2	1099	431.3	1080	429.3	1051	426.6	1051	426.5	1105	435.1

Table A.5: Harmonic vibrational frequencies (ω in cm^{-1}) and infrared intensities (IR in km mol^{-1}) for the C_{2v} DI_1 monohydrate structure computed with the haTZ basis set.

	CCSD(T)		MP2		B3LYP		B3LYP–B3BJ		M06–2X	
Irrep	ω	IR	ω	IR	ω	IR	ω	IR	ω	IR
b_1	18	2.0	19	0.4	23	0.4	20	0.4	21	0.4
b_2	100	17.9	91	13.1	79	12.0	91	10.5	124	2.6
a_1	168	3.1	164	9.7	157	9.8	166	9.9	182	8.6
b_2	230	69.0	226	70.7	234	70.2	246	71.4	242	81.8
a_2	308	0.0	310	0.0	303	0.0	308	0.0	305	0.0
a_2	350	0.0	349	0.0	344	0.0	345	0.0	350	0.0
a_1	358	1.5	356	1.9	352	1.8	353	2.0	362	2.1
b_1	512	9.4	509	0.1	504	0.1	505	0.1	515	0.2
b_2	518	16.9	515	2.8	509	2.2	509	2.2	522	3.5
a_1	519	23.7	516	5.1	512	3.8	512	3.9	523	7.3
b_1	630	143.5	631	144.2	627	145.5	633	143.4	634	162.1
a_1	763	5.3	757	3.1	751	3.6	752	3.7	779	3.2
b_2	1050	728.0	1038	345.3	1008	341.7	1009	339.5	1058	350.4
a_1	1093	966.4	1082	519.5	1054	516.4	1054	518.0	1102	532.7
b_1	1129	834.8	1118	425.0	1091	423.5	1092	423.6	1141	433.0
a_1	1710	154.5	1691	165.2	1694	177.2	1697	180.4	1693	181.9
a_1	3772	135.6	3770	153.9	3744	146.4	3743	156.1	3820	170.4
b_2	3815	94.9	3825	110.8	3776	102.8	3773	105.7	3852	128.6

Table A.6: CCSD(T)/haTZ harmonic vibrational frequencies (ω in cm^{-1}) and infrared intensities (IR in km mol^{-1}) for the C_{2v} DI_1 monohydrate structure computed analytically and via finite differences of analytic gradients and dipole moments.

	Analytic		Finite Differences	
Irrep	ω	IR	ω	IR
b_1	18	2.0	18	0.4
b_2	100	17.9	100	10.3
a_1	168	3.1	168	9.5
b_2	230	69.0	230	71.1
a_2	308	0.0	308	0.0
a_2	350	0.0	350	0.0
a_1	358	1.5	358	1.9
b_1	512	9.4	512	0.1
b_2	518	16.9	518	3.1
a_1	519	23.7	519	5.6
b_1	630	143.5	630	144.4
a_1	763	5.3	763	3.0
b_2	1050	728.0	1050	343.4
a_1	1093	966.4	1093	514.4
b_1	1129	834.8	1129	421.0
a_1	1710	154.5	1710	165.0
a_1	3772	135.6	3772	136.1
b_2	3815	94.9	3815	93.3

Table A.7: Harmonic vibrational frequencies (ω in cm^{-1}) and infrared intensities (IR in km mol^{-1}) for the C_s BI_1 monohydrate structure computed with the haTZ basis set.

	CCSD(T)		MP2		B3LYP		B3LYP–B3BJ		M06–2X	
Irrep	ω	IR	ω	IR	ω	IR	ω	IR	ω	IR
a″	74i	6.3	68i	6.1	48i	6.5	63i	6.2	85i	4.8
a′	50	2.0	46	2.1	33	1.9	40	2.1	83	0.6
a″	150	25.4	151	31.3	122	52.4	143	38.1	147	7.5
a′	165	8.4	164	8.7	167	9.9	170	9.6	178	7.0
a′	318	64.2	321	60.4	334	34.7	328	46.9	342	63.1
a″	343	1.2	342	1.0	339	0.6	338	0.8	345	2.6
a′	358	9.5	357	12.6	358	28.6	357	20.6	361	24.1
a″	513	0.0	510	0.1	506	0.6	506	0.2	514	5.6
a′	517	1.5	514	1.2	510	0.7	509	0.6	521	2.6
a′	521	9.4	518	9.1	513	7.5	514	8.1	525	10.5
a″	587	105.3	600	101.3	634	94.9	616	97.9	547	125.8
a′	764	1.8	758	2.2	752	4.9	753	3.6	781	1.2
a′	1049	392.7	1036	401.4	1000	439.3	1004	411.4	1065	379.6
a″	1103	421.5	1094	425.9	1072	424.7	1070	424.7	1108	436.0
a′	1129	466.4	1118	467.3	1088	439.7	1090	455.4	1142	499.0
a′	1712	119.9	1694	115.8	1689	100.4	1694	117.5	1695	149.3
a′	3716	245.6	3694	299.6	3602	457.4	3630	381.6	3801	184.0
a′	3859	45.4	3883	56.3	3861	38.4	3852	38.1	3889	73.9

Table A.8: Harmonic vibrational frequencies (ω in cm^{-1}) and infrared intensities (IR in km mol^{-1}) for the C_s DI_2 dihydrate structure computed with the haTZ basis set.

	2b:Mb		CCSD(T)		MP2		B3LYP		B3LYP–B3BJ		M06–2X	
Irrep	ω	IR	ω	IR	ω	IR	ω	IR	ω	IR	ω	IR
a″	20	0.8	20	0.1	20	0.8	22	0.0	20	0.1	22	0.9
a′	20	0.1	20	0.8	20	0.1	23	0.8	21	0.8	22	0.1
a′	74	12.5	74	9.8	68	12.5	56	13.4	68	11.2	91	3.5
a″	100	5.9	100	5.6	88	5.9	65	3.7	87	5.0	134	2.4
a″	158	9.0	158	8.2	155	9.0	148	10.1	155	9.2	171	4.2
a′	160	3.4	160	3.3	157	3.4	150	4.3	158	3.8	175	3.7
a′	215	122.2	216	28.4	213	122.2	220	120.2	230	119.5	214	38.1
a″	216	26.6	216	119.5	215	26.6	223	23.9	231	27.1	224	127.2
a″	278	1.9	278	1.7	278	1.9	269	3.1	277	2.1	260	1.4
a′	291	2.3	291	1.6	291	2.3	283	4.3	290	1.6	277	1.3
a′	355	1.8	355	1.6	353	1.8	348	2.0	350	1.8	356	0.9
a″	361	3.9	361	3.9	358	3.9	354	3.6	356	4.0	365	4.3
a′	510	0.9	510	1.2	507	0.9	503	1.0	503	0.8	512	2.4
a″	518	2.0	518	2.1	515	2.0	510	1.1	511	1.5	521	2.1
a′	520	5.1	520	5.3	517	5.1	512	4.4	512	4.1	524	5.6
a″	585	35.9	585	35.8	587	35.9	584	40.9	588	39.6	580	43.6
a′	602	250.5	602	251.7	604	250.5	601	246.5	605	247.0	601	280.2
a′	763	4.6	763	4.5	757	4.6	752	4.8	752	5.4	779	5.2
a′	1043	343.9	1043	343.4	1033	343.9	1007	335.9	1004	337.1	1049	352.8
a″	1088	497.5	1088	491.9	1076	497.5	1044	496.6	1048	494.3	1100	507.7
a′	1139	447.3	1139	442.0	1129	447.3	1101	452.2	1102	449.9	1153	456.9
a″	1697	220.6	1697	219.9	1679	220.6	1681	232.9	1684	235.6	1676	239.8
a′	1712	96.6	1712	98.4	1694	96.6	1696	103.0	1699	110.8	1693	115.6
a″	3778	123.0	3778	110.4	3774	123.0	3740	93.1	3746	99.0	3828	136.7
a′	3780	166.7	3779	138.3	3776	166.7	3742	212.6	3748	195.4	3830	171.4
a″	3835	59.7	3835	51.2	3848	59.7	3809	63.9	3801	78.9	3873	87.1
a′	3839	126.2	3839	105.9	3853	126.2	3813	85.5	3806	90.7	3879	137.0

Table A.9: Harmonic vibrational frequencies (ω in cm^{-1}) and infrared intensities (IR in km mol^{-1}) for the C_s DI_1WI_1 dihydrate structure computed with the haTZ basis set.

	2b:Mb		CCSD(T)		MP2		B3LYP		B3LYP–B3BJ		M06–2X	
Irrep	ω	IR	ω	IR	ω	IR	ω	IR	ω	IR	ω	IR
a″	38	1.5	39	1.3	39	1.5	42	1.8	42	1.5	33	1.0
a′	49	0.1	49	0.1	50	0.1	56	0.1	56	0.2	40	0.2
a″	99	5.3	99	4.1	90	5.3	75	4.5	88	4.2	129	0.4
a′	119	0.3	118	0.3	114	0.3	102	0.3	114	0.4	134	0.7
a′	169	8.4	169	8.2	166	8.4	160	8.4	172	8.7	180	8.3
a′	184	16.2	184	15.9	180	16.2	172	16.3	181	16.7	202	14.0
a″	243	48.1	243	46.0	242	48.1	249	47.1	259	45.1	239	31.1
a″	338	2.2	338	3.8	338	2.2	334	1.3	336	1.0	337	20.0
a′	358	2.2	357	2.2	355	2.2	350	1.8	352	1.8	360	40.7
a″	369	31.2	369	31.1	371	31.2	370	28.7	375	32.9	363	2.9
a′	437	21.5	436	21.5	438	21.5	434	20.9	445	18.3	426	21.8
a″	502	13.2	501	17.2	503	13.2	492	21.5	499	14.4	483	30.4
a′	516	2.3	516	2.5	513	2.3	508	1.7	509	1.7	520	3.3
a″	520	17.5	520	12.8	518	17.5	509	8.9	513	17.6	523	7.4
a′	523	16.6	523	17.0	520	16.6	516	13.9	517	15.1	527	19.1
a″	673	86.3	674	88.1	681	86.3	674	92.6	686	85.9	663	90.3
a′	686	219.1	686	217.3	689	219.1	683	216.9	694	217.8	689	247.6
a′	764	3.8	764	3.5	758	3.8	753	4.2	753	4.5	781	3.5
a″	1057	343.8	1057	341.6	1045	343.8	1016	341.5	1016	339.3	1066	350.5
a′	1073	409.7	1073	406.8	1062	409.7	1033	409.4	1034	407.8	1084	418.7
a′	1145	524.7	1145	518.8	1135	524.7	1108	520.4	1109	523.2	1157	537.9
a′	1702	110.7	1702	107.8	1684	110.7	1687	107.4	1689	107.2	1677	80.2
a′	1723	143.9	1723	145.7	1705	143.9	1703	169.0	1706	170.3	1697	196.2
a′	3714	246.1	3716	220.2	3706	246.1	3673	242.1	3667	258.6	3764	254.2
a′	3750	40.6	3750	29.4	3746	40.6	3721	26.9	3719	18.4	3793	16.8
a′	3790	322.4	3790	291.6	3795	322.4	3749	323.6	3745	359.2	3830	139.4
a″	3796	120.7	3795	103.6	3803	120.7	3757	112.9	3752	116.4	3830	388.7

Table A.10: Harmonic vibrational frequencies (ω in cm^{-1}) and infrared intensities (IR in km mol^{-1}) for the D_{2d} DI_2 dihydrate structure computed with the haTZ basis set.

	2b:Mb		CCSD(T)		MP2		B3LYP		B3LYP–B3BJ		M06–2X	
Irrep	ω	IR	ω	IR	ω	IR	ω	IR	ω	IR	ω	IR
e	16	0.9	16	0.8	16	0.9	19	1.0	17	1.0	17	0.9
e	16	0.9	16	0.8	16	0.9	19	1.0	17	1.0	17	0.9
e	97	11.4	97	8.9	89	11.4	76	10.7	88	9.3	122	1.2
e	97	11.4	97	8.9	89	11.4	76	10.7	88	9.3	122	1.2
a_1	145	0.0	145	0.0	142	0.0	135	0.0	143	0.0	158	0.0
b_2	176	21.3	176	21.0	172	21.3	163	21.4	173	22.0	195	19.7
e	219	71.7	219	71.7	216	71.7	221	70.5	233	71.7	235	82.1
e	219	71.7	219	71.7	216	71.7	221	70.5	233	71.7	235	82.1
b1	293	0.0	294	0.0	295	0.0	288	0.0	291	0.0	293	0.0
a2	301	0.0	301	0.0	304	0.0	296	0.0	300	0.0	300	0.0
b1	350	0.0	350	0.0	349	0.0	344	0.0	345	0.0	351	0.0
a_1	367	0.0	368	0.0	365	0.0	360	0.0	362	0.0	373	0.0
e	514	0.0	514	0.0	511	0.0	506	0.0	506	0.0	517	0.1
e	514	0.0	514	0.0	511	0.0	506	0.0	506	0.0	517	0.1
b_2	523	8.0	523	8.6	520	8.0	516	6.0	516	6.3	527	11.4
e	601	147.1	601	147.0	602	147.1	597	148.9	603	146.9	607	163.9
e	601	147.1	601	147.0	602	147.1	597	148.9	603	146.9	607	163.9
a_1	765	0.0	765	0.0	759	0.0	753	0.0	754	0.0	782	0.0
e	1088	346.7	1088	344.3	1077	346.7	1048	344.7	1049	342.7	1098	353.0
e	1088	346.7	1088	344.3	1077	346.7	1048	344.7	1049	342.7	1098	353.0
b_2	1094	623.9	1094	617.4	1083	623.9	1055	621.9	1056	625.8	1103	646.5
b_2	1703	324.0	1703	324.3	1684	324.0	1687	348.9	1689	355.3	1685	358.9
a_1	1709	0.0	1709	0.0	1691	0.0	1693	0.0	1696	0.0	1692	0.0
b_2	3781	271.9	3780	239.6	3779	271.9	3754	256.1	3753	273.4	3828	308.0
a_1	3782	0.0	3782	0.0	3780	0.0	3756	0.0	3755	0.0	3829	0.0
e	3831	103.3	3830	86.3	3842	103.3	3794	95.0	3792	97.4	3868	120.6
e	3831	103.3	3830	86.3	3842	103.3	3794	95.0	3792	97.4	3868	120.6

Table A.11: Harmonic vibrational frequencies (ω in cm^{-1}) and infrared intensities (IR in km mol^{-1}) for the C_s DI_1BI_1 dihydrate structure computed with the haTZ basis set.

	2b:Mb		CCSD(T)		MP2		B3LYP		B3LYP–B3BJ		M06–2X	
Irrep	ω	IR	ω	IR	ω	IR	ω	IR	ω	IR	ω	IR
a″	77i	6.6	78i	6.9	71i	6.6	48i	6.7	65i	6.6	93i	5.0
a″	18	0.3	18	0.3	18	0.3	21	0.0	18	0.2	22	0.7
a′	42	1.9	42	1.8	38	1.9	28	1.4	34	1.7	62	0.9
a′	89	11.5	89	9.9	80	11.5	59	9.4	77	9.8	122	3.2
a″	136	27.3	136	21.1	138	27.3	114	52.5	133	34.7	129	4.0
a′	152	5.9	152	4.6	148	5.9	141	7.9	152	8.0	167	0.5
a′	160	4.5	160	5.7	157	4.5	162	1.3	161	1.8	175	8.3
a′	219	74.3	219	72.6	219	74.3	239	77.5	238	76.0	228	79.3
a″	286	3.0	286	1.7	286	3.0	269	10.5	283	3.2	276	0.1
a′	297	67.5	297	70.2	299	67.5	321	49.8	309	59.1	309	86.7
a″	344	0.5	344	0.9	343	0.5	338	0.0	339	0.3	344	3.8
a′	365	11.4	365	10.2	363	11.4	360	16.3	361	13.7	369	9.4
a″	506	6.7	506	13.3	504	6.7	502	1.2	501	2.9	493	92.5
a′	519	2.3	519	2.5	516	2.3	510	1.9	511	1.5	518	19.2
a′	523	9.7	523	10.2	520	9.7	515	7.2	515	8.4	523	3.1
a″	540	68.2	539	68.4	550	68.2	585	8.9	565	58.2	527	12.6
a″	596	176.5	596	174.1	598	176.5	600	227.7	600	187.2	594	187.0
a′	763	5.3	763	4.9	757	5.3	751	7.6	752	7.4	780	4.5
a′	1032	373.9	1032	367.7	1020	373.9	986	400.7	987	377.3	1046	361.2
a′	1111	493.4	1111	491.2	1100	493.4	1068	474.3	1072	484.1	1125	525.2
a″	1136	417.7	1136	413.5	1127	417.7	1106	418.2	1104	417.5	1143	428.8
a′	1699	193.2	1699	201.7	1681	193.2	1682	128.2	1684	183.3	1680	254.3
a′	1711	85.8	1711	83.1	1692	85.8	1691	131.7	1696	111.8	1693	79.2
a′	3751	245.6	3751	197.4	3736	245.6	3648	397.7	3680	320.3	3823	196.3
a′	3778	150.5	3777	124.4	3772	150.5	3719	201.0	3739	163.2	3829	113.3
a′	3838	87.0	3837	74.7	3852	87.0	3825	57.1	3809	73.5	3873	103.9
a′	3863	68.6	3863	57.2	3886	68.6	3862	47.0	3853	46.8	3897	89.6

Table A.12: Harmonic vibrational frequencies (ω in cm^{-1}) and infrared intensities (IR in km mol^{-1}) for the C_s DI_1WW_1 dihydrate structure computed with the haTZ basis set.

	B3LYP	
Irrep	ω	IR
a′	13	1.0
a″	30	0.3
a′	31	0.9
a″	104	13.4
a′	148	16.4
a″	154	84.8
a′	249	6.7
a″	267	49.9
a″	337	0.1
a′	358	3.4
a′	402	49.0
a″	411	2.9
a′	505	0.6
a″	509	1.9
a′	513	4.6
a′	713	149.5
a′	750	7.3
a″	812	92.8
a″	993	325.6
a′	1055	541.3
a′	1107	422.9
a′	1675	204.7
a′	1700	87.2
a′	3460	820.2
a′	3709	209.2
a″	3726	138.9
a′	3865	36.7

Table A.13: Harmonic vibrational frequencies (ω in cm^{-1}) and infrared intensities (IR in km mol^{-1}) for the C_{3v} DI_3 trihydrate structure computed with the haTZ basis set.

	2b:Mb		MP2		B3LYP		B3LYP–B3BJ		M06–2X	
Irrep	ω	IR	ω	IR	ω	IR	ω	IR	ω	IR
a_1	20	1.6	20	1.6	22	1.5	20	1.7	22	0.1
e	21	0.0	21	0.0	24	0.0	21	0.0	22	0.0
e	21	0.0	21	0.0	24	0.0	21	0.0	22	1.8
e	67	12.5	61	12.5	51	0.0	62	10.3	79	2.9
e	67	12.5	61	12.5	52	12.5	62	10.3	79	2.9
a_2	95	0.0	76	0.0	52	12.5	83	0.0	143	0.0
a_1	148	1.0	144	1.0	135	1.0	146	1.2	161	0.8
e	149	0.1	144	0.1	135	1.0	146	1.2	164	0.5
e	149	0.1	144	0.1	136	1.3	146	1.2	164	0.4
e	199	117.6	193	117.6	200	115.0	214	115.6	192	0.0
e	199	117.6	193	117.6	200	115.0	214	115.6	210	125.7
a_2	199	0.0	198	0.0	203	0.0	214	0.0	210	125.8
a_2	258	0.0	257	0.0	251	0.0	257	0.0	251	0.0
e	271	1.5	271	1.5	266	0.9	271	1.5	268	3.7
e	271	1.5	271	1.5	266	0.9	271	1.5	268	3.7
e	361	4.9	358	4.9	353	4.5	356	5.2	364	4.7
e	361	4.9	358	4.9	353	4.5	356	5.2	364	4.7
a_1	506	11.7	504	11.7	501	10.4	501	8.3	508	18.0
e	516	0.7	514	0.7	509	0.3	510	0.6	519	0.5
e	516	0.7	514	0.7	509	0.3	510	0.6	519	0.5
e	550	25.2	550	25.2	546	29.9	552	28.9	553	27.0
e	550	25.2	550	25.2	546	29.9	552	28.9	553	27.0
a_1	573	382.0	574	382.0	571	380.2	578	376.5	579	422.0
a_1	763	6.5	757	6.5	751	7.2	752	7.7	779	6.9
e	1056	412.0	1046	412.0	1016	407.2	1017	405.9	1064	423.7
e	1056	412.0	1046	412.0	1016	407.2	1017	405.9	1065	422.8
a_1	1155	450.6	1145	450.6	1118	455.8	1120	456.0	1169	462.6
e	1692	217.3	1674	217.3	1676	226.7	1679	232.8	1671	245.4
e	1692	217.3	1674	217.3	1676	226.7	1679	232.8	1671	244.8
a_1	1713	39.3	1695	39.3	1697	51.0	1700	51.3	1694	40.7
e	3791	156.9	3792	156.9	3767	143.0	3767	156.0	3839	187.1
e	3791	156.9	3792	156.9	3767	143.0	3767	156.0	3839	186.7
a_1	3794	31.2	3795	31.2	3770	34.0	3770	36.4	3843	33.7
a_2	3846	0.0	3859	0.0	3813	0.0	3810	0.0	3884	0.0
e	3852	140.7	3866	140.7	3819	125.9	3817	128.7	3891	158.9
e	3852	140.7	3866	140.7	3819	125.9	3817	128.7	3891	158.9

Table A.14: Harmonic vibrational frequencies (ω in cm^{-1}) and infrared intensities (IR in km mol^{-1}) for the C_s DI_2WI_1 trihydrate structure computed with the haTZ basis set.

	2b:Mb		MP2		B3LYP		B3LYP–B3BJ		M06–2X	
Irrep	ω	IR	ω	IR	ω	IR	ω	IR	ω	IR
a″	15	0.2	15	0.2	18	0.2	16	0.3	14	0.2
a′	38	1.1	38	1.1	37	2.8	40	1.5	33	0.6
a″	38	2.1	39	2.1	42	2.9	42	2.1	35	1.3
a′	82	6.5	76	6.5	66	5.8	78	5.5	94	1.6
a″	97	4.9	88	4.9	71	4.3	85	3.9	124	0.6
a′	115	4.7	107	4.7	90	1.6	107	3.2	138	3.2
a′	148	0.6	145	0.6	139	0.8	146	0.8	158	0.6
a′	168	3.4	165	3.4	160	4.5	172	4.4	182	7.4
a′	183	22.6	178	22.6	170	23.4	180	23.5	201	16.1
a′	213	76.9	213	76.9	224	74.6	229	76.5	220	86.5
a″	232	47.6	230	47.6	235	44.0	246	43.6	229	42.4
a″	277	6.5	276	6.5	264	13.7	275	6.9	273	0.4
a″	336	6.1	336	6.1	332	3.9	334	3.4	318	35.9
a′	362	0.5	362	0.5	357	0.5	360	0.3	350	12.0
a″	365	24.5	363	24.5	361	20.9	366	26.5	372	0.6
a′	423	21.0	423	21.0	419	20.6	431	18.0	418	20.6
a″	468	30.9	469	30.9	456	33.7	465	32.5	450	31.7
a″	512	0.1	509	0.1	504	0.2	505	0.1	515	2.0
a′	518	2.7	515	2.7	510	2.3	511	2.1	522	3.3
a′	525	18.0	522	18.0	518	14.0	519	15.5	529	22.9
a″	572	145.6	574	145.6	571	142.7	574	146.9	571	163.2
a′	664	233.2	666	233.2	662	231.5	672	232.2	656	94.5
a″	667	85.7	675	85.7	669	92.8	681	86.3	662	261.5
a′	765	0.3	760	0.3	754	0.3	755	0.4	782	0.4
a′	1067	404.2	1057	404.2	1031	400.8	1029	402.9	1074	418.8
a″	1091	342.1	1080	342.1	1050	341.1	1052	338.8	1101	349.4
a′	1116	540.9	1104	540.9	1074	540.6	1078	538.7	1127	558.0
a′	1698	254.7	1679	254.7	1682	291.6	1684	286.1	1673	76.2
a′	1700	22.4	1682	22.4	1684	2.1	1686	16.2	1679	238.8
a′	1719	124.8	1701	124.8	1700	137.9	1703	138.7	1695	131.6
a′	3717	226.2	3708	226.2	3671	235.4	3666	250.7	3768	225.8
a′	3761	69.4	3758	69.4	3733	84.9	3732	69.0	3806	60.1
a′	3783	150.1	3778	150.1	3740	153.7	3750	155.9	3834	178.0
a′	3807	276.4	3815	276.4	3772	250.3	3768	278.1	3845	131.9
a″	3811	114.1	3819	114.1	3773	106.3	3769	109.3	3850	316.6
a′	3850	82.8	3865	82.8	3828	61.2	3819	69.4	3886	100.0

Table A.15: Harmonic vibrational frequencies (ω in cm^{-1}) and infrared intensities (IR in km mol^{-1}) for the C_3 WI_3 trihydrate structure computed with the haTZ basis set.

	2b:Mb		MP2		B3LYP		B3LYP–B3BJ		M06–2X	
Irrep	ω	IR	ω	IR	ω	IR	ω	IR	ω	IR
a	34	0.1	36	0.1	42	0.1	40	0.1	34	0.1
e	48	0.1	49	0.1	58	0.0	57	0.1	38	0.1
e	48	0.1	49	0.1	58	0.0	57	0.1	38	0.1
e	136	0.9	131	0.9	120	0.7	132	0.7	151	2.1
e	136	0.9	131	0.9	120	0.7	132	0.7	151	2.1
a	167	11.0	163	11.0	154	11.1	166	12.6	174	11.6
e	172	18.9	169	18.9	163	18.8	174	19.6	177	16.1
e	172	18.9	169	18.9	163	18.8	174	19.6	178	16.1
a	196	7.9	192	7.9	185	7.6	199	6.8	215	6.2
e	351	0.1	349	0.1	345	0.1	347	0.1	354	0.0
e	351	0.1	349	0.1	345	0.1	347	0.1	354	0.0
e	441	4.3	445	4.3	443	5.4	452	4.4	414	1.8
e	441	4.3	445	4.3	443	5.4	452	4.4	414	1.9
a	475	19.0	477	19.0	476	16.1	484	10.2	457	30.3
e	519	2.7	516	2.7	510	2.4	511	2.1	524	0.7
e	519	2.7	516	2.7	510	2.4	511	2.1	524	0.7
a	528	38.3	526	38.3	521	33.1	525	37.5	530	35.1
e	547	62.3	554	62.3	550	49.1	566	45.0	533	63.7
e	547	62.3	554	62.3	550	49.0	566	45.0	533	63.7
a	671	21.5	676	21.5	668	21.6	678	21.9	645	23.6
e	672	304.0	676	304.0	672	314.7	685	319.0	653	348.0
e	672	304.0	676	304.0	672	314.7	685	319.0	653	348.1
a	767	6.2	761	6.2	755	7.3	756	7.3	784	4.0
a	895	2.6	907	2.6	900	4.4	923	4.4	890	0.2
e	1060	378.3	1049	378.3	1019	379.2	1020	376.6	1072	378.0
e	1060	378.3	1049	378.3	1019	379.2	1020	376.6	1072	376.9
a	1158	527.6	1147	527.6	1120	521.4	1122	524.4	1171	548.4
e	1707	59.1	1690	59.1	1687	63.2	1689	63.0	1667	72.4
e	1707	59.1	1690	59.1	1687	63.2	1689	63.0	1667	72.3
a	1730	100.0	1714	100.0	1711	112.0	1714	110.1	1698	110.0
a	3635	74.2	3618	74.2	3589	34.6	3575	27.5	3691	58.9
e	3683	180.9	3671	180.9	3640	242.3	3631	283.1	3736	153.2
e	3683	180.9	3671	180.9	3640	242.3	3631	283.1	3736	153.3
e	3738	196.7	3737	196.7	3688	142.9	3681	131.7	3785	232.7
e	3738	196.7	3737	196.7	3688	142.9	3681	131.7	3785	232.6
a	3754	781.8	3753	781.8	3707	806.4	3702	862.7	3801	757.0

Table A.16: Harmonic vibrational frequencies (ω in cm^{-1}) and infrared intensities (IR in km mol^{-1}) for the C_s DI_2W_1 trihydrate structure computed with the haTZ basis set.

	2b:Mb		MP2		B3LYP		B3LYP–B3BJ		M06–2X	
Irrep	ω	IR	ω	IR	ω	IR	ω	IR	ω	IR
a″	21	1.4	7	1.4	30	2.4	25	0.8	19	0.5
a″	41	0.1	41	0.1	35	0.6	43	6.2	41	3.8
a′	53	7.3	41	7.3	43	7.2	51	0.3	50	0.5
a′	61	0.3	54	0.3	57	0.1	56	0.4	112	1.4
a′	90	16.0	79	16.0	67	7.2	83	10.8	121	2.8
a″	128	0.1	125	0.1	120	0.1	129	0.1	132	0.0
a′	162	17.4	159	17.4	153	15.4	164	17.8	173	14.4
a″	176	13.7	173	13.7	167	14.8	176	13.6	177	6.8
a″	189	5.5	191	5.5	187	2.7	200	1.8	189	11.1
a′	199	1.3	196	1.3	215	48.8	212	6.7	207	87.6
a′	204	86.0	203	86.0	255	49.9	224	85.3	218	4.6
a″	308	8.5	308	8.5	293	38.7	317	7.7	269	5.6
a′	342	7.9	341	7.9	337	7.0	339	5.6	340	17.1
a″	364	3.5	362	3.5	356	11.4	360	3.9	366	15.5
a′	371	29.6	371	29.6	362	15.4	374	35.7	368	2.1
a″	473	2.5	480	2.5	484	4.7	488	0.7	447	4.4
a′	513	0.8	510	0.8	505	0.5	506	0.5	517	1.4
a″	517	2.0	514	2.0	510	2.4	510	1.5	521	1.0
a′	521	7.1	518	7.1	514	6.4	514	6.3	524	7.4
a″	618	166.9	626	166.9	622	86.0	632	136.7	590	126.3
a″	643	136.6	651	136.6	652	210.7	658	160.2	617	204.7
a′	664	64.5	667	64.5	672	43.5	670	65.7	662	85.5
a′	705	156.1	713	156.1	710	153.0	717	155.6	708	185.8
a′	763	6.4	757	6.4	752	6.2	752	7.7	779	7.4
a′	1035	324.6	1027	324.6	1002	334.3	998	316.7	1039	337.7
a″	1082	441.4	1069	441.4	1038	433.2	1040	440.2	1095	449.7
a′	1155	521.4	1144	521.4	1118	522.2	1119	522.7	1167	536.3
a″	1688	78.5	1670	78.5	1675	74.1	1676	87.3	1665	78.8
a′	1708	276.2	1690	276.2	1690	269.8	1695	323.1	1688	369.3
a′	1721	28.8	1703	28.8	1698	28.7	1702	5.0	1697	2.9
a′	3685	324.6	3672	324.6	3636	493.4	3634	338.7	3740	342.0
a″	3739	73.8	3731	73.8	3646	81.1	3677	235.1	3779	161.7
a′	3766	258.2	3755	258.2	3697	326.4	3723	300.6	3816	250.4
a″	3774	281.4	3768	281.4	3743	190.7	3724	136.3	3819	175.8
a″	3821	54.3	3835	54.3	3779	101.8	3794	63.4	3855	84.0
a′	3828	137.6	3841	137.6	3839	48.1	3800	106.3	3865	168.5

Table A.17: Harmonic vibrational frequencies (ω in cm^{-1}) and infrared intensities (IR in km mol^{-1}) for the C_1 DI_2WW_1 trihydrate structure computed with the haTZ basis set.

	B3LYP		M06–2X	
Irrep	ω	IR	ω	IR
a	12	1.1	9	1.2
a	19	0.1	19	0.2
a	31	0.7	27	0.5
a	32	1.1	36	0.8
a	51	9.3	97	4.3
a	91	5.4	140	1.7
a	139	17.7	153	11.2
a	146	34.8	169	2.1
a	149	55.1	180	89.1
a	223	74.4	207	69.1
a	240	24.3	233	66.2
a	248	28.2	250	6.5
a	265	12.7	265	3.5
a	342	1.2	341	3.7
a	357	5.1	360	20.0
a	385	5.1	370	8.7
a	396	48.8	372	26.8
a	503	0.4	512	1.2
a	511	2.0	522	3.0
a	513	4.4	525	5.9
a	581	125.8	577	140.3
a	674	163.2	658	198.2
a	751	7.6	763	112.6
a	789	94.8	779	7.3
a	998	326.4	1041	347.6
a	1044	506.8	1100	510.5
a	1111	467.1	1163	475.0
a	1669	249.2	1665	259.7
a	1683	115.4	1677	109.9
a	1698	69.9	1693	97.7
a	3493	759.1	3607	704.4
a	3710	182.6	3802	186.7
a	3732	185.9	3830	161.1
a	3771	115.1	3840	137.4
a	3828	59.5	3885	105.8
a	3866	39.9	3934	54.1

Table A.18: Harmonic vibrational frequencies (ω in cm^{-1}) and infrared intensities (IR in km mol^{-1}) for the C_s DI_4 tetrahydrate structure computed with the haTZ basis set.

	2b:Mb		MP2		B3LYP		B3LYP–B3BJ		M06–2X	
Irrep	ω	IR	ω	IR	ω	IR	ω	IR	ω	IR
a″	4i	0.1	3i	0.1	25i	2.3	8	0.0	2i	0.1
a″	18	0.0	18	0.0	16	0.3	19	0.1	17	0.0
a′	22	0.2	21	0.2	20	0.1	21	0.5	22	1.9
a″	22	1.8	22	1.8	23	0.3	22	1.8	23	0.8
a′	55	6.6	32	6.6	24	1.6	49	8.2	70	4.1
a′	56	16.5	49	16.5	34	2.4	49	9.4	76	5.9
a′	62	3.8	51	3.8	40	14.5	54	6.7	100	3.4
a″	72	9.0	61	9.0	47	14.2	64	4.4	114	0.2
a′	135	3.0	130	3.0	123	0.4	132	0.9	147	1.6
a″	138	0.1	134	0.1	124	0.0	136	0.2	150	3.4
a′	143	2.1	140	2.1	131	2.2	141	2.1	152	1.5
a′	156	1.0	153	1.0	148	7.0	155	4.2	161	0.0
a″	176	115.8	173	115.8	158	30.9	186	5.3	167	3.0
a′	177	34.9	175	34.9	181	113.1	193	110.6	175	5.2
a″	186	13.9	181	13.9	184	40.4	194	22.1	183	70.0
a″	193	62.6	189	62.6	190	66.5	204	84.4	185	101.0
a″	202	76.4	213	76.4	230	2.0	220	79.8	201	137.3
a′	248	3.9	245	3.9	245	6.1	245	1.7	228	3.7
a″	249	5.7	249	5.7	252	4.6	248	5.3	252	1.0
a′	259	6.9	258	6.9	258	66.7	258	7.1	257	8.3
a″	360	6.3	357	6.3	350	6.2	354	6.3	363	4.5
a′	366	2.4	363	2.4	358	1.4	361	2.3	369	3.1
a″	501	9.7	503	9.7	501	9.5	502	23.9	488	1.8
a′	506	33.0	505	33.0	502	32.0	503	9.2	503	29.5
a′	507	4.1	507	4.1	504	4.6	507	2.8	508	42.4
a″	511	1.5	511	1.5	513	2.0	510	0.0	511	27.4
a′	532	30.7	530	30.7	525	34.8	528	34.4	534	32.9
a′	553	329.2	554	329.2	550	338.5	555	188.9	553	204.4
a″	554	183.1	557	183.1	557	162.2	555	334.6	554	334.6
a′	765	2.0	759	2.0	755	1.6	755	2.4	781	3.0
a′	1059	405.1	1052	405.1	1031	392.7	1024	398.4	1062	423.3
a″	1082	404.8	1071	404.8	1042	405.2	1044	402.0	1093	413.7
a′	1123	491.8	1110	491.8	1076	513.3	1084	497.4	1138	500.2
a′	1686	120.8	1668	120.8	1670	131.3	1672	123.1	1662	127.9
a″	1687	178.1	1669	178.1	1672	195.6	1674	192.7	1664	194.9
a′	1693	260.4	1674	260.4	1675	244.0	1678	293.3	1670	309.7
a′	1712	19.2	1694	19.2	1694	27.2	1699	25.5	1693	30.4
a′	3781	162.9	3769	162.9	3708	247.8	3740	168.7	3838	128.6
a″	3796	184.0	3797	184.0	3773	81.7	3772	81.9	3846	187.7
a′	3797	89.3	3797	89.3	3773	166.1	3772	193.4	3848	102.3
a′	3800	42.0	3800	42.0	3776	38.2	3776	42.1	3851	83.4
a″	3859	23.6	3873	23.6	3827	14.0	3826	24.9	3899	35.0
a″	3864	98.7	3880	98.7	3832	102.7	3832	94.8	3906	46.9
a′	3865	90.1	3881	90.1	3834	104.9	3835	90.3	3907	113.6
a′	3870	109.7	3891	109.7	3861	56.6	3848	71.4	3913	177.9

Table A.19: Harmonic vibrational frequencies (ω in cm^{-1}) and infrared intensities (IR in km mol^{-1}) for the C_s DI_3WI_1 tetrahydrate structure computed with the haTZ basis set.

	2b:Mb		MP2		B3LYP		B3LYP–B3BJ		M06–2X	
Irrep	ω	IR	ω	IR	ω	IR	ω	IR	ω	IR
a″	15	1.1	16	1.1	17	0.9	15	1.0	18	1.6
a′	18	1.7	18	1.7	21	1.7	18	1.7	20	1.9
a′	32	2.0	32	2.0	31	3.9	33	2.3	27	0.4
a′	40	2.2	40	2.2	39	6.6	42	2.8	28	0.2
a″	65	5.1	59	5.1	44	1.5	59	3.3	80	0.6
a″	69	12.3	64	12.3	53	1.6	67	9.2	81	3.5
a′	95	0.6	77	0.6	59	8.1	79	0.6	124	0.7
a″	110	1.0	105	1.0	91	0.8	104	0.8	145	2.3
a′	144	0.5	139	0.5	128	1.3	140	1.3	156	1.4
a′	144	0.9	139	0.9	130	1.4	141	1.4	157	1.1
a″	162	1.2	157	1.2	149	0.8	161	1.0	177	2.3
a′	168	7.4	164	7.4	158	7.9	170	8.3	186	4.8
a′	189	50.6	186	50.6	191	48.2	203	45.2	190	20.5
a″	192	121.3	187	121.3	191	120.5	205	121.6	206	124.8
a″	213	40.1	211	40.1	218	39.8	227	40.9	223	53.6
a′	251	0.0	251	0.0	245	0.0	250	0.1	239	0.9
a″	264	1.2	264	1.2	259	0.7	264	1.1	256	9.0
a′	324	16.4	325	16.4	323	12.5	327	13.8	321	41.9
a′	359	5.4	357	5.4	351	4.5	354	4.7	362	7.5
a′	364	25.4	362	25.4	358	24.7	361	28.9	364	24.5
a′	408	16.8	408	16.8	405	16.6	416	14.4	399	16.1
a″	462	30.2	462	30.2	448	32.4	458	32.0	442	32.1
a′	507	23.2	505	23.2	501	21.2	502	16.4	508	38.1
a″	510	1.8	508	1.8	504	2.4	506	0.6	509	8.6
a″	523	17.7	520	17.7	515	15.0	517	15.4	526	20.3
a′	532	38.4	531	38.4	527	42.6	531	44.7	534	36.5
a″	548	185.8	548	185.8	545	188.0	551	189.7	551	181.1
a′	625	277.9	626	277.9	621	276.6	632	276.8	628	315.4
a′	655	86.7	664	86.7	656	92.6	668	85.8	652	97.5
a″	765	4.1	760	4.1	754	4.3	755	4.8	782	4.2
a″	1061	403.4	1050	403.4	1019	400.9	1021	398.7	1070	414.7
a″	1081	394.6	1071	394.6	1042	384.3	1043	386.6	1089	411.2
a″	1128	479.9	1118	479.9	1090	489.1	1092	486.6	1141	491.6
a′	1688	224.5	1670	224.5	1672	236.4	1675	232.9	1666	188.7
a″	1689	197.2	1671	197.2	1673	206.7	1675	210.6	1668	218.4
a″	1705	94.7	1687	94.7	1688	135.3	1690	150.2	1679	217.9
a′	1717	55.0	1699	55.0	1698	35.1	1701	30.2	1694	13.6
a″	3725	227.8	3716	227.8	3680	235.6	3675	251.1	3774	240.0
a′	3772	61.2	3771	61.2	3748	58.3	3747	52.7	3817	53.6
a′	3796	134.5	3797	134.5	3773	118.9	3773	134.1	3845	170.4
a′	3798	76.1	3799	76.1	3775	96.0	3775	165.7	3848	106.2
a′	3816	233.4	3824	233.4	3781	194.6	3777	158.7	3857	266.3
a′	3831	88.7	3841	88.7	3796	77.6	3794	77.6	3866	93.0
a′	3857	59.2	3871	59.2	3825	53.1	3823	55.1	3898	67.0
a′	3861	140.4	3875	140.4	3828	125.7	3827	128.8	3902	161.6

Table A.20: Harmonic vibrational frequencies (ω in cm^{-1}) and infrared intensities (IR in km mol^{-1}) for the C_s DI_2WI_2 tetrahydrate structure computed with the haTZ basis set.

	2b:Mb		MP2		B3LYP		B3LYP–B3BJ		M06–2X	
Irrep	ω	IR	ω	IR	ω	IR	ω	IR	ω	IR
a″	22	0.4	22	0.4	24	0.4	25	0.4	15	0.3
a″	32	1.6	32	1.6	33	3.5	34	1.8	28	1.1
a′	43	2.6	42	2.6	38	2.9	45	2.7	33	1.5
a″	52	0.0	53	0.0	57	0.2	59	0.1	46	0.0
a′	68	1.7	64	1.7	58	0.0	64	0.8	83	0.3
a″	98	1.3	90	1.3	59	0.2	89	0.9	109	0.3
a″	102	0.6	93	0.6	77	0.8	93	0.6	122	0.4
a′	109	0.1	102	0.1	82	0.0	101	0.1	142	0.3
a″	164	0.0	161	0.0	153	5.8	163	4.8	175	1.5
a″	165	5.9	162	5.9	157	0.2	168	0.6	176	12.1
a′	167	12.5	163	12.5	159	14.6	170	14.4	185	5.0
a″	177	19.9	173	19.9	167	21.4	175	20.1	191	5.2
a′	218	82.1	217	82.1	226	81.0	233	74.2	211	28.3
a″	224	20.1	226	20.1	237	18.1	241	19.6	212	56.2
a′	328	21.7	328	21.7	324	20.0	331	14.3	306	19.0
a′	329	5.0	330	5.0	327	2.7	336	3.0	311	71.4
a″	357	16.7	355	16.7	349	12.7	355	17.2	356	28.7
a″	361	43.5	360	43.5	358	41.0	362	50.6	357	27.7
a′	402	26.1	402	26.1	399	29.2	410	27.9	393	20.7
a″	412	13.8	412	13.8	409	17.4	421	13.5	399	7.8
a″	425	9.7	424	9.7	410	7.0	421	7.6	407	5.0
a′	457	53.2	457	53.2	441	58.0	454	56.4	439	60.7
a′	516	0.6	513	0.6	508	0.2	509	0.3	519	1.3
a″	521	11.4	518	11.4	512	8.6	513	9.7	525	10.4
a′	524	27.8	521	27.8	516	22.5	518	24.2	528	34.1
a′	624	68.9	628	68.9	626	80.9	636	72.9	613	50.2
a′	638	353.3	642	353.3	639	329.4	649	353.7	630	314.7
a″	661	1.4	670	1.4	667	0.1	674	1.8	655	0.3
a′	666	198.3	675	198.3	672	219.1	679	193.7	661	319.1
a″	766	2.7	760	2.7	755	2.5	756	3.7	783	3.3
a′	1055	336.4	1046	336.4	1023	335.1	1017	332.4	1060	346.7
a′	1097	404.8	1086	404.8	1056	404.5	1060	406.0	1111	409.8
a′	1124	521.5	1112	521.5	1079	519.5	1086	517.3	1138	548.4
a″	1689	203.5	1671	203.5	1673	214.2	1675	203.7	1663	103.9
a′	1699	47.7	1681	47.7	1682	47.9	1685	59.6	1670	98.4
a′	1707	84.8	1689	84.8	1687	98.2	1690	110.3	1678	218.7
a″	1719	148.0	1701	148.0	1699	159.5	1703	157.2	1694	120.6
a′	3721	27.7	3711	27.7	3671	5.2	3669	3.5	3772	46.9
a′	3723	407.7	3713	407.7	3673	461.8	3671	487.2	3774	393.4
a′	3764	70.2	3757	70.2	3719	90.4	3730	74.3	3812	45.6
a″	3765	127.1	3759	127.1	3721	187.0	3732	149.0	3814	112.0
a″	3817	271.4	3826	271.4	3786	239.4	3781	248.0	3857	227.4
a′	3826	154.1	3835	154.1	3794	103.2	3790	132.5	3863	263.6
a″	3828	110.8	3840	110.8	3804	93.3	3795	151.7	3867	280.0
a′	3831	111.1	3844	111.1	3807	77.8	3799	66.0	3869	32.2

Table A.21: Harmonic vibrational frequencies (ω in cm^{-1}) and infrared intensities (IR in km mol^{-1}) for the C_s DI_2WW_2 tetrahydrate structure computed with the haTZ basis set.

	2b:Mb		MP2		B3LYP		B3LYP–B3BJ		M06–2X	
Irrep	ω	IR	ω	IR	ω	IR	ω	IR	ω	IR
a′	7	0.3	8	0.3	11	0.9	8	0.4	9	1.0
a′	10	0.9	10	0.9	11	0.2	11	0.9	10	0.2
a′	20	0.0	20	0.0	21	0.1	21	0.1	22	0.0
a′	25	2.2	26	2.2	28	2.7	28	2.2	23	1.7
a″	28	0.1	29	0.1	31	0.1	29	0.0	31	0.2
a″	34	1.5	34	1.5	34	1.8	35	1.3	36	1.2
a″	84	13.2	81	13.2	73	11.3	80	12.0	101	3.3
a′	105	15.8	101	15.8	90	2.3	101	15.9	137	13.3
a′	122	25.4	117	25.4	114	39.1	118	23.7	142	40.4
a′	138	66.0	136	66.0	132	61.9	140	68.1	143	5.6
a′	146	13.8	143	13.8	139	12.1	146	15.0	159	0.2
a″	147	85.9	145	85.9	141	93.9	149	84.9	163	157.9
a′	229	6.1	231	6.1	235	1.1	242	2.3	231	12.1
a″	233	83.9	233	83.9	237	42.5	246	56.3	245	71.9
a′	245	9.8	246	9.8	251	46.2	254	36.7	254	5.1
a″	246	8.8	248	8.8	253	10.7	257	13.8	254	4.4
a″	347	2.1	345	2.1	341	1.8	343	1.8	333	0.1
a″	359	1.6	357	1.6	354	0.9	357	3.6	336	3.6
a″	372	3.5	372	3.5	367	5.8	377	1.7	345	3.4
a′	375	3.9	382	3.9	379	4.7	388	9.5	347	111.5
a′	376	57.4	383	57.4	385	2.3	390	4.9	366	0.7
a′	384	59.8	385	59.8	386	114.1	392	93.2	372	6.0
a′	511	0.0	508	0.0	503	0.1	504	0.0	512	0.2
a″	520	3.9	517	3.9	512	2.4	513	3.1	524	5.0
a″	521	6.1	518	6.1	513	5.2	513	4.9	525	6.4
a″	647	50.9	649	50.9	647	54.3	657	51.2	621	53.5
a′	660	242.6	662	242.6	660	232.4	670	244.7	639	279.0
a″	763	10.1	757	10.1	752	10.9	752	12.5	749	43.6
a′	766	33.8	779	33.8	776	35.9	789	33.4	753	190.4
a″	770	150.1	782	150.1	779	156.3	792	151.8	779	8.8
a″	1031	331.5	1022	331.5	996	320.9	992	322.3	1035	346.2
a′	1087	521.8	1074	521.8	1041	522.6	1046	518.2	1100	532.9
a″	1156	467.6	1146	467.6	1119	474.2	1121	472.0	1169	473.1
a′	1684	329.4	1666	329.4	1664	316.7	1665	312.4	1658	328.4
a′	1693	114.2	1674	114.2	1671	104.2	1673	117.4	1664	110.2
a″	1705	22.5	1688	22.5	1687	57.1	1689	62.2	1679	67.3
a″	1716	37.0	1698	37.0	1699	50.7	1702	57.2	1693	72.3
a″	3588	179.6	3555	179.6	3505	208.7	3492	151.4	3614	213.8
a′	3592	1217.0	3559	1217.0	3509	1282.7	3496	1368.0	3618	1212.4
a′	3750	128.0	3735	128.0	3694	112.9	3703	106.8	3801	121.5
a′	3753	267.4	3739	267.4	3698	327.8	3707	312.3	3804	260.5
a″	3818	93.4	3828	93.4	3797	97.1	3786	125.6	3852	149.2
a′	3824	118.2	3834	118.2	3802	79.4	3791	77.8	3860	126.1
a″	3882	5.6	3908	5.6	3868	2.8	3868	5.6	3938	7.9
a′	3883	110.6	3909	110.6	3868	78.5	3868	73.2	3939	99.4

Table A.22: Harmonic vibrational frequencies (ω in cm^{-1}) and infrared intensities (IR in km mol^{-1}) for the C_1 DI_1WI_3 tetrahydrate structure computed with the haTZ basis set.

	2b:Mb		MP2		B3LYP		B3LYP–B3BJ		M06–2X	
Irrep	ω	IR	ω	IR	ω	IR	ω	IR	ω	IR
a	13	0.7	13	0.7	16	0.7	14	0.8	12	0.8
a	35	1.0	37	1.0	35	3.6	40	1.1	25	0.4
a	36	0.3	37	0.3	44	0.3	41	1.0	31	0.1
a	45	0.0	47	0.0	57	0.0	56	0.0	32	0.2
a	81	8.0	75	8.0	65	4.8	76	6.8	96	1.8
a	125	5.5	119	5.5	108	2.9	121	4.5	140	3.2
a	133	0.4	128	0.4	118	0.3	129	0.4	145	3.6
a	149	0.5	146	0.5	140	0.8	148	0.3	158	2.8
a	161	5.5	157	5.5	149	8.5	160	8.1	169	4.9
a	171	19.4	168	19.4	163	19.2	173	19.8	176	15.4
a	174	21.6	171	21.6	166	20.8	176	21.9	179	20.6
a	196	3.8	191	3.8	185	4.2	198	3.2	211	14.6
a	211	80.3	212	80.3	226	76.9	225	79.1	216	76.5
a	265	6.8	263	6.8	245	14.5	261	6.1	258	0.9
a	350	0.4	348	0.4	344	0.5	346	0.4	349	0.2
a	358	0.8	356	0.8	352	0.8	354	0.9	361	1.1
a	424	4.1	428	4.1	429	5.0	437	4.0	388	1.7
a	428	4.5	432	4.5	433	5.3	440	4.4	398	3.0
a	461	21.0	464	21.0	465	18.0	473	13.1	435	27.6
a	513	3.0	510	3.0	506	1.9	507	2.4	514	11.2
a	521	4.5	518	4.5	513	4.4	514	3.7	520	40.9
a	527	29.8	524	29.8	519	24.4	522	28.1	525	0.2
a	543	48.6	550	48.6	548	36.6	560	135.0	528	38.8
a	547	44.5	554	44.5	550	29.2	563	3.5	532	39.9
a	557	97.9	560	97.9	559	107.9	565	31.0	553	83.1
a	641	263.8	645	263.8	643	151.2	653	126.3	613	269.9
a	650	320.7	654	320.7	652	235.5	663	265.1	626	188.7
a	652	139.0	656	139.0	654	349.2	666	352.9	633	393.4
a	768	3.0	762	3.0	757	2.9	758	3.6	785	2.3
a	897	5.3	910	5.3	904	8.2	927	8.4	892	1.6
a	1054	372.9	1045	372.9	1019	368.3	1016	369.3	1066	377.1
a	1093	372.8	1082	372.8	1053	374.4	1056	371.9	1105	372.9
a	1128	544.5	1116	544.5	1085	546.0	1090	541.6	1142	563.8
a	1698	160.5	1679	160.5	1681	162.0	1683	149.5	1662	59.8
a	1705	74.7	1687	74.7	1685	77.9	1687	60.7	1664	74.3
a	1705	52.4	1688	52.4	1686	63.9	1687	106.4	1676	228.5
a	1727	82.5	1711	82.5	1709	90.3	1712	87.3	1693	69.1
a	3634	35.8	3616	35.8	3585	13.2	3569	10.3	3685	25.4
a	3686	268.4	3674	268.4	3638	326.2	3628	362.1	3736	251.1
a	3688	251.3	3676	251.3	3641	312.0	3631	349.2	3738	261.1
a	3754	130.1	3754	130.1	3710	75.9	3704	69.2	3798	139.4
a	3757	122.4	3757	122.4	3713	77.2	3708	78.0	3802	143.5
a	3774	736.1	3774	736.1	3730	734.4	3728	785.9	3819	742.4
a	3785	138.5	3779	138.5	3736	174.9	3750	139.5	3837	114.1
a	3858	80.4	3875	80.4	3840	56.3	3830	65.4	3896	99.1

Table A.23: Harmonic vibrational frequencies (ω in cm^{-1}) and infrared intensities (IR in km mol^{-1}) for the C_1 DI_2W_2 tetrahydrate structure computed with the haTZ basis set.

	2b:Mb		MP2		B3LYP		B3LYP–B3BJ		M06–2X	
Irrep	ω	IR	ω	IR	ω	IR	ω	IR	ω	IR
a	18	0.8	18	0.8	22	1.0	19	1.1	22	0.3
a	28	2.6	28	2.6	29	3.1	28	1.6	32	3.0
a	33	3.0	33	3.0	33	4.7	34	2.7	41	1.6
a	39	2.2	39	2.2	43	1.6	41	2.1	45	0.7
a	59	2.4	61	2.4	60	3.9	62	2.8	60	2.6
a	89	9.2	76	9.2	65	2.9	81	6.5	103	1.1
a	119	1.5	113	1.5	103	3.1	114	1.5	134	10.5
a	124	1.9	122	1.9	117	1.7	124	1.3	142	4.9
a	143	12.7	141	12.7	137	9.3	146	15.5	158	5.5
a	155	21.6	154	21.6	154	13.2	160	17.6	182	6.2
a	178	112.5	176	112.5	174	112.9	181	119.0	202	158.1
a	191	35.6	191	35.6	194	22.4	208	10.1	236	13.8
a	206	6.5	202	6.5	202	34.7	210	36.8	248	25.4
a	248	34.5	247	34.5	245	22.1	260	25.3	285	1.5
a	272	35.9	274	35.9	276	45.1	281	44.3	334	18.9
a	321	10.2	321	10.2	320	12.0	326	7.3	345	14.6
a	339	18.2	339	18.2	338	17.4	340	12.9	365	26.1
a	363	7.3	362	7.3	358	7.3	362	4.2	372	2.2
a	367	14.4	365	14.4	361	18.3	367	21.8	437	4.7
a	436	22.8	443	22.8	455	20.7	452	26.0	480	70.7
a	512	3.1	510	3.1	504	1.8	505	1.7	515	6.0
a	516	3.2	514	3.2	510	3.1	510	2.0	521	12.7
a	520	5.0	517	5.0	512	4.0	512	4.3	528	24.7
a	521	21.3	527	21.3	527	20.1	535	19.9	538	86.2
a	608	115.5	614	115.5	610	90.4	619	97.4	560	4.4
a	625	118.1	632	118.1	629	133.0	638	127.2	606	52.7
a	677	107.3	681	107.3	679	54.9	689	112.9	709	196.9
a	689	134.9	697	134.9	689	191.6	703	129.6	724	187.8
a	761	10.6	756	10.6	749	12.6	750	13.1	781	4.7
a	814	119.4	828	119.4	827	122.0	839	121.4	859	202.5
a	1020	336.6	1009	336.6	978	333.6	979	326.4	1063	346.2
a	1091	450.7	1080	450.7	1053	451.8	1052	449.3	1072	382.9
a	1161	508.1	1151	508.1	1124	503.8	1127	510.0	1174	577.6
a	1688	147.0	1670	147.0	1672	156.6	1672	147.8	1653	39.3
a	1699	58.0	1681	58.0	1679	62.7	1681	70.3	1666	90.7
a	1711	184.5	1693	184.5	1690	96.9	1691	105.0	1673	185.0
a	1719	43.3	1702	43.3	1700	139.5	1703	147.5	1707	114.1
a	3533	782.3	3491	782.3	3437	822.0	3422	851.9	3506	861.0
a	3676	270.9	3660	270.9	3629	283.7	3620	316.7	3716	240.1
a	3752	82.6	3738	82.6	3692	54.6	3692	405.6	3753	109.8
a	3759	497.4	3752	497.4	3702	635.0	3719	286.7	3757	194.4
a	3780	232.0	3773	232.0	3736	157.2	3746	66.8	3784	525.0
a	3798	122.1	3804	122.1	3773	106.0	3748	204.8	3813	211.1
a	3833	104.4	3845	104.4	3809	81.8	3797	98.7	3837	377.1
a	3877	60.2	3902	60.2	3865	43.4	3865	42.0	3927	51.9

Table A.24: Harmonic vibrational frequencies (ω in cm^{-1}) and infrared intensities (IR in km mol^{-1}) for the D_2 DI_4 tetrahydrate structure computed with the haTZ basis set.

	2b:Mb		MP2		B3LYP		B3LYP–B3BJ		M06–2X	
Irrep	ω	IR	ω	IR	ω	IR	ω	IR	ω	IR
b_1	4i	0.0	12i	0.0	42i	0.0	4i	0.0	6i	0.0
b_1	22	0.1	22	0.1	14	0.0	23	0.3	24	0.7
b_2	22	0.1	22	0.1	24	0.7	23	0.3	24	0.7
b_3	25	0.0	25	0.0	24	0.6	26	2.4	26	2.4
b_1	59	2.5	26	2.5	28	4.1	52	0.0	73	9.0
b_2	63	17.1	58	17.1	37	16.7	58	13.3	82	0.0
b_3	73	20.3	59	20.3	37	16.7	64	14.1	94	17.2
b_1	73	20.3	59	20.3	47	15.9	64	14.0	94	17.3
a	123	0.0	119	0.0	109	0.0	120	0.0	132	0.0
a	136	0.0	132	0.0	123	0.0	134	0.0	146	26.0
b_3	150	0.0	144	0.0	134	1.8	149	1.4	146	26.0
b_2	150	0.0	144	0.0	134	1.8	149	1.4	146	0.0
b_1	174	0.0	173	0.0	176	0.0	188	0.0	156	0.0
b_2	178	65.4	174	65.4	178	65.0	192	69.6	173	171.6
b_3	178	65.4	174	65.4	178	64.9	192	69.6	174	40.8
b_1	185	162.1	178	162.1	182	158.8	199	159.9	174	40.9
a	212	0.0	211	0.0	209	0.0	214	0.0	182	0.0
b_3	245	2.0	245	2.0	241	1.9	247	1.9	223	2.0
b_2	245	2.0	245	2.0	241	1.9	247	1.9	223	2.0
a	271	0.0	272	0.0	264	0.0	271	0.0	254	0.0
a	356	0.0	354	0.0	348	0.0	351	0.0	358	0.0
a	370	0.0	367	0.0	362	0.0	365	0.0	375	0.0
b_1	490	0.0	490	0.0	489	0.0	494	0.0	481	0.0
b_1	507	15.7	505	15.7	500	14.7	501	12.6	509	31.8
b_2	511	23.9	510	23.9	506	24.7	508	14.9	509	60.5
b_3	511	23.9	510	23.9	506	24.5	508	14.9	509	61.1
b_2	537	148.1	537	148.1	532	149.1	537	154.4	538	130.8
b_3	537	148.1	537	148.1	532	149.5	537	154.5	538	130.2
b_1	565	257.7	565	257.7	559	264.6	565	265.1	565	270.5
a	765	0.0	760	0.0	754	0.0	755	0.0	782	0.0
b_1	1084	283.3	1074	283.3	1044	283.2	1046	279.3	1097	287.5
b_2	1089	518.9	1079	518.9	1050	517.7	1051	518.9	1101	539.0
b_3	1089	518.9	1079	518.9	1050	517.7	1051	518.9	1101	539.2
a	1682	0.0	1664	0.0	1666	0.0	1668	0.0	1657	0.0
b_3	1692	292.5	1674	292.5	1675	313.2	1678	321.0	1668	329.5
b_2	1692	292.5	1674	292.5	1676	313.3	1678	321.1	1668	329.4
a	1712	0.0	1693	0.0	1695	0.0	1699	0.0	1690	0.0
a	3798	0.0	3799	0.0	3775	0.0	3775	0.0	3852	0.0
b_2	3799	194.8	3801	194.8	3776	177.2	3776	195.1	3854	232.9
b_3	3799	194.8	3801	194.8	3776	177.1	3776	195.1	3854	233.1
a	3802	0.0	3804	0.0	3779	0.0	3780	0.0	3857	0.0
b_1	3858	0.0	3872	0.0	3826	0.0	3824	0.0	3902	0.0
b_3	3862	86.6	3877	86.6	3831	76.1	3829	78.5	3908	95.1
b_2	3862	86.6	3877	86.6	3831	76.2	3829	78.5	3908	95.1
b_1	3866	171.0	3882	171.0	3835	154.4	3833	156.8	3913	198.8

Table A.25: Harmonic vibrational frequencies (ω in cm^{-1}) and infrared intensities (IR in km mol^{-1}) for the S_4 DI_4 tetrahydrate structure computed with the haTZ basis set.

	2b:Mb		MP2		B3LYP		B3LYP–B3BJ		M06–2X	
Irrep	ω	IR	ω	IR	ω	IR	ω	IR	ω	IR
a	6	0.0	9	0.0	14	0.0	9	0.0	7i	0.0
b	22	0.3	21	0.3	19	1.3	22	0.4	23	0.8
e	22	0.3	21	0.3	19	0.3	22	0.4	23	0.8
e	24	1.9	22	1.9	19	0.3	23	2.2	26	1.9
b	62	12.1	55	12.1	35	4.4	55	11.7	71	5.4
e	64	0.0	55	0.0	42	10.6	56	0.0	97	8.1
e	74	17.4	64	17.4	42	10.6	64	14.1	97	8.1
a	74	17.4	64	17.4	47	0.0	64	14.1	101	0.0
b	122	1.7	116	1.7	110	0.1	119	0.7	132	0.0
e	138	0.0	140	0.0	143	5.0	139	0.0	146	0.0
e	149	3.7	146	3.7	143	5.0	148	2.9	157	12.2
a	149	3.7	146	3.7	146	0.0	148	2.9	157	12.2
b	177	0.0	186	0.0	200	27.1	195	0.0	161	0.0
e	182	72.9	190	72.9	212	62.9	199	71.8	180	66.5
e	182	72.9	190	72.9	212	62.9	199	71.8	180	66.5
a	186	95.7	193	95.7	213	0.0	201	79.5	190	171.4
b	219	62.0	220	62.0	238	132.6	222	76.5	198	0.4
e	247	6.0	245	6.0	238	52.9	246	3.8	236	1.5
e	247	6.0	245	6.0	238	52.9	246	3.8	236	1.5
a	269	0.0	263	0.0	242	0.0	264	0.0	266	0.0
a	356	0.0	352	0.0	342	0.0	350	0.0	358	0.0
b	370	0.1	368	0.1	364	1.2	365	0.0	374	0.0
b	493	0.0	500	0.0	500	10.7	499	0.0	485	0.0
e	507	15.5	504	15.5	512	4.1	501	13.2	509	27.5
e	511	18.6	511	18.6	512	4.1	508	15.3	511	48.1
a	511	18.6	511	18.6	519	0.0	508	15.3	511	48.1
e	538	148.0	540	148.0	545	135.4	538	153.3	540	140.7
e	538	148.0	540	148.0	545	135.4	538	153.3	540	140.7
b	564	245.6	567	245.6	568	244.3	565	255.8	568	278.6
a	765	0.0	760	0.0	756	0.0	756	0.0	782	0.0
b	1084	292.4	1074	292.4	1046	313.8	1047	285.3	1093	288.3
e	1089	514.6	1080	514.6	1054	512.7	1052	515.3	1098	539.1
e	1089	514.6	1080	514.6	1054	512.7	1052	515.3	1098	539.1
b	1683	20.0	1666	20.0	1671	39.6	1669	15.6	1658	0.0
e	1692	270.3	1674	270.3	1676	236.2	1678	307.5	1670	328.4
e	1692	270.3	1674	270.3	1676	236.2	1678	307.5	1670	328.4
a	1712	0.0	1692	0.0	1687	0.0	1698	0.0	1692	0.0
e	3796	0.6	3789	0.6	3728	413.8	3769	1.1	3847	0.0
e	3797	247.9	3790	247.9	3728	413.8	3770	228.5	3849	234.6
b	3797	247.9	3790	247.9	3729	6.0	3770	228.5	3849	234.6
a	3800	0.0	3793	0.0	3732	0.0	3772	0.0	3853	0.0
a	3859	0.0	3877	0.0	3851	0.0	3829	0.0	3898	0.0
e	3863	88.9	3881	88.9	3851	72.7	3832	72.9	3904	95.5
e	3863	88.9	3881	88.9	3851	72.7	3832	72.9	3904	95.5
b	3867	144.3	3885	144.3	3853	77.0	3836	140.7	3909	199.1

Table A.26: Cartesian coordinates in Angstroms (Å) for the C_{2v} DI_1 complex at the CCSD(T)/haTZ level of theory.

B	0.000000	0.000000	-0.660794
F	0.000000	1.150449	0.167456
F	1.148320	0.000000	-1.457476
F	-1.148320	0.000000	-1.457476
F	0.000000	-1.150449	0.167456
O	0.000000	0.000000	2.784756
H	0.000000	-0.732872	2.153614
H	0.000000	0.732872	2.153614

Table A.27: Cartesian coordinates in Angstroms (Å) for the C_{2v} DI_1 complex at the MP2/haTZ level of theory.

B	0.000000	0.000000	-0.585481
F	0.000000	-1.152137	0.244491
F	-1.150078	0.000000	-1.383190
F	1.150078	0.000000	-1.383190
F	0.000000	1.152137	0.244491
O	0.000000	0.000000	2.868942
H	0.000000	0.731987	2.236278
H	0.000000	-0.731987	2.236278

Table A.28: Cartesian coordinates in Angstroms (Å) for the C_{2v} DI_1 complex at the B3LYP/haTZ level of theory.

B	0.000000	0.000000	-0.596781
F	0.000000	-1.153489	0.235020
F	-1.150890	0.000000	-1.395422
F	1.150890	0.000000	-1.395422
F	0.000000	1.153489	0.235020
O	0.000000	0.000000	2.882993
H	0.000000	0.737752	2.256607
H	0.000000	-0.737752	2.256607

Table A.29: Cartesian coordinates in Angstroms (Å) for the C_{2v} DI_1 complex at the B3LYP–B3BJ/haTZ level of theory.

B	0.000000	0.000000	-0.586934
F	0.000000	-1.153883	0.244167
F	-1.150906	0.000000	-1.384977
F	1.150906	0.000000	-1.384977
F	0.000000	1.153883	0.244167
O	0.000000	0.000000	2.867215
H	0.000000	0.737170	2.239979
H	0.000000	-0.737170	2.239979

Table A.30: Cartesian coordinates in Angstroms (Å) for the C_{2v} DI_1 complex at the M06–2X/haTZ level of theory.

B	0.000000	0.000000	-0.574613
F	0.000000	-1.145844	0.252265
F	-1.144273	0.000000	-1.368201
F	1.144273	0.000000	-1.368201
F	0.000000	1.145844	0.252265
O	0.000000	0.000000	2.844964
H	0.000000	0.736052	2.220070
H	0.000000	-0.736052	2.220070

Table A.31: Cartesian coordinates in Angstroms (Å) for the C_s BI_1 complex at the CCSD(T)/haTZ level of theory.

B	0.577046	0.008511	0.000000
F	1.931816	-0.331301	0.000000
F	0.257133	0.755405	1.145015
F	0.257133	0.755405	-1.145015
F	-0.205885	-1.180431	0.000000
O	-2.783381	-0.019459	0.000000
H	-2.010357	-0.606664	0.000000
H	-2.348652	0.839895	0.000000

Table A.32: Cartesian coordinates in Angstroms (Å) for the C_s BI_1 complex at the MP2/haTZ level of theory.

B	-0.626350	0.032309	0.000000
F	-0.350085	-0.731887	1.147126
F	0.226087	1.176595	0.000000
F	-0.350085	-0.731887	-1.147126
F	-1.960745	0.452011	0.000000
O	2.772391	-0.035540	0.000000
H	2.343951	-0.897435	0.000000
H	1.994140	0.547107	0.000000

Table A.33: Cartesian coordinates in Angstroms (Å) for the C_s BI_1 complex at the B3LYP/haTZ level of theory.

B	-0.728914	0.004234	0.000000
F	-0.566774	-0.787538	1.149823
F	0.279205	1.021868	0.000000
F	-0.566774	-0.787538	-1.149823
F	-1.989456	0.615175	0.000000
O	2.908347	0.084552	0.000000
H	2.683112	-0.849962	0.000000
H	2.030559	0.510482	0.000000

Table A.34: Cartesian coordinates in Angstroms (Å) for the C_s BI_1 complex at the B3LYP–B3BJ/haTZ level of theory.

B	-0.656494	0.022464	0.000000
F	-0.416472	-0.752112	1.148681
F	0.249339	1.130289	0.000000
F	-0.416472	-0.752112	-1.148681
F	-1.970182	0.506448	0.000000
O	2.810265	0.003686	0.000000
H	2.451317	-0.888854	0.000000
H	1.998004	0.541464	0.000000

Table A.35: Cartesian coordinates in Angstroms (Å) for the C_s BI_1 complex at the M06–2X/haTZ level of theory.

B	0.613532	0.014541	0.000000
F	0.237738	-0.708975	-1.139381
F	-0.077344	1.250425	0.000000
F	0.237738	-0.708975	1.139381
F	1.985174	0.247550	0.000000
O	-2.602934	-0.077145	0.000000
H	-2.027434	-0.849021	0.000000
H	-1.947334	0.633710	0.000000

Table A.36: Cartesian coordinates in Angstroms (Å) for the C_s DI_2 complex at the CCSD(T):MP2/haTZ level of theory.

B	0.630708	0.009952	0.000000
F	1.606778	0.998831	0.000000
F	-0.658865	0.613399	0.000000
F	0.750442	-0.795532	1.148734
F	0.750442	-0.795532	-1.148734
H	-0.691610	-0.468402	2.517409
H	-0.691610	-0.468402	-2.517409
O	-1.522436	-0.013695	2.712825
O	-1.522436	-0.013695	-2.712825
H	-1.650752	0.441691	1.871342
H	-1.650752	0.441691	-1.871342

Table A.37: Cartesian coordinates in Angstroms (Å) for the C_s DI_2 complex at the CCSD(T)/haTZ level of theory.

B	0.629793	0.009548	0.000000
F	1.605229	0.999054	0.000000
F	-0.660153	0.612164	0.000000
F	0.750050	-0.795859	1.148726
F	0.750050	-0.795859	-1.148726
O	-1.521400	-0.013209	2.714151
H	-0.690674	-0.467999	2.518361
H	-0.690674	-0.467999	-2.518361
O	-1.521400	-0.013209	-2.714151
H	-1.650349	0.441685	1.872480
H	-1.650349	0.441685	-1.872480

Table A.38: Cartesian coordinates in Angstroms (Å) for the C_s DI_2 complex at the MP2/haTZ level of theory.

B	0.750524	0.373310	0.000000
F	0.514019	1.154300	1.150586
F	0.514019	1.154300	-1.150586
F	2.057489	-0.103757	0.000000
F	-0.159072	-0.724359	0.000000
O	-1.216938	-0.511804	2.724708
H	-1.144467	-0.990229	1.889355
H	-0.655569	0.247607	2.513703
O	-1.216938	-0.511804	-2.724708
H	-0.655569	0.247607	-2.513703
H	-1.144467	-0.990229	-1.889355

Table A.39: Cartesian coordinates in Angstroms (Å) for the C_s DI_2 complex at the B3LYP/haTZ level of theory.

B	0.778551	0.370172	0.000000
F	0.522812	1.147011	1.152355
F	0.522812	1.147011	-1.152355
F	2.098528	-0.072775	0.000000
F	-0.105037	-0.749338	0.000000
O	-1.241931	-0.494674	2.736982
H	-1.170151	-1.011131	1.924713
H	-0.675235	0.257236	2.510568
O	-1.241931	-0.494674	-2.736982
H	-0.675235	0.257236	-2.510568
H	-1.170151	-1.011131	-1.924713

Table A.40: Cartesian coordinates in Angstroms (Å) for the C_s DI_2 complex at the B3LYP–B3BJ/haTZ level of theory.

B	0.769606	0.371171	0.000000
F	0.522131	1.149745	1.151601
F	0.522131	1.149745	-1.151601
F	2.083749	-0.088035	0.000000
F	-0.125816	-0.740787	0.000000
O	-1.238450	-0.508414	2.700214
H	-1.151215	-0.994382	1.870304
H	-0.674719	0.254349	2.506854
O	-1.238450	-0.508414	-2.700214
H	-0.674719	0.254349	-2.506854
H	-1.151215	-0.994382	-1.870304

Table A.41: Cartesian coordinates in Angstroms (Å) for the C_s DI_2 complex at the M06–2X/haTZ level of theory.

B	0.748054	0.369904	0.000000
F	0.512946	1.145403	1.145157
F	0.512946	1.145403	-1.145157
F	2.046593	-0.109106	0.000000
F	-0.161260	-0.721450	0.000000
O	-1.218635	-0.519935	2.670946
H	-1.124768	-0.975898	1.826939
H	-0.664720	0.253228	2.506606
O	-1.218635	-0.519935	-2.670946
H	-0.664720	0.253228	-2.506606
H	-1.124768	-0.975898	-1.826939

Table A.42: Cartesian coordinates in Angstroms (Å) for the C_s DI_1WI_1 complex at the CCSD(T):MP2/haTZ level of theory.

B	0.921372	0.063796	0.000000
F	2.308876	0.131827	0.000000
F	0.365567	1.357965	0.000000
F	0.467084	-0.628403	1.147805
F	0.467084	-0.628403	-1.147805
H	-1.602748	1.502687	0.000000
O	-2.554672	1.325314	0.000000
H	-2.574467	0.356785	0.000000
O	-1.935882	-1.582690	0.000000
H	-1.328825	-1.422692	-0.737461
H	-1.328825	-1.422692	0.737461

Table A.43: Cartesian coordinates in Angstroms (Å) for the C_s DI_1WI_1 complex at the CCSD(T)/haTZ level of theory.

B	0.921756	0.063729	0.000000
F	2.309266	0.131618	0.000000
F	0.366093	1.357972	0.000000
F	0.467405	-0.628478	1.147775
F	0.467405	-0.628478	-1.147775
O	-2.555899	1.326053	0.000000
H	-1.604443	1.505666	0.000000
H	-2.573293	0.357527	0.000000
O	-1.935927	-1.584186	0.000000
H	-1.328868	-1.423976	-0.737460
H	-1.328868	-1.423976	0.737460

Table A.44: Cartesian coordinates in Angstroms (Å) for the C_s DI_1WI_1 complex at the MP2/haTZ level of theory.

B	-1.154723	0.099700	0.000000
F	-2.544275	0.163460	0.000000
F	-0.697232	-0.592518	-1.149472
F	-0.601688	1.397411	0.000000
F	-0.697232	-0.592518	1.149472
O	2.328342	1.385061	0.000000
H	1.375582	1.559702	0.000000
H	2.347251	0.415843	0.000000
O	1.721062	-1.527283	0.000000
H	1.110714	-1.373112	0.736527
H	1.110714	-1.373112	-0.736527

Table A.45: Cartesian coordinates in Angstroms (Å) for the C_s DI_1WI_1 complex at the B3LYP/haTZ level of theory.

B	-1.179141	0.089023	0.000000
F	-2.568341	0.176574	0.000000
F	-0.732483	-0.612443	-1.150606
F	-0.603482	1.378889	0.000000
F	-0.732483	-0.612443	1.150606
O	2.361836	1.400149	0.000000
H	1.411654	1.588523	0.000000
H	2.380991	0.430068	0.000000
O	1.723786	-1.522391	0.000000
H	1.118089	-1.376658	0.742190
H	1.118089	-1.376658	-0.742190

Table A.46: Cartesian coordinates in Angstroms (Å) for the C_s DI_1WI_1 complex at the B3LYP–B3BJ/haTZ level of theory.

B	-1.159977	0.096243	0.000000
F	-2.549687	0.166833	0.000000
F	-0.705238	-0.599255	-1.150834
F	-0.600062	1.392458	0.000000
F	-0.705238	-0.599255	1.150834
O	2.333058	1.380340	0.000000
H	1.382463	1.567257	0.000000
H	2.353998	0.410076	0.000000
O	1.719767	-1.518588	0.000000
H	1.114715	-1.366737	0.741656
H	1.114715	-1.366737	-0.741656

Table A.47: Cartesian coordinates in Angstroms (Å) for the C_s DI_1WI_1 complex at the M06–2X/haTZ level of theory.

B	-1.123556	0.125938	0.000000
F	-2.507690	0.125205	0.000000
F	-0.636445	-0.540936	-1.143690
F	-0.632808	1.440637	0.000000
F	-0.636445	-0.540936	1.143690
O	2.270347	1.352094	0.000000
H	1.320762	1.533014	0.000000
H	2.308037	0.386195	0.000000
O	1.709464	-1.557033	0.000000
H	1.113425	-1.380772	0.740769
H	1.113425	-1.380772	-0.740769

Table A.48: Cartesian coordinates in Angstroms (Å) for the D_{2d} DI_2 complex at the CCSD(T):MP2/haTZ level of theory.

B	0.000000	0.000000	0.000000
O	0.000000	0.000000	-3.456108
O	0.000000	0.000000	3.456108
H	-0.519833	-0.519833	-2.828857
H	0.519833	0.519833	-2.828857
H	0.519833	-0.519833	2.828857
H	-0.519833	0.519833	2.828857
F	-0.812368	-0.812368	-0.812363
F	0.812368	0.812368	-0.812363
F	0.812368	-0.812368	0.812363
F	-0.812368	0.812368	0.812363

Table A.49: Cartesian coordinates in Angstroms (Å) for the D_{2d} DI_2 complex at the CCSD(T)/haTZ level of theory.

B	0.000000	0.000000	0.000000
F	-0.812371	-0.812371	-0.812356
F	0.812371	0.812371	-0.812356
F	0.812371	-0.812371	0.812356
F	-0.812371	0.812371	0.812356
O	0.000000	0.000000	-3.455945
H	0.519834	-0.519834	2.828656
H	-0.519834	0.519834	2.828656
O	0.000000	0.000000	3.455945
H	-0.519834	-0.519834	-2.828656
H	0.519834	0.519834	-2.828656

Table A.50: Cartesian coordinates in Angstroms (Å) for the D_{2d} DI_2 complex at the MP2/haTZ level of theory.

B	0.000000	0.000000	0.000000
F	0.000000	1.150346	0.813957
F	0.000000	-1.150346	0.813957
F	-1.150346	0.000000	-0.813957
F	1.150346	0.000000	-0.813957
O	0.000000	0.000000	3.466736
H	0.000000	0.734324	2.838020
H	0.000000	-0.734324	2.838020
O	0.000000	0.000000	-3.466736
H	0.734324	0.000000	-2.838020
H	-0.734324	0.000000	-2.838020

Table A.51: Cartesian coordinates in Angstroms (Å) for the D_{2d} DI_2 complex at the B3LYP/haTZ level of theory.

B	0.000000	0.000000	0.000000
F	0.000000	1.151199	0.815734
F	0.000000	-1.151199	0.815734
F	-1.151199	0.000000	-0.815734
F	1.151199	0.000000	-0.815734
O	0.000000	0.000000	3.494163
H	0.000000	0.740183	2.871983
H	0.000000	-0.740183	2.871983
O	0.000000	0.000000	-3.494163
H	0.740183	0.000000	-2.871983
H	-0.740183	0.000000	-2.871983

Table A.52: Cartesian coordinates in Angstroms (Å) for the D_{2d} DI_2 complex at the B3LYP–B3BJ/haTZ level of theory.

B	0.000000	0.000000	0.000000
F	0.000000	1.151696	0.814495
F	0.000000	-1.151696	0.814495
F	-1.151696	0.000000	-0.814495
F	1.151696	0.000000	-0.814495
O	0.000000	0.000000	3.467180
H	0.000000	0.739609	2.844212
H	0.000000	-0.739609	2.844212
O	0.000000	0.000000	-3.467180
H	0.739609	0.000000	-2.844212
H	-0.739609	0.000000	-2.844212

Table A.53: Cartesian coordinates in Angstroms (Å) for the D_{2d} DI_2 complex at the M06–2X/haTZ level of theory.

B	0.000000	0.000000	0.000000
F	0.000000	1.144101	0.810741
F	0.000000	-1.144101	0.810741
F	-1.144101	0.000000	-0.810741
F	1.144101	0.000000	-0.810741
O	0.000000	0.000000	3.425240
H	0.000000	0.738522	2.804462
H	0.000000	-0.738522	2.804462
O	0.000000	0.000000	-3.425240
H	0.738522	0.000000	-2.804462
H	-0.738522	0.000000	-2.804462

Table A.54: Cartesian coordinates in Angstroms (Å) for the C_s DI_1BI_1 complex at the CCSD(T):MP2/haTZ level of theory.

H	-2.889144	-0.419757	0.000000
O	-2.786081	-1.377323	0.000000
H	-1.820505	-1.454070	0.000000
F	0.044122	-0.876117	0.000000
B	-0.030365	0.551949	0.000000
F	-0.713956	0.964715	1.144191
F	-0.713956	0.964715	-1.144191
F	1.279477	1.066626	0.000000
H	2.716196	-0.333109	0.000000
O	2.929277	-1.276549	0.000000
H	2.033836	-1.637089	0.000000

Table A.55: Cartesian coordinates in Angstroms (Å) for the C_s DI_1BI_1 complex at the CCSD(T)/haTZ level of theory.

B	-0.030504	0.551283	0.000000
F	-0.714249	0.963869	1.144181
F	-0.714249	0.963869	-1.144181
F	0.044382	-0.876737	0.000000
F	1.279160	1.066398	0.000000
O	2.929707	-1.276106	0.000000
H	2.034111	-1.636347	0.000000
H	-2.888373	-0.418540	0.000000
O	-2.786659	-1.376275	0.000000
H	-1.821177	-1.454289	0.000000
H	2.716896	-0.332588	0.000000

Table A.56: Cartesian coordinates in Angstroms (Å) for the C_s DI_1BI_1 complex at the MP2/haTZ level of theory.

B	-0.605485	-0.003435	0.000000
F	0.800924	0.270349	0.000000
F	-1.171938	0.559290	1.146216
F	-1.171938	0.559290	-1.146216
F	-0.786226	-1.401852	0.000000
O	0.700603	3.137126	0.000000
H	0.949377	2.199812	0.000000
H	-0.259414	3.066626	0.000000
O	1.881418	-2.455728	0.000000
H	0.913506	-2.450166	0.000000
H	2.038818	-1.503456	0.000000

Table A.57: Cartesian coordinates in Angstroms (Å) for the C_s DI_1BI_1 complex at the B3LYP/haTZ level of theory.

B	-0.750158	-0.091469	0.000000
F	0.624651	0.324510	0.000000
F	-1.371843	0.402628	1.148557
F	-1.371843	0.402628	-1.148557
F	-0.777933	-1.505721	0.000000
O	0.937500	3.139919	0.000000
H	0.941226	2.166853	0.000000
H	-0.001512	3.345831	0.000000
O	1.949917	-2.386395	0.000000
H	0.980317	-2.381771	0.000000
H	2.128825	-1.438921	0.000000

Table A.58: Cartesian coordinates in Angstroms (Å) for the C_s DI_1BI_1 complex at the B3LYP–B3BJ/haTZ level of theory.

B	-0.649738	-0.029692	0.000000
F	0.752058	0.285752	0.000000
F	-1.231699	0.514064	1.147456
F	-1.231699	0.514064	-1.147456
F	-0.786249	-1.435109	0.000000
O	0.776602	3.128752	0.000000
H	0.956008	2.174096	0.000000
H	-0.185322	3.148924	0.000000
O	1.904090	-2.417736	0.000000
H	0.935881	-2.440102	0.000000
H	2.049616	-1.463465	0.000000

Table A.59: Cartesian coordinates in Angstroms (Å) for the C_s DI_1BI_1 complex at the M06–2X/haTZ level of theory.

B	-0.509685	0.055483	0.008546
F	0.902150	0.237445	-0.006156
F	-1.027128	0.661916	1.149460
F	-1.049518	0.651442	-1.127492
F	-0.783000	-1.318934	0.017576
O	0.523833	3.111879	-0.016045
H	0.986888	2.264879	-0.016361
H	-0.393925	2.821599	-0.005647
O	1.816239	-2.482901	-0.002448
H	0.851249	-2.494322	0.007798
H	1.971818	-1.531444	-0.009230

Table A.60: Cartesian coordinates in Angstroms (Å) for the C_s DI_1W_1 complex at the B3LYP/haTZ level of theory.

B	-0.337528	1.372176	0.000000
F	0.886391	2.045872	0.000000
F	-0.419345	0.537277	1.153487
F	-1.403974	2.273242	0.000000
F	-0.419345	0.537277	-1.153487
O	-0.436109	-2.013970	0.000000
H	-0.447082	-1.386515	0.740077
H	-0.447082	-1.386515	-0.740077
O	1.794614	-3.697021	0.000000
H	0.989004	-3.135511	0.000000
H	2.515092	-3.061600	0.000000

Table A.61: Cartesian coordinates in Angstroms (Å) for the C_{3v} DI_3 complex at the CCSD(T):MP2/haTZ level of theory.

B	0.000000	0.000000	0.558567
F	0.000000	0.000000	1.941167
F	0.000000	1.327530	0.067514
F	1.149675	-0.663765	0.067514
F	-1.149675	-0.663765	0.067514
O	0.000000	-3.211645	-0.775158
H	0.737956	-2.620448	-0.580402
H	-0.737956	-2.620448	-0.580402
O	2.781366	1.605823	-0.775158
H	1.900396	1.949313	-0.580402
H	2.638352	0.671135	-0.580402
O	-2.781366	1.605823	-0.775158
H	-2.638352	0.671135	-0.580402
H	-1.900396	1.949313	-0.580402

Table A.62: Cartesian coordinates in Angstroms (Å) for the C_{3v} DI_3 complex at the MP2/haTZ level of theory.

B	0.000000	0.000000	0.567756
F	0.000000	0.000000	1.952124
F	0.000000	1.329555	0.075626
F	1.151428	-0.664777	0.075626
F	-1.151428	-0.664777	0.075626
O	0.000000	-3.220981	-0.777860
H	0.737075	-2.629160	-0.580636
H	-0.737075	-2.629160	-0.580636
O	2.789451	1.610491	-0.777860
H	1.908382	1.952906	-0.580636
H	2.645457	0.676254	-0.580636
O	-2.789451	1.610490	-0.777860
H	-2.645457	0.676254	-0.580636
H	-1.908382	1.952906	-0.580636

Table A.63: Cartesian coordinates in Angstroms (Å) for the C_{3v} DI_3 complex at the B3LYP/haTZ level of theory.

B	0.000000	0.000000	0.623413
F	0.000000	0.000000	2.008686
F	0.000000	1.331357	0.130420
F	1.152989	-0.665678	0.130420
F	-1.152989	-0.665678	0.130420
O	0.000000	-3.219443	-0.823638
H	0.742836	-2.641032	-0.607905
H	-0.742836	-2.641032	-0.607905
O	2.788120	1.609722	-0.823638
H	1.915783	1.963831	-0.607905
H	2.658619	0.677201	-0.607905
O	-2.788120	1.609722	-0.823638
H	-2.658619	0.677202	-0.607905
H	-1.915783	1.963831	-0.607905

Table A.64: Cartesian coordinates in Angstroms (Å) for the C_{3v} DI_3 complex at the B3LYP–B3BJ/haTZ level of theory.

B	0.000000	0.000000	0.612854
F	0.000000	0.000000	1.997180
F	0.000000	1.331123	0.119842
F	1.152786	-0.665561	0.119842
F	-1.152786	-0.665561	0.119842
O	0.000000	-3.189713	-0.816969
H	0.742242	-2.610079	-0.602272
H	-0.742243	-2.610078	-0.602272
O	2.762373	1.594857	-0.816969
H	1.889273	1.947840	-0.602272
H	2.631516	0.662238	-0.602272
O	-2.762373	1.594857	-0.816969
H	-2.631516	0.662239	-0.602272
H	-1.889273	1.947840	-0.602272

Table A.65: Cartesian coordinates in Angstroms (Å) for the C_{3v} DI_3 complex at the M06–2X/haTZ level of theory.

B	0.000000	0.000000	0.545223
F	0.000000	0.000000	1.922086
F	0.000000	1.322764	0.054265
F	1.145547	-0.661382	0.054265
F	-1.145547	-0.661382	0.054265
O	0.000000	-3.184402	-0.761037
H	0.741512	-2.598131	-0.573523
H	-0.741512	-2.598131	-0.573523
O	2.757773	1.592201	-0.761037
H	1.879292	1.941234	-0.573523
H	2.620804	0.656897	-0.573523
O	-2.757773	1.592201	-0.761037
H	-2.620804	0.656898	-0.573523
H	-1.879292	1.941234	-0.573523

Table A.66: Cartesian coordinates in Angstroms (Å) for the C_s DI_2WI_1 complex at the CCSD(T):MP2/haTZ level of theory.

B	0.686755	0.065453	0.000000
F	1.811279	0.899280	0.000000
F	0.691513	-0.748113	1.146639
F	-0.487258	0.854677	0.000000
F	0.691513	-0.748113	-1.146639
O	-2.905838	-0.864092	0.000000
H	-2.230824	-0.171800	0.000000
H	-2.367846	-1.669779	0.000000
O	-0.757547	-2.913075	0.000000
H	-0.341865	-2.447229	-0.739453
H	-0.341865	-2.447229	0.739453
O	0.691513	3.554556	0.000000
H	-0.104363	3.009484	0.000000
H	1.364560	2.860600	0.000000

Table A.67: Cartesian coordinates in Angstroms (Å) for the C_s DI_2WI_1 complex at the MP2/haTZ level of theory.

B	0.677230	0.066970	0.000000
F	1.802027	0.904451	0.000000
F	0.684078	-0.748139	1.148210
F	-0.499543	0.855150	0.000000
F	0.684078	-0.748139	-1.148210
O	-2.932428	-0.864584	0.000000
H	-2.259072	-0.170369	0.000000
H	-2.388863	-1.667402	0.000000
O	-0.781365	-2.911903	0.000000
H	-0.361431	-2.447718	-0.738571
H	-0.361431	-2.447718	0.738571
O	0.697600	3.570217	0.000000
H	-0.110680	3.043948	0.000000
H	1.353026	2.858689	0.000000

Table A.68: Cartesian coordinates in Angstroms (Å) for the C_s DI_2WI_1 complex at the B3LYP/haTZ level of theory.

B	0.703144	0.061316	0.000000
F	1.813355	0.921822	0.000000
F	0.726799	-0.755630	1.148896
F	-0.488382	0.828619	0.000000
F	0.726799	-0.755630	-1.148896
O	-2.975954	-0.888570	0.000000
H	-2.315194	-0.182339	0.000000
H	-2.429081	-1.690298	0.000000
O	-0.790431	-2.917675	0.000000
H	-0.368974	-2.463688	-0.744152
H	-0.368974	-2.463688	0.744152
O	0.722055	3.605387	0.000000
H	-0.110156	3.118412	0.000000
H	1.358219	2.875414	0.000000

Table A.69: Cartesian coordinates in Angstroms (Å) for the C_s DI_2WI_1 complex at the B3LYP–B3BJ/haTZ level of theory.

B	0.688885	0.063384	0.000000
F	1.809030	0.908533	0.000000
F	0.700706	-0.752532	1.149202
F	-0.494377	0.844942	0.000000
F	0.700706	-0.752532	-1.149202
O	-2.933713	-0.865633	0.000000
H	-2.267513	-0.164414	0.000000
H	-2.393125	-1.671788	0.000000
O	-0.789283	-2.900764	0.000000
H	-0.371104	-2.442807	-0.743673
H	-0.371104	-2.442807	0.743673
O	0.684567	3.566355	0.000000
H	-0.118648	3.031843	0.000000
H	1.358202	2.871673	0.000000

Table A.70: Cartesian coordinates in Angstroms (Å) for the C_s DI_2WI_1 complex at the M06–2X/haTZ level of theory.

B	0.610226	0.090735	0.000000
F	1.761998	0.876762	0.000000
F	0.580572	-0.719908	1.142384
F	-0.527948	0.923782	0.000000
F	0.580572	-0.719908	-1.142384
O	-2.865432	-0.874299	0.000000
H	-2.203912	-0.171501	0.000000
H	-2.333431	-1.681421	0.000000
O	-0.736439	-2.930043	0.000000
H	-0.348794	-2.448816	-0.742831
H	-0.348794	-2.448816	0.742831
O	0.716397	3.541359	0.000000
H	-0.078853	2.997858	0.000000
H	1.397065	2.857669	0.000000

Table A.71: Cartesian coordinates in Angstroms (Å) for the C_3 WI_3 complex at the CCSD(T):MP2/haTZ level of theory.

B	0.000000	0.000000	1.360642
F	0.000000	0.000000	2.745467
F	0.000000	1.325206	0.868977
F	1.147662	-0.662603	0.868977
F	-1.147662	-0.662603	0.868977
O	1.244792	-1.130782	-1.916818
H	1.329122	-1.090268	-0.950609
H	0.283964	-1.206623	-2.039772
O	-1.601682	-0.512630	-1.916818
H	-1.608760	-0.605919	-0.950609
H	-1.186948	0.357392	-2.039772
O	0.356890	1.643412	-1.916818
H	0.279639	1.696187	-0.950609
H	0.902984	0.849231	-2.039772

Table A.72: Cartesian coordinates in Angstroms (Å) for the C_3 WI_3 complex at the MP2/haTZ level of theory.

B	0.000000	0.000000	1.354998
F	0.000000	0.000000	2.741590
F	-0.072859	1.325365	0.862315
F	1.184229	-0.599585	0.862315
F	-1.111370	-0.725780	0.862315
O	1.317211	-1.046026	-1.930825
H	1.399987	-1.005740	-0.963889
H	0.361866	-1.183045	-2.049870
O	-1.564491	-0.617725	-1.930825
H	-1.570990	-0.709554	-0.963889
H	-1.205480	0.278137	-2.049870
O	0.247280	1.663751	-1.930825
H	0.171003	1.715295	-0.963889
H	0.843614	0.904908	-2.049870

Table A.73: Cartesian coordinates in Angstroms (Å) for the C_3 WI_3 complex at the B3LYP/haTZ level of theory.

B	0.000000	0.000000	1.378289
F	0.000000	0.000000	2.765858
F	-0.047559	1.328803	0.885661
F	1.174557	-0.623215	0.885661
F	-1.126998	-0.705589	0.885661
O	1.376635	-0.985384	-1.941017
H	1.463702	-0.954758	-0.973955
H	0.430554	-1.172362	-2.070093
O	-1.541685	-0.699508	-1.941017
H	-1.558696	-0.790224	-0.973955
H	-1.230572	0.213310	-2.070093
O	0.165051	1.684893	-1.941017
H	0.094994	1.744982	-0.973955
H	0.800018	0.959051	-2.070093

Table A.74: Cartesian coordinates in Angstroms (Å) for the C_3 WI_3 complex at the B3LYP–B3BJ/haTZ level of theory.

B	0.000000	0.000000	1.359050
F	0.000000	0.000000	2.746086
F	-0.036818	1.328701	0.866675
F	1.169098	-0.632465	0.866675
F	-1.132280	-0.696236	0.866675
O	1.320490	-1.033496	-1.930829
H	1.410442	-0.998117	-0.964092
H	0.365995	-1.177801	-2.056871
O	-1.555279	-0.626830	-1.930829
H	-1.569616	-0.722420	-0.964092
H	-1.203003	0.271940	-2.056871
O	0.234789	1.660326	-1.930829
H	0.159174	1.720537	-0.964092
H	0.837008	0.905861	-2.056871

Table A.75: Cartesian coordinates in Angstroms (Å) for the C_3 WI_3 complex at the M06–2X/haTZ level of theory.

B	0.000000	0.000000	1.298764
F	0.000000	0.000000	2.678189
F	-0.359750	1.269196	0.804424
F	1.279031	-0.323046	0.804424
F	-0.919281	-0.946150	0.804424
O	1.244006	-1.133424	-1.895937
H	1.350781	-1.037341	-0.937984
H	0.285058	-1.215019	-2.012904
O	-1.603577	-0.510628	-1.895937
H	-1.573754	-0.651140	-0.937984
H	-1.194766	0.360642	-2.012904
O	0.359571	1.644053	-1.895937
H	0.222973	1.688481	-0.937984
H	0.909708	0.854377	-2.012904

Table A.76: Cartesian coordinates in Angstroms (Å) for the C_s DI_2W_1 complex at the CCSD(T):MP2/haTZ level of theory.

B	0.521898	-1.320983	0.000000
F	-0.294158	-1.362922	1.147401
F	1.417157	-2.378168	0.000000
F	-0.294158	-1.362922	-1.147401
F	1.236229	-0.086110	0.000000
O	-0.294158	1.322610	-2.005196
H	-0.617649	0.412072	-1.941645
H	0.497195	1.248219	-1.455990
O	-1.694728	2.982619	0.000000
H	-1.344925	2.486356	-0.756172
H	-1.344925	2.486356	0.756172
O	-0.294158	1.322610	2.005196
H	0.497195	1.248219	1.455990
H	-0.617649	0.412072	1.941645

Table A.77: Cartesian coordinates in Angstroms (Å) for the C_s DI_2W_1 complex at the MP2/haTZ level of theory.

B	1.303465	-0.129346	0.000000
F	1.112426	0.667651	-1.149242
F	2.573056	-0.688043	0.000000
F	1.112426	0.667651	1.149242
F	0.319899	-1.163842	0.000000
O	-1.467555	-0.069021	2.017916
H	-0.670020	0.475654	1.934386
H	-1.196346	-0.825432	1.481814
O	-3.443845	0.805273	0.000000
H	-2.866539	0.613392	0.756135
H	-2.866539	0.613392	-0.756135
O	-1.467555	-0.069021	-2.017916
H	-1.196346	-0.825432	-1.481814
H	-0.670020	0.475654	-1.934386

Table A.78: Cartesian coordinates in Angstroms (Å) for the C_s DI_2W_1 complex at the B3LYP/haTZ level of theory.

B	-0.458579	-1.228560	0.000000
F	0.363917	-1.232074	-1.151233
F	-1.298927	-2.333070	0.000000
F	0.363917	-1.232074	1.151233
F	-1.229266	-0.028284	0.000000
O	0.319161	1.449471	2.052432
H	0.620530	0.534347	1.936366
H	-0.502631	1.429207	1.546471
O	1.655244	3.144408	0.000000
H	1.334256	2.635922	0.762504
H	1.334256	2.635922	-0.762504
O	0.319161	1.449471	-2.052432
H	-0.502631	1.429207	-1.546471
H	0.620530	0.534347	-1.936366

Table A.79: Cartesian coordinates in Angstroms (Å) for the C_s DI_2W_1 complex at the B3LYP–B3BJ/haTZ level of theory.

B	1.305936	-0.012803	0.000000
F	1.040620	0.763916	-1.150337
F	2.622380	-0.450166	0.000000
F	1.040620	0.763916	1.150337
F	0.422083	-1.136352	0.000000
O	-1.456211	-0.207575	2.019904
H	-0.715688	0.413010	1.936916
H	-1.128416	-0.938433	1.480042
O	-3.478369	0.513020	0.000000
H	-2.894714	0.363199	0.761907
H	-2.894714	0.363199	-0.761907
O	-1.456211	-0.207575	-2.019904
H	-1.128416	-0.938433	-1.480042
H	-0.715688	0.413010	-1.936916

Table A.80: Cartesian coordinates in Angstroms (Å) for the C_s DI_2W_1 complex at the M06–2X/haTZ level of theory.

B	1.339971	-0.039248	0.000000
F	1.088134	0.734106	-1.143396
F	2.640220	-0.501356	0.000000
F	1.088134	0.734106	1.143396
F	0.439573	-1.142454	0.000000
O	-1.446370	-0.185677	1.914119
H	-0.726623	0.458464	1.882605
H	-1.074721	-0.887361	1.366009
O	-3.572629	0.467353	0.000000
H	-2.982383	0.339287	0.756299
H	-2.982383	0.339287	-0.756299
O	-1.446370	-0.185677	-1.914119
H	-1.074721	-0.887361	-1.366009
H	-0.726623	0.458464	-1.882605

Table A.81: Cartesian coordinates in Angstroms (Å) for the C_1 DI_2W_1 complex at the B3LYP–B3BJ/haTZ level of theory.

B	1.173099	-0.819593	0.009608
F	0.232812	-1.718487	-0.542687
F	2.309642	-1.497518	0.425499
F	1.502550	0.154015	-0.960312
F	0.567157	-0.160225	1.123673
O	0.025823	2.406871	-0.138636
H	0.523280	1.831036	-0.739819
H	0.079175	1.890793	0.676102
O	-2.840284	1.797709	-0.458569
H	-1.920750	2.110844	-0.456108
H	-2.761686	0.870486	-0.179840
O	-2.203722	-0.880695	0.594305
H	-1.555988	-0.520063	1.213474
H	-1.612444	-1.318526	-0.037487

Table A.82: Cartesian coordinates in Angstroms (Å) for the C_1 DI_2W_1 complex at the M06–2X/haTZ level of theory.

B	-1.131276	-0.665517	0.097232
F	-0.144853	-1.419839	0.757032
F	-2.038938	-1.499799	-0.524930
F	-1.773731	0.167487	1.020294
F	-0.487887	0.149511	-0.876350
O	-1.553702	2.746205	-0.169009
H	-1.833667	2.097561	0.488557
H	-1.058684	2.179455	-0.770249
O	4.227346	0.848084	0.360164
H	3.709650	1.479619	0.862099
H	3.557890	0.246479	-0.015296
O	2.160800	-0.765089	-0.647933
H	1.465761	-0.250275	-1.077719
H	1.641255	-1.227928	0.024054

Table A.83: Cartesian coordinates in Angstroms (Å) for the C_s DI_4 complex at the CCSD(T):MP2/haTZ level of theory.

B	0.115565	0.420169	0.000000
F	1.267506	1.205425	0.000000
F	0.475046	-0.950652	0.000000
F	-0.652812	0.693224	1.147755
F	-0.652812	0.693224	-1.147755
O	-2.666431	2.508568	0.000000
H	-2.207949	2.092391	0.740006
H	-2.207949	2.092391	-0.740006
O	-0.648435	-1.829159	2.611954
H	-0.163861	-2.030377	1.803199
H	-0.852006	-0.897692	2.460317
O	-0.648435	-1.829159	-2.611954
H	-0.852006	-0.897692	-2.460317
H	-0.163861	-2.030377	-1.803199
O	3.494457	-0.625307	0.000000
H	2.788404	-1.280341	0.000000
H	2.976129	0.190851	0.000000

Table A.84: Cartesian coordinates in Angstroms (Å) for the C_s DI_4 complex at the MP2/haTZ level of theory.

B	0.111304	0.414051	0.000000
F	1.270195	1.193846	0.000000
F	0.463147	-0.959539	0.000000
F	-0.656461	0.693389	1.149421
F	-0.656461	0.693389	-1.149421
O	-2.675651	2.522181	0.000000
H	-2.216746	2.104618	0.739198
H	-2.216746	2.104618	-0.739198
O	-0.657827	-1.827147	2.634745
H	-0.177364	-2.041917	1.827025
H	-0.852662	-0.895595	2.470126
O	-0.657827	-1.827147	-2.634745
H	-0.852662	-0.895595	-2.470126
H	-0.177364	-2.041917	-1.827025
O	3.528417	-0.598567	0.000000
H	2.866243	-1.297234	0.000000
H	2.959022	0.184092	0.000000

Table A.85: Cartesian coordinates in Angstroms (Å) for the C_s DI_4 complex at the B3LYP/haTZ level of theory.

B	0.092050	0.386917	0.000000
F	1.281428	1.126233	0.000000
F	0.396135	-0.996995	0.000000
F	-0.665102	0.696486	1.150824
F	-0.665102	0.696486	-1.150824
O	-2.753722	2.497885	0.000000
H	-2.288911	2.096546	0.744779
H	-2.288911	2.096546	-0.744779
O	-0.689034	-1.828575	2.692563
H	-0.234655	-2.058290	1.873410
H	-0.876379	-0.892954	2.542230
O	-0.689034	-1.828575	-2.692563
H	-0.876379	-0.892954	-2.542230
H	-0.234655	-2.058290	-1.873410
O	3.683281	-0.460815	0.000000
H	3.191642	-1.287394	0.000000
H	2.975728	0.202474	0.000000

Table A.86: Cartesian coordinates in Angstroms (Å) for the C_s DI_4 complex at the B3LYP–B3BJ/haTZ level of theory.

B	0.121119	0.424753	0.000000
F	1.278528	1.207904	0.000000
F	0.476748	-0.949680	0.000000
F	-0.647893	0.702081	1.150552
F	-0.647893	0.702081	-1.150552
O	-2.738552	2.444854	0.000000
H	-2.267519	2.049931	0.744306
H	-2.267519	2.049931	-0.744306
O	-0.650679	-1.823473	2.625367
H	-0.166664	-2.035068	1.818598
H	-0.853747	-0.890827	2.476575
O	-0.650679	-1.823473	-2.625367
H	-0.853747	-0.890827	-2.476575
H	-0.166664	-2.035068	-1.818598
O	3.537714	-0.578934	0.000000
H	2.872003	-1.274575	0.000000
H	2.983825	0.215120	0.000000

Table A.87: Cartesian coordinates in Angstroms (Å) for the C_s DI_4 complex at the M06–2X/haTZ level of theory.

B	0.104211	0.419504	0.000000
F	1.236269	1.222066	0.000000
F	0.488762	-0.941811	0.000000
F	-0.667718	0.673814	1.143489
F	-0.667718	0.673814	-1.143489
O	-2.667559	2.452452	0.000000
H	-2.213165	2.042475	0.743679
H	-2.213165	2.042475	-0.743679
O	-0.614392	-1.832479	2.580240
H	-0.125881	-2.019112	1.772537
H	-0.843659	-0.905980	2.447757
O	-0.614392	-1.832479	-2.580240
H	-0.843659	-0.905980	-2.447757
H	-0.125881	-2.019112	-1.772537
O	3.441707	-0.606571	0.000000
H	2.695709	-1.213432	0.000000
H	2.988910	0.245088	0.000000

Table A.88: Cartesian coordinates in Angstroms (Å) for the C_s DI_3WI_1 complex at the CCSD(T):MP2/haTZ level of theory.

B	0.257282	-0.267950	0.000000
F	1.501750	0.355633	0.000000
F	-0.471721	0.120343	1.147411
F	-0.471721	0.120343	-1.147411
F	0.412102	-1.666107	0.000000
O	-0.433639	-2.353143	-2.727495
H	-0.618798	-1.413775	-2.607369
H	-0.058446	-2.562452	-1.863433
O	-1.511462	2.550861	0.000000
H	-1.355089	1.951192	0.742025
H	-1.355089	1.951192	-0.742025
O	-0.433639	-2.353143	2.727495
H	-0.058446	-2.562452	1.863433
H	-0.618798	-1.413775	2.607369
O	1.358199	3.322049	0.000000
H	0.390625	3.281411	0.000000
H	1.599688	2.386219	0.000000

Table A.89: Cartesian coordinates in Angstroms (Å) for the C_s DI_3WI_1 complex at the MP2/haTZ level of theory.

B	0.257754	-0.268821	0.000000
F	1.501841	0.359550	0.000000
F	-0.473899	0.117846	1.149078
F	-0.473899	0.117846	-1.149078
F	0.416625	-1.668563	0.000000
O	-0.436748	-2.365204	-2.735896
H	-0.622341	-1.425949	-2.613929
H	-0.058705	-2.572400	-1.872357
O	-1.508633	2.561474	0.000000
H	-1.355017	1.959593	0.741175
H	-1.355017	1.959593	-0.741175
O	-0.436748	-2.365204	2.735896
H	-0.058705	-2.572400	1.872357
H	-0.622341	-1.425949	2.613929
O	1.359977	3.339685	0.000000
H	0.392097	3.290366	0.000000
H	1.606559	2.404984	0.000000

Table A.90: Cartesian coordinates in Angstroms (Å) for the C_s DI_3WI_1 complex at the B3LYP/haTZ level of theory.

B	0.273471	-0.271736	0.000000
F	1.518970	0.356809	0.000000
F	-0.459294	0.116731	1.150536
F	-0.459294	0.116731	-1.150536
F	0.430115	-1.672904	0.000000
O	-0.516344	-2.398359	-2.736533
H	-0.682933	-1.454794	-2.617534
H	-0.115395	-2.621170	-1.887178
O	-1.438975	2.619310	0.000000
H	-1.301894	2.020290	0.746794
H	-1.301894	2.020290	-0.746794
O	-0.516344	-2.398359	2.736533
H	-0.115395	-2.621170	1.887178
H	-0.682933	-1.454794	2.617534
O	1.449361	3.383330	0.000000
H	0.480008	3.347567	0.000000
H	1.697248	2.448953	0.000000

Table A.91: Cartesian coordinates in Angstroms (Å) for the C_s DI_3WI_1 complex at the B3LYP–B3BJ/haTZ level of theory.

B	0.289397	-0.260365	0.000000
F	1.528007	0.379659	0.000000
F	-0.446939	0.120430	1.150199
F	-0.446939	0.120430	-1.150199
F	0.460749	-1.659698	0.000000
O	-0.470561	-2.379754	-2.704063
H	-0.647857	-1.437321	-2.592349
H	-0.069900	-2.590340	-1.851378
O	-1.507176	2.552563	0.000000
H	-1.346540	1.958648	0.746234
H	-1.346540	1.958648	-0.746234
O	-0.470561	-2.379754	2.704063
H	-0.069900	-2.590340	1.851378
H	-0.647857	-1.437321	2.592349
O	1.342261	3.358444	0.000000
H	0.373673	3.303206	0.000000
H	1.609483	2.429309	0.000000

Table A.92: Cartesian coordinates in Angstroms (Å) for the C_s DI_3WI_1 complex at the M06–2X/haTZ level of theory.

B	0.288504	-0.258978	0.000000
F	1.534994	0.348240	0.000000
F	-0.433745	0.135384	1.143789
F	-0.433745	0.135384	-1.143789
F	0.425138	-1.654594	0.000000
O	-0.453639	-2.324116	-2.685670
H	-0.623123	-1.381912	-2.579801
H	-0.073865	-2.539404	-1.827006
O	-1.520533	2.507552	0.000000
H	-1.349065	1.919332	0.745777
H	-1.349065	1.919332	-0.745777
O	-0.453639	-2.324116	2.685670
H	-0.073865	-2.539404	1.827006
H	-0.623123	-1.381912	2.579801
O	1.328197	3.283398	0.000000
H	0.362311	3.249908	0.000000
H	1.581065	2.352352	0.000000

Table A.93: Cartesian coordinates in Angstroms (Å) for the C_s DI_2WI_2 complex at the CCSD(T):MP2/haTZ level of theory.

B	0.723727	-0.341745	0.000000
F	0.499883	1.047704	0.000000
F	1.434507	-0.708063	1.148679
F	-0.532487	-1.001105	0.000000
F	1.434507	-0.708063	-1.148679
O	-0.771086	-1.073851	-2.892039
H	-1.181456	-1.191535	-2.025410
H	0.162071	-1.042143	-2.636287
O	-0.771086	-1.073851	2.892039
H	0.162071	-1.042143	2.636287
H	-1.181456	-1.191535	2.025410
O	-0.771086	1.884504	-2.598906
H	-0.869019	0.958192	-2.864057
H	-0.347383	1.807494	-1.734137
O	-0.771086	1.884504	2.598906
H	-0.869019	0.958192	2.864057
H	-0.347383	1.807494	1.734137

Table A.94: Cartesian coordinates in Angstroms (Å) for the C_s DI_2WI_2 complex at the MP2/haTZ level of theory.

B	0.708692	-0.354330	0.000000
F	0.516339	1.041671	0.000000
F	1.412876	-0.737379	1.150413
F	-0.562810	-0.986844	0.000000
F	1.412876	-0.737379	-1.150413
O	-0.791953	-1.033429	-2.911466
H	-1.223227	-1.150888	-2.055052
H	0.135982	-1.027568	-2.633086
O	-0.791953	-1.033429	2.911466
H	0.135982	-1.027568	2.633086
H	-1.223227	-1.150888	2.055052
O	-0.734825	1.923505	-2.614354
H	-0.844654	0.997075	-2.877209
H	-0.315733	1.839949	-1.747820
O	-0.734825	1.923505	2.614354
H	-0.844654	0.997075	2.877209
H	-0.315733	1.839949	1.747820

Table A.95: Cartesian coordinates in Angstroms (Å) for the C_s DI_2WI_2 complex at the B3LYP/haTZ level of theory.

B	0.706281	-0.401206	0.000000
F	0.500412	0.994091	0.000000
F	1.417482	-0.777981	1.151705
F	-0.557101	-1.049358	0.000000
F	1.417482	-0.777981	-1.151705
O	-0.758370	-1.014754	-2.972321
H	-1.238962	-1.158151	-2.147174
H	0.158539	-1.016173	-2.657044
O	-0.758370	-1.014754	2.972321
H	0.158539	-1.016173	2.657044
H	-1.238962	-1.158151	2.147174
O	-0.751862	1.951256	-2.662783
H	-0.839631	1.024929	-2.937967
H	-0.342418	1.880622	-1.790630
O	-0.751862	1.951256	2.662783
H	-0.839631	1.024929	2.937967
H	-0.342418	1.880622	1.790630

Table A.96: Cartesian coordinates in Angstroms (Å) for the C_s DI_2WI_2 complex at the B3LYP–B3BJ/haTZ level of theory.

B	0.717955	-0.373826	0.000000
F	0.527375	1.023559	0.000000
F	1.421445	-0.758895	1.151101
F	-0.556944	-1.004767	0.000000
F	1.421445	-0.758895	-1.151101
O	-0.791925	-1.018216	-2.909875
H	-1.218352	-1.137184	-2.051043
H	0.142045	-1.017384	-2.652061
O	-0.791925	-1.018216	2.909875
H	0.142045	-1.017384	2.652061
H	-1.218352	-1.137184	2.051043
O	-0.747983	1.924208	-2.597418
H	-0.855775	0.999424	-2.870700
H	-0.324073	1.847076	-1.732605
O	-0.747983	1.924208	2.597418
H	-0.855775	0.999424	2.870700
H	-0.324073	1.847076	1.732605

Table A.97: Cartesian coordinates in Angstroms (Å) for the C_s DI_2WI_2 complex at the M06–2X/haTZ level of theory.

B	0.682916	-0.246865	0.000000
F	0.513661	1.145171	0.000000
F	1.373412	-0.639539	1.145405
F	-0.596442	-0.853551	0.000000
F	1.373412	-0.639539	-1.145405
O	-0.826303	-1.096794	-2.838186
H	-1.218837	-1.140564	-1.957999
H	0.114402	-1.067952	-2.619518
O	-0.826303	-1.096794	2.838186
H	0.114402	-1.067952	2.619518
H	-1.218837	-1.140564	1.957999
O	-0.678566	1.854550	-2.638946
H	-0.830772	0.930488	-2.877332
H	-0.263828	1.798946	-1.770110
O	-0.678566	1.854550	2.638946
H	-0.830772	0.930488	2.877332
H	-0.263828	1.798946	1.770110

Table A.98: Cartesian coordinates in Angstroms (Å) for the C_s DI_2WW_2 complex at the CCSD(T):MP2/haTZ level of theory.

B	-0.921627	-1.258733	0.000000
F	-2.192467	-1.806144	0.000000
F	-1.013593	0.166235	0.000000
F	-0.209865	-1.656468	1.148452
F	-0.209865	-1.656468	-1.148452
O	2.121876	2.001182	-3.536472
H	1.297706	1.546697	-3.276996
H	2.707164	1.833216	-2.793388
O	-0.209865	0.665946	2.699882
H	-0.593833	0.985994	1.873156
H	-0.087005	-0.268297	2.473159
O	-0.209865	0.665946	-2.699882
H	-0.087005	-0.268297	-2.473159
H	-0.593833	0.985994	-1.873156
O	2.121876	2.001182	3.536472
H	2.707164	1.833216	2.793388
H	1.297706	1.546697	3.276996

Table A.99: Cartesian coordinates in Angstroms (Å) for the C_s DI_2WW_2 complex at the MP2/haTZ level of theory.

B	-1.423924	0.286609	0.000000
F	-2.737832	-0.152291	0.000000
F	-0.540694	-0.837186	0.000000
F	-1.157992	1.059712	-1.150279
F	-1.157992	1.059712	1.150279
O	3.026156	-0.083981	3.593508
H	2.114428	-0.286883	3.303314
H	3.375841	0.435175	2.865308
O	0.427310	-0.637830	-2.699806
H	0.357890	-1.153097	-1.885509
H	-0.116597	0.127153	-2.454197
O	0.427310	-0.637830	2.699806
H	-0.116597	0.127153	2.454197
H	0.357890	-1.153097	1.885509
O	3.026156	-0.083981	-3.593508
H	3.375841	0.435175	-2.865308
H	2.114428	-0.286883	-3.303314

Table A.100: Cartesian coordinates in Angstroms (Å) for the C_s DI_2WW_2 complex at the B3LYP/haTZ level of theory.

B	-1.468714	0.066671	0.000000
F	-2.717600	-0.533969	0.000000
F	-0.447813	-0.934442	0.000000
F	-1.303491	0.869703	-1.152122
F	-1.303491	0.869703	1.152122
O	3.018410	0.360633	3.680115
H	2.148974	0.035148	3.367820
H	3.322227	0.933091	2.971264
O	0.539979	-0.544719	-2.714775
H	0.559943	-1.096730	-1.922588
H	-0.111932	0.125367	-2.452255
O	0.539979	-0.544719	2.714775
H	-0.111932	0.125367	2.452255
H	0.559943	-1.096730	1.922588
O	3.018410	0.360633	-3.680115
H	3.322227	0.933091	-2.971264
H	2.148974	0.035148	-3.367820

Table A.101: Cartesian coordinates in Angstroms (Å) for the C_s DI_2WW_2 complex at the B3LYP–B3BJ/haTZ level of theory.

B	-1.434680	0.288115	0.000000
F	-2.753584	-0.135182	0.000000
F	-0.563170	-0.848455	0.000000
F	-1.158549	1.058689	-1.151331
F	-1.158549	1.058689	1.151331
O	3.048199	-0.070535	3.470377
H	2.124081	-0.285943	3.225195
H	3.375450	0.435293	2.722360
O	0.425376	-0.647107	-2.689119
H	0.349036	-1.161706	-1.874736
H	-0.112064	0.127884	-2.459933
O	0.425376	-0.647107	2.689119
H	-0.112064	0.127884	2.459933
H	0.349036	-1.161706	1.874736
O	3.048199	-0.070535	-3.470377
H	3.375450	0.435293	-2.722360
H	2.124081	-0.285943	-3.225195

Table A.102: Cartesian coordinates in Angstroms (Å) for the C_s DI_2WW_2 complex at the M06–2X/haTZ level of theory.

B	-1.458842	0.054999	0.000000
F	-2.594261	0.836672	0.000000
F	-0.303899	0.890871	0.000000
F	-1.413084	-0.754144	1.144977
F	-1.413084	-0.754144	-1.144977
O	2.968680	-0.589103	-3.669581
H	2.133489	-0.187517	-3.367128
H	3.208830	-1.184724	-2.958456
O	0.576403	0.473285	2.655738
H	0.613848	0.953003	1.819404
H	-0.145978	-0.144198	2.476290
O	0.576403	0.473285	-2.655738
H	-0.145978	-0.144198	-2.476290
H	0.613848	0.953003	-1.819404
O	2.968680	-0.589103	3.669581
H	3.208830	-1.184724	2.958456
H	2.133489	-0.187517	3.367128

Table A.103: Cartesian coordinates in Angstroms (Å) for the C_1 DI_1WI_3 complex at the CCSD(T):MP2/haTZ level of theory.

B	0.758125	-0.644940	0.000980
F	2.052023	-1.168508	0.003405
F	0.053232	-1.101622	-1.124878
F	0.077895	-1.030698	1.167683
F	0.821614	0.771948	-0.044153
O	-2.516884	0.060875	1.599343
H	-1.647226	-0.366422	1.632662
H	-2.313971	0.914953	1.182637
O	-1.723776	2.051364	-0.365668
H	-0.797291	1.773490	-0.305162
H	-2.120778	1.350244	-0.909321
O	-2.732650	-0.528177	-1.238813
H	-1.823977	-0.854479	-1.327639
H	-2.872791	-0.553137	-0.277460
O	3.766044	1.155694	0.003519
H	3.502016	0.225874	0.009770
H	2.898642	1.576039	-0.015946

Table A.104: Cartesian coordinates in Angstroms (Å) for the C_1 DI_1WI_3 complex at the MP2/haTZ level of theory.

B	0.756899	-0.634165	-0.054821
F	2.056921	-1.148183	-0.081835
F	0.064525	-1.006078	-1.221598
F	0.068632	-1.116870	1.073046
F	0.810791	0.784057	0.013005
O	-2.547993	-0.084229	1.558630
H	-1.675471	-0.507918	1.571159
H	-2.340902	0.803040	1.218381
O	-1.745223	2.076554	-0.213401
H	-0.816080	1.802812	-0.169625
H	-2.128275	1.419779	-0.820362
O	-2.726207	-0.420978	-1.322792
H	-1.816505	-0.739850	-1.431356
H	-2.872491	-0.531298	-0.367511
O	3.780695	1.165296	0.103349
H	3.490609	0.244851	0.037444
H	2.924861	1.608557	0.113801

Table A.105: Cartesian coordinates in Angstroms (Å) for the C_1 DI_1WI_3 complex at the B3LYP/haTZ level of theory.

B	0.763461	-0.635864	-0.008176
F	2.072694	-1.134710	-0.011806
F	0.082475	-1.057951	-1.166618
F	0.075927	-1.091951	1.133325
F	0.801792	0.785000	0.012626
O	-2.611534	-0.131024	1.539440
H	-1.737980	-0.551155	1.578767
H	-2.409697	0.768975	1.229151
O	-1.777989	2.093878	-0.168880
H	-0.845358	1.834245	-0.112129
H	-2.148694	1.454720	-0.802671
O	-2.715856	-0.398060	-1.371261
H	-1.807539	-0.723021	-1.473843
H	-2.893918	-0.532579	-0.423895
O	3.867681	1.138211	0.019416
H	3.511986	0.237450	0.007705
H	3.057337	1.659209	0.024361

Table A.106: Cartesian coordinates in Angstroms (Å) for the C_1 DI_1WI_3 complex at the B3LYP–B3BJ/haTZ level of theory.

B	0.757040	-0.642611	-0.022961
F	2.061065	-1.150005	-0.034332
F	0.074852	-1.036003	-1.189828
F	0.064741	-1.113649	1.108593
F	0.803519	0.778530	0.024859
O	-2.568768	-0.101869	1.535954
H	-1.699553	-0.531850	1.565011
H	-2.361295	0.792687	1.212184
O	-1.744056	2.078990	-0.186328
H	-0.813858	1.811061	-0.128740
H	-2.123217	1.433204	-0.809173
O	-2.701048	-0.395545	-1.343551
H	-1.793109	-0.719896	-1.451753
H	-2.868085	-0.517903	-0.391959
O	3.775689	1.172530	0.045631
H	3.502685	0.244681	0.014934
H	2.918185	1.613023	0.056974

Table A.107: Cartesian coordinates in Angstroms (Å) for the C_1 DI_1WI_3 complex at the M06–2X/haTZ level of theory.

B	0.727103	-0.568664	-0.192823
F	2.007466	-1.098948	-0.301412
F	0.035276	-0.713158	-1.401325
F	0.017553	-1.215335	0.825755
F	0.810105	0.809336	0.115604
O	-2.378834	0.060172	1.646056
H	-1.527301	-0.395727	1.591156
H	-2.211350	0.908697	1.207200
O	-1.736406	2.020766	-0.393290
H	-0.804848	1.764749	-0.351032
H	-2.151820	1.312350	-0.909109
O	-2.786575	-0.580835	-1.162044
H	-1.869929	-0.837455	-1.334884
H	-2.854160	-0.597985	-0.194821
O	3.702161	1.122079	0.348147
H	3.483092	0.215329	0.102792
H	2.823251	1.510005	0.409544

Table A.108: Cartesian coordinates in Angstroms (Å) for the D_2 DI_4 complex at the CCSD(T):MP2/haTZ level of theory.

B	0.000000	0.000000	0.000000
F	-0.812338	0.812338	0.811963
F	0.812338	0.812338	-0.811963
F	0.812338	-0.812338	0.811963
F	-0.812338	-0.812338	-0.811963
O	0.000000	-3.520897	0.000000
H	0.505346	-2.901074	0.539701
H	-0.505346	-2.901074	-0.539701
O	3.520897	0.000000	0.000000
H	2.901074	0.505346	-0.539701
H	2.901074	-0.505346	0.539701
O	-3.520897	0.000000	0.000000
H	-2.901074	-0.505346	-0.539701
H	-2.901074	0.505346	0.539701
O	0.000000	3.520897	0.000000
H	0.505346	2.901074	-0.539701
H	-0.505346	2.901074	0.539701

Table A.109: Cartesian coordinates in Angstroms (Å) for the D_2 DI_4 complex at the MP2/haTZ level of theory.

B	0.000000	0.000000	0.000000
F	0.813625	0.813625	0.812956
F	0.813625	-0.813625	-0.812956
F	-0.813625	-0.813625	0.812956
F	-0.813625	0.813625	-0.812956
O	-3.535355	0.000000	0.000000
H	-2.914277	-0.504226	0.539618
H	-2.914277	0.504226	-0.539618
O	0.000000	-3.535359	0.000000
H	0.504213	-2.914280	-0.539631
H	-0.504213	-2.914280	0.539631
O	0.000000	3.535359	0.000000
H	-0.504213	2.914280	-0.539631
H	0.504213	2.914280	0.539631
O	3.535355	0.000000	0.000000
H	2.914277	-0.504226	-0.539618
H	2.914277	0.504226	0.539618

Table A.110: Cartesian coordinates in Angstroms (Å) for the D_2 DI_4 complex at the B3LYP/haTZ level of theory.

B	0.000000	0.000000	0.000000
F	0.815286	0.815285	0.812616
F	0.815286	-0.815285	-0.812616
F	-0.815286	-0.815285	0.812616
F	-0.815286	0.815285	-0.812616
O	-3.574209	0.000000	0.000000
H	-2.959791	-0.507337	0.544698
H	-2.959791	0.507337	-0.544698
O	0.000000	-3.574000	0.000000
H	0.506906	-2.959570	-0.545090
H	-0.506906	-2.959570	0.545090
O	0.000000	3.574000	0.000000
H	-0.506906	2.959570	-0.545090
H	0.506906	2.959570	0.545090
O	3.574209	0.000000	0.000000
H	2.959791	-0.507337	-0.544698
H	2.959791	0.507337	0.544698

Table A.111: Cartesian coordinates in Angstroms (Å) for the D_2 DI_4 complex at the B3LYP–B3BJ/haTZ level of theory.

B	0.000000	0.000000	0.000000
F	0.814395	0.814394	0.813483
F	0.814395	-0.814394	-0.813483
F	-0.814395	-0.814394	0.813483
F	-0.814395	0.814394	-0.813483
O	-3.533526	0.000000	0.000000
H	-2.918448	-0.509954	0.541524
H	-2.918448	0.509954	-0.541524
O	0.000000	-3.533503	0.000000
H	0.509821	-2.918423	-0.541649
H	-0.509821	-2.918423	0.541649
O	0.000000	3.533503	0.000000
H	-0.509821	2.918423	-0.541649
H	0.509821	2.918423	0.541649
O	3.533526	0.000000	0.000000
H	2.918448	-0.509954	-0.541524
H	2.918448	0.509954	0.541524

Table A.112: Cartesian coordinates in Angstroms (Å) for the D_2 DI_4 complex at the M06–2X/haTZ level of theory.

B	0.000000	0.000000	0.000000
F	0.810254	0.809990	0.807965
F	0.810254	-0.809990	-0.807965
F	-0.810254	-0.809990	0.807965
F	-0.810254	0.809990	-0.807965
O	-3.485661	0.000000	0.000000
H	-2.872936	-0.506482	0.543003
H	-2.872936	0.506482	-0.543003
O	0.000000	-3.485662	0.000000
H	0.506487	-2.872936	-0.542998
H	-0.506487	-2.872936	0.542998
O	0.000000	3.485662	0.000000
H	-0.506487	2.872936	-0.542998
H	0.506487	2.872936	0.542998
O	3.485661	0.000000	0.000000
H	2.872936	-0.506482	-0.543003
H	2.872936	0.506482	0.543003

Table A.113: Cartesian coordinates in Angstroms (Å) for the C_1 DI_2W_2 complex at the CCSD(T):MP2/haTZ level of theory.

B	1.921106	-0.013503	-0.097519
F	3.236391	0.158534	0.294977
F	1.066381	0.070399	1.050143
F	1.533667	0.984342	-1.007169
F	1.738654	-1.279299	-0.687034
O	-3.284422	-1.482774	-0.365993
H	-2.354613	-1.677090	-0.128379
H	-3.775554	-1.723740	0.424295
O	-0.673072	2.228948	0.279293
H	-0.286220	1.641179	0.940777
H	-0.083074	2.047578	-0.465750
O	-0.694108	-2.029580	0.467132
H	-0.004999	-2.143891	-0.202648
H	-0.319004	-1.278881	0.951418
O	-3.474133	1.471989	-0.083316
H	-3.399570	0.525989	-0.277132
H	-2.552457	1.761938	0.009847

Table A.114: Cartesian coordinates in Angstroms (Å) for the C_1 DI_2W_2 complex at the MP2/haTZ level of theory.

B	-1.449401	-1.484823	0.006989
F	-2.713693	-2.025053	0.174182
F	-1.542219	-0.051865	-0.021697
F	-0.602387	-1.847808	1.070558
F	-0.880513	-1.910673	-1.210606
O	2.696140	1.630116	-1.560234
H	1.843982	1.184202	-1.755228
H	2.557255	2.528972	-1.869551
O	0.218109	0.642964	2.172272
H	-0.484984	0.878032	1.553443
H	0.233770	-0.316425	2.041436
O	0.232333	0.502519	-2.113579
H	0.167024	-0.461261	-2.173962
H	-0.396250	0.653848	-1.390394
O	2.607793	2.120725	1.368700
H	2.686715	1.880504	0.432968
H	1.839470	1.609842	1.672868

Table A.115: Cartesian coordinates in Angstroms (Å) for the C_1 DI_2W_2 complex at the B3LYP/haTZ level of theory.

B	1.927311	-0.006811	-0.098500
F	3.237229	0.110142	0.338401
F	1.040085	0.021154	1.034865
F	1.583261	1.062845	-0.948975
F	1.731934	-1.228369	-0.776213
O	-3.285745	-1.496002	-0.277498
H	-2.351156	-1.717779	-0.069070
H	-3.770189	-1.703798	0.525687
O	-0.682827	2.292213	0.292564
H	-0.368382	1.694372	0.982226
H	-0.045656	2.103843	-0.412726
O	-0.675992	-2.113029	0.439413
H	-0.038435	-2.227420	-0.279189
H	-0.269906	-1.366874	0.910171
O	-3.476121	1.484741	-0.176386
H	-3.397453	0.526883	-0.307481
H	-2.561265	1.794056	-0.065853

Table A.116: Cartesian coordinates in Angstroms (Å) for the C_1 DI_2W_2 complex at the B3LYP–B3BJ/haTZ level of theory.

B	1.912211	-0.013472	-0.108036
F	3.232888	0.130661	0.283145
F	1.059297	0.064554	1.048236
F	1.535677	1.007381	-1.001248
F	1.706230	-1.269881	-0.719410
O	-3.265866	-1.491238	-0.372601
H	-2.336176	-1.689628	-0.120039
H	-3.781269	-1.718805	0.405545
O	-0.673235	2.248447	0.298055
H	-0.300233	1.651078	0.959324
H	-0.084539	2.072484	-0.450266
O	-0.700287	-2.039199	0.474850
H	-0.016848	-2.137177	-0.204875
H	-0.338493	-1.287357	0.968923
O	-3.449153	1.447483	-0.082479
H	-3.372283	0.501232	-0.282510
H	-2.531224	1.753602	0.014821

Table A.117: Cartesian coordinates in Angstroms (Å) for the C_1 DI_2W_2 complex at the M06–2X/haTZ level of theory.

B	2.197145	-0.019369	-0.054447
F	3.563001	0.090126	-0.203652
F	1.795121	0.475210	1.204711
F	1.528486	0.724860	-1.050241
F	1.793212	-1.363545	-0.157142
O	-3.489495	-1.618718	-0.644878
H	-2.534422	-1.620229	-0.426676
H	-3.913209	-1.900447	0.168169
O	-0.616896	1.588342	0.449451
H	0.067187	1.434715	1.116038
H	-0.097670	1.505706	-0.364424
O	-0.967790	-1.289414	0.312058
H	-0.048366	-1.508049	0.096566
H	-0.952338	-0.329404	0.444912
O	-3.550414	1.245617	0.160731
H	-3.560192	0.365221	-0.239154
H	-2.616664	1.449545	0.299411

Table A.118: Cartesian coordinates in Angstroms (Å) for the S_4 DI_4 complex at the CCSD(T):MP2/haTZ level of theory.

B	0.000000	0.000000	0.000000
F	0.870603	-0.749747	0.811696
F	-0.749747	-0.870603	-0.811696
F	-0.870603	0.749747	0.811696
F	0.749747	0.870603	-0.811696
O	0.000000	3.500566	0.324374
H	-0.497391	2.798097	0.761254
H	0.514164	2.978904	-0.302929
O	-3.500566	0.000000	-0.324374
H	-2.798097	-0.497391	-0.761254
H	-2.978904	0.514164	0.302929
O	3.500566	0.000000	-0.324374
H	2.798097	0.497391	-0.761254
H	2.978904	-0.514164	0.302929
O	0.000000	-3.500566	0.324374
H	-0.514164	-2.978904	-0.302929
H	0.497391	-2.798097	0.761254

Table A.119: Cartesian coordinates in Angstroms (Å) for the S_4 DI_4 complex at the MP2/haTZ level of theory.

B	0.000000	0.000000	0.000000
F	0.754301	0.869455	0.812047
F	0.869455	-0.754301	-0.812046
F	-0.754301	-0.869455	0.812047
F	-0.869455	0.754301	-0.812046
O	-3.510459	0.004541	0.412908
H	-2.748746	-0.462323	0.781230
H	-3.070163	0.552642	-0.246307
O	-0.004541	-3.510459	-0.412908
H	0.462323	-2.748746	-0.781230
H	-0.552642	-3.070163	0.246307
O	0.004541	3.510459	-0.412908
H	-0.462323	2.748746	-0.781230
H	0.552642	3.070163	0.246307
O	3.510459	-0.004541	0.412908
H	3.070163	-0.552642	-0.246307
H	2.748746	0.462323	0.781230

Table A.120: Cartesian coordinates in Angstroms (Å) for the S_4 DI_4 complex at the B3LYP/haTZ level of theory.

B	0.000000	0.000000	0.000000
F	-0.166833	1.141519	0.810367
F	1.141519	0.166833	-0.810367
F	0.166833	-1.141519	0.810367
F	-1.141519	-0.166833	-0.810367
O	-2.166590	-2.852640	0.550824
H	-1.337246	-2.414564	0.792652
H	-2.509658	-2.264826	-0.129856
O	2.852640	-2.166590	-0.550824
H	2.414564	-1.337246	-0.792652
H	2.264826	-2.509658	0.129856
O	-2.852640	2.166590	-0.550824
H	-2.414564	1.337246	-0.792652
H	-2.264826	2.509658	0.129856
O	2.166590	2.852640	0.550824
H	2.509658	2.264826	-0.129856
H	1.337246	2.414564	0.792652

Table A.121: Cartesian coordinates in Angstroms (Å) for the S_4 DI_4 complex at the B3LYP–B3BJ/haTZ level of theory.

B	0.000000	0.000000	0.000000
F	-0.223019	1.130020	0.813125
F	1.130020	0.223019	-0.813125
F	0.223019	-1.130020	0.813125
F	-1.130020	-0.223019	-0.813125
O	-2.161968	-2.765615	0.374934
H	-1.329600	-2.496328	0.784968
H	-2.285970	-2.058127	-0.268521
O	2.765615	-2.161968	-0.374934
H	2.496328	-1.329600	-0.784968
H	2.058127	-2.285970	0.268521
O	-2.765615	2.161968	-0.374934
H	-2.496328	1.329600	-0.784968
H	-2.058127	2.285970	0.268521
O	2.161968	2.765615	0.374934
H	2.285970	2.058127	-0.268521
H	1.329600	2.496328	0.784968

Table A.122: Cartesian coordinates in Angstroms (Å) for the S_4 DI_4 complex at the M06–2X/haTZ level of theory.

B	0.000000	0.000000	0.000000
F	-0.141868	1.136876	0.807901
F	1.136876	0.141868	-0.807901
F	0.141868	-1.136876	0.807901
F	-1.136876	-0.141868	-0.807901
O	-2.138692	-2.752901	-0.002877
H	-1.362519	-2.580780	0.540528
H	-2.163235	-1.957306	-0.544901
O	2.752901	-2.138692	0.002877
H	2.580780	-1.362519	-0.540528
H	1.957306	-2.163235	0.544901
O	-2.752901	2.138692	0.002877
H	-2.580780	1.362519	-0.540528
H	-1.957306	2.163235	0.544901
O	2.138692	2.752901	-0.002877
H	2.163235	1.957306	-0.544901
H	1.362519	2.580780	0.540528

Appendix B

Supplementary Information for Project 2

B.1 Reactants

B.1.1 C_2H ($^2\Sigma^+$)

Level of Theory:

Reference:	ROHF
Geometry:	CCSD(T)-F12a/cc-pVTZ-F12
Frequencies:	CCSD(T)-F12a/cc-pVTZ-F12
Program:	Molpro 2010.1

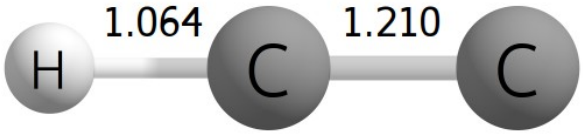

Figure B.1: C_2H

Wavefunction Diagnostics:

T_1: 0.014

D_1: 0.033

Cartesian Coordinates (Å):

C	0.000000000000	0.000000000000	-0.537842251700
C	0.000000000000	0.000000000000	0.672292694400
H	0.000000000000	0.000000000000	-1.602163091700

Rotational Constants (GHz): 43.9823985, 43.9823985

Harmonic Vibrational Frequencies (cm^{-1}):

σ^+: 3445 2021

π: 375

B.1.2 HNCO

Level of Theory:

Reference:	ROHF
Geometry:	CCSD(T)-F12a/cc-pVTZ-F12
Frequencies:	CCSD(T)-F12a/cc-pVTZ-F12
Program:	Molpro 2010.1

Wavefunction Diagnostics:

T_1: 0.015

D_1: 0.051

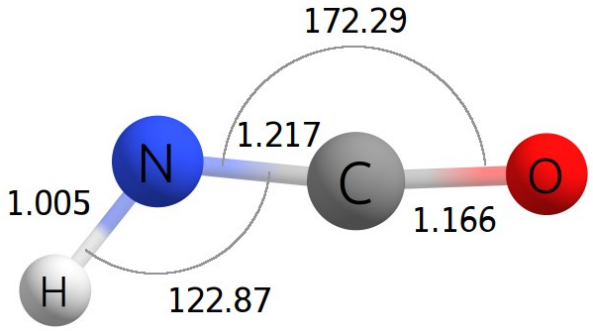

Figure B.2: HNCO

Cartesian Coordinates (Å):

N	0.000000000000	-0.080565763200	-1.207331025500
C	0.000000000000	0.038992777400	0.004189838700
H	0.000000000000	0.705936148900	-1.833005510400
O	0.000000000000	-0.003214061500	1.169291279400

Rotational Constants (GHz): 10.9175915, 11.0637799, 826.2616391

Harmonic Vibrational Frequencies (cm^{-1}):

a': 570 821 1311 2303 3686

a": 633

B.1.3 *trans*-HONO

Level of Theory:

Reference:	ROHF
Geometry:	CCSD(T)-F12a/cc-pVTZ-F12
Frequencies:	CCSD(T)-F12a/cc-pVTZ-F12
Program:	Molpro 2010.1

Wavefunction Diagnostics:

T_1: 0.018

D_1: 0.060

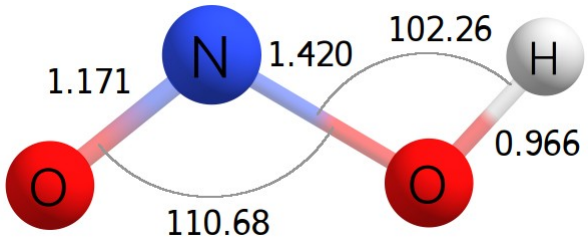

Figure B.3: *trans*-HONO

Cartesian Coordinates (Å):

N	0.000000000000	-0.495195417300	-0.146683289600
O	0.000000000000	0.224957555200	1.077562688700
O	0.000000000000	0.239107640800	-1.058334582400
H	0.000000000000	-0.484861246200	1.733149461900

Rotational Constants (GHz): 11.1752351, 12.6893335, 93.6572421

Harmonic Vibrational Frequencies (cm^{-1}):

a': 634 834 1317 1731 3777

a": 573

B.1.4 *cis*-HONO

Level of Theory:

Geometry:	MP2/aug-cc-pVTZ
Frequencies:	MP2/aug-cc-pVTZ
Program:	Psi4

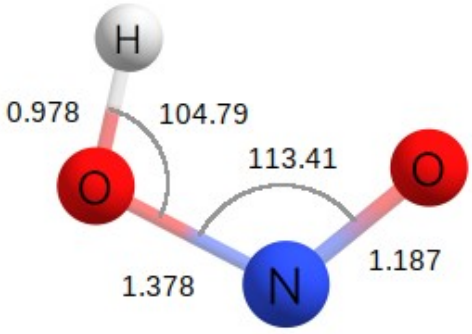

Figure B.4: *cis*-HONO

Cartesian Coordinates (Å):

N	-0.140692248224	0.500940475242	0.000000000000
O	-0.891950927124	-0.653983241826	0.000000000000
O	1.029955331231	0.302312246545	0.000000000000
H	-0.235402663668	-1.378968529740	0.000000000000

Rotational Constants (GHz): 84.47242506, 13.378268, 11.54917756

Harmonic Vibrational Frequencies (cm^{-1}):

a': 645 896 1329 1628 3608

a": 701

B.1.5 CH_3OH

Level of Theory:

Reference:	ROHF
Geometry:	CCSD(T)-F12a/cc-pVTZ-F12
Frequencies:	CCSD(T)-F12a/cc-pVTZ-F12
Program:	Molpro 2010.1

Wavefunction Diagnostics:

T_1: 0.009

D_1: 0.021

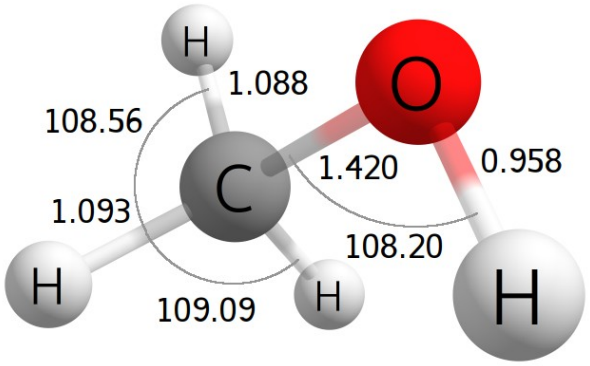

Figure B.5: CH_3OH

Cartesian Coordinates (Å):

C	0.000000000200	-0.013122552500	-0.728062632300
H	0.000000006000	1.009824433100	-1.097174950600
H	-0.890375835400	-0.520290717500	-1.108648177800
H	0.890375826000	-0.520290734500	-1.108648178400
O	0.000000000300	0.063998070000	0.689965825900
H	-0.000000004700	-0.828734362900	1.038265422500

Rotational Constants (GHz): 23.9580654, 24.8233147, 128.5452844

Harmonic Vibrational Frequencies (cm^{-1}):

a:	293	1061	1089	1181	1382	1484	1511	1521	3016	3076	3137	3864

B.1.6 C_2H_4

Level of Theory:

Reference:	ROHF
Geometry:	CCSD(T)-F12a/cc-pVTZ-F12
Frequencies:	CCSD(T)-F12a/cc-pVTZ-F12
Program:	Molpro 2010.1

Wavefunction Diagnostics:

T_1: 0.010

D_1: 0.035

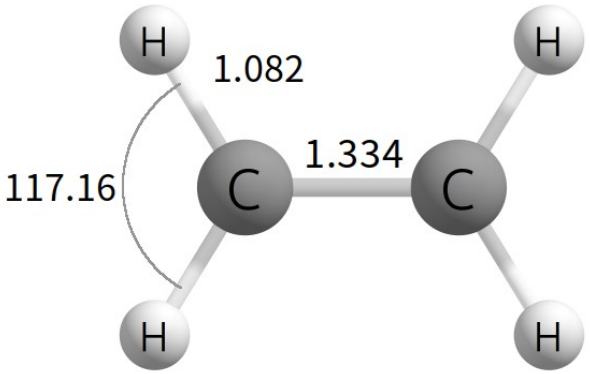

Figure B.6: C_2H_4

Cartesian Coordinates (Å):

H	-1.446173188000	-0.526428925500	0.000000000000
C	-0.364314854100	-0.558500161700	0.000000000000
C	0.364313435200	0.558501077100	0.000000000000
H	-0.101036054600	1.535684425800	0.000000000000
H	1.446166868900	0.526402477300	0.000000000000
H	0.101062021900	-1.535669798100	0.000000000000

Rotational Constants (GHz): 24.9943280, 30.1169507, 146.9467880

Harmonic Vibrational Frequencies (cm^{-1}):

a':	825	1249	1368	1478	1671	3141	3155	3222	3248
a"	950	964	1050						

B.2 Products

B.2.1 C_2H_2

Level of Theory:

Reference: ROHF

Geometry: CCSD(T)-F12a/cc-pVTZ-F12

Frequencies: CCSD(T)-F12a/cc-pVTZ-F12

Program: Molpro 2010.1

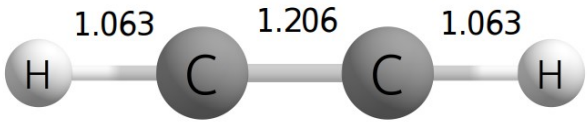

Figure B.7: C_2H_2

Wavefunction Diagnostics:

T_1: 0.012

D_1: 0.031

Cartesian Coordinates (Å):

C	0.000000000000	0.000000000000	-0.602785143000
C	0.000000000000	0.000000000000	0.602785143100
H	0.000000000000	0.000000000000	1.666005547000
H	0.000000000000	0.000000000000	-1.666005547300

Rotational Constants (GHz): 35.2829171, 35.2829171

Harmonic Vibrational Frequencies (cm^{-1}):

σ_g^+: 3502 2007

σ_u^+: 3410

π_g: 618

π_u: 749

B.2.2 NCO

Level of Theory:

Reference:	ROHF
Geometry:	CCSD(T)-F12a/cc-pVTZ-F12
Frequencies:	CCSD(T)-F12a/cc-pVTZ-F12
Program:	Molpro 2010.1

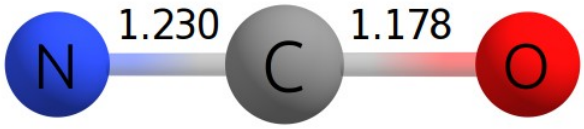

Figure B.8: NCO

Wavefunction Diagnostics:

T_1: 0.028

D_1: 0.109

Cartesian Coordinates (Å):

O	0.000000000000	0.000000000000	-1.139022616400
C	0.000000000000	0.000000000000	0.038505406300
N	0.000000000000	0.000000000000	1.268049577200

Rotational Constants (GHz): 11.6723629, 11.6723629

Harmonic Vibrational Frequencies (cm^{-1}):

a_1: 1977 1269

b_2: 581

b_1: 502

B.2.3 NO_2

Level of Theory:

Reference:	ROHF
Geometry:	CCSD(T)-F12a/cc-pVTZ-F12
Frequencies:	CCSD(T)-F12a/cc-pVTZ-F12
Program:	Molpro 2010.1

Wavefunction Diagnostics:

T_1: 0.022

D_1: 0.065

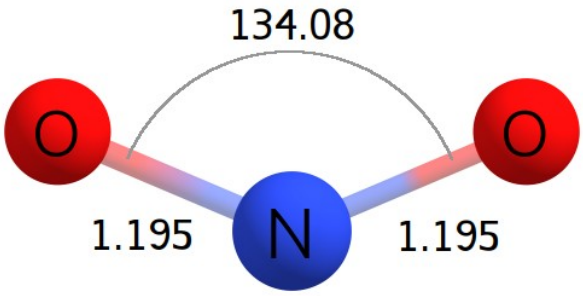

Figure B.9: NO_2

Cartesian Coordinates (Å):

O	0.000000000000	-1.100370062100	0.141917351000
N	0.000000000000	0.000000000000	-0.324215192000
O	0.000000000000	1.100370062100	0.141917351000

Rotational Constants (GHz): 12.3681279, 238.7473577, 13.0438550

Harmonic Vibrational Frequencies (cm^{-1}):

a_1: 762 1359

b_2: 1682

B.2.4 CH_3O

Level of Theory:

Reference:	ROHF
Geometry:	CCSD(T)-F12a/cc-pVTZ-F12
Frequencies:	CCSD(T)-F12a/cc-pVTZ-F12
Program:	Molpro 2010.1

Wavefunction Diagnostics:

T_1: 0.018

D_1: 0.064

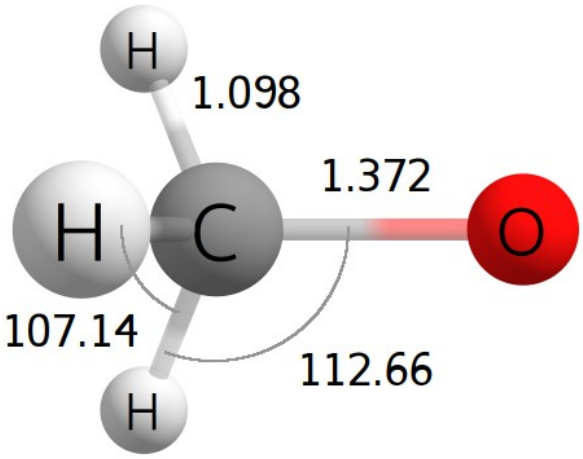

Figure B.10: CH_3O

Cartesian Coordinates (Å):

C	-0.006656777600	0.000000000000	-0.670480265700
O	-0.003790569800	0.000000000000	0.701347309300
H	-0.456511994100	0.907823768900	-1.092463965900
H	1.052517805600	0.000000000000	-0.958113985200
H	-0.456511994100	-0.907823768900	-1.092463965900

Rotational Constants (GHz): 27.6738970, 27.8629479, 157.9880589

Harmonic Vibrational Frequencies (cm^{-1}):

a': 963 1111 1387 1522 2956 3029

a": 739 1388 3040

B.2.5 CH_2OH

Level of Theory:

Geometry:	MP2/aug-cc-pVTZ
Frequencies:	MP2/aug-cc-pVTZ
Program:	Psi4

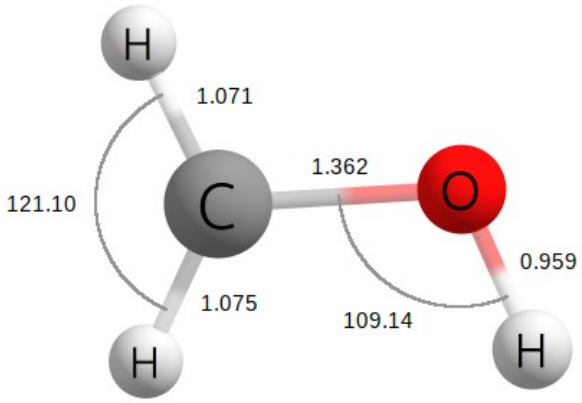

Figure B.11: CH_2OH

Cartesian Coordinates (Å):

C	0.043479616321	0.016898362841	-0.725175178004
O	-0.015235115208	-0.065950524015	0.632848136852
H	0.065712859878	0.814222329740	1.005489458859
H	-0.207738783258	0.949391499703	-1.197328907065
H	-0.133886085146	-0.918137065722	-1.217383119826

Rotational Constants (GHz): 195.03213383, 30.14272781, 26.35865559

Harmonic Vibrational Frequencies (cm^{-1}):

a:	430	619	1073	1222	1374	1520	3219	3340	3880

B.2.6 C_2H_3

Level of Theory:

Reference:	ROHF
Geometry:	CCSD(T)-F12a/cc-pVTZ-F12
Frequencies:	CCSD(T)-F12a/cc-pVTZ-F12
Program:	Molpro 2010.1

Wavefunction Diagnostics:

T_1: 0.015

D_1: 0.037

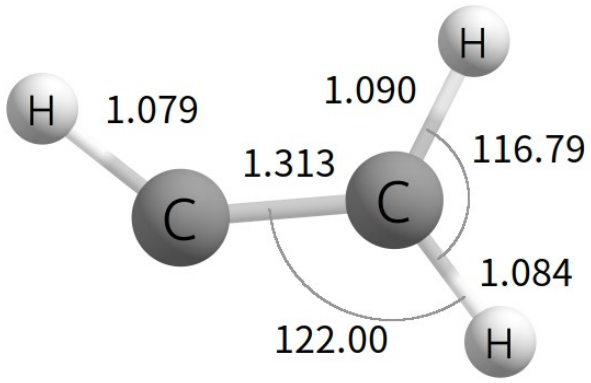

Figure B.12: C_2H_3

Cartesian Coordinates (Å):

C	-0.365263420700	-0.590682476300	0.000000000000
C	0.279716790300	0.552681348200	0.000000000000
H	-0.238899499900	1.504962138800	0.000000000000
H	1.369156015000	0.586506548500	0.000000000000
H	-0.111669804600	-1.638995384000	0.000000000000

Rotational Constants (GHz): 233.6654524, 32.5517429, 28.5714742

Harmonic Vibrational Frequencies (cm^{-1}):

a': 722 1069 1392 1618 3071 3177 3249

a": 809 911

B.3 Transition States

B.3.1 C_2H + HNCO

Level of Theory:

Reference: ROHF

Geometry: CCSD(T)-F12a/cc-pVTZ-F12

Frequencies: CCSD(T)-F12a/cc-pVTZ-F12

Program: Molpro 2010.1

Wavefunction Diagnostics:

T_1: 0.026

D_1: 0.095

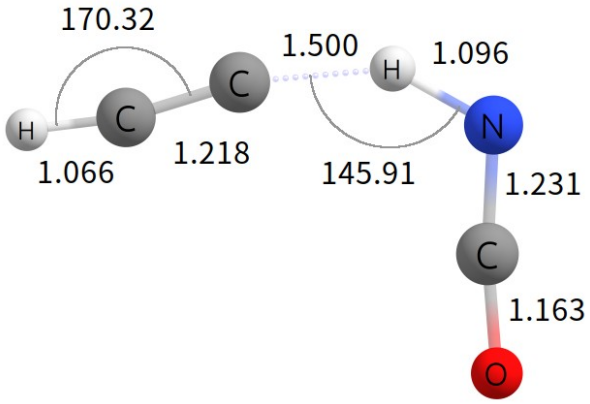

Figure B.13: C_2H + HNCO

Cartesian Coordinates (Å):

O	-0.872375158600	0.000000000000	1.902564774200
C	0.077611285500	0.000000000000	1.232060696000
N	1.163117470300	0.000000000000	0.650863886900
H	1.155581215600	0.000000000000	-0.445099605700
C	0.306348662000	0.000000000000	-1.681259489700
C	-0.573781469900	0.000000000000	-2.523215161800
H	-1.209167791600	0.000000000000	-3.379221320100

Rotational Constants (GHz): 2.4748091, 2.0771172, 12.9257552

Harmonic Vibrational Frequencies (cm^{-1}):

a': 158 416 584 742 1273 1713 1993 2237 3425 947i

a": 43 92 408 556 617

B.3.2 C_2H + *cis*-HONO

Level of Theory:

Geometry:	MP2/aug-cc-pVTZ
Frequencies:	MP2/aug-cc-pVTZ
Program:	Psi4

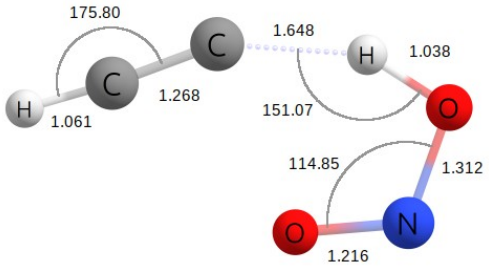

Figure B.14: C_2H + *cis*-HONO

Cartesian Coordinates (Å):

O	-0.938193288035	0.303992424446	0.001060047149
N	-0.350085191439	1.368614535539	0.000643795714
O	0.958599546775	1.275633633673	-0.000373453603
H	1.145212001793	0.254666140171	-0.000526147679
H	-0.909478308571	-3.061159596861	-0.000277234091
C	-0.244678109395	-2.234539013350	-0.000269638243
C	0.620331726235	-1.307265852142	-0.000257369246

Rotational Constants (GHz): 13.53341071, 3.50240906, 2.78234586

Harmonic Vibrational Frequencies (cm^{-1}):

a:	190*i*	93	177	239	259	603	658	764	1093	1113	1399	1583	1793	2456	3449

B.3.3 C_2H + *trans*-HONO

Level of Theory:

Reference:	ROHF
Geometry:	CCSD(T)-F12a/cc-pVTZ-F12
Frequencies:	CCSD(T)-F12a/cc-pVTZ-F12
Program:	Molpro 2010.1

Wavefunction Diagnostics:

T_1: 0.063

D_1: 0.307

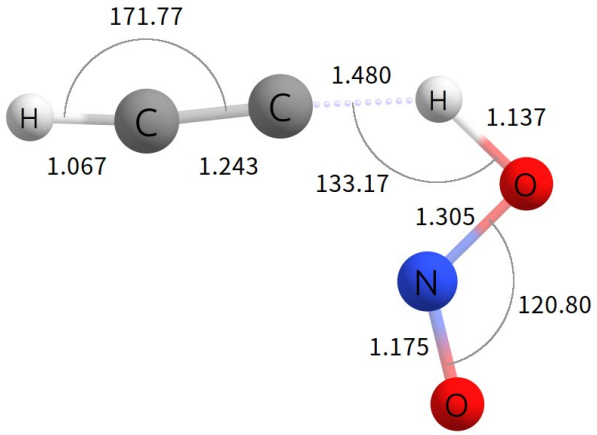

Figure B.15: C_2H + *trans*-HONO

Cartesian Coordinates (Å):

H	0.000000000000	-1.024399249200	-3.216384019500
C	0.000000000000	-0.437919922900	-2.324510242600
C	0.000000000000	0.386338738900	-1.394729710400
H	0.000000000000	1.293024481800	-0.225032035300
O	0.000000000000	1.114292044200	0.897764154500
N	0.000000000000	-0.167873490100	0.656353055700
O	0.000000000000	-0.945527146900	1.536526608100

Rotational Constants (GHz): 2.5673533, 3.2511744, 12.2062832

Harmonic Vibrational Frequencies (cm^{-1}):

a': 101 245 504 660 805 1162 1620 1814 2062 3404 1703i

a": 126 288 629 1133

B.3.4 C_2H + CH_3OH (R1)

Level of Theory:

Reference:	ROHF
Geometry:	CCSD(T)-F12a/cc-pVTZ-F12
Frequencies:	CCSD(T)-F12a/cc-pVTZ-F12
Program:	Molpro 2010.1

Wavefunction Diagnostics:

T_1: 0.033

D_1: 0.147

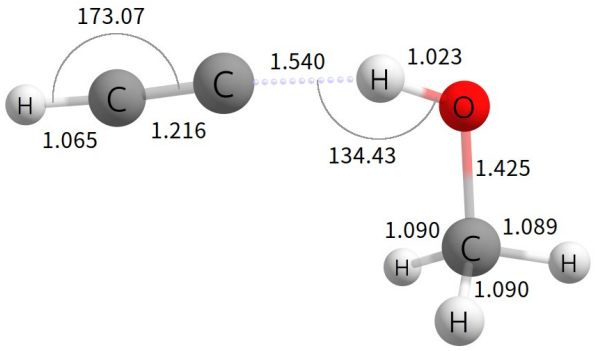

Figure B.16: C_2H + CH_3OH

Cartesian Coordinates (Å):

C	-0.136796049012	0.135383475507	1.185529601444
C	0.459300224707	-0.074977375807	2.224725919857
H	0.927382642575	-0.150819905546	3.178713334397
H	-0.758256372822	0.405906302831	-0.197791738751
O	-0.773529985043	-0.099386587801	-1.087423610640
C	0.492157269397	0.035565343791	-1.728798944281
H	0.310791175159	-0.191645382595	-2.778505392259
H	1.213451564241	-0.677865316414	-1.330184724393
H	0.883078928035	1.049046036957	-1.634845055467

Rotational Constants (GHz): 23.9580654, 24.8233147, 128.5452844

Harmonic Vibrational Frequencies (cm^{-1}):

a:	68	85	125	212	283	569	585	1027	1070	1171	1294
	1461	1484	1515	1940	2323	3037	3119	3133	3433	794i	

B.3.5 $C_2H + CH_3OH$ (R2)

Level of Theory:

Geometry:	MP2/aug-cc-pVTZ
Frequencies:	MP2/aug-cc-pVTZ
Program:	Psi4

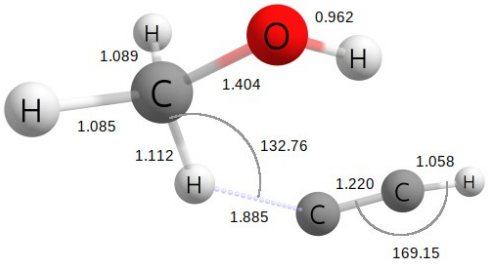

Figure B.17: $C_2H + CH_3OH$

Cartesian Coordinates (Å):

C	-0.307852120223	1.507211038556	0.209602522559
C	-1.386363987615	1.451012374396	-0.357775919536
H	1.004208781999	0.228904772617	0.652731219622
C	1.307659422490	-0.734101576948	0.187067594326
O	0.191365197660	-1.547927085382	-0.064354146998
H	1.868927476914	-0.498746475747	-0.715928024675
H	1.945536320760	-1.247557255465	0.898945974015
H	-0.479195119249	-0.991254603452	-0.471119667586
H	-2.342624979635	1.591259668514	-0.787595823113

Rotational Constants (GHz): 17.50558078, 3.59195079, 3.06225028

Harmonic Vibrational Frequencies (cm^{-1}):

a:	303i	63	89	151	173	340	474	498	1063	1091	1182	1375	1454
	1480	1523	1874	2676	3092	3173	3479	3828					

B.3.6 $C_2H + C_2H_4$

Level of Theory:

Reference:	ROHF
Geometry:	CCSD(T)-F12a/cc-pVTZ-F12
Frequencies:	CCSD(T)-F12a/cc-pVTZ-F12
Program:	Molpro 2010.1

Wavefunction Diagnostics:

T_1: 0.019

D_1: 0.064

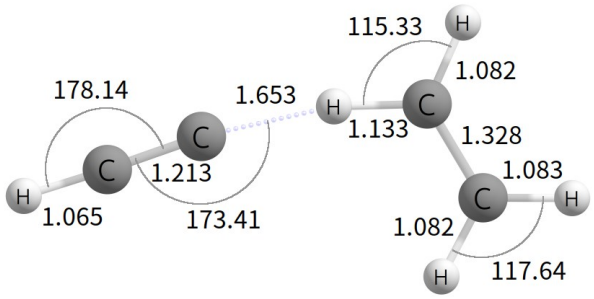

Figure B.18: $C_2H + C_2H_4$

Cartesian Coordinates (Å):

H	-3.475782783100	0.598247085600	0.000000000000
C	-2.467378185900	0.256570090800	0.000000000000
C	-1.331987159300	-0.169697077100	0.000000000000
H	0.272054861600	-0.569131967900	0.000000000000
C	1.403818902500	-0.622064219500	0.000000000000
C	2.107514997600	0.504456965800	0.000000000000
H	1.621847777000	1.471654917000	0.000000000000
H	3.190767101500	0.486014855800	0.000000000000
H	1.820651882200	-1.620892312500	0.000000000000

Rotational Constants (GHz): 34.83446821, 2.528453954, 2.357346368

Harmonic Vibrational Frequencies (cm^{-1}):

a':	269i	33	116	548	791	1190	1331	1431	1649	1936	2107	3141	3198	3235
	3440													
a":	44	167	543	907	942	975								

B.4 Pre-reactive complex

B.4.1 C_2H + CH_3OH (R1)

Level of Theory:

Geometry: CCSD(T)-F12a/cc-pVTZ-F12

Frequencies: CCSD(T)-F12a/cc-pVTZ-F12

Program: Molpro 2010.1

Wavefunction Diagnostics:

T_1: 0.023

D_1: 0.091

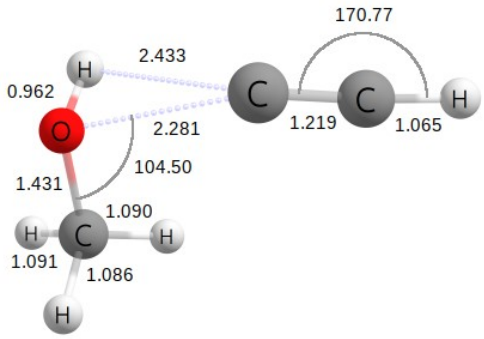

Figure B.19: C_2H + CH_3OH (R1)

Cartesian Coordinates (Å):

C	0.970275482838	0.772730881527	-0.305920740993
C	0.930053249848	1.874295133478	0.215459614495
H	0.298958920666	-1.273317841604	0.827418946689
O	-0.070673827321	-1.241440200420	-0.059996239182
C	-1.460131327862	-0.916483461871	0.042118111452
H	-2.004002569625	-1.721353159484	0.539425381860
H	-1.826363077430	-0.809212313977	-0.975052281726
H	-1.606571848696	0.022631682243	0.576534062920
H	1.018268415437	2.878534794926	0.559469741851

Harmonic Vibrational Frequencies (cm^{-1}):

a: 20 81 119 180 218 443 551 558 1038 1076 1176 1367 1473
1507 1513 1941 3037 3112 3157 3431 3819

B.4.2 C_2H + CH_3OH (R2)

Level of Theory:

Geometry:	MP2/aug-cc-pVTZ
Frequencies:	MP2/aug-cc-pVTZ
Program:	Psi4

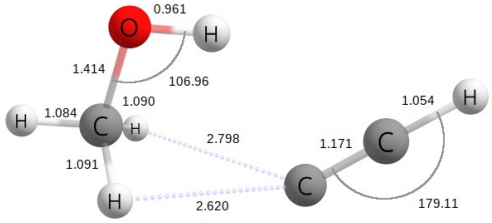

Figure B.20: C_2H + CH_3OH

Cartesian Coordinates (Å):

C	-0.355155442445	1.529473387116	-0.001292256334
C	-1.465173496488	1.548887531847	-0.375119579169
H	1.227932841668	-0.191167710510	1.180128315340
C	1.373025737357	-0.853769649700	0.325336468332
O	0.200524409641	-1.581480595426	0.016330246238
H	1.724758524212	-0.267754769410	-0.524259205395
H	2.140142695206	-1.574755760819	0.585103806704
H	-0.485135438269	-0.937617368450	-0.181681439342
H	-2.464203930311	1.582713176663	-0.710318688857

Rotational Constants (GHz): 18.55029149, 3.20695739, 2.78360581

Harmonic Vibrational Frequencies (cm^{-1}):

a:	32i	69	111	134	140	428	811	812	1075	1104	1195	1400	1493
	1536	1544	2541	3048	3095	3173	3588	3837					

B.4.3 C_2H + *cis*-HONO

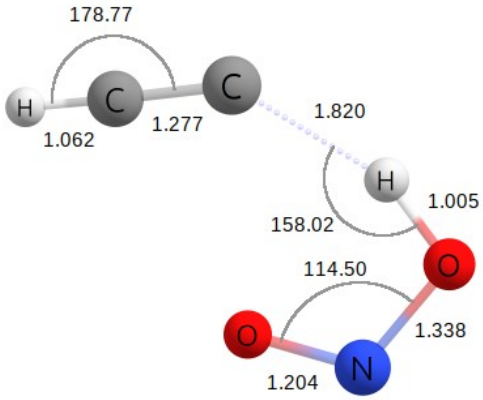

Figure B.21: C_2H + *cis*-HONO

Level of Theory:

Geometry:	MP2/aug-cc-pVTZ
Frequencies:	MP2/aug-cc-pVTZ
Program:	Psi4

Cartesian Coordinates (Å):

O	-0.995852844159	0.426239342892	0.001046306245
N	-0.373711820944	1.456752006277	0.000347180268
O	0.955782449855	1.302547919964	-0.000028808549
H	1.125753588560	0.311822591363	-0.000015238219
H	-1.002736021723	-3.026363202312	-0.000241295739
C	-0.220143716887	-2.309144291749	-0.000705799030
C	0.739635782330	-1.466722473635	-0.001280683891

Rotational Constants (GHz): 12.08098927, 3179.79488, 2517.24096

Harmonic Vibrational Frequencies (cm^{-1}):

a:	83	95	156	203	217	591	635	727	969	1036	1433	1596	1765	3045	3442

Appendix C

Supplementary Information for Project 3

Table C.1: Residuals (in cm^{-1}) of the CMA-0A data from the reference harmonic frequencies (in cm^{-1}) for $(H_2O)_2$ using natural internal coordinates with cartesian force constants.

Reference	CMA-0A										
CCSD(T)	MP2						CCSD(T)				
aTZ	DZ	haDZ	aDZ	TZ	haTZ	aTZ	DZ	haDZ	aDZ	TZ	haTZ
130.0	2.0	1.0	0.1	6.8	0.5	0.1	5.0	1.3	0.1	3.9	0.7
143.4	17.0	1.9	1.0	7.1	0.1	0.5	14.0	2.8	3.2	7.1	0.0
153.5	24.3	2.0	0.4	-0.4	0.0	0.3	25.7	1.3	-1.2	2.1	0.1
185.1	-5.8	-0.1	0.0	-2.6	0.0	-0.2	-5.3	0.5	-0.4	-2.5	-0.1
359.8	-0.2	-0.7	-0.3	0.0	0.0	0.0	-0.3	-0.8	-0.3	0.0	0.0
621.8	-9.4	-0.4	0.2	-2.0	0.3	0.3	-9.0	-0.2	0.2	-2.0	0.2
1646.3	0.1	0.0	0.0	0.1	0.0	0.0	0.1	0.0	0.0	0.1	0.1
1667.5	-0.1	0.0	0.0	0.0	0.0	0.0	-0.1	0.0	0.1	0.0	0.0
3731.1	1.2	0.0	0.1	0.1	0.0	0.0	1.8	0.0	0.1	0.1	0.0
3805.5	-0.1	0.0	0.0	0.0	0.0	0.0	0.0	0.0	0.0	0.0	0.0
3891.4	-1.1	-0.1	-0.1	-0.1	0.0	0.0	-1.7	-0.1	-0.1	-0.1	0.0
3911.1	0.0	0.0	0.0	0.0	0.0	0.0	0.1	0.1	0.0	0.0	0.0

Table C.2: Residuals (in cm^{-1}) of the CMA-0A data from the reference harmonic frequencies (in cm^{-1}) for $(NH_3)_2$ using natural internal coordinates with cartesian force constants.

Reference	CMA-0A										
CCSD(T)	MP2						CCSD(T)				
aTZ	DZ	haDZ	aDZ	TZ	haTZ	aTZ	DZ	haDZ	aDZ	TZ	haTZ
42.8	1.5	0.4	0.4	0.5	0.3	0.3	1.3	0.4	0.6	0.5	0.2
60.4	0.5	0.8	1.5	0.3	0.1	0.1	0.6	1.4	1.0	0.3	0.3
105.0	−0.1	0.2	0.2	0.1	0.1	0.1	−0.1	0.2	0.4	0.1	0.1
141.1	0.1	0.0	−0.4	0.0	0.1	0.0	0.1	0.0	−0.3	0.0	0.1
238.1	0.1	0.0	0.0	0.2	0.0	0.0	0.1	0.0	−0.2	0.1	0.0
381.9	0.4	−0.1	0.2	0.1	0.0	0.1	0.1	−0.1	0.0	0.0	0.0
1083.0	2.8	0.1	0.2	0.8	0.0	0.0	2.7	0.1	0.3	0.5	0.0
1094.3	−2.5	0.1	−0.1	−0.7	0.0	0.0	−2.5	−0.1	−0.3	−0.4	0.0
1665.0	−0.3	−0.3	−0.3	−0.3	−0.4	−0.2	−0.3	−0.3	−0.3	−0.4	−0.5
1674.1	0.0	0.0	0.1	0.0	0.0	0.0	0.1	0.0	0.0	0.0	0.0
1677.9	0.3	0.3	0.3	0.4	0.4	0.2	0.3	0.3	0.4	0.3	0.6
1696.7	0.1	0.1	0.1	0.0	0.0	0.0	0.0	0.0	0.0	0.0	0.0
3438.5	0.2	0.0	0.0	0.0	0.1	0.1	0.7	0.0	0.1	0.0	0.0
3461.1	−0.1	0.0	0.0	0.0	0.0	0.0	0.0	0.0	0.0	0.0	0.0
3562.8	−0.3	−0.1	−0.1	0.0	−0.1	−0.1	−0.7	−0.1	−0.1	−0.1	−0.1
3587.5	−0.2	0.0	0.0	−0.2	−0.3	0.0	−0.2	−0.4	0.0	−0.1	−0.1
3587.7	0.1	0.2	0.6	0.2	−0.2	0.1	0.2	−0.2	1.0	0.0	0.1
3591.3	0.0	−0.1	−0.5	0.1	0.5	0.0	0.0	0.7	−1.0	0.2	0.1

Table C.3: Residuals (in cm^{-1}) of the CMA-0A data from the reference harmonic frequencies (in cm^{-1}) for $H_2O\cdots NH_3$ using natural internal coordinates with cartesian force constants.

Reference	CMA-0A										
CCSD(T)	MP2						CCSD(T)				
aTZ	DZ	haDZ	aDZ	TZ	haTZ	aTZ	DZ	haDZ	aDZ	TZ	haTZ
19.2	4.6	0.1	0.6	0.3	0.3	0.1	4.1	0.1	0.7	0.3	0.3
166.3	2.3	2.2	0.1	0.7	0.1	0.3	2.5	1.1	0.3	1.0	0.1
175.0	−0.1	0.3	0.0	0.8	0.0	0.1	−0.2	0.2	0.0	0.6	0.1
198.3	−1.2	−1.1	0.1	−0.2	0.0	−0.2	−1.3	−0.2	−0.1	−0.6	0.0
449.5	−0.1	−0.1	0.1	−0.1	0.0	0.0	−0.1	−0.2	0.0	−0.1	0.0
698.2	−0.1	0.0	0.1	−0.2	0.1	0.1	0.0	0.0	0.0	−0.1	0.0
1112.6	0.2	0.1	0.1	0.0	0.0	0.0	0.2	0.1	0.1	0.0	0.0
1663.2	0.8	0.2	−0.2	−0.1	0.6	0.8	1.9	−0.2	0.0	0.4	−0.2
1672.9	0.4	0.2	0.2	0.1	0.1	0.1	0.4	0.3	0.3	0.2	0.1
1689.4	−1.0	−0.3	0.1	0.1	−0.6	−0.9	−2.1	0.0	−0.1	−0.5	0.1
3465.0	0.0	0.0	0.0	0.0	0.0	0.0	0.0	0.0	0.0	0.0	0.0
3590.5	0.0	0.0	0.0	−0.1	0.6	3.5	0.0	0.3	0.7	0.0	−0.1
3594.2	−0.1	0.0	0.0	0.0	0.0	8.8	0.0	−0.1	−0.2	0.0	0.0
3620.4	1.0	0.1	0.1	0.2	−0.6	−12.2	1.2	−0.2	−0.5	0.1	0.1
3883.3	−1.0	−0.1	−0.2	−0.1	−0.1	0.0	−1.1	−0.1	−0.1	−0.1	0.0

Table C.4: Residuals (in cm^{-1}) of the CMA-0A data from the reference harmonic frequencies (in cm^{-1}) for $H_2O\cdots C_2H_2$ using natural internal coordinates cartesian force constants.

Reference	CMA-0A										
CCSD(T)	MP2						CCSD(T)				
aTZ	DZ	haDZ	aDZ	TZ	haTZ	aTZ	DZ	haDZ	aDZ	TZ	haTZ
71.1	2.4	0.0	1.3	1.3	0.1	0.2	3.0	0.0	1.2	1.4	0.2
78.2	18.5	1.0	1.3	3.5	1.2	0.1	18.5	0.8	1.7	2.7	0.7
122.7	−4.6	0.6	0.2	0.8	0.2	0.0	−8.4	0.7	2.6	0.5	0.2
126.4	−8.0	−1.0	2.0	−2.7	−0.8	0.0	−4.1	−1.0	1.8	−1.9	−0.5
194.1	−0.1	0.4	2.3	0.0	0.0	0.0	0.0	0.6	5.0	0.0	0.0
621.6	0.9	0.9	0.3	0.0	0.2	0.0	0.5	1.1	0.1	0.0	0.3
627.1	3.3	0.7	0.3	1.2	0.1	0.0	2.4	1.0	−0.2	0.8	0.2
808.7	−0.8	−0.7	−0.7	−0.1	−0.2	0.0	−0.5	−0.9	−0.9	−0.1	−0.2
826.8	−2.7	−0.6	−0.9	−1.0	−0.1	0.0	−2.1	−0.9	−1.2	−0.7	−0.2
1646.9	0.0	0.0	0.0	0.0	0.0	0.0	0.0	0.1	0.1	0.0	0.0
1985.6	0.0	0.0	0.0	0.0	0.0	0.0	0.0	0.0	0.1	0.0	0.0
3360.0	1.3	1.1	0.2	0.7	1.2	0.1	0.6	0.5	0.0	0.2	0.6
3479.2	−1.3	−1.1	−0.2	−0.7	−1.2	−0.1	−0.6	−0.5	−0.1	−0.2	−0.6
3809.7	0.0	0.0	0.0	0.0	0.0	0.0	0.0	0.0	0.0	0.0	0.0
3917.4	0.0	0.0	0.0	0.0	0.0	0.0	0.0	0.0	0.0	0.0	0.0

Table C.5: Residuals (in cm^{-1}) of the CMA-0A data from the reference harmonic frequencies (in cm^{-1}) for $(HCONH_2)_2$ using natural internal coordinates cartesian force constants.

Reference	CMA-0A										
CCSD(T)	MP2						CCSD(T)				
aTZ	DZ	haDZ	aDZ	TZ	haTZ	aTZ	DZ	haDZ	aDZ	TZ	haTZ
55.1	5.4	0.0	0.2	0.2	0.1	0.1	9.9	0.1	0.2	0.7	0.0
128.9	0.2	0.6	1.9	0.0	0.4	0.2	0.3	0.1	0.9	0.0	0.1
138.5	0.2	0.0	0.0	0.3	0.1	0.0	0.3	0.0	0.0	0.1	0.0
162.7	9.0	0.5	2.8	0.4	0.5	0.3	13.3	0.0	1.3	1.1	0.1
181.1	0.0	0.1	−0.1	−0.2	0.0	0.0	0.1	0.1	0.1	−0.1	0.0
227.6	0.1	0.0	0.0	0.0	0.0	0.0	0.1	0.1	0.0	0.0	0.0
457.0	−0.5	−0.1	0.3	0.2	−0.1	0.0	−1.1	0.0	0.4	0.2	0.0
472.7	−2.7	−0.1	0.2	0.1	−0.1	−0.1	−4.2	0.0	0.4	0.0	0.0
606.3	0.1	0.0	0.1	0.0	0.0	0.0	0.1	0.0	0.1	0.0	0.0
627.8	0.2	0.0	0.0	0.0	0.0	0.0	0.2	0.0	0.1	0.0	0.0
823.2	−0.1	0.0	−0.5	−0.1	0.0	0.0	−0.2	0.0	−0.4	−0.2	0.0
856.7	0.3	0.1	0.1	0.0	0.0	0.0	0.2	0.0	0.0	−0.1	0.0
1061.6	−0.1	0.0	−0.1	0.0	0.0	0.0	−0.1	0.0	−0.1	0.0	0.0
1071.2	−0.3	−0.1	−0.4	0.0	0.0	0.0	−0.2	0.0	−0.2	0.0	0.0
1094.8	1.3	0.8	0.7	0.1	0.1	0.1	0.9	0.4	0.3	0.0	0.0
1101.7	1.4	0.8	0.6	0.1	0.1	0.1	1.0	0.4	0.3	0.0	0.0
1334.1	1.2	0.3	0.5	0.2	0.1	0.1	1.0	0.2	0.4	0.1	0.0
1348.0	1.2	0.4	0.5	0.3	0.3	0.2	1.0	0.4	0.7	0.1	0.0
1417.3	0.2	−0.3	0.4	0.0	0.0	0.0	0.0	0.0	−0.1	0.0	0.0
1417.5	0.5	0.9	0.4	0.0	−0.1	0.0	0.0	−0.1	−0.1	0.0	0.0
1640.6	4.5	1.3	1.6	1.0	0.5	0.3	3.3	0.5	0.7	0.2	0.0
1652.0	0.1	−0.1	0.0	0.2	0.1	0.0	0.1	−0.1	−0.1	0.0	0.0
1740.2	−6.4	−2.2	−2.6	−1.3	−0.6	−0.5	−4.6	−0.9	−1.1	−0.2	0.0
1769.5	−1.9	−0.8	−1.0	−0.3	−0.2	−0.2	−1.3	−0.3	−0.5	−0.1	0.0
3008.5	0.1	0.0	0.0	0.0	0.0	0.0	0.0	0.0	0.0	0.0	0.0
3010.6	0.0	0.0	0.0	0.0	0.0	0.0	0.0	0.0	0.0	0.0	0.0
3308.2	0.2	0.0	0.0	0.0	0.0	0.0	0.2	0.0	0.0	0.0	0.0
3358.1	0.2	0.0	0.0	0.0	0.0	0.0	0.3	0.0	0.1	0.0	0.0
3688.2	−0.2	−0.1	−0.1	0.0	−0.1	0.0	−0.3	−0.1	−0.1	0.0	0.0
3688.3	−0.2	0.0	−0.1	0.0	0.1	0.0	−0.3	−0.1	−0.1	0.0	0.0

Table C.6: Residuals (in cm^{-1}) of the CMA-0A data from the reference harmonic frequencies (in cm^{-1}) for $(HCOOH)_2$ using natural internal coordinates cartesian force constants.

Reference	CMA-0A										
CCSD(T)	MP2						CCSD(T)				
aTZ	DZ	haDZ	aDZ	TZ	haTZ	aTZ	DZ	haDZ	aDZ	TZ	haTZ
69.5	0.1	0.1	0.1	0.1	0.0	0.1	0.2	0.1	0.2	0.2	0.0
168.2	0.2	0.0	0.1	0.5	0.1	0.1	0.1	0.2	0.3	0.2	0.0
175.9	0.2	0.1	0.1	0.0	0.1	0.0	0.1	0.0	0.1	0.0	0.0
211.1	−0.1	0.1	0.0	−0.3	0.0	0.0	0.1	0.0	−0.1	−0.1	0.0
252.6	0.3	0.0	0.0	0.1	0.0	0.0	0.3	0.0	0.0	0.1	0.0
277.1	0.1	0.1	0.1	0.1	0.1	0.1	0.2	0.2	0.2	0.1	0.1
682.2	0.1	0.1	0.1	0.0	0.0	0.0	0.1	0.0	0.0	0.0	0.0
710.8	0.1	0.0	0.0	0.0	0.0	0.0	0.1	0.0	0.0	0.0	0.0
963.2	1.0	0.5	0.4	0.3	0.2	0.2	0.6	0.3	0.2	0.1	0.1
987.1	1.1	0.4	0.3	0.2	0.1	0.2	0.8	0.2	0.1	0.1	0.1
1080.2	−0.8	−0.4	−0.3	−0.2	−0.1	−0.1	−0.6	−0.1	−0.1	0.0	0.0
1101.7	−0.9	−0.3	−0.2	−0.1	0.0	−0.1	−0.6	−0.1	0.0	0.0	0.0
1250.2	0.9	0.4	0.4	0.8	0.5	0.3	0.7	0.2	0.2	0.1	0.0
1254.8	0.9	0.4	0.3	0.7	0.6	0.4	0.3	0.1	0.1	0.1	0.0
1401.5	3.0	1.0	0.7	1.1	1.6	0.9	0.5	0.0	0.0	0.1	0.1
1404.2	0.4	0.4	0.3	0.4	0.6	0.5	0.1	−0.1	−0.1	0.0	0.0
1458.2	−2.4	−0.7	−0.3	−1.4	−1.7	−0.9	0.0	0.0	0.1	0.0	−0.1
1486.8	1.6	0.3	0.4	−0.5	−0.6	−0.4	1.4	0.2	0.3	0.0	0.0
1708.0	−2.4	−0.8	−0.9	−0.5	−0.3	−0.3	−1.7	−0.3	−0.3	−0.1	0.0
1772.6	−0.9	−0.4	−0.5	−0.3	−0.2	−0.2	−0.6	−0.1	−0.1	−0.1	0.0
3094.7	1.5	3.0	2.4	0.1	0.1	0.1	0.7	1.5	1.1	0.0	0.0
3098.5	7.4	20.8	39.2	0.1	0.1	0.1	0.8	16.7	5.9	0.0	0.0
3190.6	−7.2	−20.4	−38.6	−0.1	−0.1	−0.1	−0.9	−16.4	−5.8	0.0	0.0
3294.4	−1.5	−2.8	−2.3	−0.1	−0.1	−0.1	−0.7	−1.4	−1.1	0.0	0.0

Table C.7: Residuals (in cm^{-1}) of the CMA-0A data from the reference harmonic frequencies (in cm^{-1}) for $(H_2O)_3$ using natural internal coordinates cartesian force constants.

Reference	CMA-0A										
CCSD(T)	MP2						CCSD(T)				
aTZ	DZ	haDZ	aDZ	TZ	haTZ	aTZ	DZ	haDZ	aDZ	TZ	haTZ
170.52	7.5	0.8	1.1	3.1	1.7	0.8	7.5	0.5	2.8	3.5	0.4
180.27	7.9	0.7	2.5	1.4	0.3	0.3	8.1	0.8	6.0	1.8	0.1
186.63	2.8	−0.3	−0.2	−0.4	−1.0	−0.4	2.0	0.0	0.3	−0.4	−0.2
196.32	−6.6	0.5	−1.9	−0.1	−0.2	−0.2	−5.7	0.4	−2.8	0.0	0.1
218.29	0.0	0.4	0.2	0.1	−0.1	0.0	0.6	0.5	1.2	0.1	0.0
238.74	1.4	−0.4	0.3	0.4	0.1	0.1	1.1	−0.5	0.3	0.4	0.1
340.2	5.2	0.1	−0.1	0.4	0.0	0.0	5.1	0.0	0.1	0.4	0.0
352.42	−4.0	0.3	−0.3	−0.4	0.1	0.1	−4.0	0.1	0.4	−0.6	0.0
438.37	2.2	0.0	0.0	0.0	0.0	0.0	2.0	0.1	0.4	−0.1	0.0
565.25	−1.6	−0.1	0.0	−0.2	0.0	0.0	−1.7	−0.1	0.1	−0.4	0.0
654.79	−1.6	−0.1	0.0	−0.3	0.0	0.0	−1.6	−0.1	0.3	−0.4	0.0
854.91	−1.2	−0.1	0.1	−0.1	0.0	0.0	−1.1	0.0	0.4	−0.2	0.0
1657.87	0.1	−0.3	−0.5	−0.4	−0.5	−0.5	0.1	−0.3	−0.5	−0.4	−0.5
1659.9	1.1	0.3	0.5	0.4	0.4	0.4	1.3	0.3	0.6	0.4	0.4
1681.57	−1.3	0.1	0.1	0.0	0.1	0.1	−1.5	0.1	0.1	0.0	0.1
3605.15	0.6	0.2	0.3	0.1	0.1	0.1	0.5	0.0	−0.1	0.0	0.0
3662.01	0.7	0.2	0.2	0.1	0.1	0.0	0.7	0.1	−0.1	0.0	0.0
3669.43	0.6	0.2	0.2	0.1	0.1	0.0	0.6	0.1	0.0	0.0	0.0
3882.83	−0.1	−0.1	−0.2	0.2	0.1	0.1	−0.4	−0.1	−0.2	0.1	0.0
3886.84	−1.0	−0.2	−0.3	−0.1	−0.1	−0.1	−0.7	−0.1	−0.2	−0.1	0.0
3887.53	−0.7	−0.2	−0.3	−0.3	−0.2	−0.1	−0.6	−0.1	−0.2	−0.1	0.0

Table C.8: Residuals (in cm^{-1}) of the CMA-0A data from the reference harmonic frequencies (in cm^{-1}) for $CH_3NO\cdots NH_3$ using natural internal coordinates cartesian force constants.

Reference	CMA-0A										
CCSD(T)	MP2						CCSD(T)				
aTZ	DZ	haDZ	aDZ	TZ	haTZ	aTZ	DZ	haDZ	aDZ	TZ	haTZ
56.15	26.8	1.3	15.1	6.2	0.3	0.1	29.3	1.0	16.5	6.8	0.3
91.61	−0.4	−0.3	−7.6	4.9	−0.1	0.1	−1.7	−0.3	−7.8	5.4	0.1
96.66	2.4	0.4	0.4	0.5	0.1	0.0	2.4	0.3	0.5	0.6	0.0
105.8	−1.4	−0.3	0.0	−0.4	0.0	0.0	−1.3	−0.2	0.0	−0.5	0.0
128.3	8.5	−0.1	−1.4	−3.1	0.0	0.0	7.5	−0.1	−2.3	−4.0	−0.2
178.21	−14.1	−0.1	−0.5	−1.7	0.0	0.0	−14.6	0.0	−0.4	−1.8	0.0
278.35	0.3	0.0	−0.1	0.2	0.0	0.0	0.3	0.1	−0.1	0.1	0.0
580.16	0.1	0.1	0.1	0.1	0.1	0.1	0.0	0.1	0.1	0.0	0.0
875.19	0.6	0.4	0.4	0.0	0.0	0.0	0.4	0.3	0.3	0.0	0.0
989.5	0.2	0.0	0.0	0.0	0.0	0.0	0.3	0.0	0.0	0.0	0.0
1086.58	0.1	0.1	0.1	0.0	0.0	0.0	0.1	0.0	0.0	0.0	0.0
1166.42	0.0	0.0	0.0	0.1	0.0	0.0	−0.1	0.1	0.0	0.0	0.0
1396.32	−0.1	0.0	0.0	0.1	0.3	0.3	0.1	0.1	0.2	0.0	0.0
1472.4	0.7	0.4	0.5	−0.1	0.1	0.1	0.9	0.5	0.8	0.1	0.0
1482.66	−0.3	0.0	0.0	0.0	0.0	0.0	−0.3	0.0	0.0	0.0	0.0
1579.79	−0.7	−0.5	−0.6	−0.1	−0.4	−0.4	−0.8	−0.8	−0.9	−0.1	0.0
1671.25	0.0	0.0	0.0	0.0	0.0	0.0	−0.1	0.0	−0.1	0.0	0.0
1684.07	0.0	0.0	0.0	0.0	0.0	0.0	0.0	0.0	0.0	0.0	0.0
3027.49	0.0	0.1	0.0	0.1	0.1	0.1	0.0	0.0	0.0	0.0	0.0
3116.72	−0.1	0.0	0.0	0.0	0.0	0.0	−0.1	0.0	0.0	0.0	0.0
3147.76	−0.1	−0.1	0.0	−0.1	−0.1	−0.1	−0.1	0.0	0.0	0.0	0.0
3454.04	0.0	0.0	0.0	0.0	0.0	0.0	0.2	0.0	0.0	0.0	0.0
3580.35	−0.2	0.0	0.0	0.0	0.0	0.0	−0.3	0.0	0.0	0.0	0.0
3587.4	0.0	0.0	0.0	0.0	0.0	0.0	0.0	0.0	0.0	0.0	0.0

Table C.9: Residuals (in cm^{-1}) of the CMA-0A data from the reference harmonic frequencies (in cm^{-1}) for $C_2H_4 \cdots C_2H_2$ using natural internal coordinates cartesian force constants.

Reference	CMA-0A							
CCSD(T)	MP2						CCSD(T)	
aTZ	DZ	haDZ	aDZ	TZ	haTZ	aTZ	DZ	haDZ
33.6	0.2	0.1	0.3	0.5	0.3	0.0	0.3	0.1
35.4	1.2	1.3	3.8	1.8	0.6	0.4	2.3	0.9
78.4	0.1	0.9	0.7	0.2	0.2	0.1	0.1	1.7
82.3	0.0	−0.8	2.0	−0.3	−0.2	0.0	0.2	−1.5
99.4	−0.3	−0.3	0.9	−0.6	−0.2	−0.1	−0.7	0.0
611.9	1.5	0.6	−0.3	0.0	0.1	0.0	0.6	0.6
613.4	0.1	0.5	0.0	0.4	0.1	0.0	0.4	0.5
775.4	−0.7	−0.5	−0.1	0.0	0.0	0.0	−0.4	−0.5
780.0	−0.5	−0.4	−0.3	−0.3	−0.1	0.0	−0.3	−0.4
817.6	0.1	0.0	0.0	0.0	0.0	0.0	0.0	0.0
936.4	0.0	0.0	0.0	0.0	0.0	0.0	0.0	0.0
967.2	0.0	0.0	0.0	0.0	0.0	0.0	0.0	0.0
1042.9	0.0	0.0	0.0	0.0	0.0	0.0	0.0	0.0
1240.8	0.0	0.0	0.0	0.0	0.0	0.0	0.0	0.0
1364.4	1.7	1.8	1.7	0.0	0.0	0.0	1.4	1.6
1472.8	0.0	0.0	0.0	0.0	0.0	0.0	0.0	0.0
1663.8	−1.3	−1.4	−1.3	0.0	0.0	0.0	−1.1	−1.2
1989.5	0.0	0.0	0.0	0.0	0.0	0.0	0.0	0.0
3131.7	0.0	0.0	0.0	0.0	0.0	0.0	0.0	0.0
3149.3	0.0	−0.1	0.0	0.0	0.0	0.0	0.0	−0.1
3213.5	0.0	0.0	0.0	0.0	0.0	0.0	0.0	0.0
3239.9	0.0	0.0	0.0	0.0	0.0	0.0	0.0	0.0
3375.3	0.3	0.4	0.0	0.3	0.4	0.1	0.1	0.1
3486.8	−0.4	−0.4	0.0	−0.3	−0.4	−0.1	−0.1	−0.1

Table C.10: Residuals (in cm^{-1}) of the CMA-0A data from the reference harmonic frequencies (in cm^{-1}) for $(C_2H_4)_2$ using natural internal coordinates cartesian force constants.

Reference	CMA-0A										
CCSD(T)	MP2						CCSD(T)				
aTZ	DZ	haDZ	aDZ	TZ	haTZ	aTZ	DZ	haDZ	aDZ	TZ	haTZ
62.6	0.2	2.1	1.8	0.1	0.3	0.1	0.1	2.6	2.3	0.1	0.7
63.1	0.2	2.1	1.8	0.1	0.3	0.1	0.0	2.5	2.2	0.4	0.7
73.7	0.0	0.0	0.0	0.0	0.0	2.2	0.0	0.0	0.0	−0.3	0.0
79.4	0.0	0.0	0.0	0.0	0.0	−2.1	0.0	0.1	0.0	0.0	0.0
103.7	−0.1	−1.2	−1.1	0.0	−0.2	0.0	0.0	−1.5	−1.3	0.0	−0.4
104.7	−0.1	−1.2	−1.1	0.0	−0.1	0.0	0.0	−1.4	−1.3	0.0	−0.4
817.4	0.1	0.0	0.1	0.0	0.0	0.0	0.0	0.0	0.1	0.0	0.0
825.4	0.1	0.0	0.0	0.0	0.0	0.0	0.0	0.0	0.0	0.0	0.0
936.0	0.0	0.0	0.0	0.0	0.0	0.0	0.0	0.0	0.0	0.0	0.0
942.5	0.0	0.1	0.0	0.0	0.1	0.0	0.0	0.1	0.0	0.0	0.0
964.3	0.0	0.0	0.0	0.0	0.0	0.0	0.0	0.0	0.0	0.0	0.0
964.3	0.0	0.0	0.0	0.0	0.0	0.0	0.0	0.0	0.0	0.0	0.0
1026.3	0.0	0.0	0.0	0.0	0.0	0.0	0.0	−0.1	0.0	0.0	0.0
1047.6	0.0	−0.1	0.0	0.0	−0.1	0.0	0.0	0.0	0.0	0.0	0.0
1242.4	−0.1	−0.1	−0.1	−0.1	−0.1	−0.1	−0.1	−0.1	−0.1	−0.1	−0.1
1242.4	0.1	0.1	0.1	0.1	0.1	0.1	0.1	0.1	0.1	0.1	0.1
1360.6	1.7	1.7	1.9	0.0	0.0	0.0	1.3	1.4	1.6	0.0	0.0
1369.6	1.9	1.7	1.8	0.0	0.0	0.0	1.6	1.5	1.6	0.0	0.0
1474.1	−0.1	−0.1	−0.1	−0.1	−0.1	−0.1	−0.1	−0.1	−0.1	−0.1	−0.1
1474.1	0.1	0.1	0.1	0.1	0.1	0.1	0.1	0.1	0.1	0.1	0.1
1661.4	−1.3	−1.2	−1.5	0.0	0.0	0.0	−1.0	−1.0	−1.3	0.0	0.0
1666.4	−1.5	−1.3	−1.3	0.0	0.0	0.0	−1.2	−1.1	−1.2	0.0	0.0
3132.1	0.0	0.0	0.0	0.0	0.0	0.0	0.0	−0.1	0.0	0.0	0.0
3132.1	0.0	0.0	0.0	0.0	0.0	0.0	0.0	0.0	0.0	0.0	0.0
3148.3	0.0	−0.1	0.0	0.0	0.0	0.0	0.0	0.0	0.0	0.0	0.0
3149.3	0.0	−0.1	0.0	0.0	0.0	0.0	0.0	−0.1	0.0	0.0	0.0
3212.1	−0.2	−0.2	−0.2	−0.2	−0.2	−0.2	−0.2	−0.2	−0.2	−0.2	−0.1
3212.1	0.0	0.0	−0.1	0.0	0.0	0.0	0.0	0.0	−0.1	0.0	0.0
3237.8	0.0	0.1	0.0	0.1	0.1	0.1	0.0	0.1	0.1	0.1	0.1
3237.9	0.1	0.2	0.2	0.2	0.2	0.2	0.1	0.2	0.2	0.2	0.2

Table C.11: Residuals (in cm^{-1}) of the CMA-0A data from the reference harmonic frequencies (in cm^{-1}) for $(HF)_2$ using natural internal coordinates cartesian force constants.

Reference	CMA-0A										
CCSD(T)	MP2						CCSD(T)				
aTZ	DZ	haDZ	aDZ	TZ	haTZ	aTZ	DZ	haDZ	aDZ	TZ	haTZ
161.2	1.3	0.2	0.9	0.8	0.1	0.1	2.3	1.3	1.6	1.0	0.1
218.2	−0.5	0.9	−0.5	−0.4	0.1	0.0	−1.2	−0.8	−0.2	−0.6	0.0
471.7	0.5	0.5	0.5	0.5	0.5	0.5	0.5	0.5	0.4	0.6	0.5
576.0	−0.1	−0.4	0.0	0.0	0.0	0.0	−0.1	0.0	0.2	−0.1	0.0
4009.2	0.3	−0.1	0.0	0.0	−0.1	−0.1	0.3	0.0	−0.2	0.0	−0.1
4088.4	−0.3	0.0	0.0	−0.1	0.0	0.0	−0.4	0.0	−0.2	−0.1	0.0

Table C.12: Residuals (in cm^{-1}) of the CMA-0A data from the reference harmonic frequencies (in cm^{-1}) for $(CH_4)_2$ using natural internal coordinates cartesian force constants.

Reference	CMA-0A										
CCSD(T)	MP2						CCSD(T)				
aTZ	DZ	haDZ	aDZ	TZ	haTZ	aTZ	DZ	haDZ	aDZ	TZ	haTZ
40.8	0.4	0.4	0.4	0.5	0.4	0.4	0.4	0.4	0.4	0.4	0.4
42.5	0.0	0.1	0.1	0.0	0.0	0.0	0.1	0.1	0.1	0.0	0.0
43.9	0.1	0.1	0.3	0.0	0.1	0.1	0.1	0.2	0.3	0.1	0.1
68.3	0.0	0.0	−0.1	0.0	0.0	0.0	0.0	0.0	−0.1	0.0	0.0
69.3	0.1	0.1	0.0	0.0	0.0	0.0	0.0	0.0	0.0	0.0	0.0
69.6	0.0	0.1	0.1	0.1	0.1	0.1	0.1	0.1	0.1	0.1	0.1
1344.3	0.1	−0.1	−0.1	−0.1	−0.1	−0.1	0.0	−0.1	−0.1	−0.1	−0.1
1348.5	−0.2	−0.4	−0.4	−0.5	−0.4	−1.0	−0.3	−0.5	−0.6	−1.0	−0.4
1348.5	0.3	0.1	0.1	0.1	0.2	0.4	0.3	0.1	0.1	0.5	0.1
1351.3	−0.2	−0.6	−0.5	0.1	−0.3	0.0	−0.3	−0.3	−0.1	0.1	−0.3
1351.4	0.9	0.9	0.7	0.3	0.4	0.4	0.8	0.7	0.6	0.3	0.4
1353.7	0.6	0.5	0.5	0.3	0.4	0.4	0.5	0.4	0.5	0.3	0.4
1568.0	−0.3	−0.3	−0.3	−0.2	−0.2	−0.2	−0.3	−0.3	−0.3	−0.2	−0.2
1568.1	0.3	0.2	0.2	0.2	0.2	0.2	0.3	0.3	0.2	0.2	0.2
1575.5	−0.3	−0.3	−0.3	−0.4	−0.3	−0.2	−0.4	−0.3	−0.3	−0.4	−0.4
1575.6	0.4	0.3	0.4	0.4	0.4	0.3	0.4	0.3	0.3	0.5	0.4
3026.8	0.0	0.0	0.0	0.0	0.0	0.0	0.0	0.0	0.0	0.0	0.0
3027.1	0.0	0.0	0.0	0.0	0.0	0.0	0.0	0.0	0.0	0.0	0.0
3145.0	−0.4	−1.2	−0.4	−0.7	−1.0	−0.9	−0.4	−0.9	−0.5	−0.6	−0.8
3145.0	−0.2	−0.2	−0.1	−0.3	−0.2	−0.1	−0.2	−0.1	−0.1	−0.2	−0.1
3145.6	0.0	0.1	0.2	0.3	0.2	0.2	0.1	0.3	0.2	0.3	0.3
3146.9	−0.2	0.0	−0.1	0.1	0.0	0.1	−0.5	−0.3	−0.4	0.0	0.0
3146.9	−0.2	0.3	−0.2	0.1	0.2	0.1	−0.1	0.2	−0.1	0.1	0.1
3146.9	0.4	0.8	0.4	0.5	0.7	0.7	0.7	0.8	0.9	0.5	0.7

Table C.13: Residuals (in cm^{-1}) of the CMA-0A data from the reference harmonic frequencies (in cm^{-1}) for $CH_3COOH\cdots H_2O$ using natural internal coordinates cartesian force constants.

Reference	CMA-0A
CCSD(T)	MP2
aTZ	haTZ
70.47	0.1
175.62	0.1
196.64	0.0
275.38	0.1
363.3	0.1
439.07	0.0
493.76	0.0
615.58	0.0
654.58	0.0
886.22	0.7
894.81	−0.6
1025.04	0.0
1175.72	0.0
1302.08	0.1
1401.51	0.0
1459.27	0.5
1485.84	−0.4
1494.83	0.0
1648.34	0.1
1778.75	−0.2
3058.61	0.0
3130.96	0.0
3173.89	0.0
3452.24	0.0
3650.8	0.0
3881.37	0.0

Table C.14: Residuals (in cm^{-1}) of the CMA-0A data from the reference harmonic frequencies (in cm^{-1}) for Benzene$\cdots$HCN using natural internal coordinates cartesian force constants.

Reference	CMA-0A	
CCSD(T)	MP2	
aTZ	haTZ	aTZ
13.1	1.5	0.9
13.5	2.4	1.4
80.8	0.2	0.0
81.4	0.3	0.2
100.2	−0.1	0.0
394.9	0.0	0.0
394.9	0.0	0.0
557.4	19.6	0.3
604.8	0.0	0.0
604.9	0.0	0.0
697.7	0.0	0.0
728.5	−1.5	−2.3
728.7	1.7	2.4
859.1	0.0	0.0
859.2	0.0	0.0
915.2	−10.4	−0.2
970.7	0.0	0.0
970.7	0.0	0.0
1001.0	0.0	0.0
1011.5	−1.6	0.0
1050.5	0.0	0.0
1050.8	0.0	0.0
1156.4	4.0	4.3
1186.9	0.0	0.0
1187.1	0.0	0.0
1328.2	−3.5	−3.7
1357.3	0.0	0.0
1498.2	0.0	0.0
1498.3	0.0	0.0
1625.3	0.0	0.0
1625.3	0.0	0.0
2106.2	0.2	0.1
3163.8	0.0	0.0
3178.1	0.0	0.0
3178.2	0.0	0.0
3194.4	0.0	0.0
3194.5	0.0	0.0
3204.7	0.0	0.0
3403.2	−0.1	0.0

Table C.15: Residuals (in cm^{-1}) of the CMA-0A data from the reference harmonic frequencies (in cm^{-1}) for Benzene$\cdots NH_3$ using natural internal coordinates cartesian force constants.

Reference	CMA-0A	
CCSD(T)	MP2	
aTZ	haTZ	aTZ
13.7	8.2	1.6
27.6	−1.6	7.2
46.3	−0.1	0.7
71.2	−0.2	−2.1
95.0	0.1	−0.2
139.3	−0.2	−0.3
395.0	0.0	0.0
395.7	0.0	0.0
548.0	17.3	0.2
604.8	0.0	0.0
604.9	0.0	0.0
685.0	−2.4	0.0
853.0	0.0	0.0
853.4	0.0	0.0
896.6	−7.4	−0.1
963.1	−0.6	0.0
963.9	−0.4	0.0
1001.9	0.0	0.0
1009.1	−0.3	0.0
1050.3	0.0	0.0
1050.4	0.4	0.7
1074.9	−0.4	−0.7
1154.0	4.2	4.4
1184.9	0.0	0.0
1185.3	0.0	0.0
1327.3	−3.6	−3.9
1343.3	0.0	0.0
1496.5	0.0	0.0
1496.8	0.0	0.0
1626.1	0.0	0.0
1626.4	0.0	0.0
1668.3	−0.6	−0.6
1669.1	0.7	0.7
3159.3	0.0	0.0
3173.7	0.0	0.0
3175.1	0.0	0.0
3190.9	0.0	0.0
3191.9	0.0	0.0
3202.5	0.0	0.0
3456.6	0.1	0.1
3581.2	−0.3	−0.3
3585.5	0.2	0.3

Table C.16: Residuals (in cm^{-1}) of the CMA-0A data from the reference harmonic frequencies (in cm^{-1}) for Benzene$\cdots H_2O$ using natural internal coordinates cartesian force constants.

Reference	CMA-0A	
CCSD(T)	MP2	
aTZ	haTZ	aTZ
16.3	3.7	2.3
48.9	0.8	0.7
54.5	−0.8	−0.3
97.9	0.0	0.1
138.3	0.4	0.5
237.5	0.5	0.5
394.0	0.0	0.0
396.0	0.1	0.0
554.8	10.2	0.2
604.8	0.1	0.1
605.2	0.0	0.0
687.4	0.0	0.0
853.3	0.0	0.0
853.8	0.0	0.0
899.5	−6.2	−0.1
962.3	0.0	0.0
964.3	0.0	0.0
1001.6	0.0	0.0
1009.5	−0.1	0.0
1049.9	0.1	0.0
1050.7	0.0	0.0
1154.5	4.2	4.5
1185.2	0.0	0.1
1186.0	0.0	0.0
1326.3	−3.7	−3.9
1342.4	0.0	0.0
1496.1	0.0	0.0
1496.3	0.0	0.0
1624.9	0.0	0.0
1625.9	0.0	0.0
1648.8	0.1	0.1
3161.3	0.0	0.0
3175.6	0.0	0.0
3176.9	0.0	0.0
3192.1	0.0	0.0
3193.7	0.0	−0.2
3203.7	0.0	0.2
3786.6	0.0	0.0
3895.0	0.1	0.1

Table C.17: Residuals (in cm^{-1}) of the CMA-0A data from the reference harmonic frequencies (in cm^{-1}) for Benzene$\cdots CH_4$ using natural internal coordinates cartesian force constants.

Reference	CMA-0A	
CCSD(T)	MP2	
aTZ	haTZ	aTZ
18.0	2.2	4.9
22.5	0.1	4.1
25.0	1.0	2.4
78.5	0.4	−1.1
78.8	1.2	0.3
82.4	−1.9	−1.8
394.9	0.0	0.1
395.1	0.0	−0.1
541.7	19.1	0.2
604.6	0.0	0.0
605.6	0.0	0.0
682.1	−0.5	0.0
850.9	0.0	0.0
851.0	0.0	0.0
900.4	−10.3	−0.1
961.9	0.0	0.0
962.0	0.0	0.0
1002.2	0.0	0.0
1008.5	−1.0	0.0
1054.4	1.0	0.9
1056.5	−0.8	−0.8
1153.5	4.1	4.4
1184.9	0.0	0.0
1185.0	0.0	0.0
1328.8	−3.6	−3.8
1343.1	−0.2	−0.2
1346.0	0.0	0.0
1350.9	−1.1	−1.1
1351.0	1.4	1.4
1497.8	−0.1	0.0
1498.3	−0.1	−0.1
1571.2	−0.6	−0.4
1571.2	0.6	0.4
1627.3	0.0	0.0
1627.4	0.0	0.0
3024.0	0.0	0.0
3138.6	−0.3	−0.4
3138.6	0.1	0.2
3155.0	−0.1	−0.1
3157.4	−0.1	−0.2
3172.6	0.0	0.0
3172.6	0.3	0.2
3190.3	−0.1	0.0
3190.3	0.0	0.1
3201.0	0.2	0.1